SAPIENZA
UNIVERSITÀ DI ROMA

DOTTORATO DI RICERCA IN ENERGIA E AMBIENTE
PhD Program in ENERGY and ENVIRONMENT

XXXVII Cycle

Multiscale Thermal-Hydraulic Analysis of Experimental Facilities in Support of the Lead-Cooled Fast Reactors Development

PhD Thesis

Scuola di Dottorato in Scienze e Tecnologie per l'Innovazione Industriale
Facoltà di Ingegneria Civile e Industriale
Dipartimento di Ingegneria Astronautica, Elettrica ed Energetica

Tommaso Del Moro

Advisor
Prof. Ing. Fabio Giannetti

Co-Advisor/Tutor
Dr. Ing. Mariano Tarantino
Dr. Cristiano Ciurluini

A.A. 2023-2024

(Page intentionally left blank)

SOMMARIO

L'energia nucleare è un pilastro fondamentale per ridurre le emissioni globali di carbonio e favorire la transizione verso un sistema di produzione energetica sostenibile. Nell'ambito dei reattori nucleari avanzati, i reattori veloci raffreddati a piombo (LFR, Lead-cooled Fast Reactors) rappresentano una delle tecnologie più promettenti, individuata dal Generation-IV International Forum (GIF), grazie alle loro caratteristiche avanzate in termini di sicurezza, efficienza del combustibile e riduzione dei rifiuti. Gli LFR mirano a raggiungere questi obiettivi grazie all'utilizzo di metalli liquidi pesanti (HLM, Heavy Liquid Metal) come refrigeranti e di combustibili a ossido misto (MOX, Mixed OXide), sfruttando il plutonio derivante dal riprocessamento del combustibile esausto dei reattori delle precedenti generazioni. Questo approccio consente di ridurre i rischi di proliferazione e contribuisce alla chiusura del ciclo del combustibile, rendendo questa tipologia di reattori ancora più sostenibile rispetto agli attuali riducendo al minimo la quantità di rifiuti a lunga vita. Per soddisfare tutti gli obiettivi fissati dal GIF, gli LFR devono essere economicamente competitivi con le altre tecnologie esistenti. Questo aspetto è ottenuto principalmente grazie all'uso dei refrigeranti HLM, che semplificano il design eliminando la necessità di pressurizzare il sistema primario e riducendo significativamente la pressurizzazione del contenimento in caso di incidente di perdita del refrigerante (LOCA, Loss Of Coolant Accident) rispetto ai reattori ad acqua leggera (LWR, Light Water Reactor). Gli HLM consentono anche di operare a temperature più elevate, migliorando l'efficienza del ciclo termodinamico e contribuendo all'economia degli LFR. Inoltre, le buone proprietà termofisiche degli HLM permettono un uso estensivo dei sistemi di sicurezza passivi, che operano senza input energetici esterni.

Tuttavia, gli LFR presentano diverse sfide interdisciplinari, che coinvolgono scienze dei materiali e chimica dei refrigeranti, in particolare per quanto riguarda i fenomeni di erosione e corrosione dovuti all'esposizione prolungata dei materiali strutturali agli HLM, che contaminano il refrigerante con ossidi metallici. Studi di irraggiamento sono necessari per valutare la resistenza dei materiali strutturali ai flussi di neutroni veloci e il loro impatto sulle proprietà dei materiali. È necessario sviluppare strumenti in grado di resistere a temperature elevate, ad alti valori di fluenza neutronica a spettro veloce e in un ambiente corrosivo e opaco. La sfida oggetto di questa tesi è la termoidraulica degli HLM. Fenomeni come il mescolamento in piscina e la stratificazione termica, le transizioni dalla convezione forzata a quella naturale e la termoidraulica degli elementi di combustibile devono essere analizzati sia dal punto di vista sperimentale che numerico.

Numerose organizzazioni in tutto il mondo hanno intrapreso attività sperimentali estensive per affrontare queste sfide. Il centro di ricerca ENEA di Brasimone è una delle istituzioni più attive in questo campo, sfruttando i suoi impianti sperimentali e il know-how sviluppato sugli HLM fin dai primi anni 2000. Tuttavia, l'analisi dei suddetti fenomeni termoidraulici deve essere affrontata anche dal punto di vista numerico e di simulazioni per condurre analisi di sicurezza complete ai fini del licensing dei reattori. I complessi fenomeni che si verificano negli LFR e nei loro sistemi di sicurezza presentano sfide uniche per la simulazione e la modellizzazione, poiché coinvolgono sia fenomeni locali, come i punti caldi all'interno delle barre di combustibile, sia processi su larga scala come la termoidraulica della piscina. La natura multiscala della termoidraulica degli LFR richiede lo sviluppo di strumenti numerici capaci di affrontare fenomeni a livello locale attraverso i codici di fluidodinamica computazionale (CFD, Computational Fluid Dynamics) e a livello di sistema mediante i codici di termoidraulica di sistema (STH, System Thermal-Hydraulic).

Entrambe le famiglie di codici richiedono un'ampia validazione, poiché i codici CFD non sono attualmente validati per le applicazioni nucleari, mentre alcuni codici STH sono principalmente validati per l'analisi termoidraulica degli LWR. Questa tesi affronta queste sfide sviluppando uno strumento di simulazione multiscala che accoppia il codice CFD Ansys CFX con il codice STH RELAP5/Mod3.3. Lo strumento accoppiato consente una simulazione dettagliata del comportamento degli LFR, combinando la modellizzazione a livello di sistema con l'analisi locale ad alta fedeltà dei componenti chiave, come il nocciolo e le zone in cui dominano effetti tridimensionali, come nelle configurazioni a piscina. Dopo una revisione della letteratura esistente, i metodi di accoppiamento e le lacune negli approcci di modellizzazione attuali sono identificati, e vengono valutate le applicazioni precedenti di RELAP5 e CFX in ambienti HLM. Gli approcci di accoppiamento sviluppati in questa tesi – schemi espliciti e semi-impliciti per l'avanzamento temporale e

approcci di discretizzazione del dominio per decomposizione e sovrapposizione – sono descritti, insieme a una discussione sui vantaggi e svantaggi di ciascun metodo.

Il lavoro prosegue con la validazione dello strumento numerico multiscala rispetto ai dati sperimentali provenienti da impianti rilevanti per lo sviluppo delle tecnologie LFR e di strumenti numerici. La prima attività di validazione riguarda l'impianto SIRIO, un circuito raffreddato ad acqua progettato per dimostrare la fattibilità di un innovativo sistema passivo di rimozione del calore di decadimento (DHR, Decay Heat Removal system). Il suo principio di funzionamento si basa sulla graduale degradazione della capacità di trasferimento del calore dell'Isolation Condenser (IC) grazie a gas non condensabili. Questo meccanismo dovrebbe garantire il raffreddamento a lungo termine (almeno 24 ore) senza l'intervento dell'operatore, prevenendo allo stesso tempo il congelamento anticipato del piombo. In questo caso, solo il codice RELAP5 è utilizzato per la validazione, poiché i principali fenomeni investigati sono la circolazione naturale, l'ebollizione in piscina e la condensazione in presenza di gas non condensabili, fenomeni che generalmente non rientrano nel campo di applicazione dei codici CFD. Le peculiarità dell'esperimento hanno reso necessaria un'attività di sviluppo del codice stand-alone, poiché questi fenomeni non vengono solitamente studiati in dettaglio con i codici STH. La tesi si concentra poi sull'applicazione dello strumento accoppiato per simulare la transizione dalla circolazione forzata a quella naturale in impianti raffreddati con lega eutettica Piombo-Bismuto (LBE, Lead-Bismuth Eutectic), come NACIE-UP e TALL-3D. Sebbene abbiano caratteristiche simili, come il refrigerante e le condizioni operative, differiscono per alcuni aspetti rilevanti. Ad esempio, la sorgente di calore di NACIE-UP è un simulatore di fascio di combustibile avvolto con filo, dove il trasferimento di calore nell'elemento di combustibile è un aspetto rilevante, mentre TALL-3D presenta due gambe verticali calde, consentendo l'inversione e l'oscillazione della portata tra una gamba e l'altra. Lo studio della fluidodinamica e dei regimi di trasferimento termico all'interno di una sezione di prova a piscina, come il mescolamento e la stratificazione termica della piscina, è il principale oggetto d'indagine dell'impianto.

Lo strumento accoppiato validato viene quindi applicato all'analisi termoidraulica dell'impianto sperimentale ATHENA. ATHENA, attualmente in costruzione, rappresenta una tipica configurazione LFR a piscina e differisce significativamente dagli impianti precedentemente descritti a causa delle sue dimensioni e del volume di HLM. Mentre NACIE-UP e TALL-3D contengono meno di 2 tonnellate di LBE, ATHENA ospiterà circa 800 tonnellate di piombo. ATHENA permette lo studio della chimica del refrigerante e del controllo dell'ossigeno in un grande ambiente a piscina, così come l'analisi termoidraulica di un simulatore di nocciolo composto da più elementi di combustibile, delle prestazioni della pompa meccanica e dello scambiatore di calore. Dopo la presentazione dei modelli numerici e del dimensionamento del Main Heat eXchanger (MHX) di ATHENA, vengono analizzati lo stato stazionario e due transitori di riferimento, ossia la perdita del pozzo termico (LOHS, Loss Of Heat Sink) e l'incidente di perdita di flusso (LOFA, Loss Of Flow Accident), attraverso il codice RELAP5. Il transitorio LOFA viene simulato anche utilizzando lo strumento accoppiato poiché si prevede che possa beneficiare maggiormente del contributo del codice CFD. In particolare, le basse velocità all'interno del nocciolo rendono più rilevanti fenomeni come la distribuzione del flusso tra gli elementi di combustibile e la conduzione termica all'interno del fluido, fenomeno che il codice RELAP5 trascura.

Le attività future per lo sviluppo di questo strumento di accoppiamento includeranno il test e il confronto dei suoi risultati con i dati sperimentali provenienti da ATHENA e CIRCE, un impianto a piscina refrigerato a LBE appartenente ad ENEA. Essendo due impianti sperimentali a effetti integrali (IET, Integral Effect Test) raffreddati con HLM, consentiranno un ulteriore perfezionamento e validazione dello strumento, migliorandone l'accuratezza e le capacità nel fornire supporto per le analisi su scala reattore.

ABSTRACT

Nuclear energy is a key pillar for reducing global carbon emissions and transitioning toward a sustainable energy production system. Within the framework of advanced nuclear reactors, Lead-cooled Fast Reactors (LFRs) represent one of the most promising technologies among those identified by the Generation-IV International Forum (GIF), offering significant potential due to their enhanced safety features, fuel efficiency, and waste reduction. LFRs aim to meet these objectives through to the use of Heavy Liquid Metals (HLMs) as coolants and the Mixed OXide (MOX) fuel, utilizing plutonium from reprocessed of previous generations reactors' spent fuel. This approach reduces the proliferation risk and contributes to closing the fuel cycle, making this type of reactors even more sustainable than current by minimizing the amount of long-lived waste. To meet all the goals set by the GIF, LFRs must also be economically viable, meaning that they should be competitive with the other existing technologies. This feature is achieved mainly due to the use of HLM coolants, which simplify the design by eliminating the need to pressurize the primary system, and significantly reducing the containment pressurization in case of Loss Of Coolant Accident (LOCA) compared to Light Water Reactors (LWRs). HLM also enables operation at higher temperatures, improving the efficiency of the thermodynamic cycle and contributing to the economics of LFRs. Moreover, the good thermophysical properties of HLMs allow for extensive use of passive safety systems, that operate without external energy input.

However, LFRs present several challenges that span multiple disciplines, such as material science and coolant chemistry, particularly regarding erosion and corrosion phenomena due to prolonged exposure of structural materials to HLMs, contaminating the coolant with metal oxides. Irradiation studies are necessary to assess the resistance of structural materials to fast neutrons fluxes and their impact on material properties. Instrumentation must also be developed since it must withstand high temperatures, high values of fast spectrum neutron fluence, and a corrosive and opaque environment. The challenge object of this thesis is the HLMs Thermal-Hydraulics (TH). Phenomena like pool mixing and thermal stratification, transitions from forced to natural convection, and fuel assembly TH must be analyzed from both experimental and numerical perspectives.

Many organizations worldwide have undertaken extensive experimental activities to address these challenges. The ENEA Brasimone research center is one of the most active institutions in this area, leveraging its experimental fleet and the know-how about HLMs developed since the early 2000s. However, the analysis of the aforementioned TH phenomena must also be addressed from the numerical and simulation point of view to conduct comprehensive safety analyses for reactor licensing. The complex phenomena occurring in LFRs and their safety systems present unique challenges for simulation and modelling, since they involve both local phenomena, such as hot spots within the fuel rods, and large-scale processes such as pool thermal-hydraulics. The multiscale nature of LFR TH necessitates the development of numerical tools capable of addressing both local-level phenomena through Computational Fluid Dynamics (CFD) codes, and at system-level through System Thermal-Hydraulic (STH) codes.

Both families of codes require extensive validation since CFD codes are not currently validated for nuclear applications, while certain STH codes are validated primarily for LWRs TH analysis. This thesis addresses these challenges by developing a novel multiscale simulation tool that couples the CFD code Ansys CFX with the STH code RELAP5/Mod3.3. The coupled tool enables detailed simulation of LFR behaviour by combining system-level modelling with local, high-fidelity analysis of key components, such as the core and regions where 3D effects are dominant, as in pool configurations. After a review of existing literature, the coupling methods and the gaps in current modelling approaches, previous applications of RELAP5 and CFX in HLM environments are assessed. The coupling approaches developed in this thesis – explicit and semi-implicit time-advancing schemes, and domain decomposition and overlapping discretization approaches – are described, along with a discussion of the advantages and drawbacks of each method.

The work continues with the validation of the multiscale numerical tool against experimental data from facilities relevant to the development of LFR technologies and numerical tools. The first validation activity

involves the SIRIO facility, a water-cooled loop that aims at demonstrating the feasibility of an innovative passive Decay Heat Removal system (DHR). Its working principle is based on the gradual degradation of the heat transfer capability of the Isolation Condenser (IC) thanks to non-condensable gases. This mechanism should ensure the long-term cooling (at least 24 hours) without the intervention of the operator, while preventing the early freezing of the lead. In this case, only the RELAP5 code is used for validation since the main phenomena investigated are natural circulation, pool boiling, and condensation in presence of non-condensable gases, which fall outside of the typical CFD codes application. The unique characteristics of the experiment led to the necessity of the stand-alone code development activity, since these phenomena are not typically investigated in detail with STH codes. The thesis then focuses on the application of the coupled tool to simulate the transition from forced to natural circulation in Lead-Bismuth Eutectic (LBE)-cooled facilities, such as NACIE-UP and TALL-3D. They feature similar characteristics, e.g., the coolant, the operating conditions, and the type of experiment, but differ in some relevant aspects. For instance, NACIE-UP heat source is a 19 pin wire-wrapped fuel pin bundle simulator, where fuel assembly heat transfer is a relevant aspect of the experiment, while TALL-3D features two vertical hot legs, allowing for mass flow rate inversion and oscillation from one leg to another. Study of fluid dynamics and heat transfer regimes inside a pool test section, e.g., pool mixing and thermal stratification, installed in one of the vertical legs, is the major focus of the facility.

The validated coupled tool is then applied to the TH analysis of the ATHENA experimental facility. ATHENA, currently under construction, is representative of a typical LFR pool-type configuration, and it significantly differs from the previously described facilities because of its size and the HLM inventory. While NACIE-UP and TALL-3D contain less than 2 tons of LBE, ATHENA will host approximately 800 tons of lead. ATHENA enables studies related to coolant chemistry and oxygen control in a large pool environment, as well as the TH of a multi-assembly core simulator, mechanical pump and steam generator performances. Following the presentation of the numerical models and the design of the ATHENA Main Heat eXchanger (MHX), the steady state condition and two reference transients, i.e., the Loss Of Heat Sink (LOHS) and Loss Of Flow Accident (LOFA), are analyzed through the RELAP5 code. The LOFA transient is simulated also using the coupled tool because it is expected to benefit most from the contribution of the CFD code. In particular, low velocities inside the core make phenomena such as flow distribution among assemblies and heat conduction within the fluid – neglected by RELAP5 – more relevant.

Future activities for the development of this coupling tool will include testing and comparing its results with experimental data from ATHENA and CIRCE, which is an LBE pool-type facility belonging to the ENEA experimental fleet. Being two HLM-cooled Integral Effect Test (IET) facilities, they will allow further refinement and validation of the tool, enhancing its accuracy and capabilities to provide support for reactor-scale analyses.

TABLE OF CONTENTS

LIST OF FIGURES

LIST OF TABLES

LIST OF ABBREVIATIONS

3D-TS	3D Test Section
AC	Air Cooler
ADS	Accelerator Driven System
ALFRED	Advanced Lead Fast Reactor European Demonstrator
ANSELMUS	Advanced Nuclear Safety Evaluation of Liquid Metal Using Systems
ASIV	Amphora-Shaped Inner Vessel
ASN	Autorité de Sûreté Nucléaire, Nuclear Safety Authority
ATHENA	Advanced Thermal-Hydraulic Experiment for Nuclear Application
ATHLET	Analysis of Thermal Hydraulics of LEaks and Transients
BC	Boundary Condition
BOT	Beginning of Transient
BREST	Bystryj reaktor so svincovym teplonositelem, Lead-cooled Fast Reactor
BT	Bayonet Tube
BWR	Boiling Water Reactors
CBR	Core Breeding Ratio
CEL	CFX Expression Language
CFD	Computational Fluid Dynamics
CIRCE	CIRColazione Eutettico, Eutectic Circulation
CPS	Control and Protection Shutdown
CRP	Coordinated Research Project
CS	Core Simulator
CSNI	Committee on the Safety of Nuclear Installation
DCI	Dip-Cooler Intability
DHR	Decay Heat Removal system
DES	Detached Eddy Simulation
DLL	Dynamic Link Library
dpa	Displacement per atom
EBT	Emergency Boration Tank
EC	European Commission
ENEA	Agenzia nazionale per le nuove tecnologie, l’energia e lo sviluppo economico sostenibile
EOT	End Of Transient
EPM	Electric Permanent Magnet
EU	European Union
FA	Fuel Assembly
FALCON	Fostering ALfred CONstruction
FC	Forced Circulation
FIV	Flow-Induced Vibration
FOAK	First Of A Kind
FPBS	Fuel Pin Bundle Simulator
FSI	Fluid-Structure Interaction
Gen-IV	Generation IV
GIF	Generation IV International Forum
HERO	HEavy liquid metal – pRessurized water cOoled tube

HLM	Heavy Liquid Metal
HS	Heat Structure
HTC	Heat Transfer Coefficient
HX	Heat eXchanger
IAEA	International Atomic Energy Agency
IC	Isolation Condenser
ID	Inner Diameter
IET	Integral Effect Test
INEL	Idaho National Engineering Laboratory
IRSN	Institut de Radioprotection et de Sûreté Nucléaire, Institute for Radiation protection and Nuclear safety
ISI&R	In-Service Inspection and Repair
IW	Inter-Wrapper
JBR	Junction Box Routine
KTH	Kungliga Tekniska Högskolan, Royal Institute of Technology
LBE	Lead-Bismuth Eutectic
LEADER	Lead European Advanced DEmonstrator Reactor
LES	Large Eddy Simulation
LESTO	LEad fast reactor Safety design and TOols
LFR	Lead-cooled Fast Reactor
LFR-AS	Lead-cooled Fast Reactor – Amphora Shaped
LHT	Lead Heat Transfer
LMFR	Liquid Metal Fast Reactor
LMTD	Logarithmic Mean Temperature Difference
LOCA	Loss Of Coolant Accident
LOFA	Loss Of Flow Accident
LOHS	Loss Of Heat Sink
LMFR	Liquid Metal Fast Reactors
LWR	Light Water Reactor
MCP	Main Circulation Pump
MH	Main Heater
MHX	Main Heat eXchanger
MOX	Mixed OXide
MPI	Message Passing Interface
NACIE	NAtural CIrculation Experiment
NACIE-LHT	NAtural CIrculation Experiment – Lead Heat Transfer
NACIE-UP	NAtural CIrculation Experiment – Upgrade
NC	Natural Circulation
NCG	Non-Condensable Gas
NGT	Non-condensable Gas Tank
NEXTRA	Newcleo eEvamped eXperiments, Testing and steam generator tube Rupture Analysis
NPP	Nuclear Power Plant
NRC	Nuclear Regulatory Commission
OD	Outer Diameter
OTHELLO	Oxygen controlled Thermal Hydraulic Experimental Lead LOop
P&ID	Piping and Instrumentation Diagram

PERSEO	in-Pool Energy Removal System for Emergency Operation
PIACE	Passive IsolAtion CondEnser
PRZ	Pressurizer
PT	Pressure Transducer
PWR	Pressurized Water Reactors
R&D	Research and Development
RANS	Reynolds-Averaged Navier-Stokes
R.C.	Research Center
RELAP	Reactor Excursion and Leak Analysis Program
RI	Research Infrastructure
SAM	System Analysis Module
SEALER	Swedish Advanced Lead Reactor
SESAME	thermal hydraulics Simulations and Experiments for the Safety Assessment of MEtal cooled reactors
SFA	Spent Fuel Assembly
SG	Steam Generator
SG-RCP	Steam Generator – Reactor Coolant Pump
SGTR	Steam Generator Tube Rupture
SIET	Società Informazioni Esperienze Termoidrauliche
SIRIO	Sistema di rimozione della potenza di decadimento per reattori nucleari innovativi, Decay heat removal system for innovative nuclear reactors
SMR	Small Modular Reactor
SOCL	Start Of Coefficient Loop
SoT	Start of Transient
SOTT	Start Of The Timestep
SRS	Servizi di Ricerche e Sviluppo
STSG	Spiral Tube Steam Generator
STH	System Thermal-Hydraulic
TC	ThermoCouple
TFM	Thermal Flow Meter
THETIS	Thermal-hydraulic Helical Tubes Innovative System
THINS	Thermal-Hydraulics of Innovative Nuclear Systems
TMDPJUN	Time Dependent Junction
TMDPVOL	Time Dependent Volume
TRACE	TRAC/RELAP Advanced Computational Engine
TW	Time Window
UDF	User Defined Function
U.S.	United States
V&V	Verification and Validation
WP	Work Package

LIST OF SYMBOLS

Latin symbols

A	Reynolds number independent RELAP5 flow energy loss coefficient (non-dimensional) or cross sectional area (m^2)
B	Multiplicative factor of the Reynolds-dependent RELAP5 flow energy loss coefficient (non-dimensional)
C	Exponent of the Reynolds-dependent RELAP5 flow energy loss coefficient (non-dimensional)
c_p	Specific heat at constant pressure (J/kg °C)
D	Diameter (m)
E	Energy (J)
F	Results of CFX calculation or two-phase correction (enhancing) factor for the single phase forced convection (non-dimensional)
f	Friction factor (non-dimensional) or the ATHENA-to-ALFRED power ratio (non-dimensional)
G	Results of RELAP5 calculation or mass flux (kg/m^2 s)
g	Gravity acceleration (m/s^2)
H	Relative elevation (m)
h	Heat transfer coefficient (W/m^2 °C) or mass transfer coefficient (m/s) or enthalpy (J/kg)
K	Local pressure drop coefficient (non-dimensional)
k	Thermal conductivity (W/m °C)
L	Length (m)
M	Molecular weight (amu)
$\dot{m}$	Mass flow rate (kg/s)
N	Number (non-dimensional)
$\hat{n}$	Unit vector parallel to the flow direction (non-dimensional)
Nu	Nusselt number (non-dimensional)
P	Power (MW)
p	Pressure (Pa) or pitch (m)
Pe	Peclet number (non-dimensional)
Pr	Prandtl number (non-dimensional)
$\dot{Q}$	Power (W)
q"	Heat flux (W/m^2)
Re	Reynolds number (non-dimensional)
S	Surface area (m^2) or suppression factor for the nucleate boiling (non-dimensional)
SF	Scaling factor of an experimental facility
s	Multiplicative scaling factor (non-dimensional)
T	Temperature (°C)
t	Time (s)
tol	Tolerance (non-dimensional)
U	Velocity (m/s) or overall heat transfer coefficient (W/m^2 °C)
V	Volume (m^3)
X	Boundary condition for CFX calculation or generic quantity specified in the text
x	Linear abscissa (m) or flow quality (non-dimensional)

Y	Boundary condition for RELAP5 calculation
Z	Shah correlating parameter (non-dimensional)

Greek symbols

Δ	Difference
δ	Liquid film thickness (m)
ε	Roughness (µm)
μ	Dynamic viscosity (Pa s)
ν	Kinematic viscosity (m^2/s)
π	Pi (non-dimensional)
ρ	Density (kg/m^3)
σ	Error (°C)
τ	Stress tensor (Pa)
Φ	Calibration coefficient for the RELAP5 laminar friction factor (non-dimensional)
ω	Underrelaxation factor (non-dimensional)

Subscripts and superscripts

b	Bulk condition
fg	Difference between the saturated vapor and liquid phase
fr	Friction
grav	Gravitational
h	Hydraulic
i	Internal iteration counter of the coupled calculation or interfacial condition
j	Timestep counter
k	Internal iteration or timestep counter
L	Laminar
l	Liquid phase
man	Manufacturer
nb	Nucleate boiling
r	Reduced value
ref	Reference value
s	Sensible
sat	Saturation condition
sp	Single phase
std	Standard
sym	Symmetry
T	Turbulent
tp	Two phase
v	Vapor phase
w	Wall
x	Projection along the x-direction

1 INTRODUCTION

1.1 Generation-IV and the Lead Fast Reactors

The advancement of nuclear technology has continuously evolved to meet the growing demands for sustainable and safe energy production [1] [2]. Generation IV (Gen-IV) [3] nuclear reactors represent the latest phase in this evolution, focusing on innovative designs that aim to address the limitations and challenges faced by previous generations of reactors. These next-generation reactors, promoted by the Generation IV International Forum (GIF) [4], are expected to provide significant improvements in safety, efficiency, sustainability, and waste management [5].

Lead-cooled Fast Reactors (LFRs) [6] [7] are among of the most promising technologies that aim to address the Gen-IV goals in the following way:

- Sustainability: the low neutron absorption cross section and poor moderating power of lead enable effective fuel burning thanks to the fast neutron spectrum. Indeed, it allows a breeding ratio of about 1, i.e., converting the fertile uranium to fissile plutonium, and burning the minor actinides which represent most of the long half-lives radioisotopes.
- Economics: the simple design reduces the building time, capital cost, operation and maintenance costs, making the electricity produced by LFRs competitive with other energy sources. This is possible thanks to the good thermo-physical properties of lead, and in particular to the high boiling temperature at atmospheric pressure (1737°C), which allows for operation at low pressure, eliminating the need for pressure control systems, as well as containment pressurization in case of Loss Of Coolant Accidents (LOCAs). Moreover, the primary system of the LFRs can be housed in the same vessel of the reactor core, further reducing the dimensions and the complexity of the system. The high boiling point also allows for operation at high temperatures, with a core outlet temperature up to 550°C, significantly increasing the efficiency of the thermal cycle with respect to the Light Water Reactors (LWRs). However, additional technological solutions must be considered compared to LWRs, e.g., systems designed to keep lead above its freezing temperature (327°C) when the reactor is not in operation, as well as coatings for materials in contact with lead to prevent corrosion. Conducting an economic evaluation and comparison with LWRs is not straightforward, as there are still no commercial LFRs. Ref. [8] provides a review of the economics and finance of LFRs, collecting many contributions claiming that – except for the First Of A Kind (FOAK) – LFRs will be competitive with LWRs.
- Safety and reliability: the high atomic mass and density of lead provides effective shielding against gamma rays, reducing worker exposure. The good neutronic and thermo-physical properties of the coolant allow the adoption of high pitch to diameter ratio in the core, reducing pressure drops and pumping power. This is a key aspect in cases of accidental scenarios, as the system is effective in removing decay power even in natural circulation, reducing the need for active systems. Other advantages of the high density include promoting fuel dispersion in the event of core melting, preventing critical conditions, and avoiding steam entrainment at the core inlet in case of Steam Generator Tube Rupture (SGTR).
- Proliferation resistance and physical protection: the MOX (Mixed OXide) fuel is composed of uranium and plutonium oxides, and actinides that make these systems unattractive for extraction of weapon-usable materials. The long life of the core does not allow the production of weapon-grade plutonium. Physical protection is ensured by the coolant, which is inert to air and water, and it does not contain flammable substances. Containment pressurization is also avoided in the case of catastrophic events or sabotage.

1.2 LFR landscape worldwide

In Europe, several projects devoted to the development of LFRs are ongoing, namely ALFRED [9] [10] (Advanced Lead Fast Reactor European Demonstrator), LFR-AS-200 (Lead Fast Reactor – Amphora Shaped

– 200 MW) [11], BREST-OD-300 (Bystryj reaktor so svincovym teplonositelem, Lead-cooled Fast Reactor) [12], and SEALER (Swedish Advanced Lead Reactor) [13] [14]. The development of ALFRED is promoted by the FALCON consortium [15], formed in 2013 by RATEN ICN [16] (Romania), Ansaldo Nucleare [17] and ENEA [18] (Italy). The LFR-AS-200 is developed by the *new*cleo company [19], which aims to design, build, and operate Gen-IV lead-cooled Small Modular Reactors (SMRs). The BREST-OD-300 is promoted and funded by the Russian government, and it is currently in the most advanced state of development. The SEALER project is developed by the Blykalla company (Sweden) [20], which aims to construct and deploy SMRs to produce 500 TWh clean energy annually, reducing CO_2 emissions by approximately 0.5 Gton/year (~1% of global emissions).

ALFRED Project

ALFRED was identified as the LFR demonstrator for a Lead-based SMR, intended to bridge the final gap between research and industrial application. It has a core power of a few hundred MWth, which can be easily scaled up to a commercial size. The objective of FALCON is to build a FOAK by 2035–2040.

The conceptual design of ALFRED was originally developed within the framework of the LEADER (Lead European Advanced DEmonstrator Reactor) [21] [22] [23] project by taking advantage of research and collaborations promoted by the European Commission. More recently, the ALFRED concept has been revised and improved to increase safety performance, readiness, flexibility, and robustness [24] [25] [26] [27]. Drawings of the LEADER and FALCON configurations are shown in Figure 1 and 2, respectively.

The primary system configuration was revised to minimize Thermal-Hydraulic (TH) issues specific to Liquid Metal Fast Reactors (LMFRs) such as thermal stratification, thermal striping, free level fluctuations, and gas entrainment, and their effects on the components. In the first stage, the molten lead temperature is limited to values compatible with the selected materials, eliminating the need for protective measures such as coatings or oxygen-driven self-passivation. As ALFRED is a prototype, the core includes a hot channel to test advanced Fuel Assemblies (FAs) and corrosion-resistant alumina coatings on fuel pins for the next stages at higher temperatures.

No temporary in-vessel storage of spent fuel is foreseen in the current design. Refueling will be performed from the top, keeping the assemblies below the lead free level to avoid the risk of losing cooling for a stuck assembly during handling. Due to the lack of sufficiently mature under-lead In-Service Inspection (ISI) techniques, the concept of removable components has been extended to the core barrel and restraint system. In this way, out-of-vessel ISI and Repair (ISI&R) are allowed, as well as the testing of improved concepts for all the primary components that can be easily extracted.

ALFRED will adopt a staged approach: starting with low-temperature conditions, the core outlet temperature will be gradually increased, bridging the gap between current technology and the desired commercial performance. As the demonstration program provides operational experience and addresses safety concerns through improved margins, a parallel Research and Development (R&D) program will supply the former with the advanced technology and design options to enhance the competitiveness of the commercial fleet. The demonstrator itself will, therefore, qualify technological solutions intended for subsequent steps, providing the evidence required for licensing, as discussed with the Romanian safety authority.

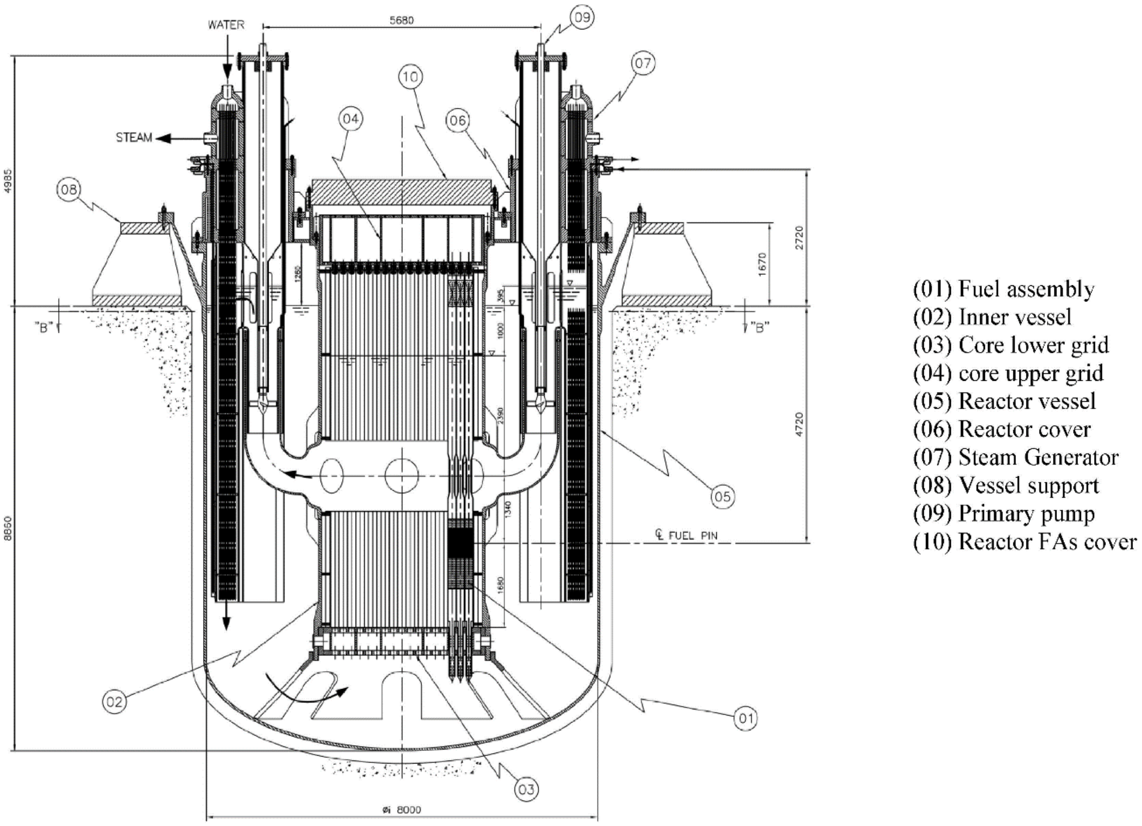

Figure 1 – ALFRED reactor conceptual scheme based on the LEADER project [24]

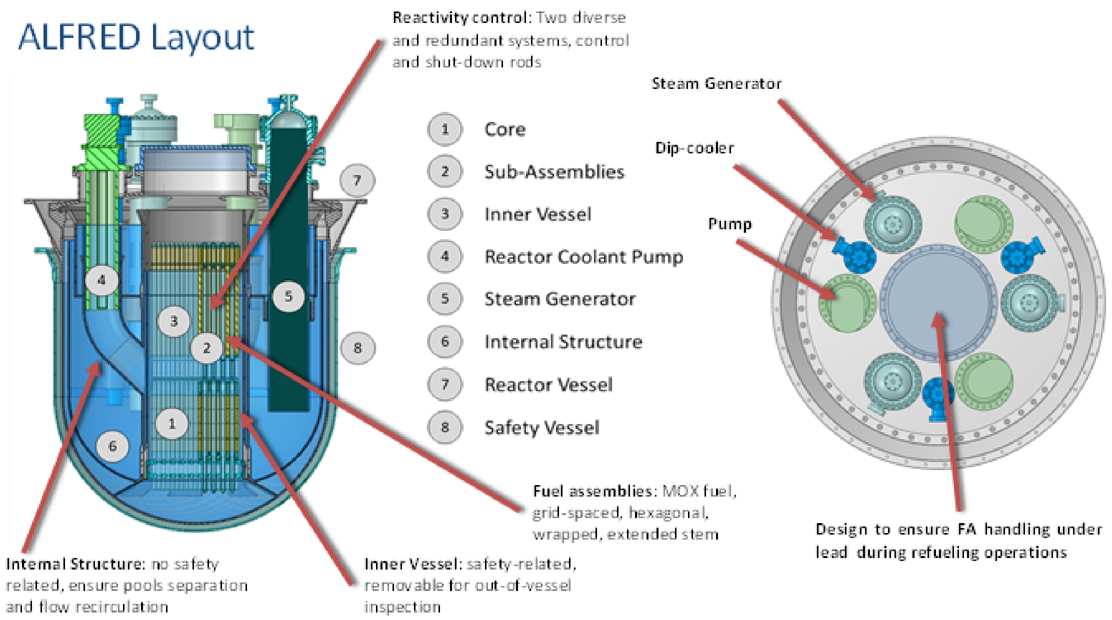

Figure 2 – ALFRED layout in the FALCON (staged approach) configuration [27]

LFR-AS-200 Project

*new*cleo aims to realize its vision of advanced modular reactors and a closed fuel cycle by the early 2030s. The company is designing, building, and preparing to operate Gen-IV Small Modular LFRs, with its commercial model named LFR-AS-200 (LFR-Amphora-Shaped, 200 MW electrical power). A conceptual scheme is shown in Figure 3. In parallel, *new*cleo is developing a facility in France for the production of MOX fuel for fast reactors, using available separated materials from Gen-II and Gen-III NPPs (Nuclear Power Plants) spent fuel. This MOX fuel will supply the demonstrator, the FOAK reactor, and future reactor fleets. The demonstrator and the MOX plant are in the pre-licensing phase, with technical discussions initiated with ASN (Autorité de Sûreté Nucléaire, Nuclear Safety Authority), and IRSN (Institut de Radioprotection et de Sûreté Nucléaire, Institute for Radiation protection and Nuclear Safety) in mid-2023 to evaluate design maturity and prepare for formal regulatory processes.

ENEA, a key partner for *new*cleo, has played a crucial role in advancing lead-cooled nuclear technology over the last decades, providing both theoretical and experimental expertise. *new*cleo's R&D program encompasses multiple non-nuclear experimental campaigns, culminating in the validation of developed solutions through PRECURSOR, a 10 MW large-scale Integral Effect Test (IET) facility. PRECURSOR, as well as most of *new*cleo's experimental platform, will be built and operated at the ENEA Brasimone site.

The primary reactor design, LFR-AS-200, leverages lead properties to enhance plant simplicity and compactness, ensuring passive safety. This innovative design differs significantly from previous LFR concepts. Key innovations include the elimination of intermediate loops, reduced primary system volume, and a compact reactor building, all of which contribute to competitive electricity costs. The reactor is designed for energy production, including non-electrical applications such as ammonia and hydrogen production. It will use stockpiled plutonium and, potentially, recycle minor actinides, minimizing the long-lived transuranic waste burden. The breeding ratio is 0.9 without blanket assemblies, adjustable through core design adaptations if needed.

The LFR-AS-200 is a pool-type reactor with all primary components housed within the reactor vessel. Its key features include a thermal power of 480 MWth, core inlet/outlet temperatures of 420/530°C, FAs suspended above the lead free level, six Spiral-Tube Steam Generators (STSG), six primary pumps, six dip coolers for the Decay Heat Removal systems (DHR) – three for normal shutdown and three for emergency – and the Amphora-Shaped Inner Vessel (ASIV). There is no need for an in-vessel refueling machine.

*new*cleo's smaller LFR-AS-30 will serve as a key irradiation facility, leveraging its neutron spectrum characteristics to validate new fuel types, components, and technologies. This reactor will also play a crucial role in raising operational temperatures and improving efficiency across the LFR fleet.

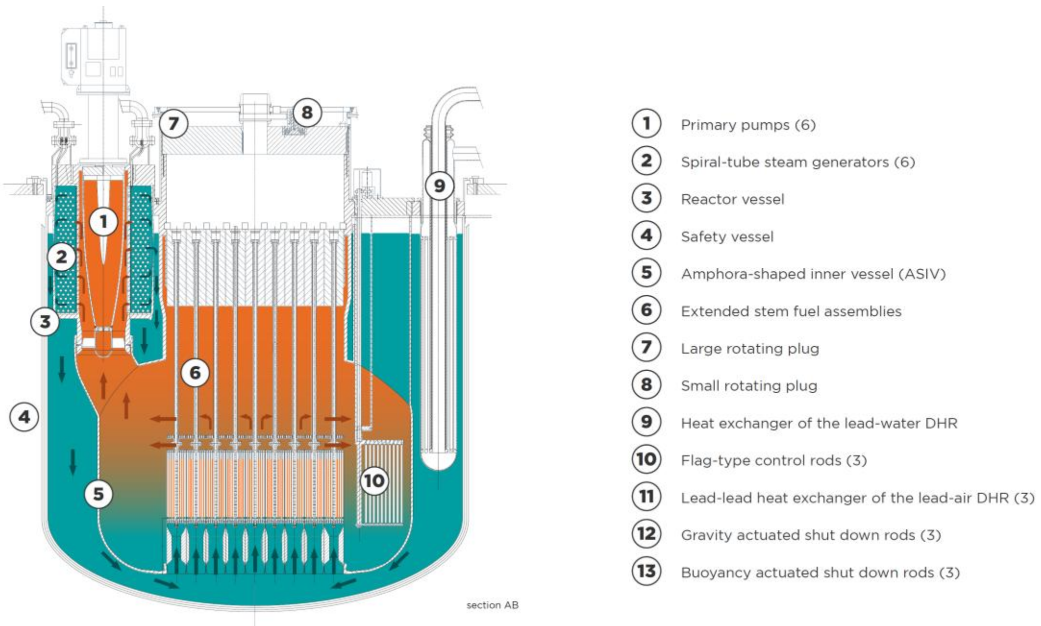

Figure 3 – LFR-AS-200 overview [19]

BREST-OD-300 Project

The BREST-OD-300 [28] is an advanced LFR developed by Russia as part of its national program to establish a closed nuclear fuel cycle [29], where spent fuel can be reprocessed and reused, thereby minimizing long-lived radioactive waste. With an electrical output of 300 MW, the reactor is designed for inherent safety and sustainability, utilizing lead as a coolant and PuN-UN (uranium plutonium mononitride) fuel, which features high density and high thermal conductivity, and it is compatible with lead and the cladding of chromium ferritic martensitic steel. Combined with the properties of lead, nitride fuel allows a complete breeding in the core (Core Breeding Ratio, CBR≥1), resulting in a small operating reactivity margin ($\Delta\rho<\beta_{eff}$). The safety analysis has shown that none of the considered initiating events involving a fast introduction of reactivity up to its full margin, and interruption of the forced coolant circulation result in accidents with fuel damage and inadmissible radioactive releases. This feature is made possible thanks to the high degree of passive safety due to the properties of lead, which provides strong protection against overheating.

The FA design allows radial coolant overflow in the core in such a way to prevent overheating of an eventual damaged FA. The pool-type design consists of a lead circuit housed in a central and four peripheral cavities in a concrete steel-lined vessel. The central cavity houses the core barrel along with the reflector, the CPS (Control and Protection Shutdown) rods and the SFA (Spent Fuel Assembly) storage, while the peripheral cavities accommodate the SG-RCP (Steam Generator – Reactor Coolant Pump) units, heat exchangers of the emergency and normal cooldown systems, filters and auxiliary components. Radial uniformity of the FA radial power distribution is obtained by placing assemblies with smaller diameters rods in the central regions and larger diameters in the peripheral regions, allowing a lead mass flow rate distribution with a peak in the central region.

The BREST-OD-300 design does not require high-pressure systems nor intermediate cooling loops, simplifying the plant's architecture and enhancing economic competitiveness. The BREST-OD-300 intends to demonstrate the reactor operation in different modes, serving as a prototype for future medium sized reactors, contributing to the development of sustainable and efficient nuclear power for the future.

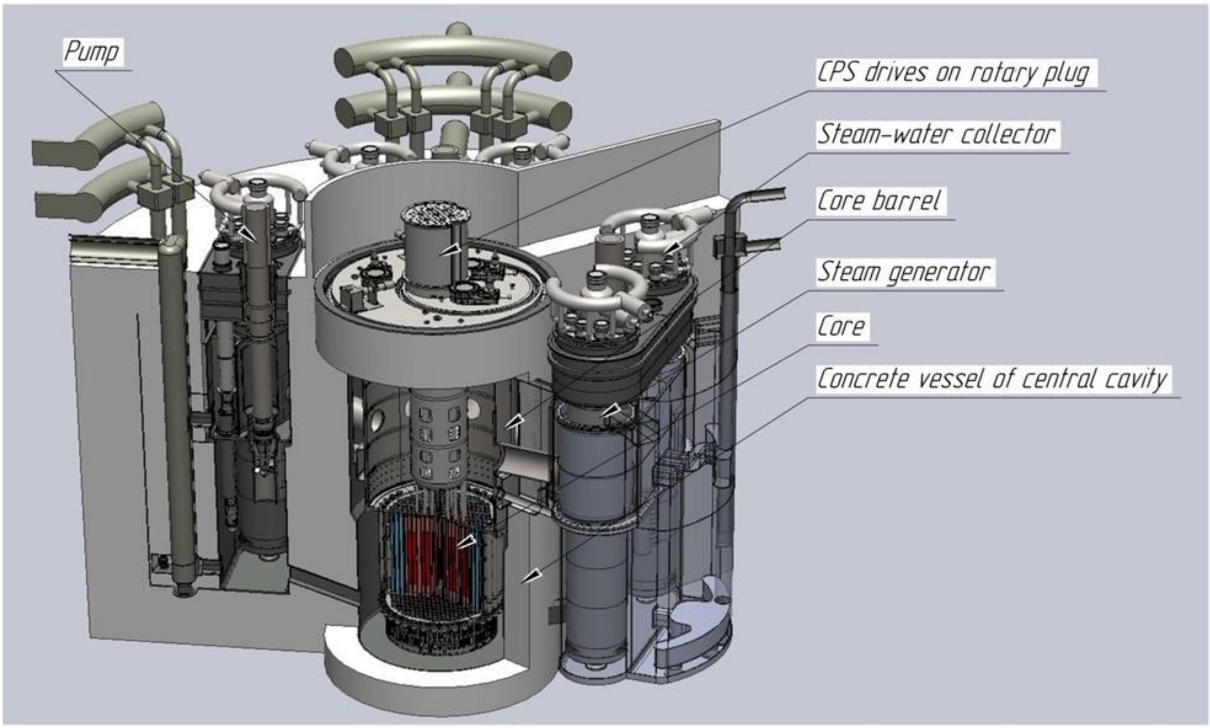

Figure 4 – BREST-OD-300 overview [28]

SEALER Project

SEALER is a 55 MW compact, passively safe reactor designed by Blykalla [13] for commercial power generation (see an overview and the primary system layout in Figure 5). The fuel residence time is 25 years, allowing operation without fuel replacement and significantly reducing fuel management costs. This feature is due to a higher uranium density, which allows the fuel to be used longer than the standard UO_2 fuel. Uranium nitride, in particular, contains 40% more uranium per unit volume, resulting in a 40% longer fuel life. This also leads to better safety margins (operating at > 1500°C below its melting point) due to seven times higher thermal conductivity in the fuel compared to the oxide. Although this fuel is difficult to manufacture using conventional methods, Blykalla employs the “Spark Plasma Sintering” technique, assisted by hot pressing, to sinter fuel pellets by directly converting enriched UF_6 in streaming NH_3.

Passive safety is achieved by removing decay heat from the core via natural convection of the lead coolant. In the event of a core-disruptive accident, volatile fission products are retained within the lead, ensuring that evacuation of nearby residents would not be necessary. The main advantages of the reactor compactness consist in less residual heat to be removed and in fostering scalability and repeatability in production.

Blykalla addresses the issue of lead corrosiveness and erosivity by developing steel alloys that protect the core components. They developed three aluminum-alloyed steels: an aluminum oxide-forming steel for protecting cladding tubes, an austenitic steel for protecting reactor vessels, and a martensitic steel suited for lead pump impellers.

The first Blykalla’s nuclear reactor will be the SEALER-One: it will function as a demonstrator of their technology, as well as to be used for pyrolysis and steam production. The licensing process is currently underway, and the selected location for SEALER-One is in Nyköping – a site of the Studsvik operator – where criticality is expected to be achieved by 2029. The commercial SMR unit, named SEALER-55, features a modular structure that allows reactors to be produced in factories and shipped to the final location. Serial production is expected to start in the early 2030s.

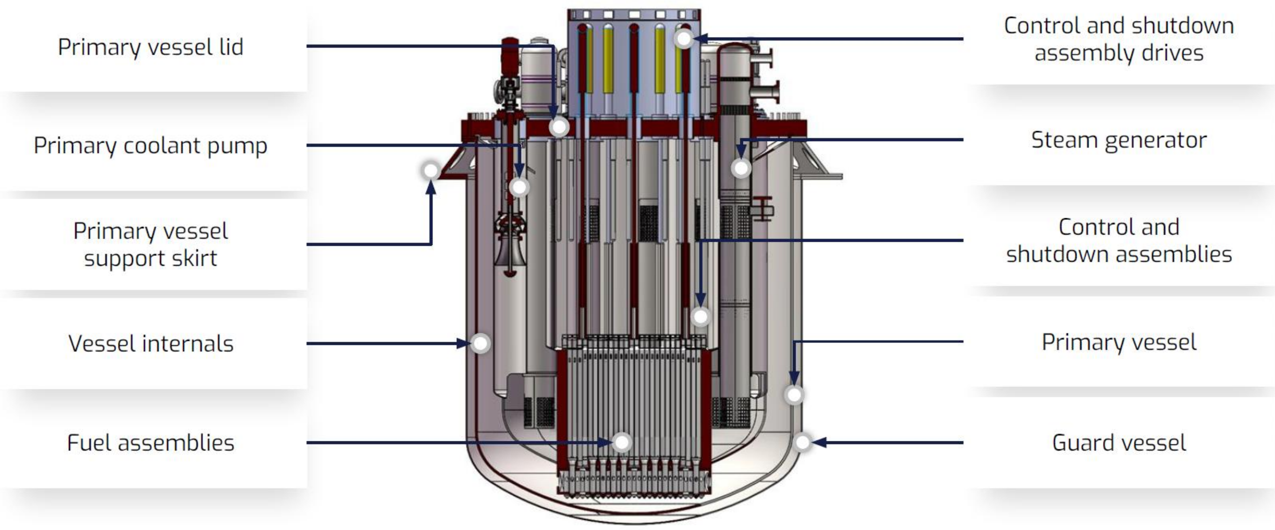

Figure 5 – SEALER primary system layout [30]

1.3 Experimental infrastructures in support of LFR development

An extensive R&D activity has been undertaken in the EU (European Union) to improve understating of the design, operation and maintenance of the systems and components of LFRs, and to bridge the gap to a commercial deployment of such reactors. The most relevant technological issues are related to the following topics:

- Material studies and coolant chemistry: key phenomena in which lead is involved are erosion and corrosion. Long-term exposure of structural material to lead can result in the corrosion and embrittlement of the structures, and contamination of the coolant by metal oxides. Possible countermeasures are the online coolant purification, and the oxygen control in the lead, which must be within a certain window in order to not dissolve the metals in the coolant (too low oxygen content) and to prevent lead oxides formation (too high oxygen content). At temperatures higher than 500°C, corrosion is accelerated even if the oxygen is controlled. A solution that is under investigation is the application of coatings deposited on the structure walls.
- Irradiation studies: such studies are focused on the definition of the resistance of structural materials to fast neutron fluxes in terms of thermal stresses and dpa (displacement per atom), determining the effect of irradiation on the corrosion, embrittlement, creep and swelling phenomena.
- Neutronic studies: the characterization of neutronic properties of the materials, including structural material, the coolant and the fuel throughout their life cycle is required to reduce uncertainties in the prediction of the core performances under fast neutron flux.
- TH properties: the most relevant issues are related to:
    - Pool TH in forced and natural convection (mixing, thermal stratification, stagnant zones, pressure drops), and transition from forced to natural convection.
    - Fuel assembly TH, with the aim of designing the assembly to optimize the heat transfer from the fuel to the coolant both in forced and natural convection. Other topics to be investigated are the subchannel flow distribution and heat transfer, cladding temperature profile and hot spot, vibrations induced by the flow, and Fluid-Structure Interaction (FSI).
- Instrumentation: challenges arise when selecting instrumentation to be inserted into a high temperature, corrosive, and non-transparent environment, with a fast neutron spectrum. Suitable instrumentation must be developed to withstand such an environment while maintaining reliability for long time.

In this framework, ENEA Brasimone and Bologna Research Centers (R.C.s) are supporting the development of ALFRED and LFR-AS-200 from the experimental and numerical points of view [31]. In particular, ALFRED's Research Infrastructure (RI) [32] is located in Mioveni (Romania), where ALFRED itself will be situated, taking advantage of the ENEA expertise and know-how developed since the early 2000s. The allocated budget is 22 M€. The RI consists of six experimental facilities (see Figure 6), each covering a specific R&D topic:

- ATHENA: it is a large pool facility with a diameter of 3.2 m and the same height as ALFRED (10 m) aimed at testing large to full scale components in conditions representative of the reactor. ATHENA (Advanced Thermal-Hydraulic Experiment for Nuclear Application) will be mainly devoted to performing tests related to pool TH, heat transfer through the bypass region in a multi-assembly core, primary pump performances, transition from forced to natural circulation, SGTR, and fuel assembly partial blockage. It will host about 800 tons of lead, making it the biggest pool type facility in the world.
- ChemLab: it is a chemistry laboratory directly connected to ATHENA, and it aims at investigating Heavy Liquid Metals (HLMs) and material science. It will support the study of issues such as oxygen monitoring and control in the coolant, as well as the interaction of liquid lead with the structural materials, in support of AHTENA and ALFRED. The laboratory consists of two sections, the first dedicated to experimental tests on oxygen control, solubility, and corrosion of structural materials in liquid lead, while the second is a metallographic laboratory for characterizing the amount of metals dissolved in the coolant after their interaction.
- Meltin'Pot: it is a research platform composed of four modules, with the goal to address the phenomena of (i) fuel-coolant interaction, (ii) fuel dispersion and relocation in the coolant in a severe accidental scenario, (iii) retention of fission products in lead and/or migration in cover gas, (iv) retention of polonium isotopes in lead. It aims at supporting the ALFRED licensing demonstrating its

safety in case of core damage. It is the only "hot" facility of the RI; therefore, it will be hosted in a dedicated hot cell.

- HELENA-2: it is a loop facility aimed at characterizing the TH behavior of the core FA under forced and natural circulation regimes. Flow-Induced Vibration (FIV) tests and qualification of control rod drive mechanisms are also foreseen.
- Hands-ON: it is a pool type facility aimed at simulating the fuel handling operation, demonstrating the capabilities of the ALFRED handling machine and validating a fuel handling procedure for regular and deformed subassemblies.
- ELF: it is a large-scale pool-type facility devoted to reliability and long running tests of the main primary components under forced and natural circulation conditions. It will host a 5 MW core simulator, three SGs, three pumps and three DHR-loops. It aims at (i) investigating TH in steady state conditions, (ii) demonstrating the long term operation of an active oxygen control system of a LFR primary system, (iii) investigating long term effects of lead on coatings and structural materials, (iv) demonstrating the reliability of components in relevant scale, (v) reproducing the transition from forced to natural circulation during a simulated protected Loss Of Heat Sink (LOHS) with Loss Of Flow Accident (LOFA).

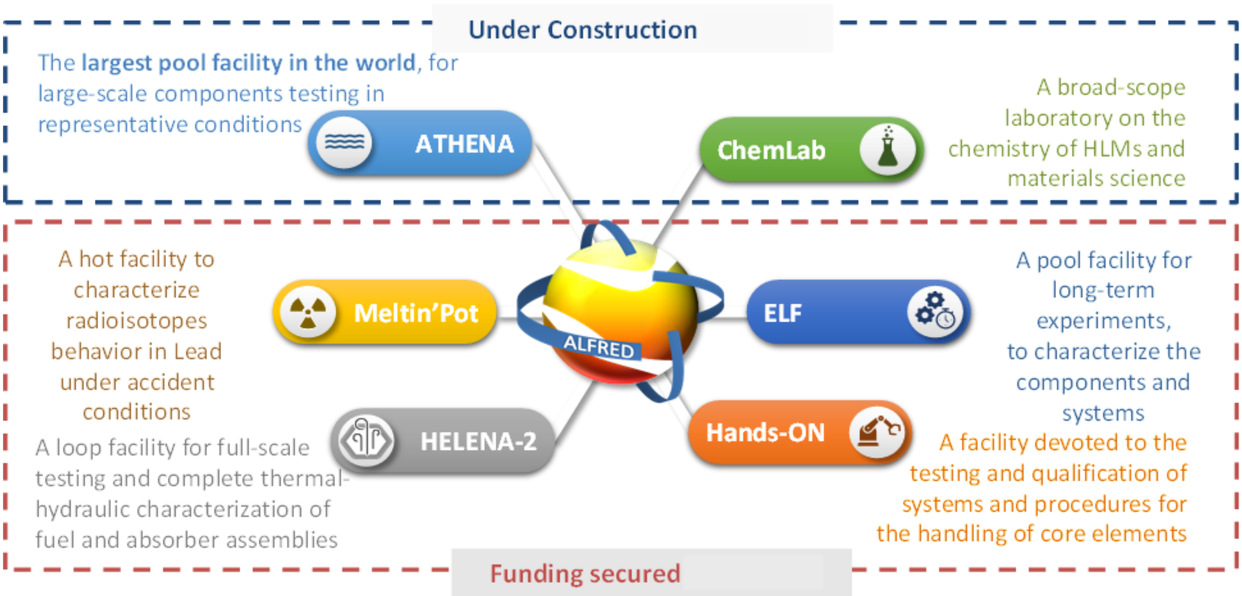

Figure 6 – ALFRED Research Infrastructure

Regarding the experimental R&D activities related to the LFR-AS-200, *new*cleo, in collaboration with ENEA, SRS [33] and Fucina [34], is currently building its experimental platform primarily at ENEA Brasimone R.C., leveraging the already existing experimental facilities, such as the NACIE loop for heat transfer studies and the CIRCE pool for SGTR tests, and constructing new ones in the available halls. The facilities that will address *new*cleo's experimental R&D needs are the following:

- NACIE-LHT (ENEA): it is an upgrade to the NACIE facility to study Lead Heat Transfer (LHT) in cross flow with water, a representative configuration of the *new*cleo SG.
- CIRCE-NEXTRA (ENEA): it is devoted to (i) long-duration endurance tests of axial flow pumps operating with HLMs, (ii) TH tests on DHR component and system, and (iii) SGTR tests in the CIRCE facility.
- TAPIRO (ENEA): it is a research reactor to develop a more accurate nuclear database for fast neutron reactors.
- MATLAB: it is a chemical laboratory for material studies to validate the microstructure and mechanical performance.

- LEAD/CHEM LAB: it is a chemical laboratory for studies of materials' mechanical properties in lead, including slow strain rate tests, creep, long-term creep, and creep-fatigue.
- CORE1 & CORE2: loops for corrosion and erosion studies in flowing lead.
- CAPSULE: corrosion tests in stagnant lead on various steels, both bare and coated.
- EFESTO: it is a small pool installed on a shaking table for fluid-structure interaction and sloshing experiments.
- HUSTLE: it will be used to develop, test and calibrate various ultrasonic and visual inspection techniques for LFR vessel ISI purposes.
- MANUT: infrastructure for fuel/component handling and control rod actuation.
- OTHELLO: a lead loop for TH studies and component testing. It will house several test sections: (i) a heated Fuel Pin Bundle Simulator (FPBS) to characterize the heat transfer in the LFR FA under forced and natural circulation regimes, (ii) an unheated FPBS to investigate mainly FA pressure losses and flow induced vibration, (iii) a SG test section to characterize full-length spiral tubes heat transfer and investigate flow maldistributions and transients, and (iv) a freezing and remelting test section to investigate such phenomena in SG relevant configuration.
- DCI: Dip-Cooler Instability testing for DHR TH.
- PRECURSOR: a pool-type large-scale integral test facility (10 MW), composed of a "power to volume" scaled primary system, and a closed loop secondary system featuring an alternator-turbine unit and a condenser.

1.4 PhD activity and objectives

The main objective of the thesis is to develop a numerical tool which enables multiscale simulations to support the safety analysis of LFRs. Multiscale simulations are carried out thanks to the coupling between two codes, which are typically applied at different length scales. In this work, the System Thermal-Hydraulic (STH) code RELAP5/Mod3.3 and the Computational Fluid Dynamics (CFD) code Ansys CFX have been selected to develop the coupling tool.

To apply the developed coupled tool to the safety analysis of LFRs, a code validation campaign against experimental data is needed. For this reason, several suitable experimental data sets have been selected to be compared with the coupled tool numerical results. The final activity is the application of the coupled tool to perform pre-test simulations of the ATHENA experimental facility, in support of ALFRED reactor development. However, due to the similar design of the LFR concepts mentioned in Sect. 1.2, some phenomenological aspects of ATHENA can be considered representative of the LFR family.

To achieve the objectives of this work, several key activities were undertaken. First, a literature review was conducted to examine previous applications of the RELAP5 and Ansys CFX codes in HLM environments and to assess their performance in simulating complex phenomena. Following this, experimental facilities suitable for supporting LFR development were identified, and their experimental data were analyzed. The RELAP5 source code was then modified to more accurately simulate Gen-IV passive systems and complex TH phenomena. This modified version of RELAP5 was subsequently validated as a stand-alone tool.

Next, an STH and CFD coupling tool was developed to perform multiscale simulations with different spatial and temporal discretization schemes. The coupled tool was then validated against experimental data to ensure its performance. Subsequently, both STH and CFD models were developed to perform TH simulations of experimental facilities relevant to LFR development, such as NACIE-UP and TALL-3D facilities. Finally, a multiscale simulation of the ATHENA facility was conducted using the validated coupled tool, contributing to the definition and the pre-test analysis of two transients to be tested on the facility. As soon as experimental data become available, ATHENA will contribute to the development of the numerical tool with an increased confidence in reproducing relevant phenomena expected in a typical LFR system.

The activities carried out in this thesis and their logical connections are graphically represented in the flowchart in Figure 7.

1.5 Structure of the thesis

This thesis is structured in five sections. The first section provides the framework of the activities and the current status of the development of Gen-IV LFRs, along with an overview of the projects that are at a relevant stage of development and the major R&D needs that must be addressed in order to validate codes, materials, components, and systems for LFRs. It also includes a summary of the main activities performed to pursue the objective of the thesis, which is the development of a numerical tool able to couple the STH code RELAP5/Mod3.3 and the CFD code Ansys CFX.

Section 2 describes the background in which the activities take place, and in particular, the state of the art of the most relevant coupling methods and tools developed worldwide is provided. After a brief overview of the RELAP5 and CFX codes, a detailed description of the coupled tool is given.

Section 3 deals with the validation of the coupling tool against experimental data obtained from experimental facilities relevant to the development of LFRs. The description of each experimental facility, along with the numerical models and the simulation results, is presented.

After the validation activity, multiscale simulations of the ATHENA integral test facility are presented in Section 4. In particular, accidental scenarios representative of LOHS and LOFA are considered.

Section 5 contains a summary and conclusion of the thesis. Future activities and improvements related to this work are proposed.

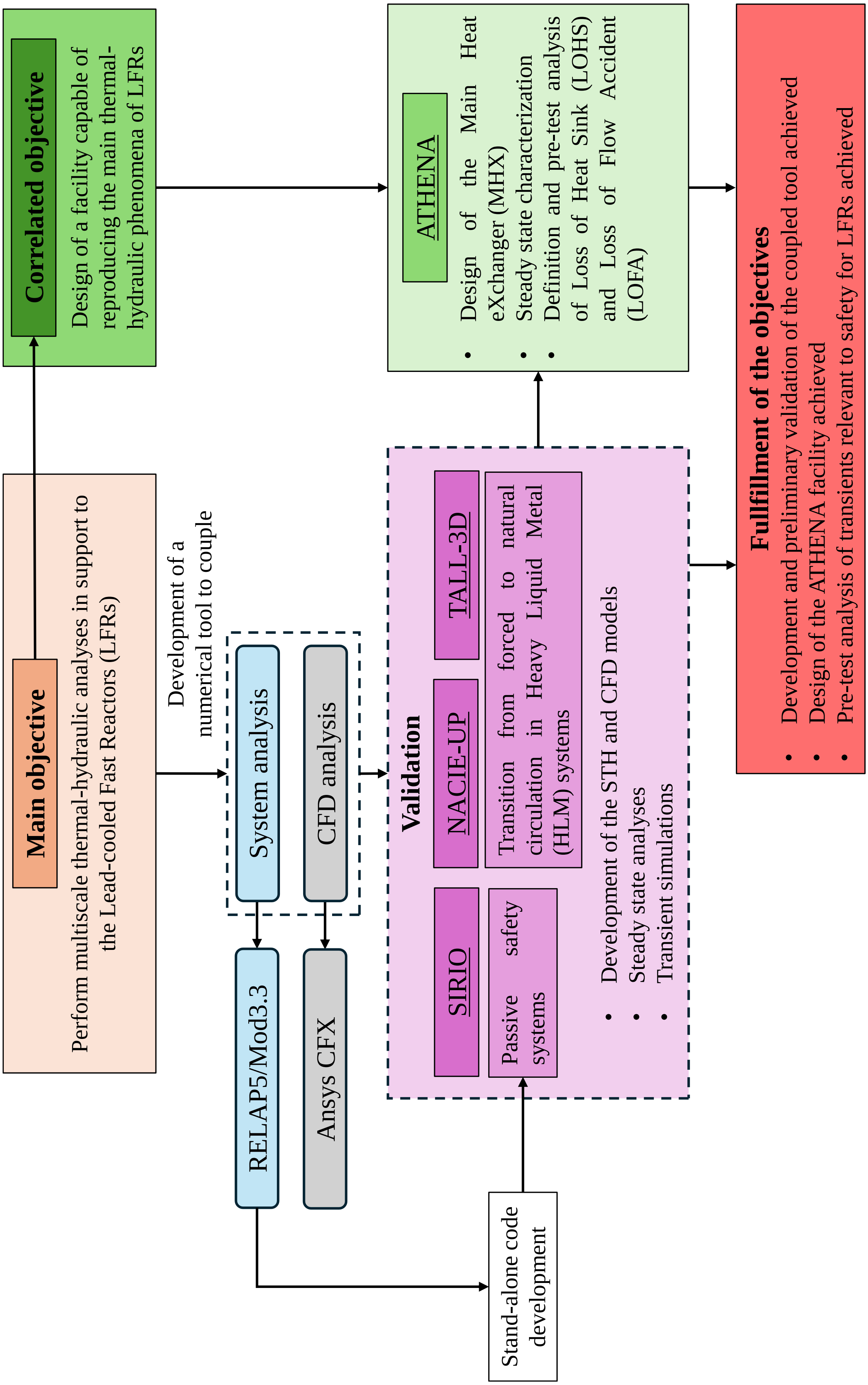

Figure 7 – Thesis flowchart

2 CODE COUPLING FOR MULTISCALE THERMAL-HYDRAULIC ANALYSIS

This section provides the rationale behind the development of coupled tools, along with an overview of their deployment over the past years. A brief description of RELAP5 and Ansys CFX codes is provided in Sect. 2.2 and 2.3, respectively. Sect. 2.4 presents the coupled tool developed in this work and the implementation of routines and scripts to manage the coupling. A focus on two different numerical time advancing schemes is given in Sect. 2.5, while two different domain discretization approaches are described in Sect. 2.6.

Although this section is limited to the description of the methods and the code, the validation activity of the coupled tool is addressed in Sect. 3.

2.1 Background

TH analysis of nuclear reactors encompasses numerical simulations at various scales. Over the years, a range of TH codes have been developed for design, safety assessment, and analysis of TH phenomena in nuclear systems. These codes are designed for different problem scales, depending on the phenomena being studied [35]. For instance, Direct Numerical Simulation (DNS) is used at the smallest scales to solve the Navier-Stokes equations, whereas STH codes are employed for system-level analysis, where computational efficiency is crucial, though at the cost of increased approximations and empirical correlations [36] (referred to as "increasing modelling" in Figure 8). Figure 8 also graphically shows other code families with increasing order of detail from STH to DNS codes, passing through subchannel, RANS (Reynolds Averaged Navier-Stokes)-based CFD, and LES (Large Eddy Simulation).

In nuclear reactors, the occurrence of phenomena across different time and length scales necessitates a multiscale approach to TH analysis. STH codes are widely adopted for evaluating large-scale systems, where the presence of substantial heat and mass sources allows for many simplifications [37]. These codes have been essential for safety analyses in licensing processes for water-cooled reactors, and their application to next-generation reactors is promising as well [31]. Their typically lower computational cost compared to CFD, and their versatility in handling multi-phase and multi-component scenarios make STH codes fundamental to nuclear technology development.

The performance of STH codes applied to LFRs has been examined in several studies [38] [39] [40]. Although these codes have demonstrated capability in system-level simulations, limitations, also present for water applications [41], remain, particularly in simulating inherently multidimensional phenomena such as heat and mass transfer in pools. Additionally, extensive experimental campaigns are often necessary to capture all the relevant TH conditions for complex components.

In contrast, CFD has emerged as a powerful tool for simulating complex three-dimensional TH phenomena. However, the high computational demands of CFD pose a challenge for large-scale applications [42]. Research has thus focused on developing reduced-scale models that can be computed in reasonable time frames for design applications, as well as for developing digital twins of nuclear reactors. These efforts have led to advancements in porous media modelling, coarse meshing techniques, and next-generation turbulence models [43] [44].

To address multiscale problems effectively, coupled simulations combining the strengths of both STH and CFD codes have been developed [45]. Various STH codes, such as RELAP5 [46], ATHLET [47], TRACE [48], SAM [49] have been coupled with CFD tools like Ansys Fluent [50], Ansys CFX [51], and STAR-CCM+ [52]. These coupled approaches have been applied to both Gen-III and Gen-IV reactor technologies.

Aumiller et al. [53] were among the first to propose the coupling of RELAP5-3D© with CFX, introducing a methodology and demonstrating its feasibility for nuclear reactor analysis through a proof-of-concept calculation. Since then, numerous research efforts aimed at addressing challenges such as data exchange, temporal synchronization, and interface stability. Bertolotto et al. [54] contributed to these advancements by exploring single-phase mixing with a coupled CFX-TRACE, enabling more accurate flow predictions in complex geometries, which has proved beneficial for transient scenario analysis. Martelli et al. [55] [56] [57] introduced an alternative method, developing a MATLAB© interface for coupling RELAP5 and FLUENT, which was applied to NACIE and CIRCE facility. This approach successfully simulated complex TH phenomena in HLM-cooled reactors, including natural circulation and thermal stratification. A further example of RELAP5/FLUENT coupling is reported in Ref. [58], where a preliminary validation of the method was conducted against experimental data from TALL-3D facility [59]. Li et al. [60] also advanced the field by coupling FLUENT and RELAP5 using Dynamic Link Library (DLL) technology and Fluent User Defined Functions (UDFs), employing an explicit coupling method that was validated with test cases such as a pipe blowdown scenario, proving effective for both single and two-phase flows. More recent developments by Grunloh and Manera [61] [62] introduced a multiscale domain overlapping strategy, coupling CFD (STAR-CCM+) and system codes (TRACE) by dynamically adjusting the spatial resolution at the interface, enhancing stability and accuracy for transient simulations relevant to nuclear safety. Additional validation of hybrid domain overlapping methods was provided by Huxford et al. [63] [64] through the coupling of CFD and STH codes like SAM, yielding reliable predictions for reactor transients in various safety-relevant scenarios.

Despite significant advancements, challenges remain in establishing best practices for coupled simulations in HLM environments and determining when these methods provide clear benefits compared to stand-alone simulations. In this thesis, a novel coupling approach has been developed between the CFD code Ansys CFX and the STH code RELAP5/Mod3.3, with the goal of creating a lean tool capable of conducting system-level analyses while focusing on specific components or fluid sections requiring detailed CFD modelling. This tool uses in-house scripts for data post-processing and exchange, fully managed within Ansys CFX, offering improved flexibility, customization, and optimized data transfer compared to previously developed methods. The final goal is to simulate the TH behavior of HLM-cooled reactors by leveraging the strengths of both code families in a multiscale approach. The RELAP5/Mod3.3 and Ansys CFX coupling tool is intended to be validated against existing experimental data and future experimental facilities [65], as detailed in this thesis. The following sections will further elaborate on the methodology employed in this tool.

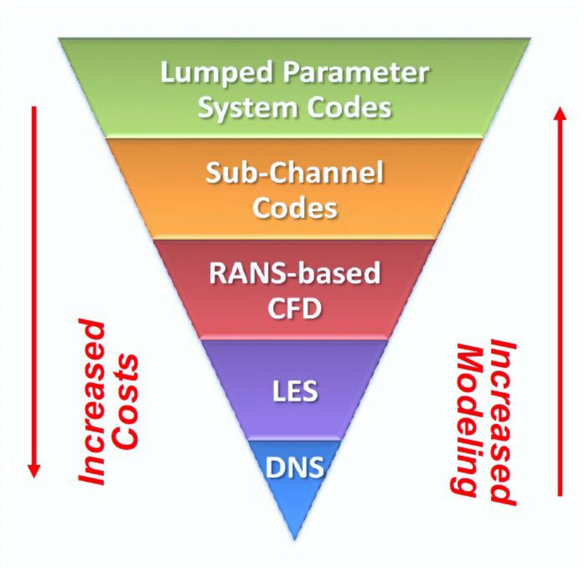

Figure 8 – Thermal-hydraulic codes hierarchy [35]

2.2 RELAP5 code

RELAP5 (Reactor Excursion and Leak Analysis Program) [66] [67] [68] [69] is a TH code for nuclear system analysis and is continuously assessed by various international institutions. Extensive qualification projects, as well as sensitivity and uncertainty analyses of physical models, have been conducted worldwide [70]. Extensive literature exists on the code description, capabilities, and applications. RELAP5 is a code for studying LWR transient analysis, developed at Idaho National Engineering Laboratory (INEL) for the U.S. Nuclear Regulatory Commission (NRC). The RELAP5 code has been developed for best estimate simulation of LWR coolant system transients during normal and off normal conditions. The code models the coupled behaviour of the reactor coolant system and the core (point kinetic) for simulating accidents in LWR.

RELAP5 is a code written in FORTRAN 77 that solves one-dimensional fluid-dynamic problems related to one-dimensional problems of heat exchange. A generic modelling approach is used. It allows the simulation of a variety of TH systems, such as turbines, condensers, and secondary feedwater systems. The component models also include pumps, valves, pipes, heat releasing or absorbing structures, reactor point kinetics, electric heaters, jet pumps, etc. In addition, special process models are included for effects such as form loss, flow at an abrupt area change, branching, choked flow, boron tracking, and non-condensable gas transport. This code is highly versatile and can be used to simulate a wide variety of hydraulic and thermal transients, including non-nuclear systems involving mixtures of steam, water, non-condensable gases and solutes (although only boron is accounted for in RELAP5 as solute).

RELAP5 code is based on one-dimensional, transient, non-homogeneous and non-equilibrium hydrodynamic model for the steam and liquid phases and uses a set of six partial derivative balance equations. It can model a non-condensable component in the steam phase, which is assumed to move with the same velocity and have the same temperature as the vapor phase. Therefore, all properties of the gas phase are mixture properties of the steam/non-condensable mixture [66]. A semi-implicit numeric scheme is used to solve the equations inside control volumes connected by junctions. The balance equations of mass and energy are solved in the centre of the volumes for each phase; therefore, the fluid scalar quantities (pressure, energy, density, and void fraction) are evaluated at this location. The balance equation of the momentum is solved in correspondence of the junctions: here the vector quantities (velocities) are computed. Moreover, in the separate-phases model adopted by the code it is important to establish the flow regime from which the conservation laws at the interface of the two phases (friction force at the interface) and the conservation laws for each phase (friction force to the wall) depend.

Heat flow paths are also modelled in a one-dimensional direction, using a staggered mesh to calculate temperatures and heat flux vectors. All the solid components (walls of pipes, nuclear fuel pins, heat exchangers, etc…) can be simulated as heat structures capable of transferring heat by conduction and exchanging between the related volumes (maximum two volumes). The convective heat transfer coefficient, besides factors such as velocity, is affected by the flow field or hydraulic geometry surrounding the surface. The user can use pre-defined convection boundary types for available configurations [71].

The solution timestep is defined by the user at the beginning of the input, even though the code can gradually halve the timestep during the computation to meet the convergence criteria. The reduction of the timestep ends when a minimum value set by the user is reached with a consequent exit from the calculation process.

2.3 Ansys CFX code

Ansys CFX [51] [72] is a widely used CFD software developed by Ansys Inc. [73], designed to solve complex fluid flow and heat transfer problems. It has been continually enhanced and validated in a wide range of applications across various industries, including nuclear, aerospace, and automotive engineering. The software is known for its high accuracy in simulating turbulent flows, multiphase interactions, and FSI, among others. Due to its versatility, CFX has been applied extensively in nuclear reactor analysis, specifically for the study of coolant flow, heat transfer, and mixing phenomena. The code development and verification have also been extensively documented for nuclear reactor safety applications [74] [75] and liquid metals applications within European projects such as THINS (Thermal-Hydraulics of Innovative Nuclear Systems) [76] and SESAME (thermal hydraulic Simulations and Experiments for the Safety Assessment of MEtal cooled reactors) [77] [78]. The ongoing ANSELMUS (Advanced Nuclear Safety Evaluation of Liquid Metal Using Systems) [79] project aims, among other objectives, to produce experimental data for assessing FA safety and validating CFD codes.

Ansys CFX is based on a cell-vertex mixed finite volume/finite element method to solve the Navier-Stokes equations. In vertex-based schemes, flow variables are stored at the mesh element vertices. The code employs a coupled technique, simultaneously solving all transport equations across the entire domain through a false timestep algorithm. To expedite convergence, the linearized system of equations is preconditioned to reduce eigenvalue disparities.

The software can handle both steady-state and transient analyses and is particularly suited for high-performance simulations involving complex geometries and physical models. CFX solves the conservation equations for mass, momentum, and energy in three-dimensional space. The code supports both structured and unstructured meshes, allowing flexibility in grid generation for complex geometries.

A major strength of CFX lies in its ability to model turbulent flows using a variety of turbulence models such as RANS, LES, and Detached Eddy Simulation (DES). It also includes multiphase flow models for simulating phase interactions, which are relevant for nuclear applications involving liquid metals or gas bubbles [80], as well as combustion and electromagnetic hydrodynamic models. Heat transfer is modelled through convective, conductive, and radiative mechanisms. Ansys CFX allows the use of various Boundary Conditions (BCs), including predefined convection models for different flow regimes. The software's robust solver and efficient parallel processing capabilities make it suitable for large-scale simulations required in nuclear TH.

CFX is integrated with other Ansys tools, such as Ansys Mechanical, to perform multiphysics simulations. This allows for coupled FSI analyses, where fluid forces and thermal effects are considered simultaneously with structural deformations. The user interface is highly interactive, offering pre-processing tools for mesh generation, post-processing tools for result visualization, and scripting options for advanced automation.

The software adopts an implicit time-stepping method for transient simulations, ensuring stability and accuracy in simulations with small timesteps. The timestep is user-defined but can be adapted automatically during the solution process to meet convergence criteria. The solver monitors solution stability and adjust the timestep, if necessary, to achieve accurate results.

2.4 RELAP5 – Ansys CFX coupled code

The coupling enables the integration of detailed CFD analyses within system-level STH calculations, providing multiscale simulation capabilities. This thesis presents a coupling methodology between the STH code RELAP5/Mod3.3 and the CFD code Ansys CFX [81]. The classification of the methodology discussed follows the guidelines in Ref. [58], considering six key characteristics (see Figure 9):

- Code Integration: Determines whether a single code solves all subsystems (referred to as "Monolithic"), resulting in stronger coupling, or whether separate solvers are used for each sub-system ("Partitioned").
- Coupling Execution: Describes whether information exchange flows only in one direction from one code to the other ("Off-line" or "One-way") or whether both codes provide feedback ("In-line" or "Two-way").
- Synchronization: Refers to the temporal coordination of information transfer, which may rely on either "Identical Time Steps" or "Sub-cycling Approaches".
- Information Exchange Type: Specifies whether the codes run concurrently ("Parallel") or sequentially ("Sequential").
- Spatial Domain: Defines whether part of the domain is simulated by the STH code and the other by the CFD code ("Decomposition") or whether the entire domain is simulated by the STH code, with partial overlap by the CFD domain ("Overlapping").
- Numerical Scheme: Refers to the solver's time-discretization, which may be "Explicit", "Semi-implicit", or "Fully implicit".

Both RELAP5 and Ansys CFX are stand-alone codes with closed structures, limiting direct modification of their solvers. Consequently, a partitioned coupling approach has been adopted. The coupling methodology employs two-way communication to fully leverage the benefits of coupling, although the option for one-way data exchange is available to the user. Data exchange occurs sequentially due to the significant difference in simulation times between CFD and STH codes. Synchronization is achieved using a sub-cycling approach. The next section provides a comprehensive overview of the tool, outlining the choices made regarding the spatial domain discretization and the numerical time-stepping scheme.

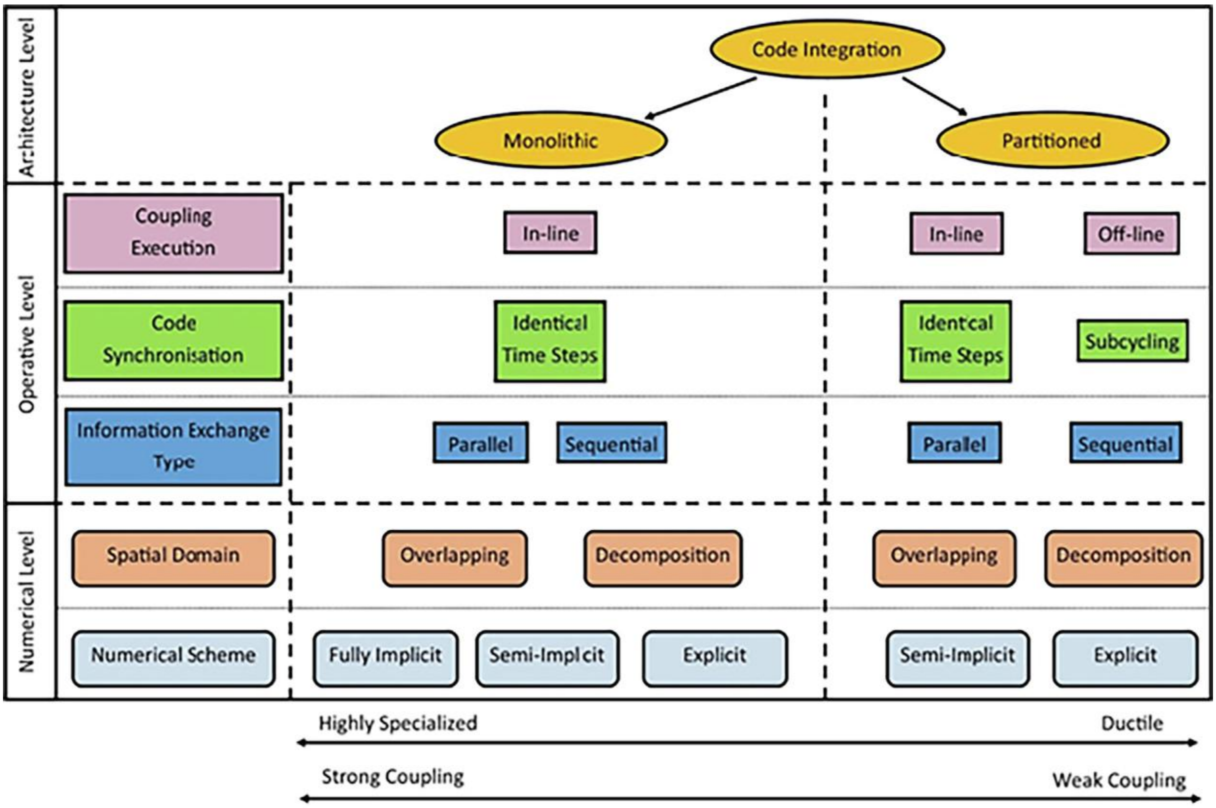

Figure 9 – Code coupling classification [82]

CFX has been designated as the master code due to its capability to read custom FORTRAN subroutines – named “Junction Box Routines” (JBRs) – which can manage the coupling simulation execution while avoiding the need for an intermediate tool for data exchange. This choice also facilitates the extraction of CFD results by adopting rapid and accessible instructions to manage data exchange within the memory allocated for the master operations. JBRs are inserted by the user in the setup of the CFD calculation and are called at specific “time-locations” during the CFX execution (see Figure 10). The optimal selection of these time-locations is critical for minimizing memory usage and reducing the computational cost of executing the scripts, while still allowing CFX to parallelize computations across multiple processors. The master processor is responsible for managing the data exchange between codes. In CFX, the only time-locations where the memory of the master CPU is replicated across all processors are those beginning with “User Input” (e.g., “User Input (master only)”, “User Input Start of the Time Step”) [51] (see Figure 10). Therefore, the routines handling the BC exchange between the two codes are inserted into these time-locations to ensure proper operation of the Message Passing Interface (MPI). Further details on how JBRs are used in different coupling schemes are provided in Sect. 2.5.

The cycling of the two codes is independent, allowing for different timesteps. The coupling timestep corresponds to the CFX timestep, while the RELAP5 timestep can be equal to or a fraction of the coupling timestep. The number and function of the FORTRAN routines are largely dependent on the numerical time advancing scheme. However, shared tools are necessary to manage the RELAP5 files. The RELAP5 restart file (*.rst*) is used to initiate the coupled calculation. It contains the “pre-coupling” RELAP5 results and stores the results of subsequent timesteps during the coupled simulation. At the beginning of each timestep, the BCs are stored and transferred to an input file (*.inp*), where the corresponding data in the restart file is updated.

Two in-house developed Python executables are used in this coupling process:

- *Modify_input_R5*: This executable inserts the RELAP5 BCs and sets the timestep and the end time for the RELAP5 run in the input file.
- *Read_R5*: This executable post-processes the binary restart file, extracting the plot records and saving them in a plot file (*.plt*), isolating the restart blocks required for the next RELAP5 timestep, and generating a *.csv* file containing the BCs for CFX. The user defines the plot frequency.

Since the current version of the coupling tool lacks a graphical user interface, a simple text file (*.dat* or *.txt*) is used, where the user specifies the variables for exchange and parts of the coupled calculation setup. The text file is formatted so that the FORTRAN routines can interpret the data correctly.

Synchronization is achieved by using a fraction of the coupling timestep for the STH code and ensuring that the final time of the RELAP5 run matches the current CFX simulation time plus its current timestep. This approach allows for adaptive coupling timesteps, with the RELAP5 timestep adjusting accordingly. The ratio between the CFX (or coupling) timestep and the RELAP5 timestep can be greater than or equal to 1 (though a ratio of 1 is discouraged). This means that RELAP5 can run with smaller timesteps, improving the tool's robustness with minimal impact on overall simulation time, given the lower computational cost of RELAP5. The following sections describe the numerical time advancement schemes and domain discretization methods implemented in the newly developed tool.

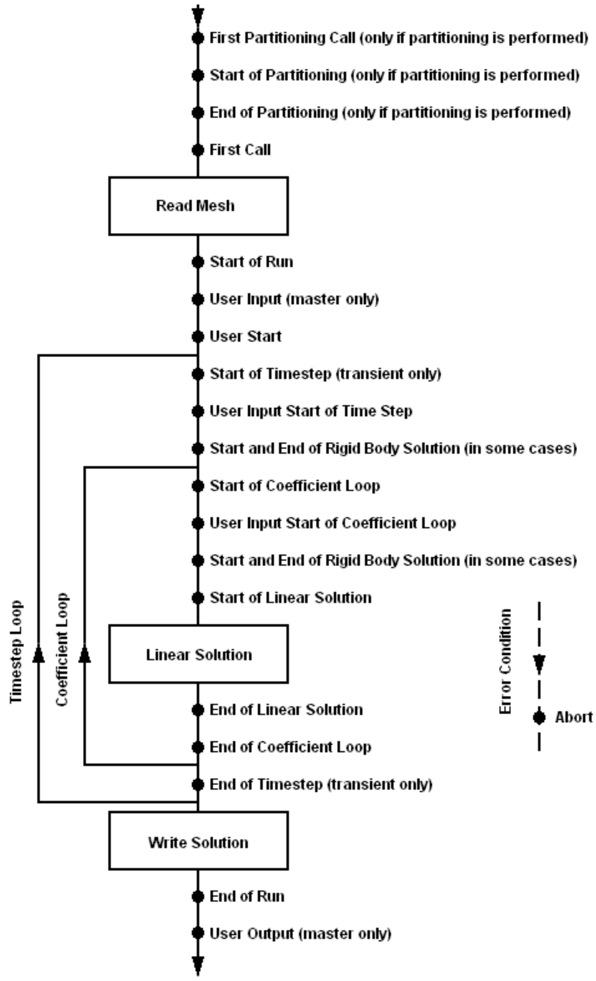

Figure 10 – Time locations available during the Ansys CFX solver operation at which a junction box routine can be called [51]

2.5 Numerical time advancing scheme

In this section, two numerical time advancing schemes are presented. First, an explicit scheme was developed (see Sect. 2.5.1) to test the coupling approach. Its main characteristic is its simplicity, which allows a relatively easy implementation, although it can lead to numerical instabilities in fast developing transients. The countermeasures to overcome such instabilities consist mainly of reducing the timestep of the coupled calculation or adopting a semi-implicit time advancing scheme. For this reason, Sect. 2.5.2 presents the semi-implicit scheme, which, in principle, allows for the use of larger timesteps at the cost of several iterations within the same timestep, while switching to an explicit-like scheme when the system approaches a new steady state condition after a transient.

2.5.1 Explicit scheme

The explicit time-advancing scheme is the simplest and fastest, as the results from the current timestep of one code are applied as BCs for the next timestep of the other code. A schematic representation of the communication between the two codes is shown in Figure 11. However, a key limitation of this approach is that it generally restricts the timestep size and results in less frequent communication between the codes per timestep [83].

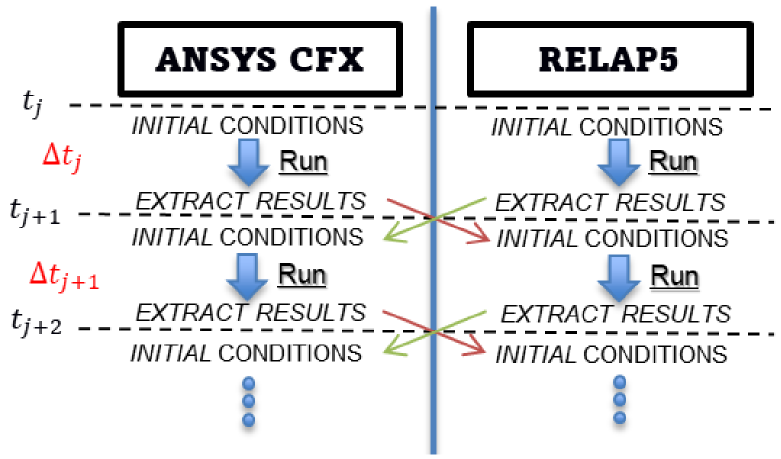

Figure 11 – Diagram describing the time-stepping process in an explicit scheme, highlighting the sequence of code execution and information exchange

In the explicit scheme, exchanged data are applied as constant BCs throughout each timestep in both the CFX and RELAP5 codes. This represents the main approximation of the method, which is valid as far as the timestep is sufficiently small.

Let's define X^j and Y^j as the BCs for CFX and RELAP5 at the *j*-th time instant, respectively, and $F(X)$ and $G(Y)$ as the results of the codes' runs. In general, X can represent a TH quantity such as mass flow rate, temperature, pressure, heat flux, etc. In an explicit time-advancing scheme, we can express the relationship as:

$$\begin{aligned} Y^j &= F(X^{j-1}) \\ X^j &= G(Y^{j-1}) \end{aligned} \qquad (1)$$

For the BCs to be exchanged from one code to another, proper manipulation is needed. More specifically, the CFX results (imposed to RELAP5 as BCs) are averaged at the boundary surfaces, while the 1D RELAP5 results are multiplied to a non-dimensional 3D profile. In this case, the user should extract such a profile from a preliminary CFX simulation. While the RELAP5 results are stored in an external text file, the CFX results are not; instead, they are directly written in the RELAP5 input file by means of an in-house Python-written executable.

The CFX memory management is in charge of specific FORTRAN routines, which are organized into one User CEL (CFX Expression Language) function and three JBRs [51]. The User CEL function is responsible for setting the variables coming from RELAP5 as BCs for the CFX timestep (making 1D results suitable for a 3D calculation) and is called automatically by the CFX code. JBRs are generic FORTRAN scripts called at specific time locations within the CFX run. In the coupled simulations, several JBRs are called, each performing different tasks. In the explicit scheme, the following JBRs are used:

- *jbr_userinput*: This routine is called before the first timestep begins. It reads the necessary data from the *.dat* file (referred to as the "info file"), including the names and paths of the RELAP5 files, as well as the CFX and RELAP5 variables to be exchanged.
- *jbr_userinput_sott*: Called at the start of each timestep (*sott* stands for "start of the timestep"), this routine reads the RELAP5 results that must be passed to CFX.
- *jbr_endofthetimestep*: This routine is executed at the end of each timestep and is responsible for the following:
  - Modifying the RELAP5 input file with the results from the CFX timestep (via the *Modify_input_R5*).
  - Running the RELAP5 timestep(s).
  - Post-processing the RELAP5 restart file (via *Read_R5*).
  - Extracting the variables to be passed back to CFX (via *Read_R5*).
  - Appending the latest results to a *.plt* file and reducing the size of the *.rst* file to prevent large file manipulation (via *Read_R5*).

A schematic showing the time points at which these routines are called is provided in Figure 12.

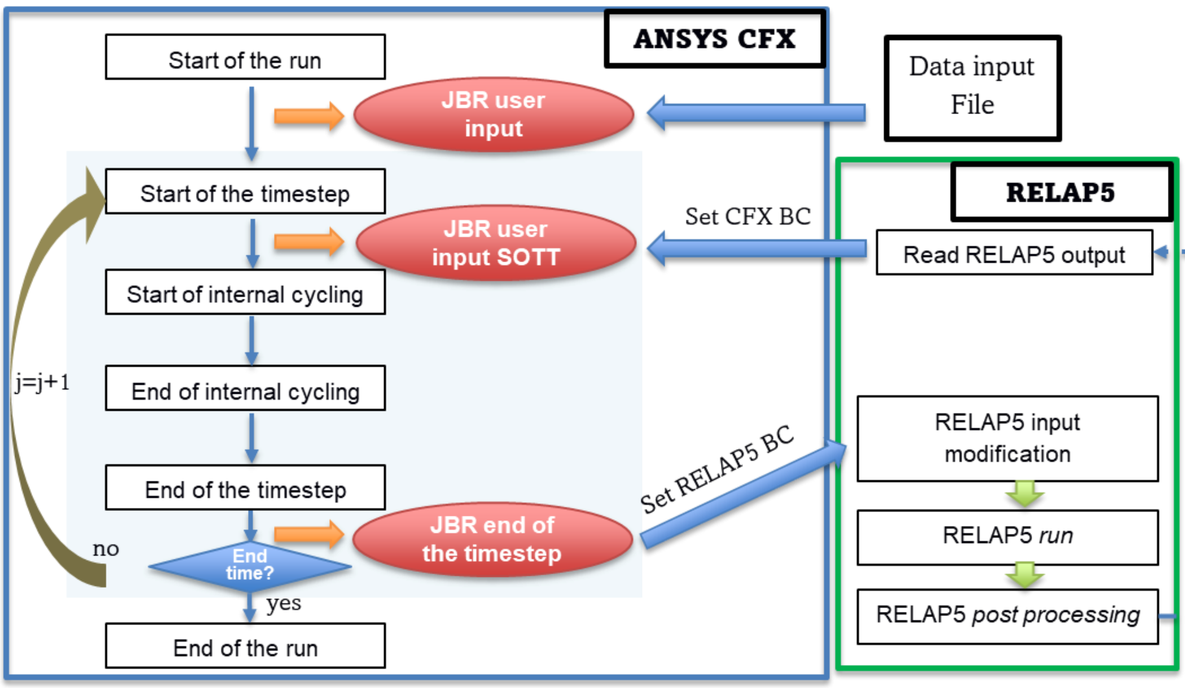

Figure 12 – Coupling methodology between Ansys CFX and RELAP5 in the explicit scheme.

2.5.2 Semi-implicit scheme

The semi-implicit scheme differs from the explicit one by considering the results of the other code during internal iterations. However, it is not a fully implicit scheme since the solvers remain separate and the equations are not solved entirely implicitly. For this reason, the semi-implicit scheme represents the most advanced approach when using codes such as CFX and RELAP5.

In this scheme, the calculation over the same timestep is iterative until the difference between the BCs of two consecutive iterations (i and $i-1$), relative to the results at the current iteration, is smaller than a specified tolerance (*tol*):

$$\frac{|X_i^j - X_{i-1}^j|}{|X_i^j|} < tol \tag{2}$$

or the user-defined maximum number of internal cycles is reached. Even though X in Eq. (2) represents a generic TH quantity, *tol* is a unique value for all the exchanged BCs, as it is the relative difference and not the absolute one. It is calculated at the end of each iteration to check the convergence of the calculations. The check on the BCs assumes that, from equal BCs, the same solution is given by the codes (see Figure 13).

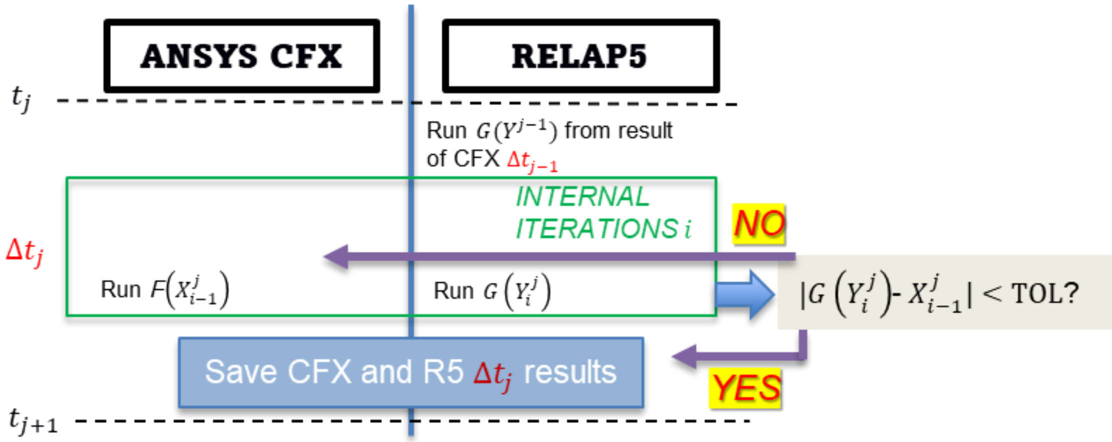

Figure 13 – Diagram describing the time-stepping process in a semi-implicit scheme during a single coupling timestep, highlighting the sequence of code execution and the convergence check in the internal iteration.

During the internal iterations of the current timestep, BCs are not constant as in the explicit scheme but instead reflect the influence of the current results from the other code. For RELAP5, which may operate with a fraction of the coupling timestep, the BCs are updated as a linear interpolation between the results from the previous timestep (Y^{j-1}) and those obtained by CFX during the current iteration $\left(F(X_{i-1}^j) = Y_i^j\right)$. In contrast, for CFX, which computes a single timestep, the BCs are updated based on the current RELAP5 results. Since CFX uses an implicit solution method, it inherently accounts for variations in BCs during a timestep.

A new coupled timestep begins with the RELAP5 run, as in the explicit approach, using constant BCs. This ensures that the semi-implicit effect on BCs (i.e., feedback from RELAP5) is available to CFX from the first iteration. Convergence is monitored based on CFX BCs coming from RELAP5. In some cases, the tolerance may be reached after just one CFD internal iteration, following the RELAP5 run. This can potentially reduce the computational time of CFX by limiting the number of internal iterations.

An under-relaxation factor ω, defined by the user, is implemented to smooth the BCs update between two consecutive iterations within the current timestep, following the formula:

$$X_i^j = X_{i-1}^j + \omega\left[G(Y_i^j) - X_{i-1}^j\right] \tag{3}$$

where i is the internal iteration index. The under-relaxation factor ω ranges from 0 to 1 to dampen oscillations in the solution, with a default value of 1, meaning that the updated BC is not influenced by the previous iteration.

The routines are structured into one User CEL function and five JBRs, as summarized below:

- *jbr_userinput*: Performs the same functions as in the explicit scheme.
- *jbr_userinput_sott*: Called at the start of each timestep, this routine reads CFX results from the previous timestep, defines the coupling timestep, stores the previous *.rst* file as *old.rst*, and runs RELAP5 with constant BCs. The RELAP5 results are processed to update the semi-implicit BCs for CFX.
- *jbr_userinput_socl*: Invoked at the "socl" (start of coefficient loop, i.e., CFX internal iterations), except the first one, this routine reads and stores RELAP5 results from the previous loop to pass them to CFX.
- *jbr_endofthecoefficientloop*: At the end of each coefficient loop, this routine deletes the current RELAP5 results and runs a new simulation using the *old.rst* restart file with updated semi-implicit BCs. It then processes the results, compares the new CFX BCs with the previous ones, and checks for convergence. If the convergence criteria are met or the maximum number of iterations is reached, the timestep ends; otherwise, another cycle begins.
- *jbr_endofthetimestep*: Called at the end of each timestep, this routine stores the final results, appends the last result to a *.plt* file, and reduces the size of the *.rst* file to avoid handling large files.

A schematic of the semi-implicit coupled timestep is shown in Figure 14.

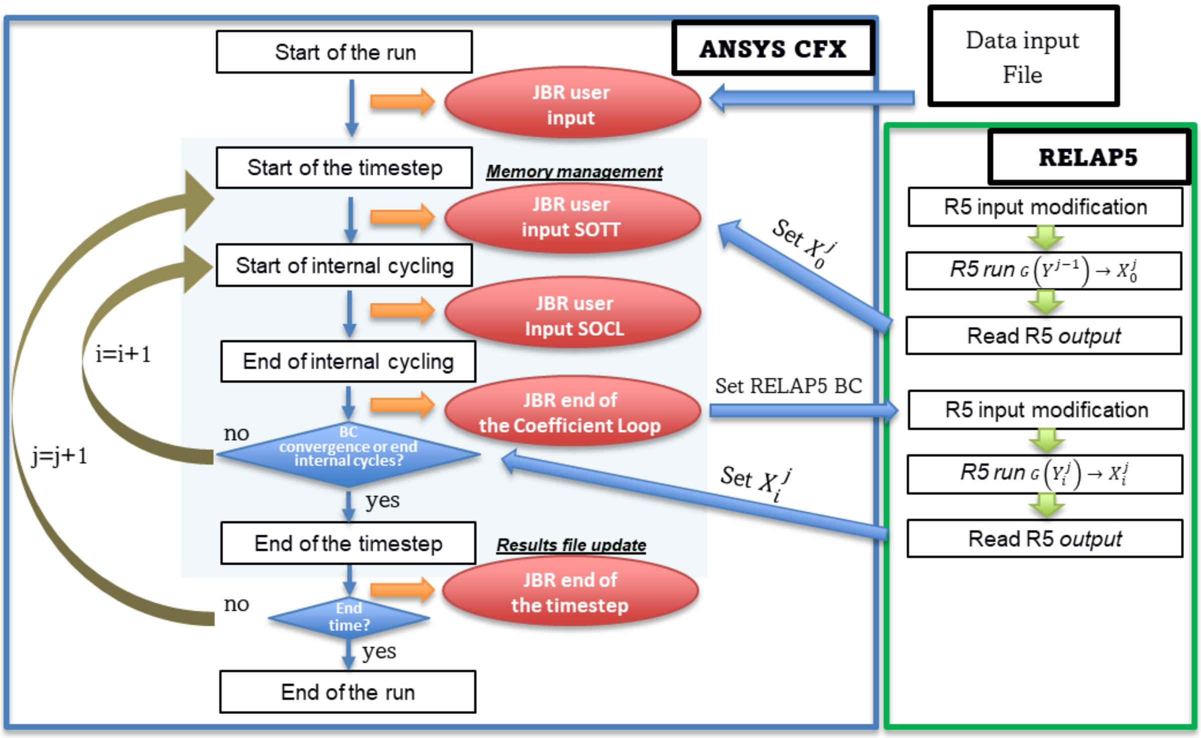

Figure 14 – Coupling methodology between Ansys CFX and RELAP5 in the semi-implicit scheme.

2.6 Domain discretization approach

Regarding the spatial discretization approach, both domain decomposition and overlapping strategies have been explored and implemented. The domain decomposition approach was first implemented since it is simpler than the domain overlapping approach, as it involves the direct exchange of BC values without the need for manipulating the quantities. However, special care must be taken to ensure that the sections where values are exchanged correspond accurately, and that the conservation of mass, momentum, and energy is verified (see Figure 15a).

In contrast, the domain overlapping approach ensures the conservation of these variables, being the entire domain modelled through the STH code. Here, the coupling is achieved by adjusting certain STH parameters to align with the CFD results (see Figure 15b). The details of the two approaches are presented in Sects. 2.6.1 and 2.6.2, respectively.

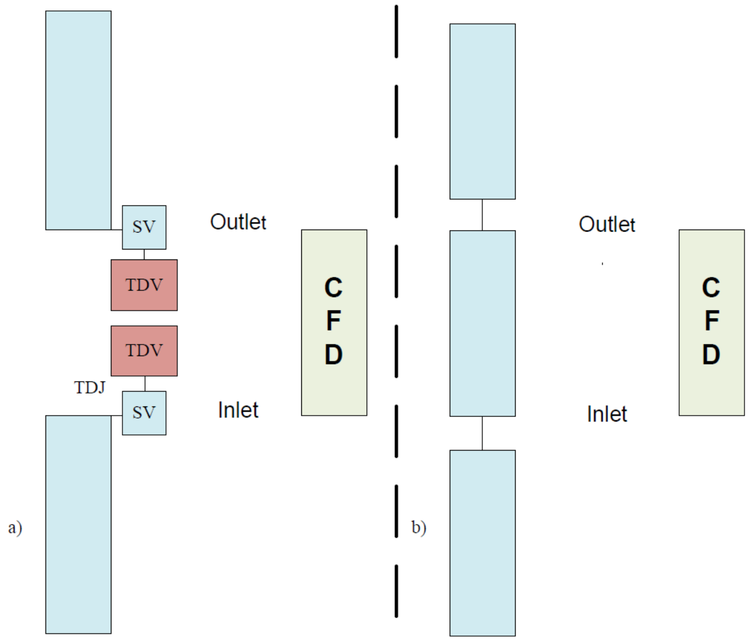

Figure 15 – RELAP5/Mod3.3 schematization of the nodalization in the domain decomposition (a) and overlapping (b) approach.

2.6.1 Domain decomposition

To adopt the domain decomposition approach with the CFX-RELAP5 tool, the CFX domain must be carefully defined. An opening BC is the most flexible solution, as it allows reverse flow phenomena at the CFD inlet and outlet. At one of the boundaries, velocity (or mass flow rate) should be specified as a uniform, constant value if the pressure losses due to flow development are negligible. Alternatively, a non-dimensional map, assumed to be constant throughout the simulation, can be applied. With this method, it is important to verify whether the mass flow rate, derived from the product of the STH velocity and the velocity map, aligns with the intended value. At the opposite boundary, relative pressure is set to zero. Additionally, the inlet and outlet temperatures in the CFD domain can either be uniform across the area or governed by a non-dimensional map. Typical quantities retrieved by the STH code include velocity, fluid temperature, and thermal BCs such as heat flux or wall surface temperature.

Challenges related to STH BCs arise from the way RELAP5 computes pressure and temperature at the center of the element volume. This becomes critical in vertical domains, especially with HLMs, where gravitational effects are significant. The most effective solution involves placing the surface for information exchange at the boundary of one RELAP5 volume and connecting it to a small horizontal volume (see Figure 15) such that the surface's and the center of the horizontal volume's absolute heights correspond. In RELAP5, the friction pressure drop in a fluid volume can be set to zero using a specific flag, ensuring that the pressure computed in the horizontal volume accurately matches that at the boundary surface. The temperature is also extracted from the horizontal volume, even though a slight time delay due to the crossing of the fluid in the volume is introduced. However, the delay can be minimized by adopting a small axial length for the volume.

RELAP5 BCs are imposed through two time-dependent volumes connected to the two small horizontal volumes. For a vertical domain, where the outlet is at a higher elevation than the inlet, the pressure is computed as follows:

$$\begin{aligned} p_{inlet}^{k} &= p_{outlet}^{k-1} + \Delta p_{CFX}^{k} \\ p_{outlet}^{k} &= p_{inlet}^{k-1} - \Delta p_{CFX}^{k} \end{aligned} \tag{4}$$

where p is the static pressure, and the index $k-1$ corresponds to the last RELAP5 run, representing either the previous timestep $j-1$ in an explicit scheme or the last internal iteration $i-1$ in the semi-implicit approach. The term Δp_{CFX} accounts for the gravitational forces as follows:

$$\Delta p_{CFX} = Relative\ Pressure_{Inlet} - Relative\ Pressure_{Outlet} + \rho_{ref}\ g\ H \tag{5}$$

where the pressures (relative to a user-specified reference value) are evaluated at the “inlet” and “outlet” boundaries, ρ_{ref} is a user-specified reference density, g is the acceleration of gravity, and H is the elevation change from the inlet to the outlet surfaces. The temperatures applied in the time-dependent volumes are mass flow-averaged values from the corresponding CFX surfaces, while the CFX mass flow rate is imposed through a time dependent junction connected to one of the time dependent volumes.

2.6.2 Domain overlapping

For the domain overlapping approach, the CFX BCs are imposed as described previously, as the requirements remain consistent across both methods. However, in RELAP5, the domain is closed, and the feedback from the CFD code is not directly applied by passing variable values. Instead, adjustments are made to certain model parameters. While the conceptual approach is similar for all CFD-STH couplings, the practical implementation of this methodology depends on which parameters are available in the STH code.

To align the pressure drops in RELAP5 with those computed in CFX, two methods have been developed and can be applied: adjusting the friction factor (f) or modifying the local pressure loss coefficients (K). Therefore, these modifications can be distributed across the entire corresponding CFD domain or localized in specific junction components, respectively. The impact of this approach is problem-dependent, and it is up to the user to decide the best strategy.

<u>Solution with the friction factor f</u>

This approach is based on the method presented in Ref. [63] and allows simplifying the overlapped domain representation by reducing the number of volumes needed in RELAP5 to 3 volumes: a single central volume with the same vertical height as the CFD overlapped domain, and two small horizontal volumes at the upper and lower boundaries, similar to the decomposition approach. The central volume should reproduce the CFX pressure drop by defining a suitable friction factor (f_{RELAP5}). The correlation between the f_{RELAP5} and Δp_{CFX} comes from the momentum conservation equation of the two codes:

RELAP5/Mod3.3
$$\rho\frac{\partial U}{\partial t} + \frac{1}{2}\rho\frac{\partial U^2}{\partial x} = -\frac{\partial p}{\partial x} - \frac{1}{2}\frac{f_{RELAP5}}{D_h}\rho U|U| - \rho g \tag{6}$$

Ansys CFX
$$\rho\frac{\partial \boldsymbol{U}}{\partial t} + \rho\boldsymbol{U}\cdot\nabla\boldsymbol{U} = -\nabla p + \nabla\cdot\bar{\bar{\boldsymbol{\tau}}} - \rho\boldsymbol{g} \tag{7}$$

where the symbols in bold indicate vector quantities, and $\bar{\bar{\boldsymbol{\tau}}}$ is the stress tensor. When using an explicit coupling scheme, correcting for the local acceleration pressure term (first term on the left-hand side of the equations) in the STH code is not straightforward, as this term results from velocity updates at each timestep. However, since the tool is applied to incompressible flows, it can be reasonably assumed that the difference in the calculation of this term by CFX and RELAP5 for the domain overlapping is negligible, as long as fluid velocities remain consistent. Therefore, only the non-local acceleration pressure drop terms (i.e., convective acceleration, gravity, and friction) need to be adjusted [61] [62].

To ensure that the total pressure drop in the CFD domain matches the one computed by RELAP5, the sum of the pressure gradient and the local acceleration pressure drop is substituted into Eq. (6). The RELAP5 friction factor can then be computed as:

$$f_{RELAP5} = \frac{2D_h}{\rho U|U|}\left(\left[-\frac{1}{V}\int_V \left(\nabla p + \rho\frac{\partial \boldsymbol{U}}{\partial t}\right)\cdot \hat{n}\, dV\right]_{CFX} - \frac{\rho}{2}\frac{\partial U^2}{\partial x} - \rho g\right) \tag{8}$$

The scalar product between the CFD terms ("3D" terms) and the unit vector $\hat{n}$ parallel to the flow direction has been performed to convert them into "1D" quantities. This makes them consistent with the RELAP5 1D formulation of the momentum equation. Consequently, only the projection of such vectors along the RELAP5 flow path has been considered. The CFD informed term ($[\dots]_{CFX}$) is explicitly evaluated in the following way:

- $\frac{1}{V}\int_V (\nabla p \cdot \hat{n}) dV = \Delta p_{CFX}/L = (p_{outlet} - p_{inlet})/L$. It is the pressure difference across the boundaries, divided by the distance between them, i.e., the difference in absolute height.
- $\frac{1}{V}\int_V \left(\rho\frac{\partial \boldsymbol{U}}{\partial t}\cdot \hat{n}\right) dV = \frac{1}{V}\int_V \rho\frac{\partial U_x}{\partial t} dV$. It is the volume-averaged product of the density and the time derivative of the velocity along the flow direction.

Issues arise when the system velocities approach zero since the denominator of Eq. (8) tends to zero while the numerator does not tend to zero like the square of the velocity, leading to infinite friction factor values. To prevent numerical instabilities, a user-defined upper limit for the friction factor has been implemented.

Moreover, when velocities are low, relatively small numerical errors or the miscalculation of the density can cause the sign of the sum in parentheses to disagree with the actual velocity direction, resulting in a negative friction factor. To address this, the RELAP5 source code was modified to allow for the introduction of a momentum source in the overlapped fluid volume through a negative friction factor. While this adjustment may slightly distort the pressure matching between the two codes at low velocities, the overall impact on the simulation is generally negligible in most cases.

To match temperatures at the boundaries and in the central volume, three "fake" heat structures – characterized by infinite thermal conductivity and null thermal inertia – are connected to each of the three fluid volumes. These particular thermal properties prevent significant distortions in the simulated domain, i.e., to minimize the temperature gradient and the time delay of the heat transfer to the fluid due to the conduction inside the solid. In particular:

- The small horizontal volumes are connected to heat structures in which a fixed temperature BC is imposed by CFX.
- The single volume representing the overlapped domain is connected to a heat structure that imposes a temperature such that the domain's average density matches that of the CFX domain. In such a way, inconsistencies between the two codes in the gravitational term calculation in the momentum equations are limited. Although better consistency of the gravitational terms would be achieved with the integral average along the vertical flow direction in the domain, the volume-averaged density has been used because of its simplicity and has been considered a good approximation.

Solution with the K loss coefficient

An alternative solution has been developed to overcome numerical instabilities at low velocities and/or flow reversal. To adopt this solution, it is not necessary to simplify the geometry of the model, but it can be kept as the RELAP5 stand-alone one. Then, the following modifications must be made:

- Set the distributed pressure drops to zero in the RELAP5 overlapped domain using a dedicated flag in the code.
- Set all local pressure drops to zero, except for one junction, which can be located at the inlet section connecting with the rest of the loop.
- With the assumption that the entire pressure drop is now concentrated at this single point, the local pressure drop coefficient (K) can be modified to match the CFX value.

The local pressure drop coefficient is related to the CFD pressure drops and the fluid velocity at the inlet section as follows:

$$K = \frac{2\left(\Delta p_{CFX} - \rho_{ref}\, g\, H\right)}{\rho_{inlet}\, U_{inlet}^2} \tag{9}$$

As highlighted in the "friction factor case", this ratio may yield very large values if the velocity approaches zero. To avoid dealing with small denominators, an alternative formulation for the K value is proposed, assuming that the time derivative of the K value is proportional to the discrepancy between the pressure drops (Δp) computed by the two codes:

$$\frac{\partial K(t)}{\partial t} = s \cdot (\Delta p_{CFX} - \Delta p_{RELAP5}) \cdot sign(U_{inlet}) \tag{10}$$

Integrating Eq. (10) across the timestep it becomes:

$$K^k = K^{k-1} + s \cdot \frac{\left(\Delta p_{CFX}^{k-1} - \Delta p_{RELAP5}^{k-1}\right) + \left(\Delta p_{CFX}^{k-2} - \Delta p_{RELAP5}^{k-2}\right)}{2} \cdot \Delta t \cdot sign(U_{inlet}) \tag{11}$$

The terms in this equation are defined as follows:

- s: A user-defined scaling factor that allows for the relaxation of the K variation. Larger scaling factors speed up convergence between the two pressure drop values, but if chosen too large, they can result in instability (oscillations or divergence). This value is not known a priori and must be selected based on experience and trial.
- Δt: The timestep size.
- Δp and K: Total pressure drop and K values evaluated at the last and second-to-last timesteps (indicated by the superscript k) in the explicit scheme, or CFX internal iterations in the semi-implicit scheme. Strictly speaking, this integration scheme is valid only in the semi-implicit approach – where the K values and the· $(\Delta p_{CFX} - \Delta p_{RELAP5})$ terms correspond at the respective timesteps. However, it can be considered valid, and it has also been successfully applied in the explicit scheme, as far as the timestep is sufficiently small (which is still a general requirement for the method), preventing large variations of the Δp within the coupling timestep.
- $sign(U_{inlet})$: The sign of the inlet velocity, which ensures that the pressure drop in the domain is correctly inverted when flow reversal occurs.

This formulation ensures that the local pressure drop coefficient is increased when RELAP5 underestimates the pressure variation in previous timesteps and decreased when the opposite is true. The main advantage of this solution consists in the computation of the total pressure drop from CFX without discriminating among the various terms of the momentum equation, and without divergent K values at low velocities. However, such formulation depends on a user-defined scaling factor that should be calibrated for each simulation since it can lead to numerical instabilities in some cases.

3 CODES VALIDATION FOR THE THERMAL-HYDRAULIC ANALYSIS OF LFRS

This section is divided into four subsections: the first three are devoted to the comparison of simulation results with experimental data provided by different facilities, whereas the last one contains a summary of the results and a preliminary qualitative assessment of the codes' performances. Sect. 3.1 contains the post-test analysis of SIRIO experimental facility through RELAP5/Mod3.3 code. Here, RELAP5 stand-alone is considered since the phenomena involved do not necessarily require the use of a CFD or a STH/CFD coupled calculation. Moreover, in this subsection, the post-test analysis by the RELAP5 code brought out the necessity of modifications to the source code to reproduce relevant phenomena for Gen-IV related passive systems.

It must be highlighted that the modifications detailed in Sect. 3.1 were implemented within an already modified version of the RELAP5/Mod3.3 code, since its standard version does not contain the HLMs properties as coolants. Specifically, the modifications reported in Sect. 3.1 are in addition to previous modifications of the source code to incorporate the thermo-physical properties of HLMs and to simulate the coexistence of HLMs and non-condensable gases within the same hydraulic volume, along with the implementation of suitable heat transfer correlations [84] [85].

After such modifications, the coupled RELAP5/Ansys CFX tool has been used to simulate experiments conducted in the NACIE-UP (Sect. 3.2) and TALL-3D (Sect. 3.3) facilities. This validation process starts with a case (NACIE-UP) in which the coupled code is not expected to dramatically change the STH results, and then it switches to a case (TALL-3D) in which the facility is designed to enhance the effect of the CFD contribution in the coupled simulations.

3.1 SIRIO

In the field of R&D activities, whenever innovative designs approach the state of the art in the nuclear industry, it is necessary to verify the operation of such systems and components. Experimental facilities are thus needed to verify the functioning of systems, study the relevant phenomena involved, and demonstrate the technical feasibility of innovative designs. Moreover, configurations not supported by experimental evidence require the generation of a reference database, enriching also the literature related to such phenomena [86]. Additionally, as outlined in the IAEA's guidelines [87], any numerical code used in safety analysis must undergo a Verification and Validation (V&V) process to confirm the correct implementation of mathematical models and its accuracy. The experimental results obtained from these facilities are critical for developing numerical models capable of predicting the behavior of the system under investigation as accurately as possible.

Experiments carried out at SIRIO facility [88], along with the related numerical post-test analysis, aim at demonstrating the technical feasibility of an innovative passive DHR, and assessing the capability of computer codes in reproducing complex phenomena involved in this system. The post-test analysis described in this section aims also at providing a STH validated code to be used in coupled simulations involving Gen-IV systems. As outlined in Sect. 3.1.4, modifications to the RELAP5 source code were made necessary to reproduce phenomena not involved in the validation process related to LWRs applications.

The experimental tests were carried out within the Work Package (WP) 3 of the HORIZON2020 Passive IsolAtion CondEnser (PIACE) project [89], which was funded by the European Commission (EC) and lasted from 2019 to 2022. The related post-test analysis has been carried within the WP4.1 (System Prototype Design and System Analysis Behavior – Post test analysis) [90] [91]. The project aimed at investigating experimentally and numerically passive DHRs involving four different nuclear technologies: LFRs, PWRs (Pressurized Water Reactors), ADSs (Accelerator Driven Systems), and BWRs (Boiling Water Reactors). In this section, only the experiment related to the LFR configuration is considered since it is the one of interest for Gen-IV applications.

3.1.1 Description of the facility

SIRIO (Sistema di rimozione della potenza di decadimento per reattori nucleari innovativi) facility, owned by ENEA and located at the SIET [92] laboratories in Piacenza (Italy), was designed and built within the SIRIO project [93] to test a passive DHR for innovative nuclear reactors. SIRIO was intended to reproduce 1:1 in height the ALFRED DHR [94] [95], but it was then refurbished within the PIACE project and used to simulate DHRs also for other nuclear technologies. Such innovative system aims at providing a safe long-term cooling of the reactor coolant system with no need of external action or energy supply, being capable to passively control the heat removed by the ultimate heat sink through Non-Condensable Gas (NCG). This concept is of particular interest for LFRs, since the primary system must be properly cooled, while preventing the early freezing of lead to maintain the coolability and the integrity of the reactor. This concept can also be extended to other nuclear technologies, e.g. water-cooled reactor, since the passive control of the heat transfer capability can smooth thermal stresses on the materials, fluid internal thermal gradients and the depressurization rate.

The rationale behind this concept is based on the progressive injection of NCG in the Isolation Condenser (IC) tubes as the decay power reduces in time. Such injection reduces the condensation rate in the tubes, thus maintaining a relatively high temperature at the IC outlet, preventing the early freezing of the lead due to the cold water ingress in the SG. The control is based on the equilibrium of the total pressure between the NGT and the IC. When the decay power is high, the NCG are "pushed" into the NGT by the high pressure of the steam inside the loop. As the decay heat reduces, the unbalance between the power input and output reduces the steam pressure and temperature. The steam pressure reduction allows the NCG stored in the tank to enter the IC collector from the bottom, increasing their partial pressure in the tubes and degrading the condensation heat transfer. Consequently, the removed power reduces maintaining an equilibrium with the core power, while the secondary loop pressure, and temperature as well, remains almost constant and at high values because of the increase of the partial pressure of the NCG.

The design of SIRIO follows the "power to volume" scaling approach, which consists of maintaining constant the ratio between thermal powers and volume, i.e., power densities. The operational pressure, the height of the components and their relative elevations are kept constant as well since they are related to the natural circulation driving force. The scaling factor was obtained by the volumes' ratio of the Non-condensable Gas Tank (NGT) foreseen for ALFRED and the one already available at SIET, that was originally used as the Emergency Boration Tank (EBT) in the SPES-3 experimental facility [96]. The scaling factor results in:

$$SF = \frac{ALFRED\ NGT}{SIET\ EBT} = \frac{6\ m^3}{0.127\ m^3} \approx 47 \tag{12}$$

Even though the scaling was performed from the ALFRED design developed in the LEADER project [22] [23], and the most updated configuration [25] has been subject to modifications, the scaling is still representative of ALFRED. Table 1 contains the main features of the ALFRED design in the LEADER project, the design for the ALFRED Stage 2, and SIRIO facility.

The sizing of the main components was carried out by scaling the geometry of one ALFRED SG according to the scaling factor of Eq. (12). The number of tubes of the SIRIO SG can be easily evaluated from:

$$N_{tubes\ SG,SIRIO} = \frac{N_{tubes\ SG,ALFRED}}{SF} = \frac{510}{47} = 10.85 \approx 11 \tag{13}$$

where the ratio has been approximated to 11 since it is the closest integer number. To calculate the power of the SIRIO SG, it is necessary to first evaluate the specific power of the tubes. Moreover, since SIRIO is intended to be representative of the ALFRED SG in DHR mode, only the 7% of the scaled power of a ALFRED SG' tube is provided to the SIRIO's one:

$$P_{tube\,SG,SIRIO} = \frac{P_{SIRIO}}{N_{tubes\,SG,SIRIO}} = \frac{P_{ALFRED}}{N_{SGs} \cdot N_{tubes\,SG}} \cdot 7\% = \frac{300\,MW}{8 \cdot 510} \cdot 7\% \approx 5.15\,\frac{kW}{tube} \tag{14}$$

Therefore, the total power provided by the SIRIO SG is:

$$P_{SIRIO} = P_{tube\,SG,SIRIO} \cdot N_{tubes\,SG,SIRIO} = 5.15\,\frac{kW}{tube} \cdot 11 \approx 55\,kW \tag{15}$$

The choice of removing a tube from the four composing the bayonet design to simplify manufacturing and reduce costs in SIRIO was also adopted for the revised design of ALFRED. Therefore, an initial distortion became a more representative feature compared to the LEADER design. Even though the LEADER configuration envisaged 8 SGs, each one composed of 510 tubes [97], while the revised one foresees 3 SG with 880 tubes each, SIRIO SG is still representative of the ALFRED design because the specific power removed per tube remained almost the same (75.5 vs 75.8 kW/tube in full power operation). The tube length (6 m) remained the same in both the configurations.

The sizing of the IC starts with the consideration that the ALFRED IC is sized to remove 1% of the core power. Therefore, following the same approach of Eq. (13) would lead to less than one tube, as shown in Eq. (16):

$$N_{tubes\,IC,SIRIO} = \frac{N_{tubes\,IC,ALFRED}}{SF} = \frac{16}{47} = 0.34 \tag{16}$$

Therefore, it has been decided to realize a single tube shorter than the full-scale one. Since the ALFRED IC tube is 2 m long, the SIRIO IC tube should be:

$$L^*_{tube\,IC,SIRIO} = L_{tube\,IC,ALFRED} \cdot N_{tubes\,IC,SIRIO} = 2\,m \cdot 0.34 = 0.68\,m \tag{17}$$

However, it should also be considered that the ALFRED IC features both the inlet and outlet collectors immersed in the pool. The collectors, which are two spheres with an internal diameter of 0.44 m (as reported in Table 1), have an internal heat transfer area of 0.608 m^2 each. Given that the tubes have an inner diameter of 29.46 mm, the equivalent length of the collectors can be calculated as:

$$L_{eq,IC\,coll} = \frac{2 \cdot S_{IC\,coll,ALFRED}}{\pi \cdot ID_{tube}} = \frac{2 \cdot 0.608\,m^2}{\pi \cdot 0.02946\,m} = 13.14\,m \tag{18}$$

Dividing the result of Eq. (18) by the scaling factor yields an additional length of 0.28 m for the SIRIO IC tube calculated in Eq. (17). The final sizing of the SIRIO IC consists of a single tube with an immersed length in the pool of:

$$L_{tube\,IC,SIRIO} = L^*_{tube\,IC,SIRIO} + \frac{L_{eq,IC\,coll}}{SF} = 0.68\,m + 0.28\,m = 0.96\,m \tag{19}$$

Deformations caused by the scaling procedure on the main operational parameters are reported in Table 2, focusing on key factors such as thermal flux and power density. Due to practical constraints (e.g., use of commercial piping), some components do not perfectly adhere to the ideal theoretical scaling [98]. The discrepancy (Δ) between the theoretical and adopted scaling has been calculated as follows:

$$\Delta = \frac{X_{theoretical} - X_{SIRIO}}{X_{theoretical}} \tag{20}$$

where X represents a generic quantity that has been scaled. The distortion resulted in about -1.0% for thermal flux and decay power. Additionally, volume deformations were observed, including 13.0% for water volume, -1.8% for gas volume, and 1.63% for total volume (water + gas).

These discrepancies result in a deformation of about 11.5% for power density (based on total stored water volume). When comparing SIRIO with ALFRED in the LEADER configuration, deformations of -2.86% for thermal flux and -12.4% for power density are observed. Similarly, comparing SIRIO with ALFRED Stage 2 yields a -5.7% deformation for thermal flux and 13.1% for power density. Despite these deviations, SIRIO can be considered representative of both configurations, as the distortions are of the same order of magnitude. These deformations are acceptable as long as the expected physical phenomena are preserved.

Figure 16 shows the conceptual scheme of the SIRIO facility, and an overview of the facility is provided in Figure 17. It is mainly composed of:

- A SG with 11 bayonet tubes (BTs). The drawings of the BTs are shown in Figure 18 and 19, while pictures of the component are reported in Figure 20 and 21. Each BT is inserted into a pipe, and the resulting gap is filled with molten salt which allows the natural circulation of the salt inside the gap itself. In this way, the power coming from heating cables installed on the external surface can be distributed to the tube that faces the steam-water on the secondary side, avoiding the burnout of the heaters due to the non-constant level of the two-phase mixture. Ref. [88] contains a CFD analysis of the molten salt gap, proving its capability to enable the simulation of the ALFRED SG temperature profile on the secondary side. The innermost tube is 3 m long instead of the 6 m of the bayonet, and the annular region between the first and the second tubes is filled with static water, which acts as an insulator between the riser and the downcomer of the BT.
- An IC composed of a single tube immersed in a water pool at atmospheric pressure. Pictures are shown in Figure 22 and 23 and the drawing is reported in Figure 24.
- A bypass Heat eXchanger (HX), composed of two parallel tubes immersed in a water pool at atmospheric pressure. It is used to remove the nominal power to achieve a steady state. Its 3D drawing is reported in Figure 25 together with the IC.
- A NGT, where NCG is stored when the SG works in normal operation. It is connected to the IC outlet by means of the gas line. The NCG used in the experimental tests is air.

It is important to note that the system is not equipped with a pump, meaning that it can work only in natural circulation. It is specified also that only one heat sink at a time can work. In the "steady state" phase, water circulates in the "bypass loop", composed of the SG and the HX which are connected by the riser and the downcomer highlighted in green in Figure 16. When the "transient mode" (or "DHR mode") is triggered, the HX is isolated and the water circulates in the loop composed of the SG, the riser (in common with the bypass loop), the IC, and the downcomer highlighted in red in Figure 16 containing a orifice at the bottom. The NGT is also involved during the transient mode since it is connected to the bottom of the IC.

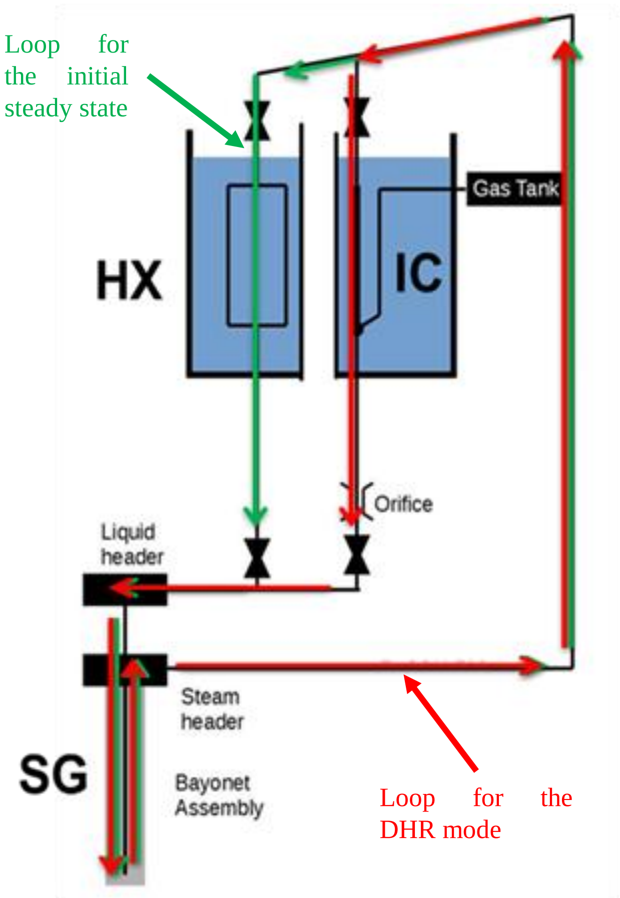

Figure 16 – SIRIO conceptual scheme

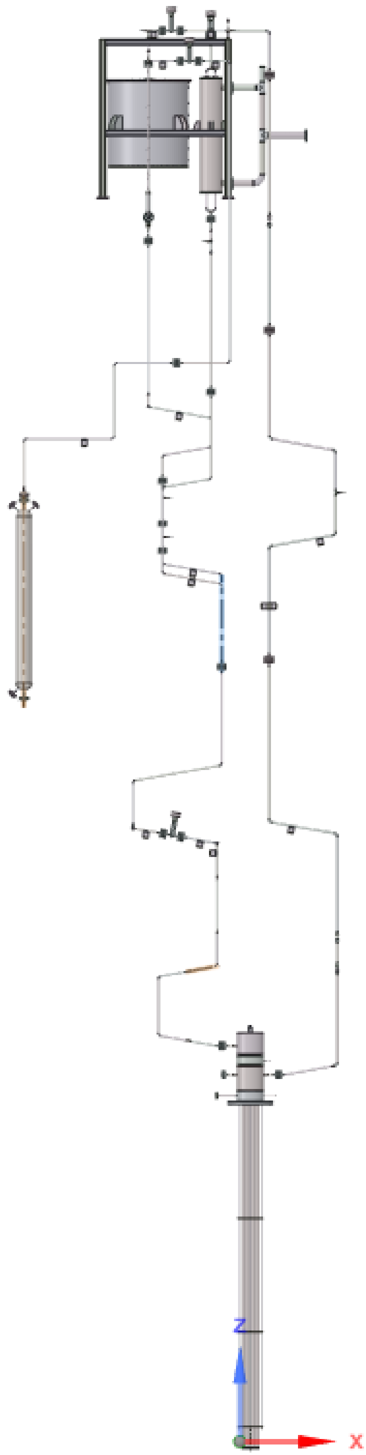

Figure 17 – Overview of the SIRIO facility

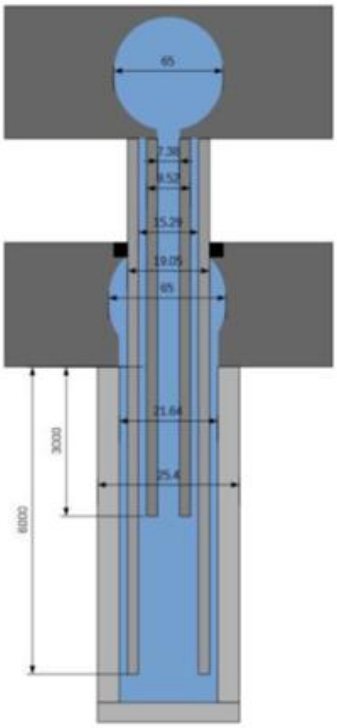

Figure 18 – Schematic of the SIRIO SG bayonet tube geometry

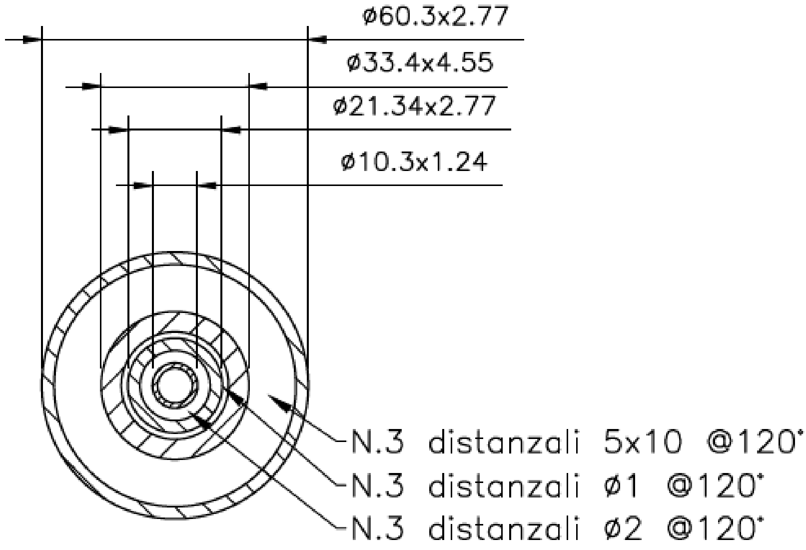

Figure 19 – Cross section view of the SIRIO SG tubes

Figure 20 – Picture of the SIRIO SG bayonet tubes

Figure 21 – Picture of the SIRIO SG head

Figure 22 – Picture of the SIRIO IC

Figure 23 – Detail of the thermocouples inside the SIRIO IC pool

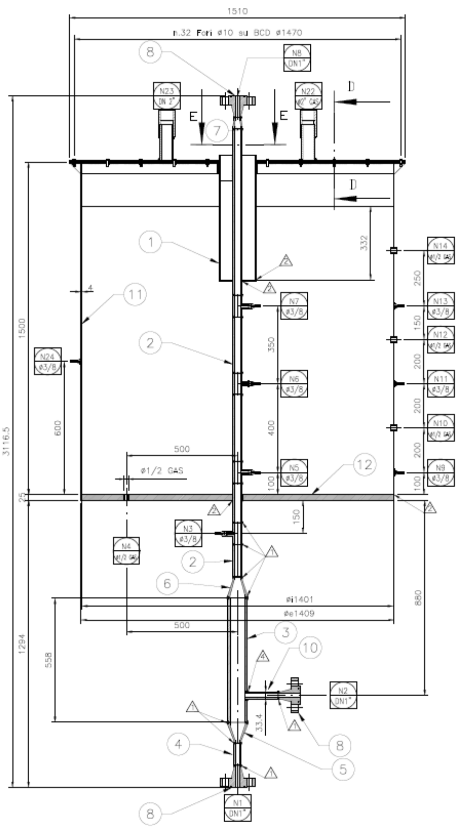

Figure 24 – Drawing of the SIRIO IC

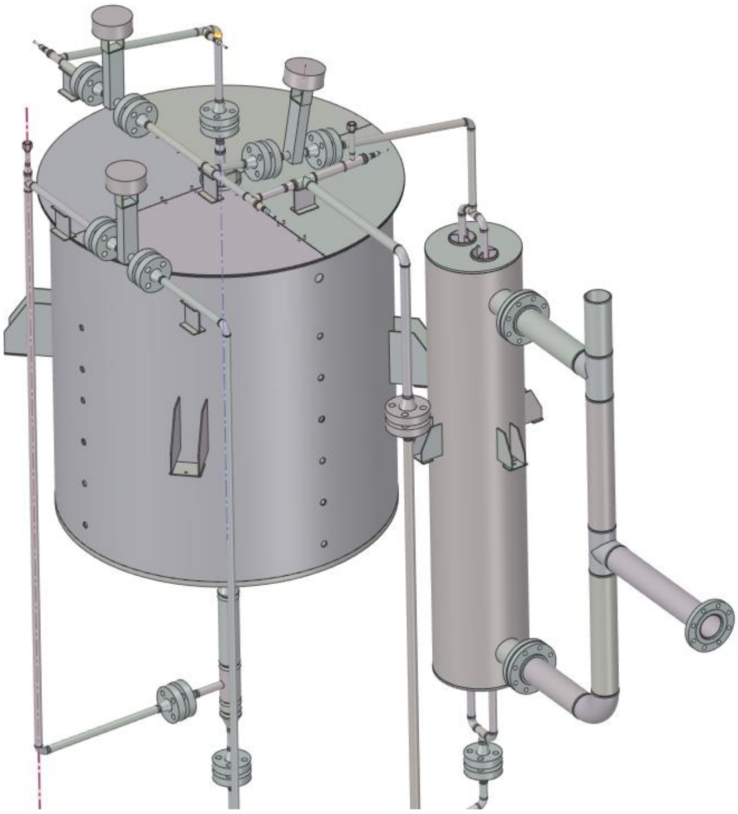

Figure 25 – 3D drawing of the SIRIO IC and HX

Table 1 – Comparison of the main features of ALFRED (LEADER), ALFRED (Stage 2) and SIRIO

Parameter	**ALFRED (LEADER)**	**ALFRED (Stage 2)**	**SIRIO**
Total Power	300 MW	200 MW	55 kW
Number of Steam Generators	8	3	1
Number of tubes (x1 SG)	510	880	11
SG tube type	double wall bayonet	single wall bayonet	single wall bayonet
Number of coaxial tubes	4	3	3
Tube length [m]	6	6	6
SG Heat source	Nuclear	Nuclear	Electrical
IC tubes	16 x 2 m	16 x 2 m	1 x 0.68 m
IC collectors' inner diameter [m]	0.44	N/A	-

Table 2 – Deformation of SIRIO with respect to the theoretical scaling and variation to ALFRED

Parameter	**Unit**	**Deformation Scaled Facility – SIRIO**	**Variation to ALFRED (LEADER)**	**Variation to ALFRED (Stage 2)**
Decay Power	kW	-1%	--	--
Power/tube	kW	-1%	-2.9%	-5.7%
Thermal flux	kW/m^2	-1%	-2.9%	-5.7%
Water volume	L	13.0%	--	--
Gas volume	L	-1.8%	--	--
Total volume	L	1.6%	--	--
Power density	kW/L_{water}	11.5%	-12.4%	13.1%

3.1.2 Experiment description

The SIRIO facility can operate in two different phases: the "steady state" and "transient" modes. The steady state is achieved by adjusting the water level in the HX pool until the power balance is achieved. Therefore, during the steady state, water circulates inside the SG where it is heated, then it flows in the riser and goes to the HX where it is cooled, and eventually it enters back the SG. In this phase, the valves upstream and downstream of the IC are closed and the ones of the HX are open. During the steady state phase, the IC is full of NCG at 110 bar, as outlined in Table 3.

Once the initial conditions are achieved, the "transient" mode is triggered. The Start of Transient (SoT) consists in the closure of the bypass HX valves. In this way, the system no longer has a heat sink, causing a pressure increase in the system. When the set point of 190 bar is reached, the IC inlet valve opens, allowing the steam to flow towards the IC, where it condenses. In the very first seconds, the steam flow at the IC outlet is subdivided into two main streams: one goes to the NGT, pushing the NCG inside the tank, while the other condensed stream is collected above the valve downstream of the IC. To allow the formation of a water column above the orifice to enhance natural circulation, a 60 seconds delay is set for the opening of the valve downstream of the IC. At this moment, the facility operates in "transient" mode, where the heat source is still represented by the SG, while the heat sink has switched to the IC. They are connected by the riser (the same piping as the initial steady state), and the downcomer containing the orifice. The loops involved in the two operational phases are qualitatively represented in the synoptic in Figure 26 and 27.

In the first 2000 s of transient operation, the SG continues to provide the full power of 55 kW. This delay represents the thermal inertia of the full-scale primary system, since it is not physically simulated in the facility. After 2000 s, a decay heat curve is imposed by the power control system (see Figure 28), simulating the decay curve foreseen for ALFRED, with an increase of 5 kW to compensate for part of the facility's heat losses.

Table 3 summarizes the BCs for the experiment. Water is pressurized at 180 bar during the steady state, as the ALFRED secondary system. The total amount of water used in the experiment is about 75 kg, which, at the end of the experiment, is distributed among:

- the bypass HX region, which is between the HX isolation valves.
- the IC loop, which is involved during the transient.
- the NGT, where a certain amount of water enters in the first part of the transient because of the initial pressure difference between the water and the gas regions.

The orifice diameter is set to 5 mm, but an experimental sensitivity analysis is envisaged in future experimental campaigns to assess its impact on natural circulation during the transient.

Table 3 – SIRIO experimental boundary conditions

Parameter	**Unit**	**Value**
Water inventory	kg	75
Water pressure	bar	180
Gas pressure	bar	110
Thermal power supplied during the steady state	kW	55
Valve PV-613 set point	bar	190
Valve PV-615 delay	s	60
Orifice diameter	mm	5

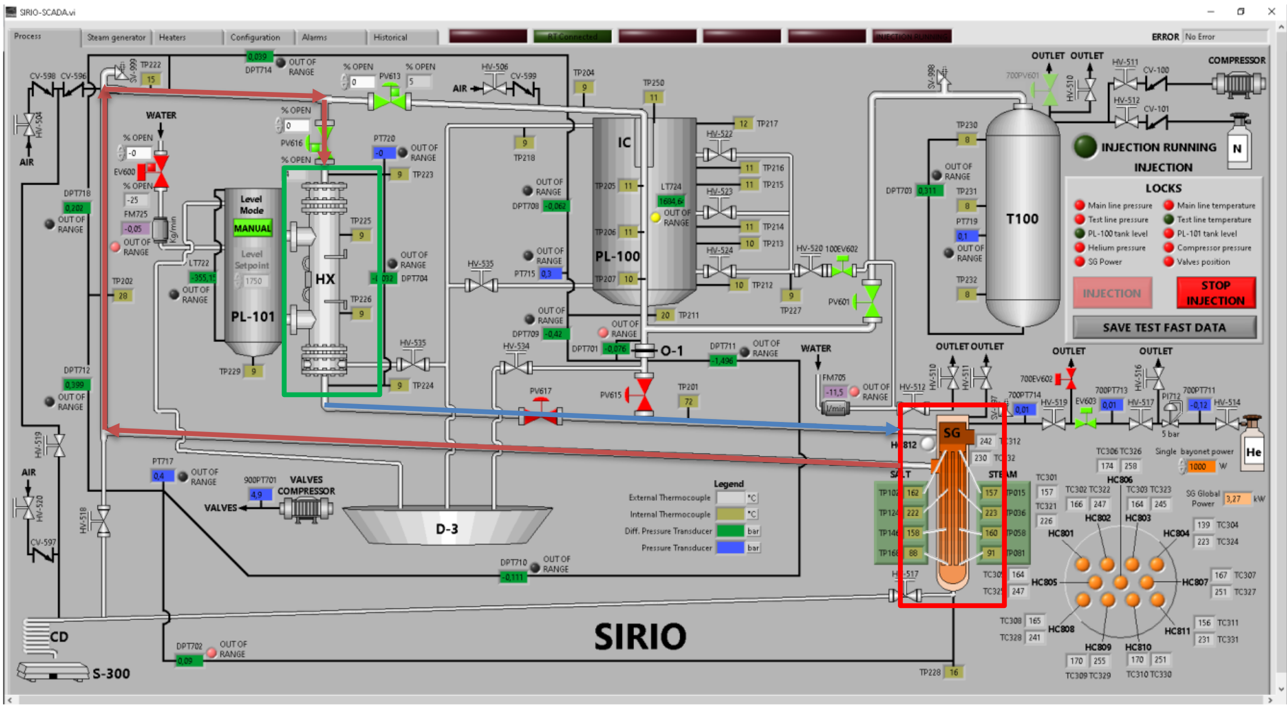

Figure 26 – SIRIO synoptic: steady state operation

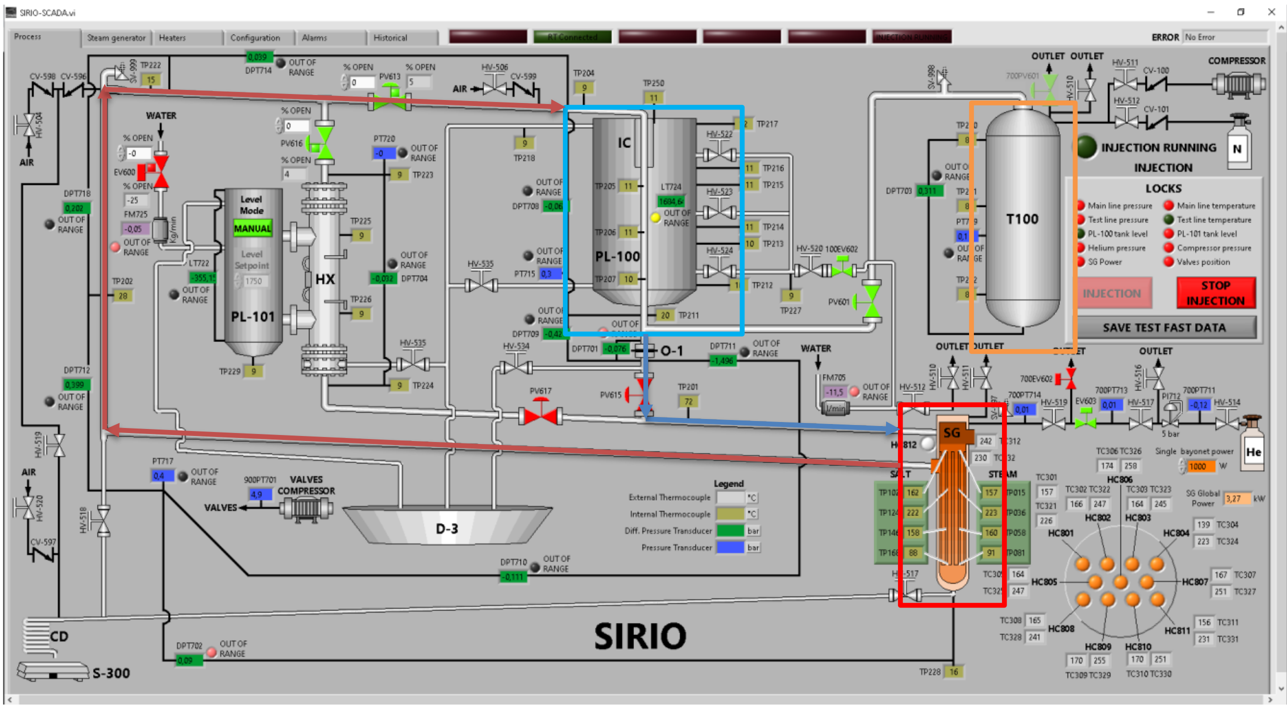

Figure 27 – SIRIO synoptic: transient operation

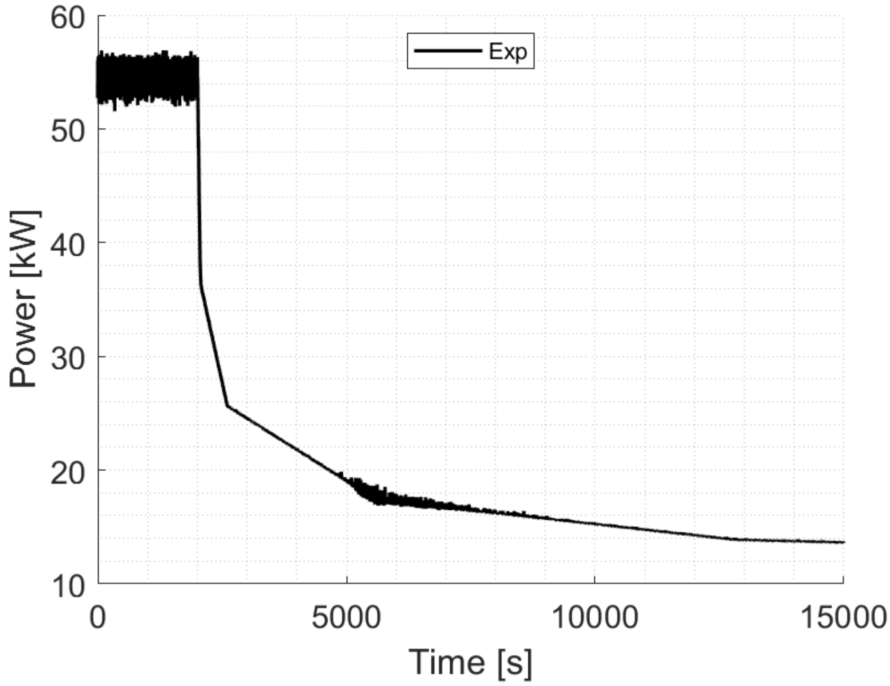

Figure 28 – Power provided to the SG during the transient (decay curve)

3.1.3 Numerical models

The numerical model of the SIRIO facility has been realized using the RELAP5/Mod3.3 code. The model includes PIPE, SINGLE JUNCTION, and VALVE components for fluid regions, and HEAT STRUCTURES (HS) to simulate solid components. Non-active regions, i.e., where significant heat transfer and strong temperature gradients are not expected, have an average mesh size of ~20 cm, while active regions such as the bypass HX, the IC, and the SG are discretized with fluid volumes of ~10 cm.

Contrary to the models presented in Sect. 3.2.3 and 3.3.3, the so called "sliced modelling approach" [132] has not been used. It consists in discretizing fluid elements at equivalent absolute heights with the same axial length to better simulate the natural circulation conditions. However, the geometrical asymmetries of the facility would have made the application of this method more complicated than in the NACIE-UP and TALL-3D cases. Nevertheless, the relatively small hydraulic cells adopted for the discretization of the facility make the misalignment of the centers of the cells located at the same absolute height negligible compared to the overall height of the facility, thus avoiding significant distortions in simulating the natural circulation.

Since molten salts are not implemented in RELAP5, a HS with the thermal properties of Dynalene MS-2 [99] (thermal conductivity and volumetric heat capacity) simulates the molten salt gap. Heat is provided by a HS with internal power generation, simulating the heating cables. Piping insulation is provided by a 5 cm rockwool layer modelled as a HS. Heat transfer to the environment is modelled assuming a room temperature of 15°C and a convective Heat Transfer Coefficient (HTC) of 8 W/m² °C. The nodalization is shown in Figure 29.

The calibration of the orifice pressure drop has been carried out thanks to a preliminary characterization during the commissioning phase with liquid water at ambient pressure and temperature. From the pressure drop measurement, the mass flow rate during the experiment can be estimated using the correlation in Figure 30. Absolute pressure and temperature measurements allow to evaluate properties such as density and viscosity. To evaluate the orifice pressure loss coefficient, only the friction pressure drop has been considered, and the gravitational contribution has been removed according to the following relation:

$$K = \frac{2 \cdot (\Delta p_{measured} \cdot 10^5 + \rho \cdot g \cdot H) \cdot \rho}{G^2} \tag{21}$$

where:

- $\Delta p_{measured}$ is the pressure drop measured by the differential pressure transducer in bar.
- ρ is the density calculated at the local temperature and pressure.
- H is the distance between the pressure taps upstream and downstream of the orifice.
- G is the mass flux, i.e., the ratio between the mass flow rate and the flow area.

The K coefficients evaluated during the transient through Eq. (21) have been associated with the related Reynolds number upstream of the orifice, which is calculated once the mass flow rate and viscosity are known. From the experimental points shown in Figure 31, the following Reynolds-dependent pressure loss coefficient has been calculated and implemented into the junction representing the orifice:

$$K_{RELAP5} = 462 + 1.011 \cdot 10^9 \cdot Re^{-1.424} \tag{22}$$

Even though the model is geometrically representative of SIRIO, there are some known limitations of the code, and their assessment was among the objectives of the PIACE project. A phenomenon of concern is heat transfer through the closed cavity between the annular riser and the downcomer of the SG BTs. Even though it is relevant for the regenerative heat transfer within the SG, it could not be addressed because of the lack of instrumentation inside the downcomer of the BTs. For the current analysis, it has been decided to model this region as a regular fluid region with a closed end.

Another limitation of the code is the simulation of mass and energy transport inside the pools. Phenomena such as thermal stratification and natural convection cannot be properly modelled by means of 1D components. Such a limitation has been addressed only from a nodalization point of view, since it has been noted that the discretization of the IC pool with two parallel pipes – representing two concentric regions of the pool – connected with cross junctions led to a better simulation of stratification and pool mixing. This was an outcome of the post-test activity, since temperature measurements inside the pool allowed the comparison with the RELAP5 results.

Concerning the heat transfer mechanism from the IC tube to the pool, it is expected that pool boiling will occur since the fluid inside the tube is at high temperature (~330°C, corresponding to the saturation temperature at the system pressure). Since RELAP5 does not include a specific correlation for nucleate pool boiling, the Chen correlation [100] [101] [102] for two-phase flow boiling is generally used:

$$h_{tp} = S \cdot h_{nb} + F \cdot h_{sp,l} \tag{23}$$

where:

- h_{nb} is the nucleate boiling HTC evaluated through the Forster and Zuber correlation [103] for pool boiling:

$$h_{nb} = 0.00122 \left(\frac{k_l^{0.79} c_{p,l}^{0.45} \rho_l^{0.49}}{\sigma^{0.5} \mu_l^{0.29} h_{fg}^{0.24} \rho_g^{0.24}} \right) \Delta T_{sat}^{0.24} \Delta p_{sat}^{0.75} \tag{24}$$

- $h_{sp,l}$ is the single phase forced convection HTC evaluated through the Dittus-Boelter correlation [104]:

$$h_{sf,l} = 0.023 \cdot Re_l^{0.8} \cdot Pr_l^{0.4} \cdot \frac{k_l}{D_H} \tag{25}$$

- S is a suppression factor for the nucleate boiling.
- F is the two-phase correction (enhancing) factor for the single phase forced convection.

In the version of the code adopted in this work, the correlation selected for pool boiling is the Cooper correlation [105] (see Eq. (26)), which was implemented in the RELAP5/Mod3.3 source code by Sapienza University of Rome in 2020 [41] [106] and validated against experimental data from the PERSEO facility [107] [108], featuring an IC similar to the SIRIO's IC. The correlation is the following:

$$h = 55\left(p_r^{0.12-0.2\log_{10}\varepsilon}\right)(-\log_{10} p_r)^{-0.55} M^{-0.5} q"^{0.67} \tag{26}$$

where:

- h is the heat transfer coefficient.
- p_r is the reduced pressure, i.e., ratio of the actual pressure to the critical pressure.
- ε is the roughness in μm.
- M is the molecular weight of the fluid.
- $q"$ is the heat flux.

Concerning the heat transfer mechanism inside the tube, condensation with and without the presence of NGC occurs during the experiment. RELAP5 deals with only film-wise condensation, while drop-wise condensation is not considered since water is able to wet the wall. In the original version of RELAP5/Mod3.3, the Nusselt theory [109] is adopted for laminar film condensation, and the Shah correlation [110] is used for turbulent regime. RELAP5 then calculates the condensation HTC as the maximum of the two. The Nusselt theory assumes that heat transfer is due to conduction across the liquid film. In vertical geometry, the local film thickness is evaluated as follows:

$$\delta_z = 0.9086\left(\frac{\mu_l^2 Re_l'}{g\rho_l(\rho_l - \rho_g)}\right)^{\frac{1}{3}} \tag{27}$$

where Re_l' is the condensate Reynolds number per unit width of the surface. In RELAP5, the approximation $\rho_l \gg \rho_g$ is adopted, so that the local HTC is evaluated as:

$$h_{Nu} = \frac{k_l}{\delta_z} = k_l\left(\frac{\nu_l^2}{g}\right)^{-\frac{1}{3}} 1.1\,(Re_l')^{-\frac{1}{3}} \tag{28}$$

where ν_l is the liquid kinematic viscosity, i.e., the ratio between dynamic viscosity and density. For the turbulent condensation regime, the Shah correlation is adopted, which is based on a "liquid only" approach, meaning that the entire mixture is assumed to be liquid, to which the non-dimensional numbers are referred to, and then corrections considering the steam quality are applied. The correlation is the following:

$$h_{Shah,1979} = h_{sf,l}(1-x)^{0.8}\left(1 + \frac{3.8}{Z^{0.95}}\right) \tag{29}$$

where $h_{sf,l}$ is the single-phase HTC evaluated as in Eq. (25), x is the flow quality, and Z is the Shah correlating parameter defined as:

$$Z = \left(\frac{1}{x} - 1\right)^{0.8} p_r^{0.4} \tag{30}$$

Sapienza implemented in the RELAP5/Mod3.3 source code the latest upgraded version of the Shah correlation [111] [112] [113], which extended the applicability of its correlation to a wider range of flow rates (in particular low flow rates) and reduced pressures. Shah attributed the discrepancies at high reduced pressures to the viscosity ratio of the phases and the reduced pressure itself:

$$h_{Shah,2009} = h_{Shah,1979} \left(\frac{\mu_l}{14\,\mu_g} \right)^{(0.0058+0.557 p_r)} \tag{31}$$

An alternative model, proposed by Vierow and Schrock [114], is available in the code. It consists of applying an enhancing factor to the Nusselt equation to consider the effect of the shear of the gas phase on the liquid film, and a suppression factor to account for the non-condensable effect.

In the previous work conducted by Sapienza, another correlation was implemented to consider the laminar-wavy film condensation. In fact, when dealing with film condensation, two regimes can be distinguished: the “gravity-controlled” and the “shear-controlled” regimes. In the gravity-controlled condensation, it is assumed that the gas phase is almost stagnant, and momentum exchange between the two phases is negligible. Within this regime, the liquid film can be:

- laminar. This regime is described by the Nusselt theory, which assumes that heat is transferred only by conduction across the liquid film. The correlation is reported in Eq. (28).
- laminar-wavy, where heat transfer is enhanced by the waviness of the film as the film Reynolds number becomes greater than a transition value (generally around 30). Sapienza added the Kutateladze correlation [115] to the set of equations available in RELAP5:

$$h_{Kut} = k_l \left(\frac{\nu_l^2}{g} \right)^{-\frac{1}{3}} 0.756\,(Re_l')^{-0.22} \tag{32}$$

- turbulent, and it is composed of a laminar sublayer and a turbulent region. Transition to turbulent film in general occurs at film Reynolds number of ~1800. It is worth noting that the film can be turbulent even if the gas phase is almost static. Heat transfer is dominated by convective mechanism, and it can be described by Blangetti and Schlunder [116], who based the analysis on their turbulence model, which predicts an increasing HTC as the film Reynolds number increases:

$$h_{Bla} = k_l \left(\frac{\nu_l^2}{g} \right)^{-\frac{1}{3}} 0.00402\,(Re_l')^{0.4} Pr_l^{0.65} \tag{33}$$

  Or in alternative, also the Labuntsov correlation [117] is available in the literature:

$$h_{Lab} = k_l \left(\frac{\nu_l^2}{g} \right)^{-\frac{1}{3}} 0.023\,(Re_l')^{0.25} Pr_l^{0.5} \tag{34}$$

  Since turbulent film condensation is not addressed in the RELAP5 code (as highlighted also in previous works by Papini and Cammi [118] and Bersano et al. [119]), the above correlations were implemented during this work.

In the shear-controlled regime, instead, the gas velocity is much higher than the liquid, thus turbulence can be induced by the vapor shear effect on the condensate layer, and eventually some droplets can be entrained in the main gas central core (assuming an annular flow regime) reducing the film thickness and thus enhancing the heat transfer to the wall. In these cases, turbulence can be induced even at lower film Reynolds number compared to a “gravity-controlled” case. It must be noted that in “shear-controlled” condensation, tube orientation is unimportant, and Shah correlation can be used to evaluate the HTC. Schematic of film condensation is shown in Figure 32, which is taken from the Chen work [120], who developed a general film condensation correlation by combining Eq. (32) and (33) for the gravity-controlled regime (neglecting the laminar regime), and the Soliman correlation [121] for the shear-controlled regime, instead of the Shah correlation used in RELAP5. The trend of the nondimensional condensation HTC on a vertical plate is represented in Figure 33 (from Ref. [122]). A decreasing trend is shown up to condensate Reynolds number of ~1800, since the main heat transfer mechanism is conduction across the liquid film, therefore its thermal resistance increases as the film thickens. Then, convection plays an important role, contributing to increase the HTC as the film Reynolds number increases.

When non-condensable gases are present, they tend to migrate from the bulk to the gas-liquid interface, where they accumulate since they do not condense. In this way, they form a "barrier" for the migration and condensation of the steam at the interface. RELAP5 addresses this calculation with the Colburn and Hougen [123] diffusion method, which is based on a thermal balance to evaluate the interface steam partial pressure (and temperature). One of the assumptions is that the mass transfer coefficient can be obtained by applying the Heat and Mass Transfer Analogy (HMTA). The balance equation equals the heat transferred by condensing vapor to the interface (latent heat) and the heat transferred through the condensate film. The latent heat is evaluated as:

$$q"_v = m"_v \cdot h_{fg} = h_m h_{fgb} \rho_{vb} \ln\left(\frac{1-\frac{p_{vi}}{p}}{1-\frac{p_{vb}}{p}}\right) \tag{35}$$

where:

- h_m is the mass transfer coefficient. It is obtained from the HMTA by applying correlations for the turbulent, laminar and natural convection HTC in terms of mass transfer, i.e., substituting the Nusselt number with the Sherwood number, and the Prandtl number with the Schmidt number.
- ρ_{vb} is the saturation vapor density at its partial pressure in the bulk (p_{vb}).
- p_{vi} is the steam partial pressure at the interface.
- p is the total pressure.
- h_{fgb} is the latent heat of vaporization evaluated at p_{vb}. It must be noted that, since condensation occurs at the gas-liquid interface, the latent heat of vaporization should be evaluated at p_{vi}. This is part of the modifications implemented in the source code within this work. Therefore, in the final equation, h_{fgb} is substituted by h_{fgi}.

The heat transferred through the film to the wall is calculated as:

$$q"_l = h_c(T_{vi} - T_w) \tag{36}$$

where:

- T_{vi} is the saturation temperature at the interface steam partial pressure.
- T_w is the wall temperature.
- h_c is the condensation HTC evaluated with the correlations previously described.

From the balance equation, p_{vi} can be calculated iteratively, and the corresponding T_{vi} as well:

$$q"_l = q"_v \rightarrow h_m h_{fgb} \rho_{vb} \ln\left(\frac{1-\frac{p_{vi}}{p}}{1-\frac{p_{vb}}{p}}\right) = h_c(T_{vi} - T_w) \tag{37}$$

The modifications to the source code proposed in this work concerning the NCG effect during condensation consist in replacing h_{fgb} with h_{fgi}, and also considering the sensible heat transfer through the diffusion layer in Eq. (37). In this way, it becomes:

$$q"_l = q"_v + q"_s \rightarrow h_c(T_{vi} - T_w) = h_m h_{fgi} \rho_{vb} \ln\left(\frac{1 - \frac{p_{vi}}{p}}{1 - \frac{p_{vb}}{p}}\right) + h_s(T_{vb} - T_{vi}) \quad (38)$$

where:

- h_s is the convection HTC calculated for the gas phase.
- T_{vb} is the saturation temperature evaluated at p_{vb}.

The schematic of the film condensation in the presence of NCG, along with the terms of the balance equation (38), is shown in Figure 34.

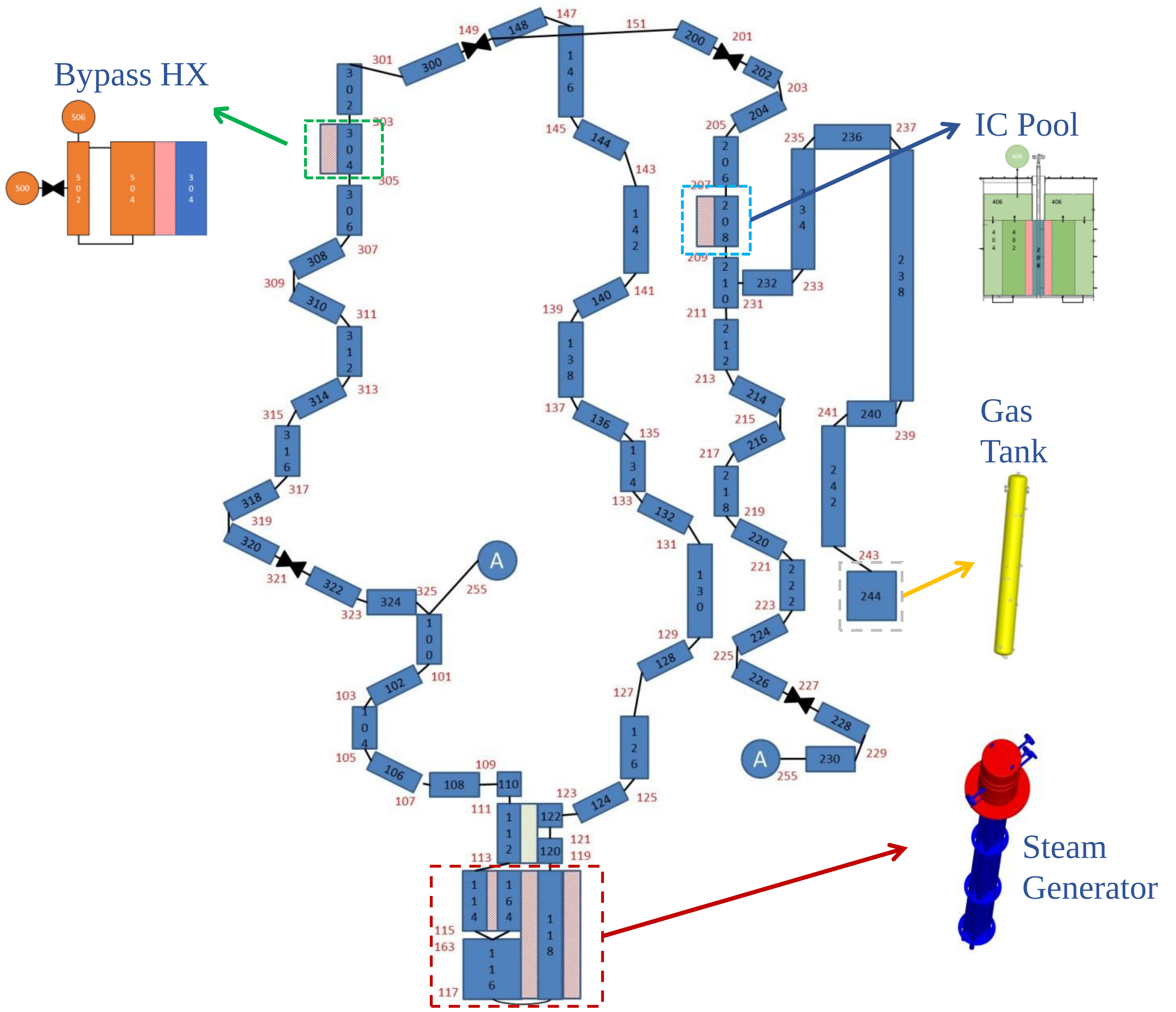

Figure 29 – RELAP5 nodalization of SIRIO facility

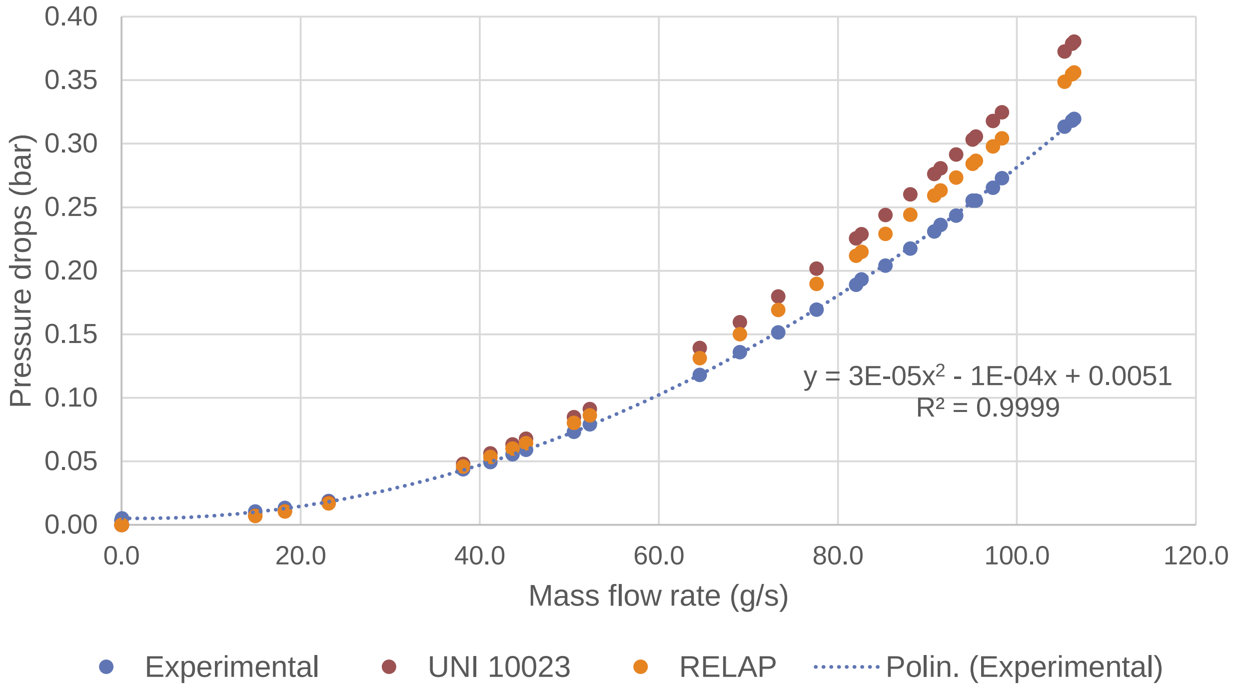

Figure 30 – Characterization of the orifice

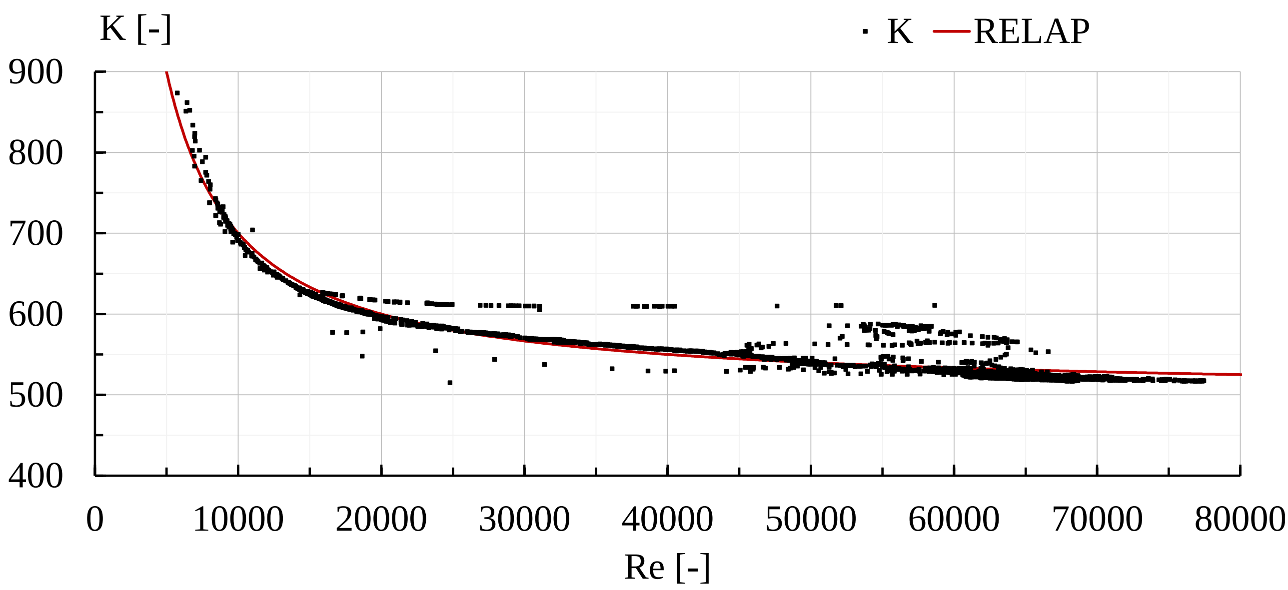

Figure 31 – Calibration of the orifice pressure loss coefficient

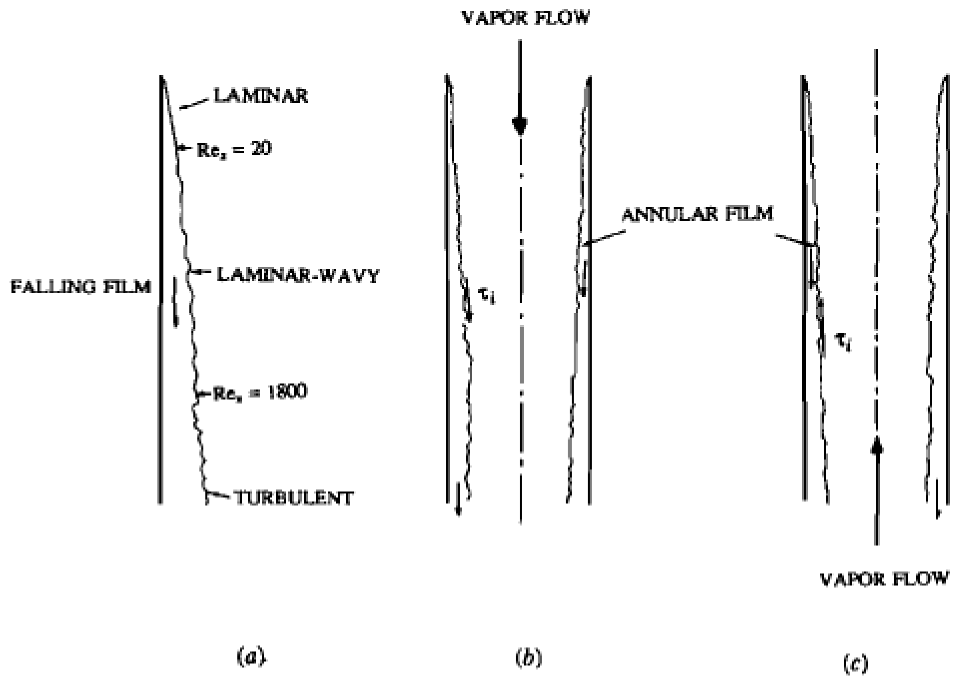

Figure 32 – Schematic of film condensation onto a plate (a), cocurrent (b) and countercurrent (c) annular film condensation inside a vertical tube [120]

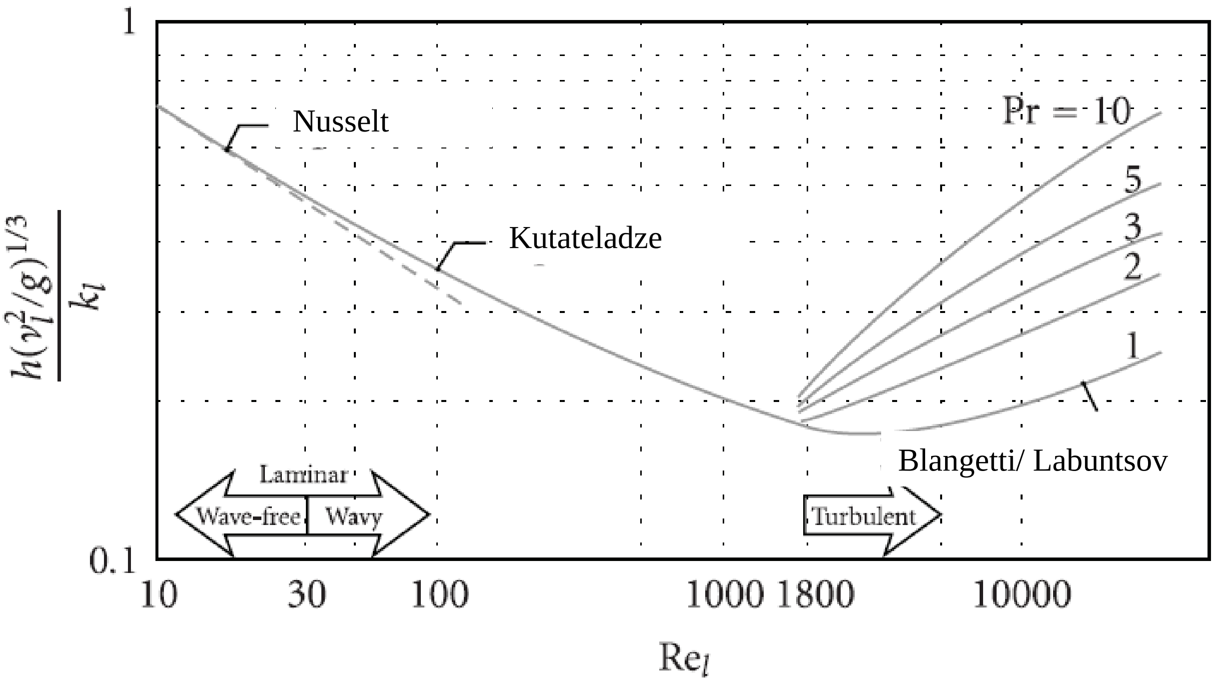

Figure 33 – Nondimensional heat transfer coefficient vs condensate Reynolds number on a vertical plate [122]

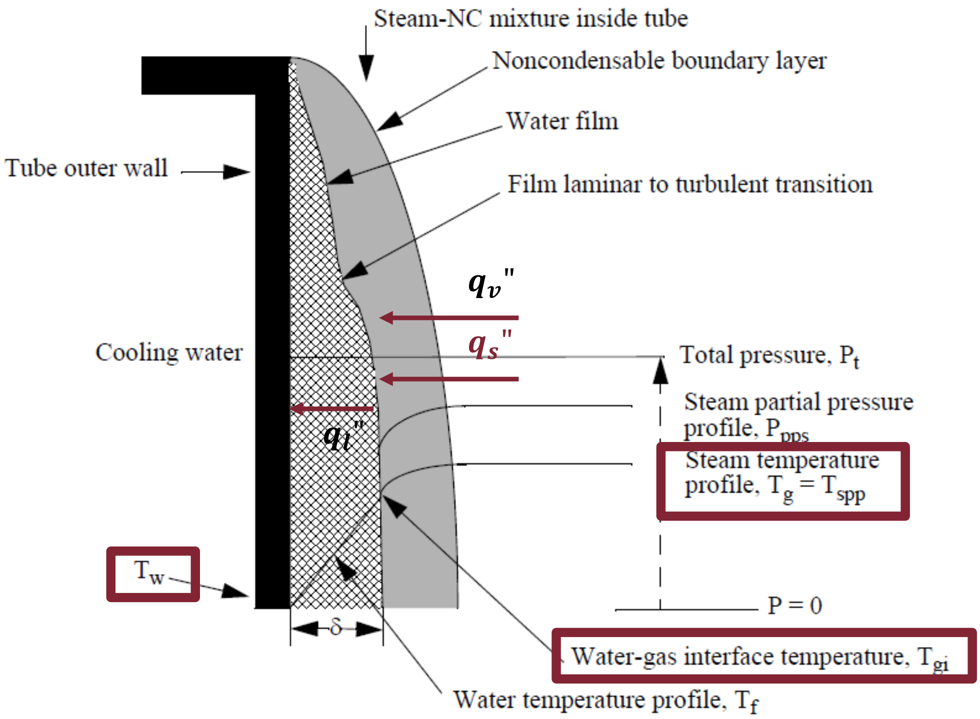

Figure 34 – Schematic of film condensation in presence of non-condensable gas with the terms involved in the balance equation highlighted

3.1.4 Simulation results

A numerical steady state has been achieved through a 15000 s "null transient" calculation. The initial conditions have been set to match the experimental water inventory in the primary loop (about 75 kg), as reported in Table 3. The level in the bypass HX pool has been adjusted by a control system to remove the net power provided to the fluid, i.e., the input SG power (55 kW) minus the contribution of the circuit heat losses. Table 4 shows that the RELAP5 calculation generally underestimates the thermal field inside the primary loop of about 5°C. It is worth noting that during the steady state, the bypass loop was full of liquid water due to a filling ratio higher than required. In fact, all temperatures in the loop are lower than the saturation temperature at 180 bar, i.e. about 355°C. The water flow rate inside the loop is estimated at 171 g/s but no comparison with experimental data is possible due to the lack of a mass flow meter.

The transient starts with the closure of the HX inlet and outlet valves. Since the system has no more a heat sink, pressure starts to increase until the set point of 190 bar is reached (in 34 s), triggering the opening of the IC inlet valve which allows the expansion of the fluid in the IC branch, initially filled with NCG. Part of the steam – condensing in the IC –is collected at the bottom of the IC (upstream of the outlet valve), and part goes towards the NGT. The water collected in the NGT was measured experimentally at the end of the experiment and it resulted in 15 liters, as reported in Table 5. After a 60 seconds delay, also the valve downstream of the IC opens, starting the natural circulation inside the loop. Power is kept constant at 55 kW in the first 2000 s of "DHR mode" and then decreases, simulating a decay heat curve (see Figure 28).

As shown in Figure 35, pressure quickly drops to an intermediate value between 190 and 110 bar, and then slightly increases in the first 150 s because natural circulation has not yet established. Figure 36 reports the comparison between the experimental numerical pressure trends in the first 2000 s, i.e., the steady state in the "DHR mode", and it is shown the significant improvement due to the implementation of the turbulent film condensation (Blangetti and Labuntsov). The original RELAP5 version is labelled as "RELAP5 old", and in the following figures only the new version results are presented and label simply as "RELAP5". It is shown that the original RELAP5 predicts a pressure increase even though the power provided by the SG is constant and the experimental value achieved a quasi-steady state after 500 s, meaning that the heat exchange in the IC, i.e., condensation, is underestimated. With the new version of the code, the steady state is correctly achieved, even though with a small delay compared to the experiment.

The temperatures at the IC inlet and outlet (see Figure 37 and 38, respectively) are slightly overpredicted in the short term (the first 2000 s). The IC inlet temperature trend reflects those of the pressure since saturated steam enters the IC tube, while the temperature at the outlet is below the saturation temperature at the loop pressure because it is linked to the steam partial pressure at that location. The main discrepancies between the numerical and experimental results consist in a different initial transient in the first 500 s and bigger oscillations of the numerical curve. The average values of the two curves at the end of the 2000 s steady state differs of about 15°C.

Similar discussion can be done for the SG inlet and outlet temperatures: at the outlet, temperature is linked to the total pressure, while at the inlet, the temperature is a result of the heat exchange in the IC. In fact, the inlet temperature shown in Figure 39 achieves almost the same value of the IC outlet, even though the trend does not present oscillations. The outlet temperature (see Figure 40) agrees with the experimental value because of the good prediction of the total pressure. The initial disagreement of few degrees is due to the different initial conditions.

After 2000 s, as soon as power decreases, the system starts to depressurize from 140 to 130 bar between 2000 and 3600 s. In this time window, the experimental and numerical trends (see Figure 41) are in good agreement. At this moment, NCG further diffuses in the IC, degrading its performances and allowing the pressure to remain at a pseudo steady state value. In the RELAP5 calculation, the depressurization rate is slightly overpredicted since pressure reached an equilibrium value of about 115 bar.

As soon as NCG diffuses in the IC, they increase the pressure drop in the loop, and together with the reduction of the input power, causes a reduction of the mass flow rate which is reflected by the increase of the temperature drop across the IC. However, the presence of NCG is the IC is underestimated by the code since both the temperatures remain at higher values compared to the experimental ones. The reduction of the inlet temperature below the saturation value (see Figure 42) suggests that NCG have also reached that location, while in the simulation the temperature remains at the saturation point at the total pressure. At the outlet, strong oscillations occur, and the average temperature is below the simulation values (see Figure 43), meaning that the bottom of the tube is almost full of NCG.

As for the short term, the SG inlet temperature – linked to the IC outlet value – decreases much quickly in the experiment (see Figure 44), while at the outlet, a better agreement can be found since the temperature corresponds to the saturation (see Figure 45). Therefore, if the loop pressure is well calculated, also this value will agree with the experiment.

Concerning the pool temperatures, Figure 46 shows three thermocouples at different elevations in the pool. A 5°C difference in the initial value is due to the different initialization, but the increasing trend is in quite good agreement with the experiment. The major difference is that thermal stratification occurs in the experiment, while temperatures in the RELAP5 simulation have almost the same value. This error was expected since RELAP5/Mod3.3 is a one-dimensional code with known limitations in properly representing complex 3D flow paths and phenomena occurring in large fluid volumes, in particular if the nodalization is coarse. Conversely, a qualitative good agreement can be found in the long term trend of the pool temperatures (see Figure 47), where a certain stratification becomes visible also in the simulation, though less pronounced than in the experiment. The change in the rate of temperature increase in the simulation also matches the experimental trend.

Table 5 reports the distribution of the initial water inventory within the facility measured after the end of the test. It can be observed that the total inventory is respected since it was the initial water loaded in the loop. The water remained between the bypass HX inlet and outlet valves is about 5.5 kg, and the calculated value well agrees with the measured one since the volume and the temperature field are the same. The water extracted from the NGT is about 15 kg, 8 kg less than the simulation result. This is due to the migration towards the tank of part of the water throughout the transient, while in the experiment, only at the Beginning Of Transient (BOT) water goes in the NGT because of the initial pressure difference. The rest of the water remains in the loop, i.e., 44 vs 54 kg in the simulation and in the test, respectively. The lower water inventory remained in the loop after the switch to the DHR mode can partly explain the general overestimation of the temperature field in the loop.

These simulations, carried out within the PIACE project, provided a proof of the improvements of the RELAP5/Mod3.3 code in simulating condensation in presence of non-condensable gas at high pressure. As emerged from the comparison with experimental data, further activities are needed to improve the model or the code itself. A more comprehensive study is also needed to investigate these complex phenomena relevant to the development of safety systems for Gen-IV reactors. However, given the complexity of the phenomena involved, the availability of the experimental data, and the simulation results with the original RELAP5 code, this preliminary validation can be considered satisfactory for the purpose of the work presented in this thesis. Therefore, an updated and improved version of the code can be provided to the coupled tool.

Table 4 – Experimental vs RELAP5 initial conditions

Parameter	**Unit**	**Exp.**	**RELAP5**	**Error**
Water Inventory	kg	74.6	73.0	-2.1%
Water loop pressure	bar	178.1	180.0	1.1%
Gas pressure	bar	110.7	110.0*	-
Thermal power supplied during the steady state	kW	55**	55*	-
SG fluid inlet temperature	°C	307.4	301.7	-5.7°C
SG fluid outlet temperature	°C	348.1	343.7	-4.4°C
HX fluid inlet temperature	°C	343.6	340.1	-3.5°C
HX fluid outlet temperature	°C	310.2	303.4	-6.8°C
Gas Tank temperature	°C	23.4	20.0*	-
Water mass flow rate	g/s	N/A	171	-
**imposed as boundary conditions* ***oscillations around the average value due to the control system*				

Table 5 – Experimental vs RELAP5 water distribution among the main regions of the facility

Water inventory	**Unit**	**Exp.**	**RELAP5**	**Error**
Total	kg	74.6	73.0	-2.1%
Non-condensable gas tank	kg	14.7	23.3	59%
Bypass HX line	kg	5.5	5.4	-1.8%
IC loop	kg	54.4	44.3	-18.6%

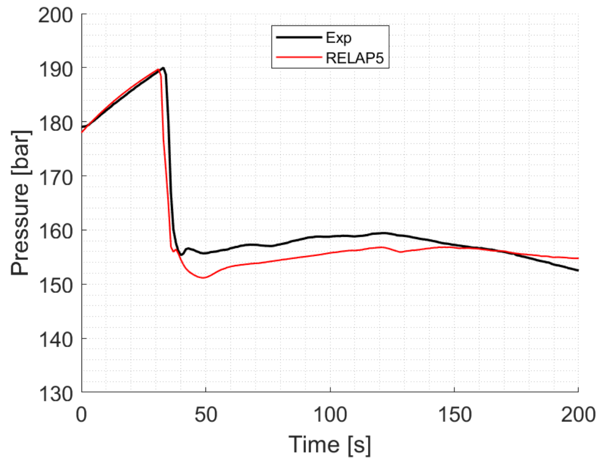

Figure 35 – Pressure trend in the first 200 s

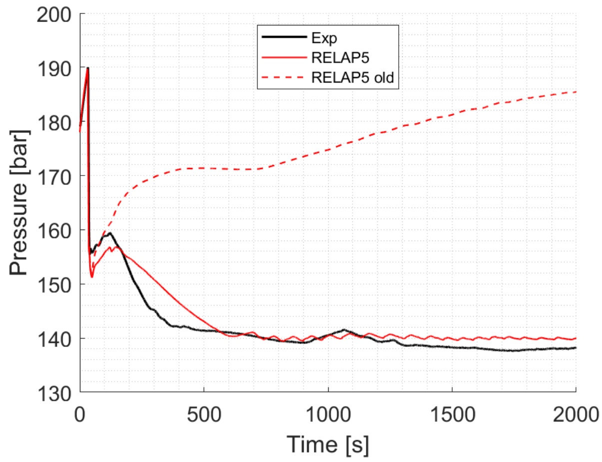

Figure 36 – Comparison between the experimental, the new and the old RELAP5 versions pressure trend in the first 2000 s

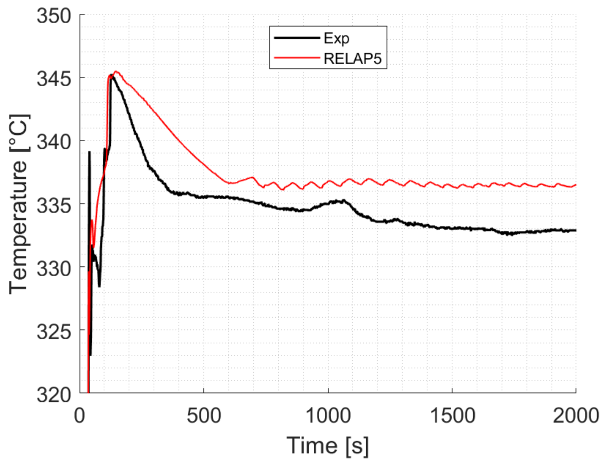

Figure 37 – Experimental vs RELAP5 IC inlet temperature in the first 2000 s

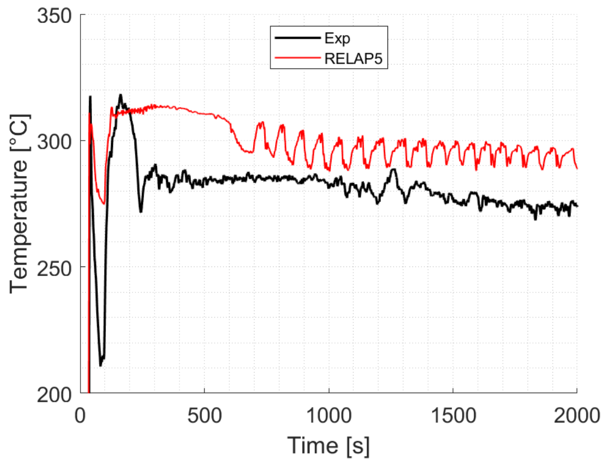

Figure 38 – Experimental vs RELAP5 IC outlet temperature in the first 2000 s

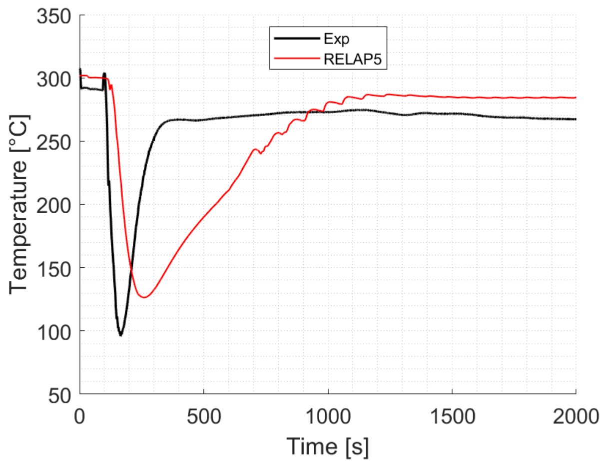

Figure 39 – Experimental vs RELAP5 SG inlet temperature in the first 2000 s

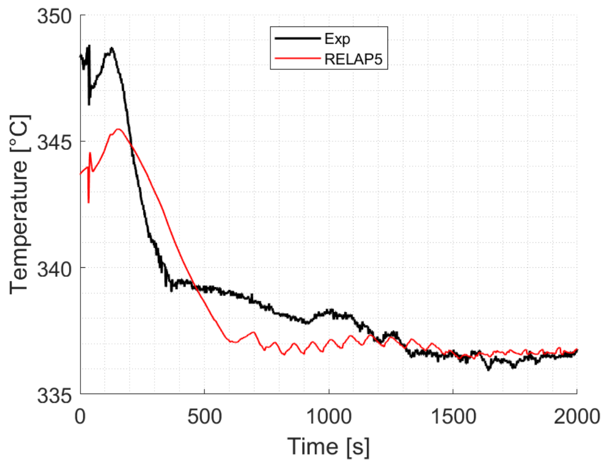

Figure 40 – Experimental vs RELAP5 SG outlet temperature in the first 2000 s

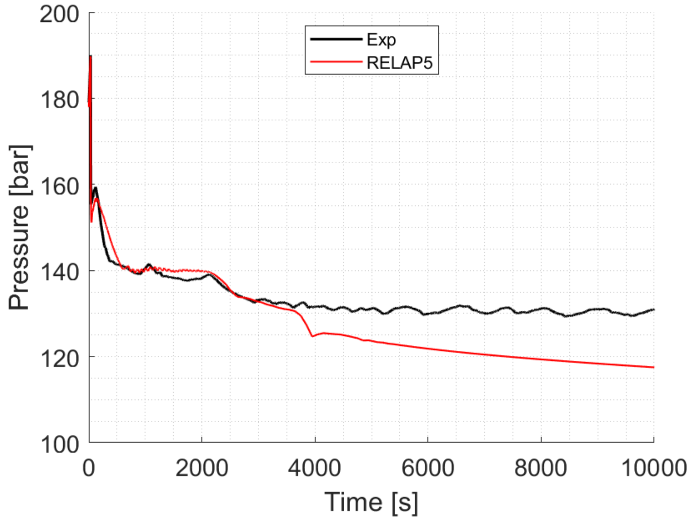

Figure 41 – Experimental vs RELAP5 pressure trend in the long term

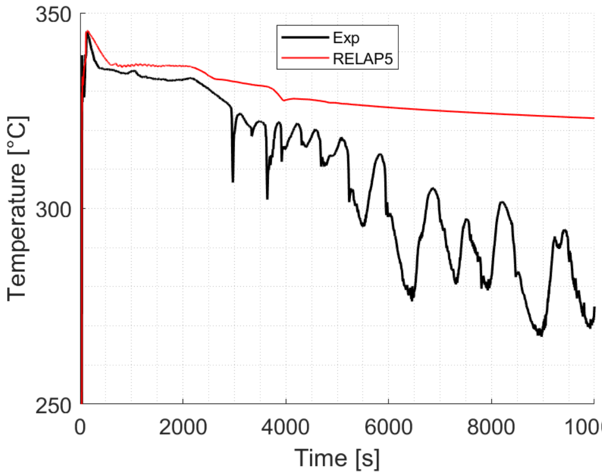

Figure 42 – Experimental vs RELAP5 IC inlet temperature in the long term

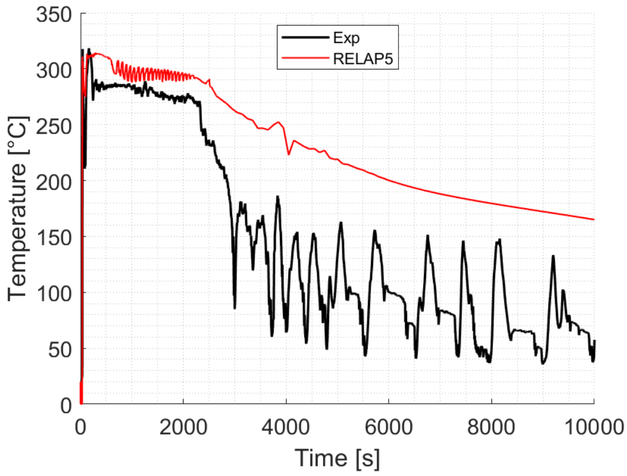

Figure 43 – Experimental vs RELAP5 IC outlet temperature in the long term

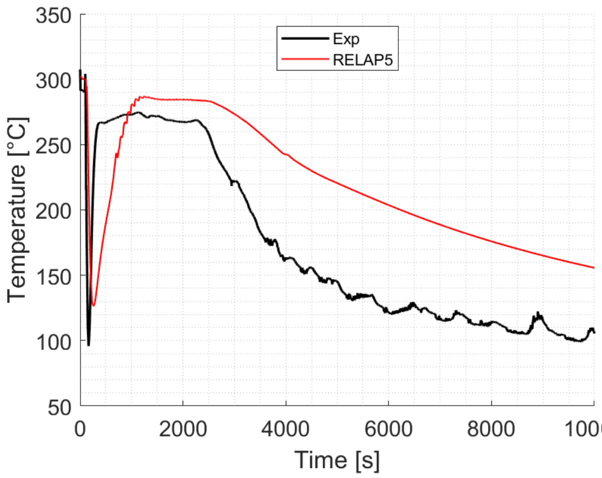

Figure 44 – Experimental vs RELAP5 SG inlet temperature in the long term

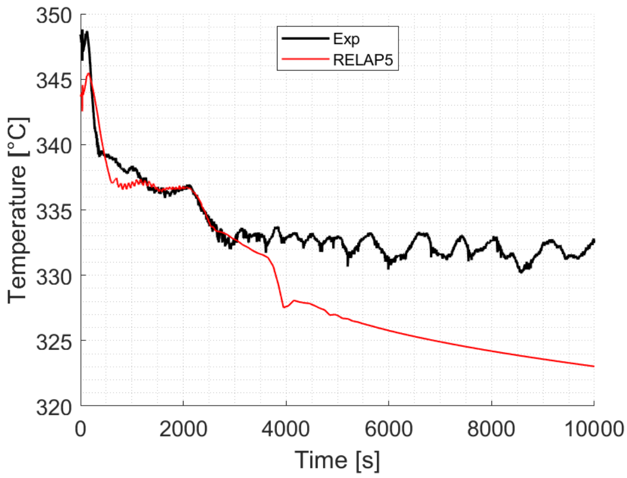

Figure 45 – Experimental vs RELAP5 SG outlet temperature in the long term

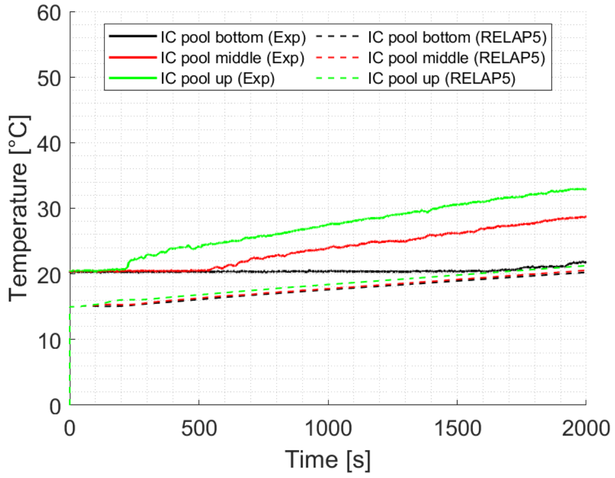

Figure 46 – Experimental vs RELAP5 pool temperatures in the first 2000 s

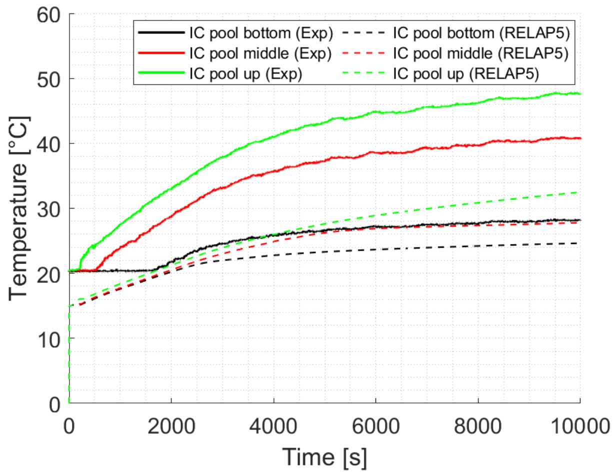

Figure 47 – Experimental vs RELAP5 pool temperatures in the long term

3.2 NACIE-UP

As a first step toward the validation of the coupling architecture developed in this thesis, experimental data produced by the NACIE-UP (NAtural CIrculation Experiment – UPgrade) facility at ENEA Brasimone R.C. have been used. In the following subsections, the description of the facility and the experiments performed are provided, along with the presentation of the numerical models and simulation results. The post-test analysis is part of the IAEA's international Coordinated Research Project (CRP) I31038, named "Benchmark on Transition from Forced to Natural Circulation Experiment with Heavy Liquid Metal Loop" [124] [125]. STH, CFD and coupled simulations were conducted within WP 1, 2 and 4, respectively.

3.2.1 Description of the facility

NACIE-UP [126] [127] is a rectangular loop cooled by Lead-Bismuth Eutectic (LBE), with an overall height of 7.7 m and a width of 2.4 m. The loop consists of several components, including an electrically heated FPBS located at the riser section's base, an expansion vessel at the top, and a double-wall tube HX at the upper section of the downcomer. LBE circulation is driven by a gas lift system, which injects argon into the riser to enhance natural circulation. The facility is equipped with several ThermoCouples (TCs) that monitor temperatures throughout the loop and within the FPBS. Figure 48 provides a schematic representation of the facility, showing the qualitative location of loop TCs and Pressure Transducers (PTs) located at the top and bottom of the riser. The mass flow rate is measured by a prototypical Thermal Flow Meter (TFM) [128], developed by ENEA in collaboration with Thermocoax, whose working principle is based on the energy balance between the power supplied by the instrument and the temperature difference across it.

The FPBS consists of 19 wire-wrapped electrical rods arranged in a triangular lattice with a pitch-to-diameter ratio of approximately 1.28. Each pin has a diameter of 6.55 mm, and the wire, which is 1.75 mm in diameter, is helically wrapped around the pin with an axial pitch of 262 mm. The pins are 2000 mm long, with 600 mm serving as the active length. In the "pre-active" length, around 8-10% of the total power is transferred to the fluid due to axial conduction and the Joule effect, as this region has lower electrical resistance. The pins are held in place by a grid downstream of the FPBS, and the bundle is housed in a hexagonal wrapper. TCs are installed within the FPBS on three planes (Plane 1, Plane 2, and Plane 3) at 38 mm, 300 mm, and 532 mm from the active region's start. One selected pin, Pin 3, is equipped with wall-embedded TCs at 43.7 mm intervals beyond Plane 1 [127]. Figure 49 illustrates the bundle's active and non-active regions, as well as the positions of the instrumented planes, while Figure 50 provides a cross-sectional view of the pin bundle.

The expansion vessel accommodates the LBE's thermal expansion and maintains system pressure using a cover gas volume. It is equipped with two level sensors to set the LBE level during the filling process.

The HX is of shell-and-tube design, with seven double-wall tubes separating the LBE from the water in the secondary coolant loop by a gap filled with AISI 316L powder and pressurized air. LBE flows tube side from top to bottom, while the secondary fluid in the "low power section" (0-30 kW) moves in cross-flow relative to the LBE. In the "high power section" (30-250 kW), water flows in countercurrent to the LBE. The secondary side (not represented in the figures) is a pressurized water loop operating at 16 bar, featuring a circulation pump, pressurizer, and air cooler. In the experiments considered in this thesis, only the "high power section" of the HX was used.

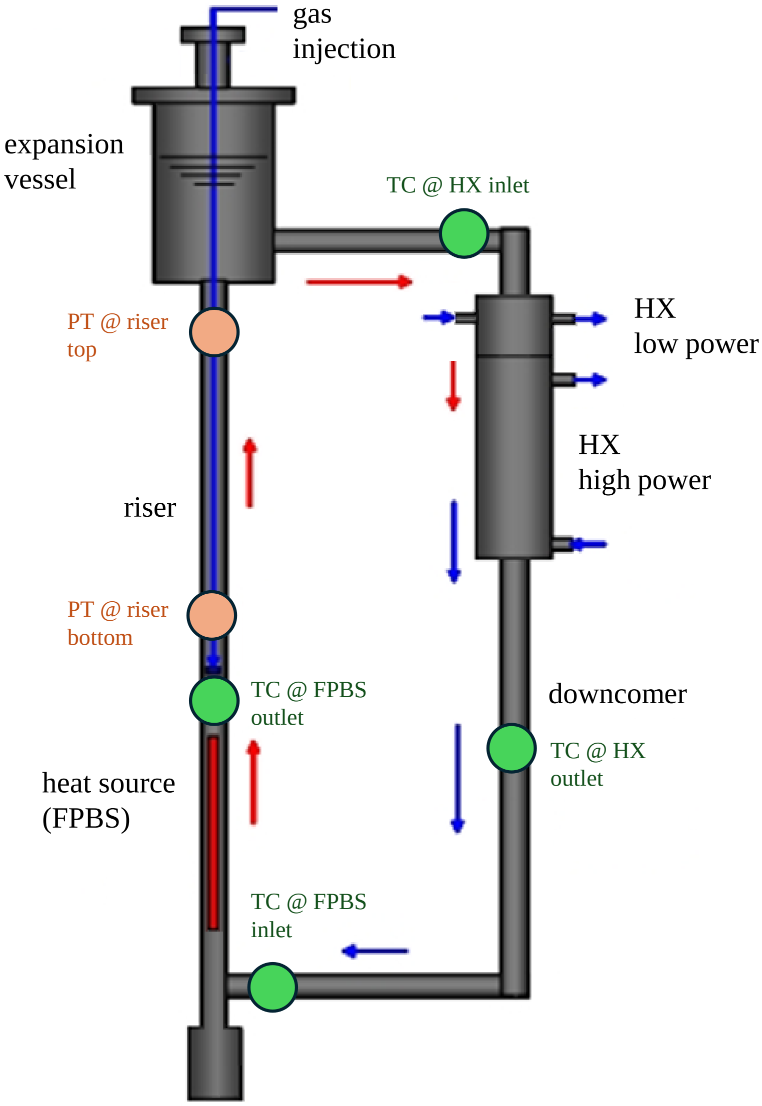

Figure 48 – Schematic drawing of the NACIE-UP primary loop [127]

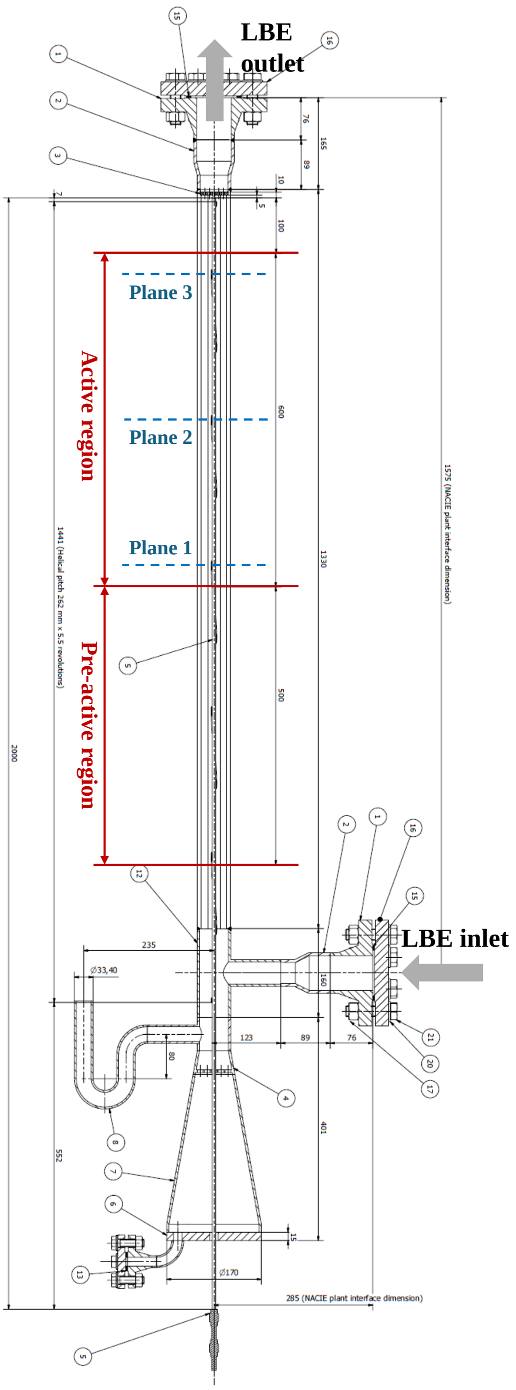

Figure 49 – NACIE-UP FPBS layout and instrumented planes

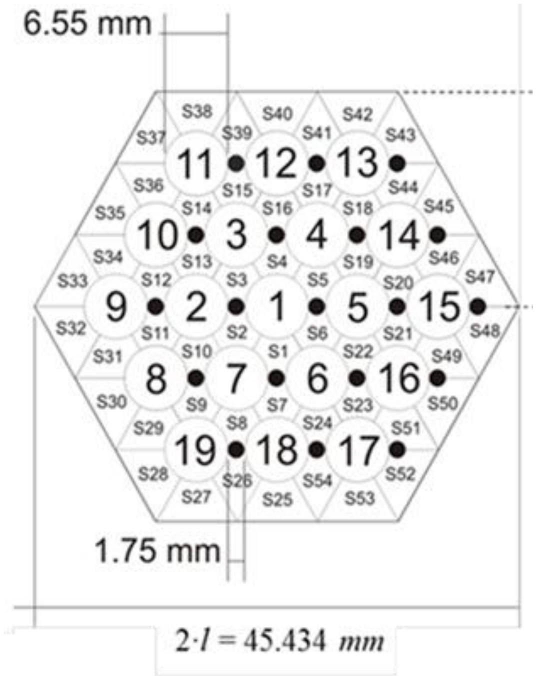

Figure 50 – NACIE-UP FPBS cross-sectional view

3.2.2 Experiments description

The experimental tests (named as ADP06 and ADP10) [129] [130] considered for this validation activity analyze the transition between two steady states: one characterized by forced circulation, where the LBE flow is enhanced through gas injection in the riser line, and another where natural circulation is established. The transition occurs when the gas injection is stopped, causing a sharp drop in the LBE mass flow rate. At this point, the only driving force promoting LBE flow is natural circulation. As the FPBS power remains constant throughout the tests, the temperature difference across the FPBS increases, leading to a temperature increase in the riser (hot leg) and a lower temperature in the downcomer (cold leg). To achieve a new equilibrium, i.e., to exchange the same amount of power to the HX, the average temperature of the LBE loop increases because a higher temperature gradient between the primary and secondary sides of the HX is needed if the mass flow rate is reduced.

In the initial steady state of both tests, gas is injected at a constant flow rate of 10 Nl/min. The secondary side operates with pressurized water at 16 bar, maintaining a constant temperature of 170°C at the HX inlet and a volumetric flow rate of 10 m³/h. At t = 0 s, the gas injection is stopped (dropping to zero within 1 second), while all other parameters remain unchanged. The system eventually stabilizes at a new steady state, which is maintained for over 30 minutes. Table 6 summarizes the experimental conditions, referring to "Steady state 1" and "Steady state 2" as the initial and final steady states of the transient.

The tests differ in the number and arrangement of active pins (as shown in Figure 51):

- In the ADP10 test, all 19 pins are powered, leading to symmetrical heating of the assembly, with a total power of 30 kW and an average surface heat flux of 127.9 kW/m².
- In the ADP06 test, only the 7 central pins are powered, though the total power remains at 30 kW. Consequently, the average heat flux on the pin surface is higher at 347.1 kW/m².

Temperatures throughout the loop are monitored by TCs with an accuracy of ±1.5°C, while the LBE mass flow rate is measured using the TFM. The uncertainty of the mass flow rate measurement depends on the heater power, inlet temperature, and flow rate, with a maximum uncertainty of approximately 5% for these experiments, as calculated using the formula derived in Ref. [128].

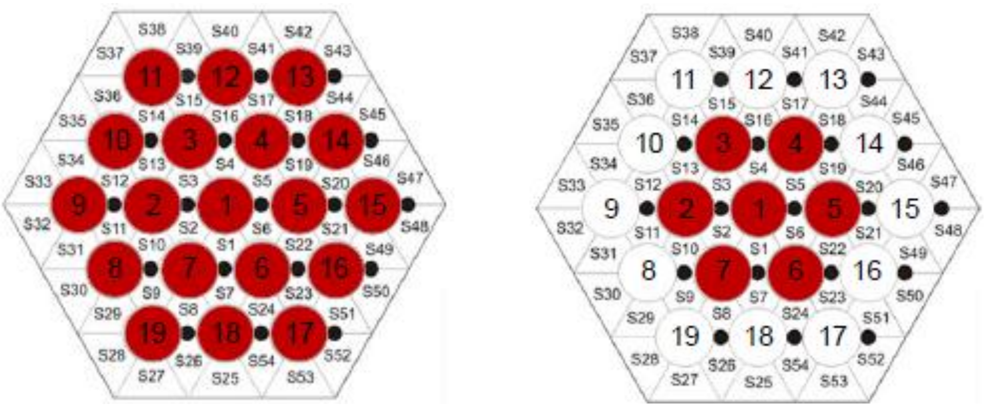

(a) (b)

Figure 51 – Active pins (in red) during ADP10 (a) and ADP06 (b) tests [127]

Table 6 – Experimental boundary conditions for ADP10 and ADP06 tests

Parameter	**ADP10**		**ADP06**	
	Steady state 1	**Steady state 2**	**Steady state 1**	**Steady state 2**
$\dot{m}_{gas}$ [Nl/min]	10	0	10	0
$\dot{Q}_{tot}$ [kW]	30	30	30	30
q'' [kW/m^2]	127.9	127.9	347.1	347.1
$\dot{m}_{H_2O}$ [m^3/h]	10	10	10	10
T_{inlet,H_2O} [°C]	170	170	170	170
p_{H_2O} [bar]	16	16	16	16

3.2.3 Numerical models

STH model

The model of the NACIE-UP facility [131] was developed using the RELAP5/Mod3.3 code, which was specifically modified to incorporate the thermo-physical properties of HLMs and to simulate the coexistence of HLMs and non-condensable gases within the same hydraulic volume [84] [85]. The model represents the fluid regions through PIPE components, which are interconnected by SINGLE JUNCTION components. All the solid structures, such as the pipe walls and insulator material, are modelled using HEAT STRUCTURES. In this way, the thermal inertia of the system is also considered, and the heat losses have been modelled with a constant convective HTC and room temperature of 8 W/m² °C and 10°C, respectively.

The mesh size varies depending on the region: in the active zones (e.g., FPBS and HX), where significant heat exchange and thermal gradients occur, the mesh size is about 5 cm. In non-active regions, where the temperature is relatively uniform, the maximum mesh size reaches 12 cm, with a smooth transition between the two. The "sliced modelling approach" [132] is used throughout the facility to accurately capture the system's behavior under natural circulation conditions.

The secondary side of the HX is modelled only in its active portion, with BCs like inlet temperature, mass flow rate, and outlet pressure imposed by TIME DEPENDENT VOLUMES (TMDPVOL) and a TIME DEPENDENT JUNCTION (TMDPJUN). The thermal conductivity of the gap between the coaxial tubes in the HX, filled with stainless steel powder and pressurized air, is calculated using the following equation [133]:

$$k_{powder} = 0.3 + 0.005 \cdot (T - 200) \tag{39}$$

where T is the temperature in °C, and k is the thermal conductivity in W/m °C. Figure 52 provides a graphical representation of the nodalization.

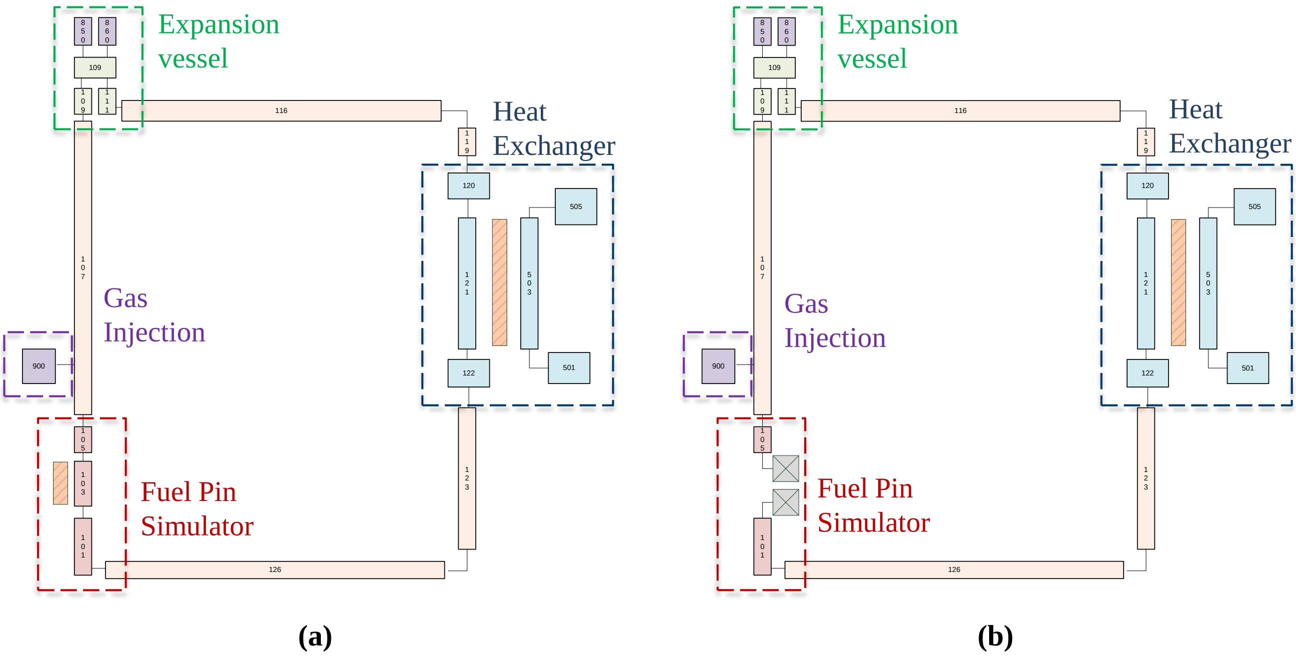

Figure 52 – Nodalization of the NACIE-UP loop: RELAP5 stand-alone closed loop (a) and coupled model open loop (b)

Since RELAP5 allows users to input Reynolds-dependent friction factors and form loss coefficients, different correlations have been applied in various sections of the NACIE-UP facility model. Localized pressure drops were calculated using formulas from Ref. [134], while the Cheng and Todreas correlation for wire-wrapped tube bundles [135] [136] was used for the FPBS. In the laminar flow region, RELAP5 permits the friction factor to be inversely proportional to Reynolds number (Re), while in the turbulent flow region, a relation of ~Re^{-C} can be chosen, as shown in Eq. (40). For the transition region, spanning Re values from 2200 to 3000, RELAP5 linearly interpolates between laminar and turbulent regimes [66]. The actual friction factor correlation in the Re range of interest has been approximated using the following equations, with calibration coefficients provided in Table 7. A comparison between the Cheng and Todreas correlation and RELAP5 for wire-wrapped tube bundles is illustrated in Figure 53.

$$\begin{cases} f_L = \dfrac{64}{\Phi_S \cdot Re} & if\ Re < 2200 \\ f_{L,T} = \left(3.75 - \dfrac{8250}{Re}\right)\left(f_{T,3000} - f_{L,2200}\right) + f_{L,2200} & if\ 2200 < Re < 3000 \\ f_T = A + B \cdot Re^{-C} & if\ Re > 3000 \end{cases} \tag{40}$$

Table 7 – Coefficients for the calibration of the FPBS pressure drops in the RELAP5 model

Constant	Φ_S	A	B	C
Value	0.45	0.021	31.66	0.856

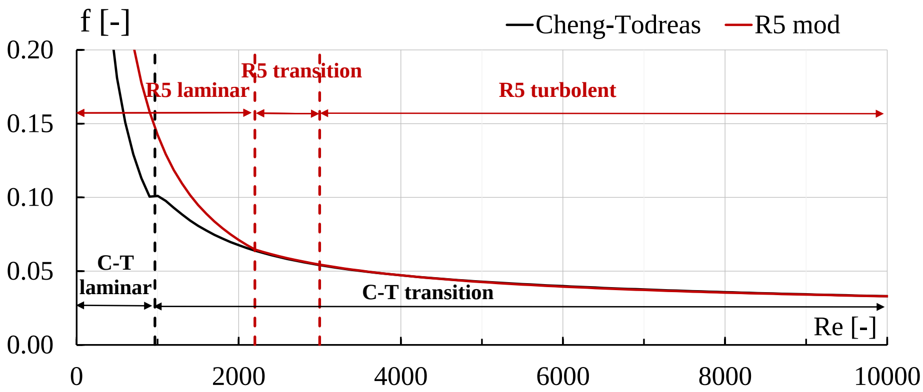

Figure 53 – Cheng and Todreas vs RELAP5 correlations for wire wrapped tube bundles

Further investigation into experimental data highlighted issues when simulating the natural circulation regime (Steady State 2). The temperatures of the hot and cold legs, measured at the FPBS and HX outlet, were 362.5°C and 199.5°C, respectively. Using benchmark specifications and data from the 2015 HLM Handbook [137], the density difference ($\Delta\rho$) and pressure head (Δp_{head}) for natural circulation were calculated as:

$$\Delta p_{head} = \Delta\rho \cdot g \cdot H = \left(\rho_{@199.5°C} - \rho_{@362.5°C}\right) \cdot g \cdot H = 9.7\ kPa \tag{41}$$

where g is the gravitational constant, and H is the height difference between the FPBS and HX thermal barycenters.

The experimentally determined mass flow rate of 1.31 kg/s during the final steady state corresponds to a Re ~ 3600. From Figure 53, a friction factor of 0.05 can be obtained, and the pressure drop across the FPBS is calculated as:

$$\Delta p_{FPBS} = \left(f \cdot \frac{L}{D_H}\right) \cdot \left(\frac{1}{2} \cdot \rho \cdot u^2\right) = 3.5\ kPa \tag{42}$$

where L is the axial length of the FPBS, D_H is the hydraulic diameter of the bundle, ρ and u are the bulk density and velocity at the FPBS inlet section, respectively. This value is aligned with both analytical and numerical calculations from RELAP5, which confirmed that the most significant pressure drop occurs in the FPBS. A discrepancy between the pressure head for to natural circulation (Δp_{head}) and the hydraulic resistance could be caused by additional factors not modelled, such as oxide deposits in the downcomer, which could increase pressure drops locally [138].

To calibrate the model, a concentrated pressure drop was added at the downcomer base, represented by a constant K coefficient. However, during simulations of forced circulation, a mismatch in mass flow rate arose, and it was attributed to an underestimation by RELAP5 of the void fraction profile in the riser. This discrepancy was mitigated by artificially doubling the argon gas mass flow rate in the riser, which corrected the void fraction profile but highlighted the need for improved drift-flux models for HLM/non-condensable gas systems in future developments. In fact, even in the modified version of RELAP5/Mod3.3, the drift-flux models adopted in the case of HLM/non-condensable are the same developed for the water/non-condensable case. During ADP10 and ADP06 tests, at the BOT, when forced circulation is promoted by the gas injection, the flow in the riser section is characterized by the following features: upflow and high mass flux (> 100 kg/m^{2}s). In these conditions, the EPRI model is adopted by the code [139]. In particular, the computed average void fraction is half of the experimental one. Thus, the model proved to not be suitable for HLMs. For the scope of this thesis, to compensate for this code limitation, the gas mass flow rate injected in the riser was doubled, matching in this way the void fraction profile calculated starting from the experimental data. Nevertheless, in the future developments of the activity, it is planned to implement more appropriate drift flux models for the HLM/non-condensable case.

CFD model

To reduce computational costs, the CFD model focuses solely on the 600 mm active region of the FPBS. This domain encompasses the LBE fluid, the external solid wrapper made of AISI316L stainless steel, the wires, and the pins. Three different materials are considered for the solid components, as outlined in Table 8. The contribution of Inconel600, which is present inside the real FPBS pins, is neglected in this simulation due to its minimal impact. Instead, the simulation treats the interior of the pin as a single Bohrium Nitride (BN) domain. A schematic of the pin's internal structure is depicted in Figure 54.

Table 8 – Diameters of the different parts of the pin in the active region [125]

Part	**Internal diameter [mm]**	**External diameter [mm]**
Clad (AISI316L)	5.08	6.55
Heating tube (Inconel600)	3.35	3.53
Central conductor (Copper)	-	2.31
1st insulant layer (BN)	2.31	3.35
2nd insulant layer (BN)	3.53	5.08

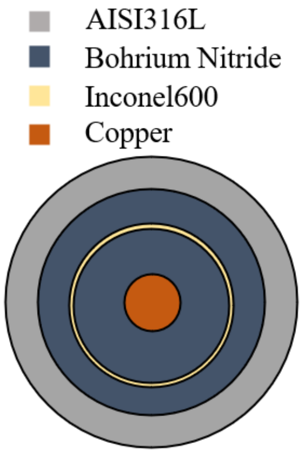

Figure 54 – Schematic of the pin materials

To optimize the mesh structure and reduce the number of nodes, the domain was divided into different bodies both axially and radially, allowing to obtain a structured mesh in each region. However, this approach led to a large number of interfaces, limiting the number of partitions for the coupled simulation due to the time required for interface interpolation.

At the FPBS inlet, a fully developed velocity and temperature profile was imposed based on results from a preliminary simulation, which included in the domain two helical pitches upstream of the active region to obtain the inlet conditions. The turbulence model selected for this simulation is the SST $k - \omega$ model with a constant turbulent Prandtl number (Pr_t) of 1.5, as previous sensitivity analyses indicated minimal differences in the range of 1.5 to 2 [43] [140]. An adiabatic condition was applied to the outer wall of the solid structure, while the fluid boundary layer at the walls was resolved with a $y^+ \sim 1$ at all fluid-solid boundaries. An upwind advection scheme and the default solver options in Ansys CFX – which employs the Rhie-Chow algorithm – were used.

A grid independence study, reported in Table 9, was conducted under ADP10 initial steady state conditions to determine the ideal number of nodes, balancing accuracy with computational cost. Various meshes were tested, modifying the near-wall treatment and element size in both the radial (*Radial ref)* and axial (*Axial ref)* directions. A *Coarse improved* mesh consisting of 4.5 million nodes (Figure 55) was ultimately selected, achieving less than a 10% discrepancy compared to the finest meshes.

The stand-alone CFD model have been used exclusively for steady-state analysis, while STH and coupled models have been run for the entire transient or specific time windows of the transient. Therefore, the CFD results presented focus on the initial steady states of the different tests, as the primary goal of the work is to evaluate the performance of the coupled tool.

Table 9 – Grid independence study of the FPBS CFD model

	Unit	**Coarse**	**Coarse improved**	**Reference**	**Radial ref**	**Axial ref**
n° of nodes (•10^6)	-	4.2	4.5	6.4	33.5	29.3
Δp	mbar	28.4	31.1	31.4	33.6	33.8
ΔT *in-out*	°C	80.1	80.3	80.3	80.3	80.4
T point	°C	319.0	321.2	322.5	323.1	323.7

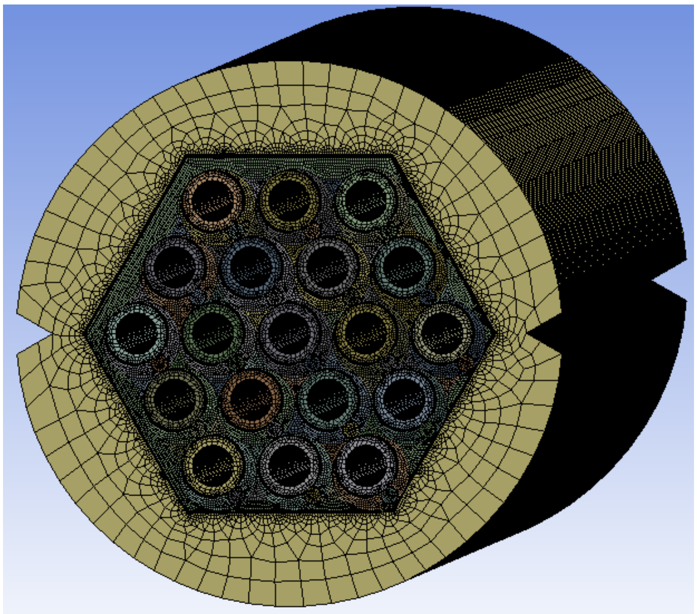

Figure 55 – Coarse improved mesh

STH/CFD coupled model

For the coupled simulation, the RELAP5 model was modified by removing the active part of the FPBS and replacing it with TMDPVOLs and TMDPJUNs, where the BCs from the CFD calculations are imposed. The approach adopted in this work is therefore the domain decomposition. A preliminary steady-state calculation using the RELAP5 "open loop" model (Figure 52b) was performed to generate a restart file for the coupled simulation. The BCs for this "open loop" model were based on the steady-state values of the entire loop.

In the coupled run, the two-way exchange of information includes (graphically represented in Figure 56):

- mass flow rate at the outlet (from CFX to RELAP5).
- outlet temperature (from CFX to RELAP5).
- total pressure drop along the FPBS active length (from CFX to RELAP5).
- inlet mass flow rate (from RELAP5 to CFX).
- inlet temperature in the FPBS (from RELAP5 to CFX).
- pressure at the FPBS outlet (from RELAP5 to CFX).

The pressure drop is used to calculate the absolute pressure at the outlet TMDPVOL in the RELAP5 domain (FPBS inlet), which is updated at each timestep using the following equation:

$$p_1 = \Delta p_{fr,CFX} + \Delta p_{grav} + p_2 \qquad (43)$$

where:

- p_1 is the pressure at the FPBS inlet (see Figure 56).
- $\Delta p_{fr,CFX}$ is the friction term calculated by the CFD.
- Δp_{grav} is the gravitational term.
- p_2 is the absolute pressure at the FPBS outlet boundary, computed by RELAP5 at the previous timestep (see Figure 56). It must be noted that even though p_2 is passed from RELAP5 to CFX, it is not used as BC, but it is involved only for the evaluation of p_1.

This method allows to set the relative pressure to zero at the CFD model outlet, which helps reduce the residuals in the momentum equation. The inlet mass flow rate in the CFD corresponds to the value calculated by RELAP5 at the "open loop" outlet. A non-dimensional velocity map was applied at the CFD domain inlet, obtained by averaging the fully developed flow maps of initial and final steady-state CFD simulations, with a similar procedure used for the inlet temperature distribution. These choices were aimed at reducing computational time while maintaining simulation accuracy.

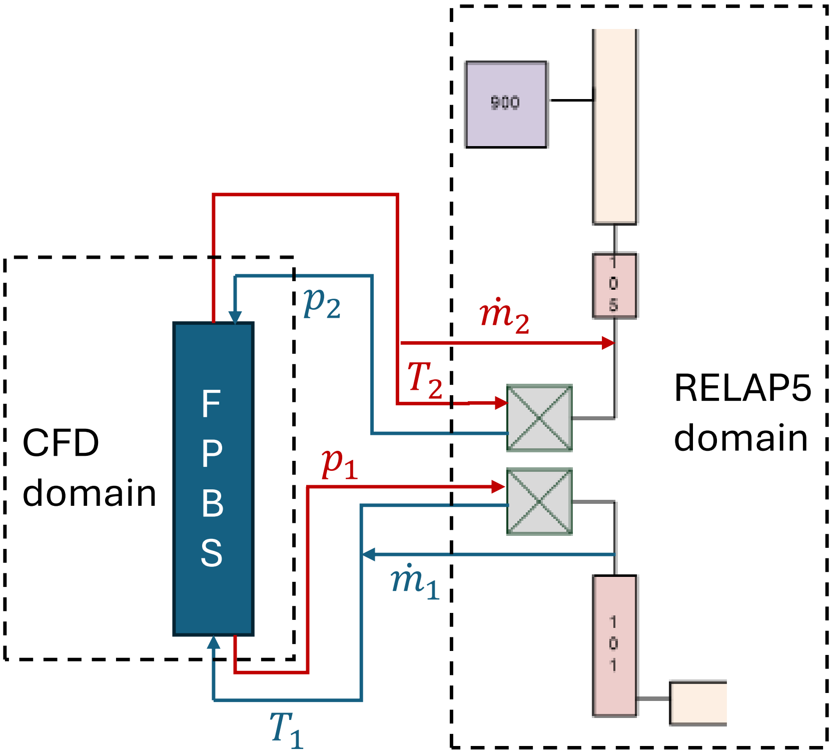

Figure 56 – Exchanged parameters in the coupled simulation

3.2.4 Simulation results

System-level analysis

The steady states have been achieved through a 5000 s null-transient simulation, using the constant BCs described in Section 3.2.2. Coupled simulations have been run with constant timesteps for both the CFD and RELAP5 codes, with the RELAP5 timestep set to one-tenth of the CFX one to enhance stability. A preliminary sensitivity analysis varied the timestep from 10^{-3} s to $2{\cdot}10^{-2}$ s, showing negligible differences. To reach a new steady state after variable exchange between the codes, an additional 10-second null transient simulation was performed. At this point, the gas injection is stopped, and the transient is initiated.

The experiments achieved two different steady states, and the results for each steady state in all tests are presented in Table 10 and 11, where BOT represents the initial condition, and EOT (End Of Transient) represents the final condition. No significant differences were observed between the ADP10 and ADP06 tests in terms of loop parameters, as the FPBS power remained the same, with the only difference being the distribution among the pins. A comparison between simulation results and experimental data shows that the maximum discrepancy (~5%) was observed in the ADP06 test's BOT mass flow rate, comparable to the uncertainty of the TFM measurement. The largest discrepancy in temperature (approximately 12°C) was at the FPBS outlet at the EOT of the ADP10 test. This deviation, despite accurate predictions of inlet temperature, is consistent with the slight overestimation of the mass flow rate, and it could be due also to the uncertainty in the correlation for LBE's specific heat capacity in the RELAP5/Mod3.3 code.

The coupled simulations closely match the stand-alone RELAP5 results for both tests. Furthermore, the results of the two coupled calculations are nearly identical, as the only differing factor is the power distribution among the pins in the FPBS. The main difference is observed at the FPBS outlet temperature in the CFD domain, while the remaining quantities are computed by RELAP5.

The moment when the gas injection is stopped marks the SoT, considered as t=0 s in both the RELAP5 and coupled simulations. During the transient phase, the thermal power from the FPBS, along with the water temperature and mass flow rate on the secondary side of the HX, remain constant. As with the steady-state analysis, comparisons between the experimental data and simulation results for the transient phase focus on the loop parameters, as the STH code cannot accurately predict local temperatures within the FPBS.

Table 10 – Experimental vs RELAP5 vs coupled results (ADP10 test)

	Parameter	Unit	Exp	RELAP5	Error	Coupled	Error
BOT	*LBE $\dot{m}$*	kg/s	2.56	2.52	-1.6%	2.60	1.6%
	T in FPBS	°C	225.56	223.16	-2.40°C	223.25	-2.31°C
	T out FPBS	°C	305.24	299.03	-6.21°C	299.74	-5.50°C
	T in HX	°C	301.58	296.93	-4.65°C	295.05	-6.53°C
	T out HX	°C	220.53	218.62	-1.91°C	218.79	-1.74°C
*EOT**	*LBE $\dot{m}$*	kg/s	1.31	1.34	2.3%	-	-
	T in FPBS	°C	207.45	207.22	-0.23°C	-	-
	T out FPBS	°C	362.44	350.45	-11.99°C	-	-
	T in HX	°C	353.28	345.94	-7.34°C	-	-
	T out HX	°C	199.36	200.02	0.66°C	-	-
* Results of the coupled calculation at EOT are not available since it ends at 1500 s							

Table 11 – Experimental vs RELAP5 vs coupled results (ADP06 test)

	Parameter	Unit	Exp	RELAP5	Error	Coupled	Error
BOT	*LBE $\dot{m}$*	kg/s	2.66	2.52	-5.3%	2.60	-2.3%
	T in FPBS	°C	227.67	223.40	-4.27°C	223.25	-4.42°C
	T out FPBS	°C	304.35	299.27	-5.08°C	300.32	-4.03°C
	T in HX	°C	301.39	297.22	-4.17°C	295.05	-6.34°C
	T out HX	°C	222.74	218.80	-3.94°C	218.79	-3.95°C
*EOT**	*LBE $\dot{m}$*	kg/s	1.33	1.34	-0.8%	-	-
	T in FPBS	°C	207.67	207.33	-0.34°C	-	-
	T out FPBS	°C	359.93	350.56	-9.37°C	-	-
	T in HX	°C	351.20	346.18	-5.02°C	-	-
	T out HX	°C	199.62	200.11	0.49°C	-	-
* Results of the coupled calculation at EOT are not available since it ends at 1500 s							

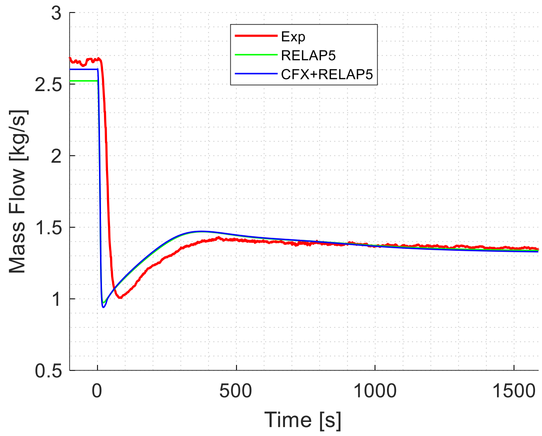

Figure 57 – Experimental vs RELAP5 vs coupling mass flow rate (ADP06)

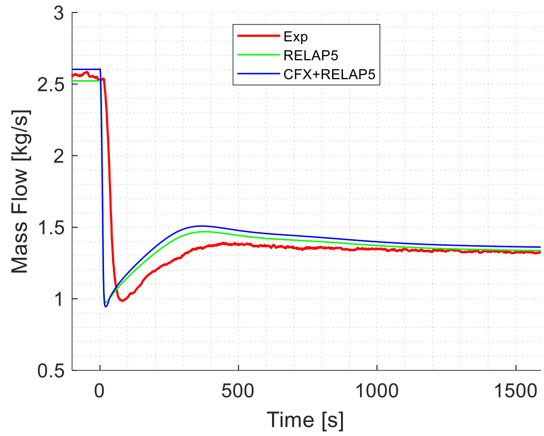

Figure 58 – Experimental vs RELAP5 vs coupling mass flow rate (ADP10)

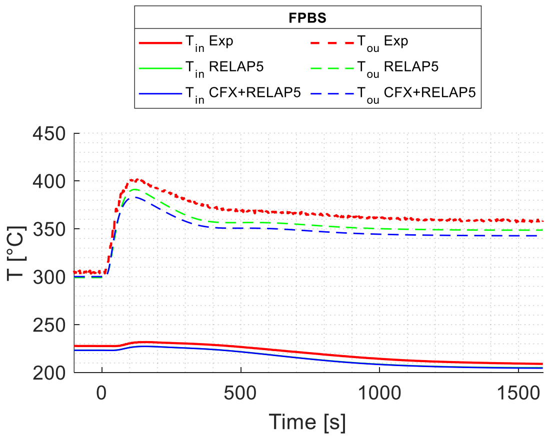

Figure 59 – Experimental vs RELAP5 vs coupling FPBS temperature (ADP06)

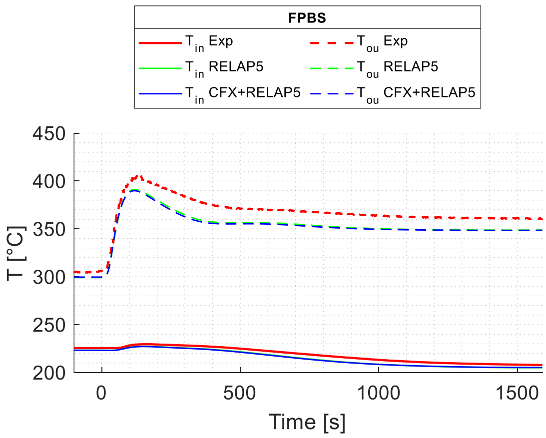

Figure 60 – Experimental vs RELAP5 vs coupling FPBS temperature (ADP10)

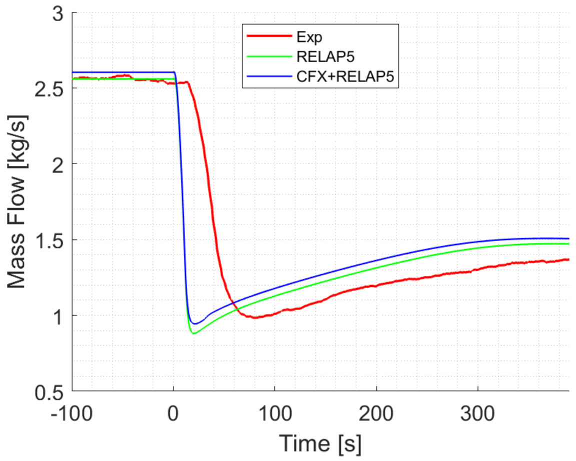

Figure 61 – Experimental vs RELAP5 vs coupling mass flow rate at the beginning of the transient (ADP10)

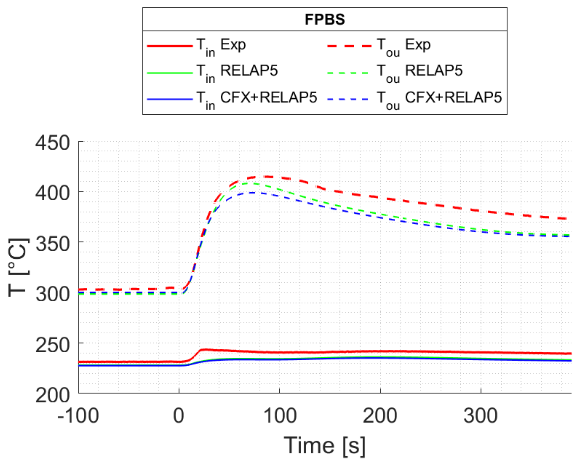

Figure 62 – Experimental vs RELAP5 vs coupling FPBS temperature at the beginning of the transient (ADP10)

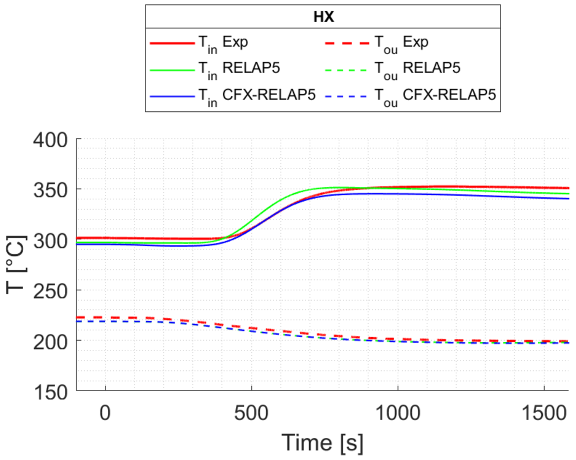

Figure 63 – Experimental vs RELAP5 vs coupling HX temperature (ADP06)

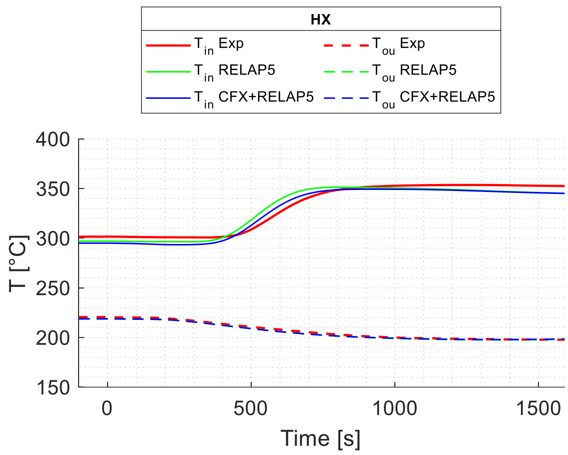

Figure 64 – Experimental vs RELAP5 vs coupling HX temperature (ADP10)

Figure 57 and 58 show that the LBE mass flow rate quickly drops to approximately 1 kg/s once the gas injection ceases, and after about 1500 s, a new steady state is achieved as natural circulation establishes. The experimental delay in observing the mass flow reduction can be attributed to the inherent delay in the TFM's response rather than any physical cause. This delay is not present in the TCs' data, as evidenced by the close timing of temperature changes in the FPBS (Figure 59 and 60) between the experimental and simulation results. Temperatures within the FPBS react rapidly to mass flow changes since the FPBS operates under an imposed heat flux, meaning that temperature fluctuations correspond directly with changes in mass flow. Further evidence is provided by a zoomed-in view of the initial transient period in Figure 61 and 62, illustrating the discrepancy in mass flow rate compared to experimental data while confirming a close match in temperature results.

As observed in the steady-state simulations, the coupled and stand-alone RELAP5 results closely align, as the transition to natural circulation in the loop is primarily governed by phenomena that can be accurately represented by a 1D model. Minor discrepancies result from the more detailed modelling of the FPBS and different pressure drops calculation in the component.

The agreement between experimental and numerical values for the FPBS inlet and outlet temperatures (see Figure 59 and 60) supports the correct representation of the mass flow rate transition. However, a slight delay is noted in the HX inlet and outlet temperatures (see Figure 63 and 64), likely due to incomplete modelling of the system's heat capacity. Part of the metallic shell structure is not included in the simulation due to its minor impact on system behavior and complex geometry, but its influence becomes noticeable in the medium term (500-1000 s). Again, the trends predicted by RELAP5 and the coupled tool show close alignment, confirming that a 1D representation is adequate for capturing the relevant TH phenomena in this scenario.

The key advantage of using the coupled tool lies in its ability to provide detailed CFD analysis of the FPBS, once proper BCs such as mass flow rate and inlet temperature are provided by a system-level RELAP5 calculation, all while maintaining a reasonable computational time.

FPBS detailed analysis

The comparison between the CFD and experimental data focused on local temperatures measured at 67 TC positions. The experimental BCs, discussed in Section 3.2.1 and detailed in [125], describe the test setup, including the TCs' locations.

For the steady-state simulation at the BOT, the results for tests ADP06 and ADP10 are shown in Figure 65 and 66, respectively. These figures plot experimental and numerical temperatures as a function of the TC number, with the x-axis divided into bulk, wall, and Pin 3 TC sections. Bulk and wall thermocouples are further categorized by three axial planes.

The CFX simulation shows good agreement with the experimental data, with an average error of less than 5°C in both cases (see Table 12). The ADP10 case presents more uniform temperature profiles, with minimal discrepancies across the domain. In contrast, ADP06 shows a non-uniformity due to the non-heated region at the outer rank of the bundle. While the overall temperature trends are well-represented, internal (heated) regions exhibit slight overestimations, and external regions are slightly underestimated. This could be due to an underestimation of radial velocities influenced by wire-generated turbulence. Figure 67 and 68 highlight these discrepancies, particularly at Plane 3 TC locations, where ADP06 shows larger errors.

Errors on the first measurement plane might arise from the simplified modelling approach that excludes the hydraulic and thermal flow development before the active region. However, the similar error magnitude in the second plane suggests that such a velocity map is an effective approximation. The largest discrepancies between the simulation and experimental data are observed at the third measurement plane, while Pin 3 TCs show good qualitative agreement in both tests across the heated length.

Figure 69 and 70 compare experimental results with the coupled simulation's predicted local temperatures for TC 12 (bulk) and TC 49 (wall). The coupled tool shows similar trends to the experimental data, with a good agreement at the initial and final steady state conditions, with slightly higher discrepancy during the transition. Such discrepancies can likely be attributed to differences between the experimental and numerical LBE mass flow rates, as previously discussed.

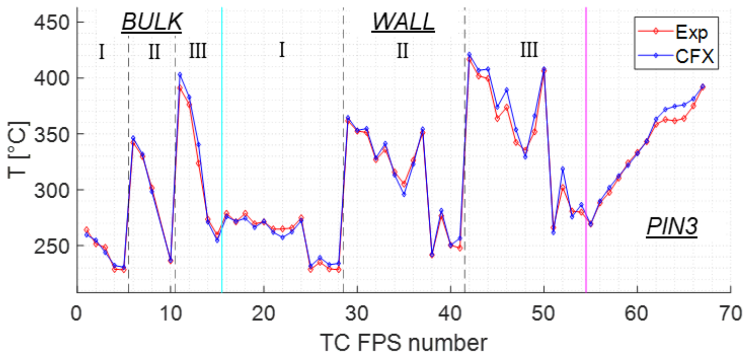

Figure 65 – TCs temperature comparison for the BOT steady state (ADP06)

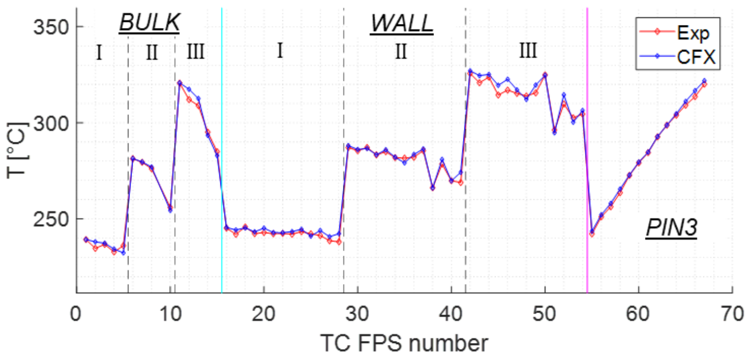

Figure 66 – TCs temperature comparison for the BOT steady state (ADP10)

Table 12 – Mean and maximum temperature difference between CFD and experiment

$\Delta T_{Exp\ vs\ CFX}$ [°C]	ADP10		ADP06	
	mean	*max*	*mean*	*max*
Error Plane 1	1.66	4.27	3.48	7.61
Error Plane 2	1.04	5.33	4.06	11.92
Error Plane 3	2.69	5.62	7.72	16.75
Error Tot	1.68	5.62	4.98	16.75

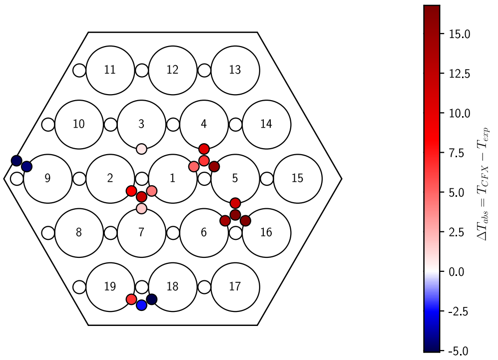

Figure 67 – Ansys CFX BOT steady state, temperature comparison on Plane 3 (ADP06)

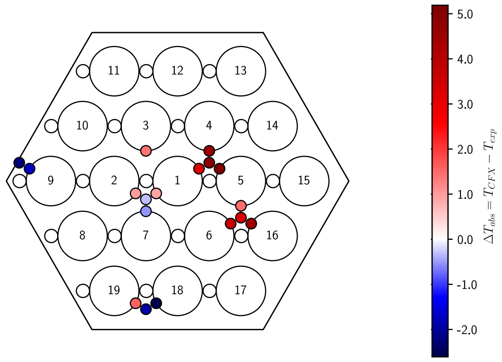

Figure 68 – Ansys CFX BOT steady state, temperature comparison on Plane 3 (ADP10)

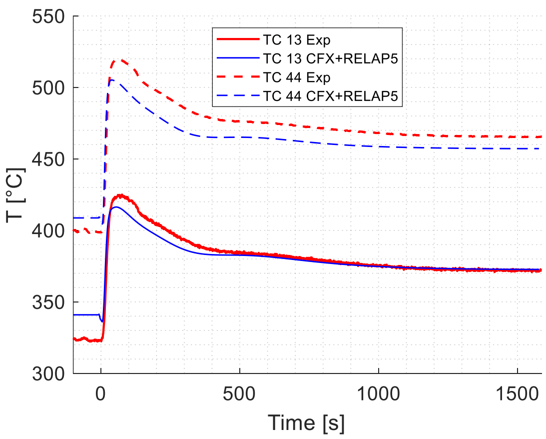

Figure 69 – Experiment vs coupling TC13 and TC44 temperature comparison (ADP06)

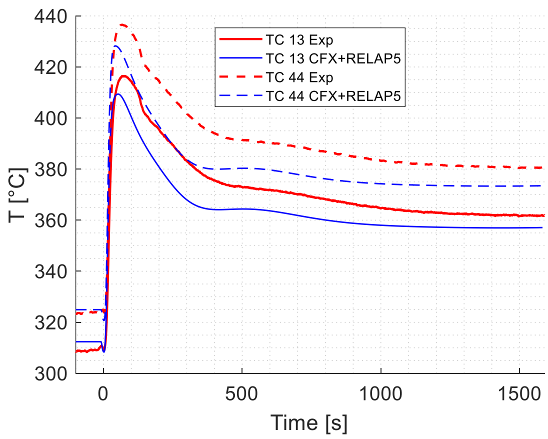

Figure 70 – Experiment vs coupling TC13 and TC44 temperature comparison (ADP10)

3.3 TALL-3D

The second step for the validation of the coupling tool has involved the TALL-3D facility, located at KTH Royal Institute of Technology. As with NACIE-UP, the description of the facility and the experiment performed are provided, as well as the numerical models and simulation results are presented. The experiment is part of the framework of the SESAME project, in which the TALL-3D facility was identified as one of the best solutions to validate STH/CFD coupled tools.

3.3.1 Description of the facility

TALL-3D [141] experimental facility, shown in Figure 71, is mainly composed of a primary loop containing LBE and a secondary loop using Dowtherm RP as the coolant. The overall height of the facility is 6.5 m.

The primary loop is mainly composed of a sump tank (on the left), which serves to store, melt, and supply LBE to the loop; three vertical legs connected by two horizontal sections. The left vertical leg contains a 27 kW rod-type electric Main Heater (MH) – composed of a single pin with Outer Diameter (OD) 8.2 mm and heated length 870 mm – at the bottom (Figure 72a) and an expansion tank at the top. The right vertical leg hosts a counter-current HX (Figure 72b) at the top and an Electric Permanent Magnet (EPM) pump at the bottom (Figure 72c). The central leg contains a pool-type 3D Test Section (3D-TS).

The 3D-TS is a cylindrical, stainless steel vessel connected to the primary loop from the top and bottom (Figure 73a). It is equipped with a 15 kW band heater around the upper two-thirds of the section to promote thermal stratification in the LBE pool. A circular deflecting plate inside the section enhances pool mixing by redirecting the flow. The inlet tube has a smaller diameter (17/23 mm ID/OD) compared to the outlet (27.8/33.4 mm), consistent with the piping dimensions of the main loop.

Thermal insulation is provided by ISOVER Tape Lock 7300 and Nano T Ultra, with Nano T Ultra being used only around specific regions of the test section, while the rest of the loop is insulated with ISOVER Tape Lock 7300.

In Figure 73b, the TCs inside the 3D-TS are reported for a generic plane “x” of the four measuring planes present. To compare in a single plot the TCs experimental data with the simulation results and validate the pool modelling, an ordered vector has been constructed considering only the instruments in the fluid with the following order: CIP, BP, IPT, ILW.

In normal operation, LBE flows downward in the HX leg, upward in the MH and the 3D legs. However, during transients, the flow direction in all legs can reverse, depending on the heater power and initial conditions.

The secondary loop is a closed system utilizing Dowtherm RP, a synthetic organic heat transfer fluid, to cool the primary loop. The fluid circulates clockwise (referring to Figure 71), starting from the oil tank, through a rotary pump, passing through the primary HX, and then through a secondary HX capable of removing up to 40 kW of heat before returning to the oil tank.

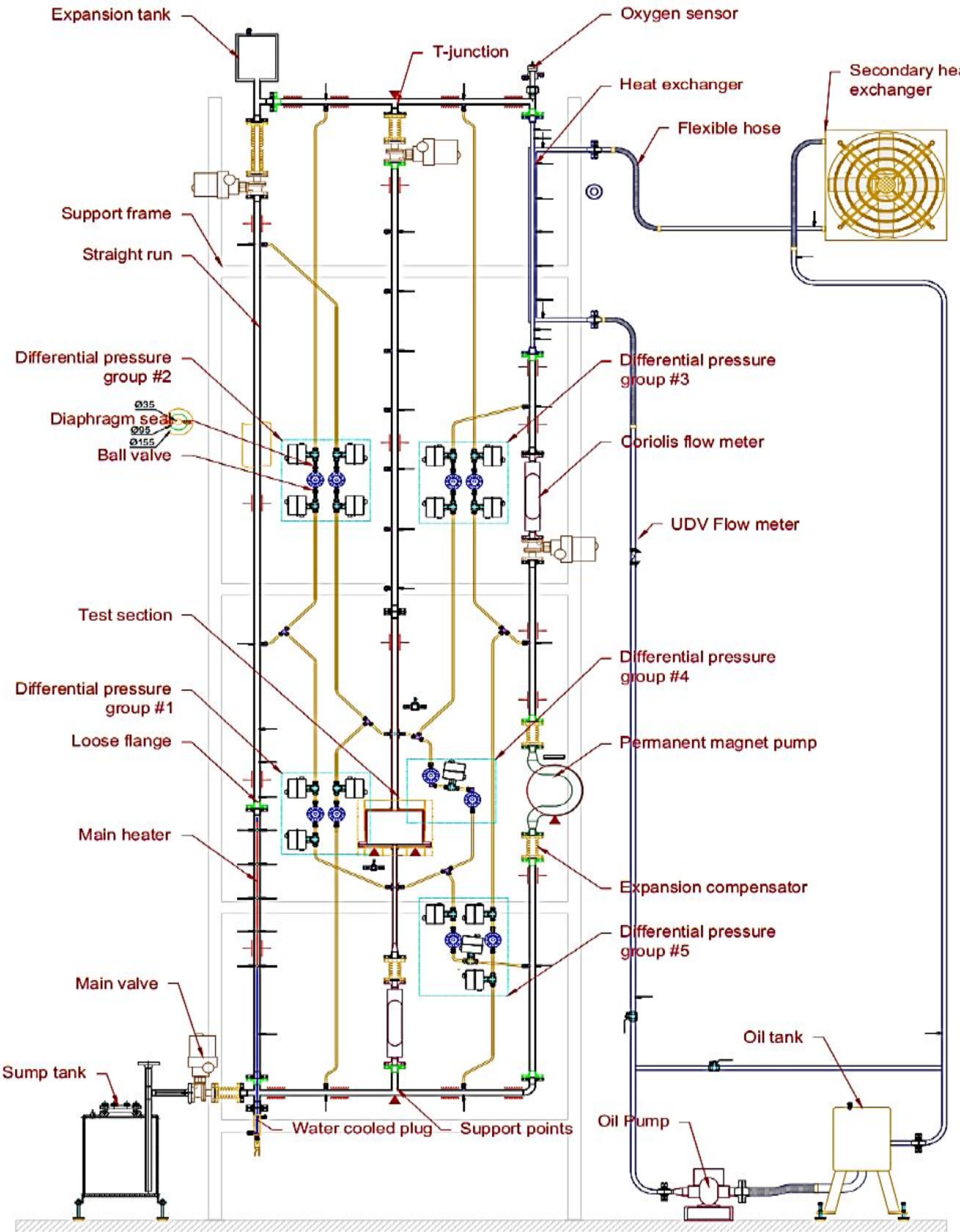

Figure 71 – TALL-3D facility main components [141]

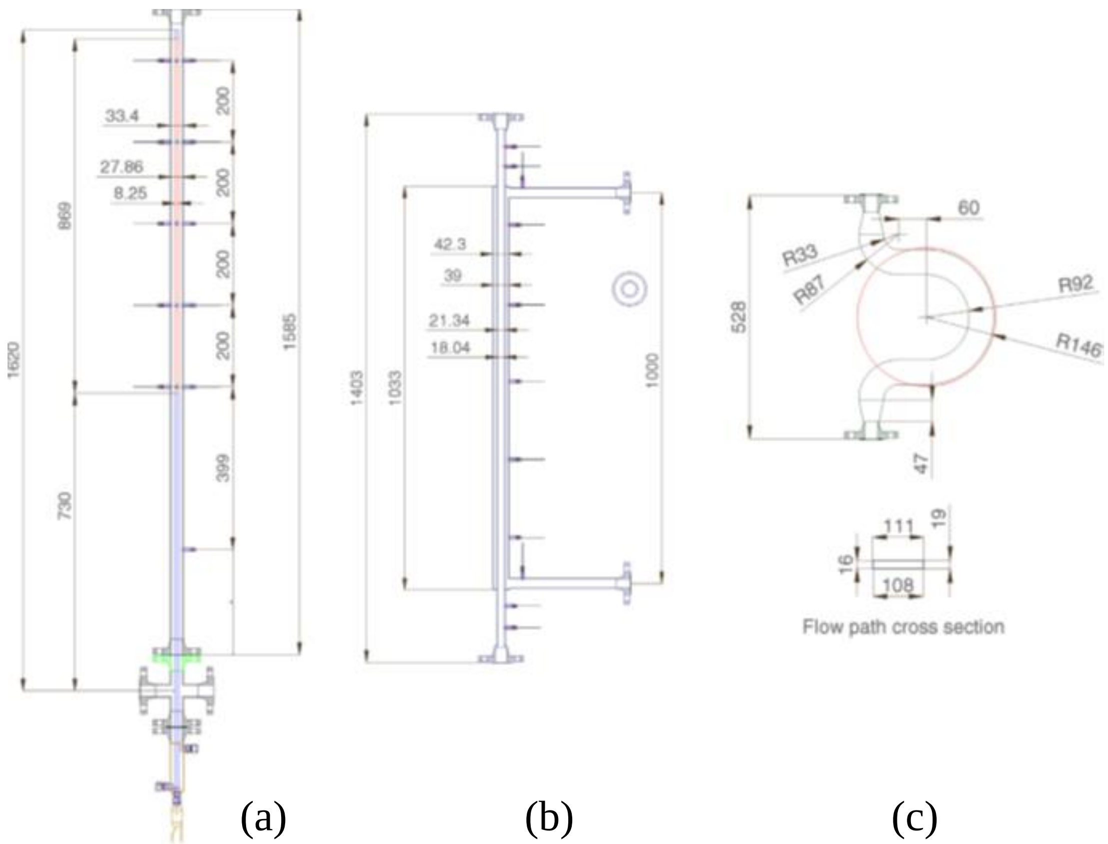

(a) (b) (c)

Figure 72 – Design drawings of main loop components: main heater (a), heat exchanger (b), LBE pump (c) [141]

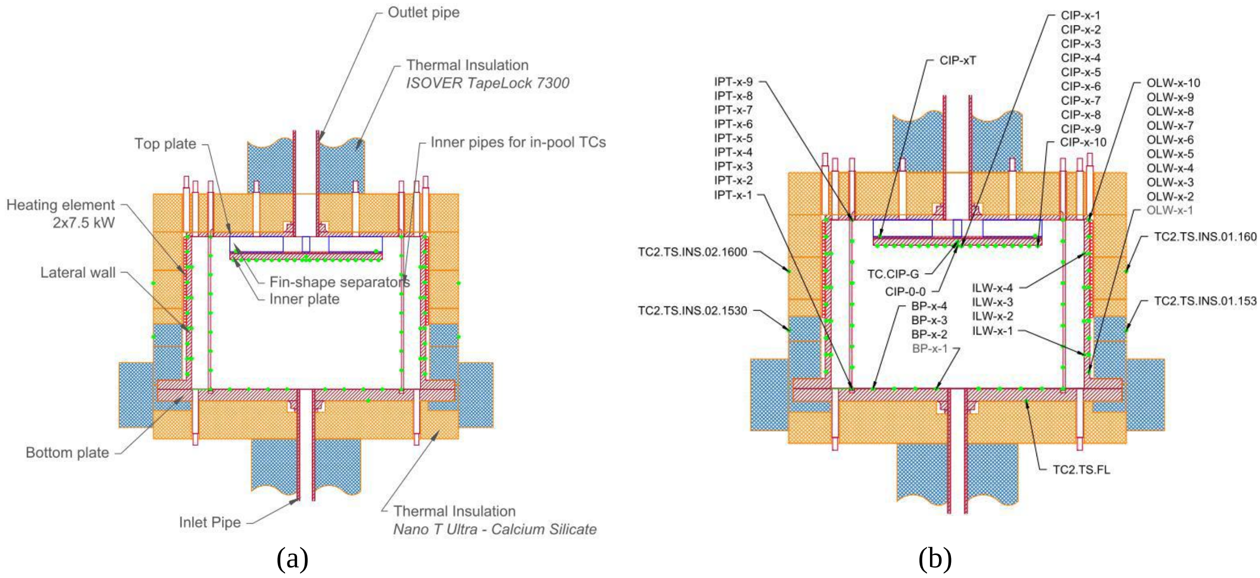

(a) (b)

Figure 73 – TALL-3D test section: components (a) and thermocouples position and nomenclature (b) [141]

3.3.2 Experiment description

To validate the coupled tool, the transition from Forced to Natural Circulation (FC and NC, respectively) is analyzed, highlighting the importance of feedback mechanisms and the effectiveness of the coupling methodology used. The transient begins from a FC steady-state with a mass flow rate of 3.34 kg/s in the HX leg, which is split between the MH leg at 2.03 kg/s and the 3D-TS leg at 1.31 kg/s. During this phase, the MH and 3D-TS heaters are continuously operational, providing 3.2 kW and 4.0 kW of thermal power, respectively.

The theoretical basis of this experiment revolves around exploiting the three-dimensional effects within the 3D-TS. In particular, a counteracting effect occurs between the entering nozzle jet, which enhances mixing within the section, and the buoyant boundary layer on the heater wall, which promotes thermal stratification.

In forced steady-state circulation, the jet at the 3D-TS bottom is strong enough to mix the fluid inside the volume. Once the EPM pump is shut off, the mass flow rates in all legs decrease and the driving force for circulation shifts to temperature gradients between the hot and cold legs. The switch to natural circulation reduces the mixing effect of the jet and the development of thermal stratification within the pool [59].

The initial and final steady state conditions of this transient are outlined in Table 13 and correspond to the experimental test TG03.S301.04 conducted during the SESAME project's first test series [42].

Table 13 – Experimental test initial and final steady state conditions

Parameter	**Units**	**Initial steady state (FC)**	**Final steady state (NC)**
Main heater electric power	W	3234	3235
3D-TS electric power	W	4048	4027
Heat exchanger LBE mass flow rate	kg/s	2.03	0.25
3D-TS LBE mass flow rate	kg/s	1.31	0.27
MH down section LBE temperature	°C	234.5	202.0
MH top section LBE temperature	°C	246.5	283.92
HX top section LBE temperature	°C	250.2	280.0
HX down section LBE temperature	°C	236.0	211.9
3D-TS down section LBE temperature	°C	235.4	201.8
3D-TS top section LBE temperature	°C	254.1	294.7

3.3.3 Numerical models

<u>STH model</u>

The facility model [142] in RELAP5 employs a combination of PIPE, SINGLE JUNCTION, VALVE and PUMP components. A total of 380 fluid volumes are used to discretize the system, maintaining an average mesh length of 5 cm, with a mesh length-to-diameter ratio greater than 1. The "sliced modelling approach" [132] is applied to ensure that elements at the same height have equal lengths, optimizing the model for the natural circulation regime.

The primary loop's working fluid is LBE, and the free surface in the loop is set in PIPE 134. The BC for pressure is defined using TMDPVOL 140. As for the NACIE-UP case, the realization of the HLM-gas interface has been made possible thanks to a proper modification to the RELAP5 source code [84]. The EMP depicted in Figure 74 is modelled using the PUMP component in RELAP5, typically designed for mechanical pumps. Therefore, adjustments have been made to account for the power provided by the pump to the LBE.

To simulate pressure losses at T-junctions, loss coefficients are evaluated according to Ref. [134], and flow meters and ball valves are calibrated using the approach in Ref. [141]. On the secondary loop, since RELAP5 does not contain the Dowtherm RP thermo-physical properties, water has been used with proper operational adjustments, i.e., pressure has been slightly increased to avoid vaporization on the secondary side. TMDPVOLs and TMDPJUNs set BCs for temperature, pressure, and mass flow rate.

The heat transfer between fluids and solid structures, like heaters and pipes, is modelled using HEAT STRUCTURES components. Specifically, the MH and 3D-TS heaters are represented by structures with internal heat generation, while the heat transfer between LBE and the secondary fluid in the heat exchanger is modelled through a HS representing the thickness of the tube. To account for the different heat transfer properties of water and Dowtherm RP, a “fouling” factor has been inserted on the secondary side of the heat structure representing the HX tube, meaning that a multiplicative factor of the water side HTC (calculated by the code) makes the component exchange the correct power. While such a simplification can work in steady state conditions, discrepancy will arise during the transient because of the different thermo-physical and transport properties of the two fluids. Other solid structures (e.g., valves and flow meters) are treated as adiabatic to be representative of their thermal inertia. Insulation around the system accounts for heat losses, assuming a heat transfer coefficient of 8 W/m² °C and a surrounding temperature of 10°C.

For the coupled simulation, the system model is modified accordingly to the selected spatial discretization method, as outlined in the following subsection. This ensures a proper variable exchange and BC impositions between CFD and RELAP5 in coupled simulations.

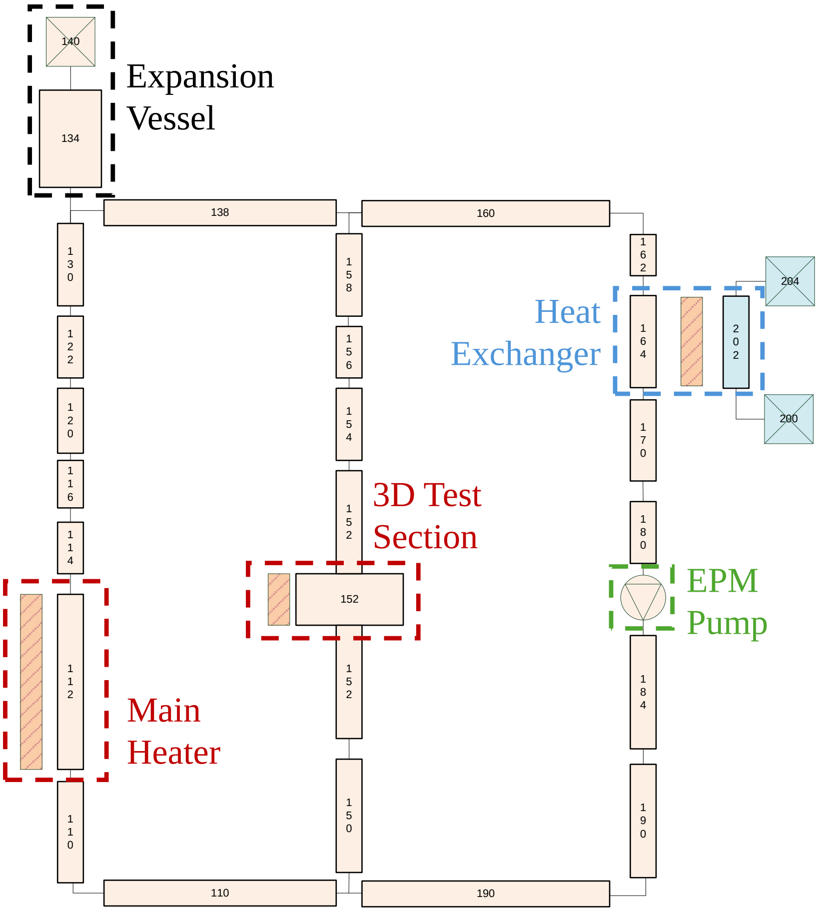

Figure 74 – RELAP5 nodalization of TALL-3D facility

CFD model

The CFD model of the 3D-TS takes advantage of the quasi-axisymmetric conditions of the pool to simplify the simulation. Although features like fin-shaped separators and TCs do break the axisymmetry, their effect has been neglected because of their small volume compared to the test section and their limited impact on the flow. Since the TCs are placed symmetrically along four equally spaced planes, axisymmetric experimental data to be compared with the CFD results is obtained by averaging the measurements from these planes.

To account for uncertainties, a total experimental error (σ_{tot}) is computed as:

$$\sigma_{tot} = \sqrt{\sigma_{man}^2 + \sigma_{sym}^2 + \sigma_{std}^2} \tag{44}$$

where:

- σ_{man} is the manufacturer's accuracy, and it is equal to 1.5°C.
- σ_{sym} is the standard deviation among the four measuring planes. It indicates the agreement between the four measuring planes, i.e., symmetry.
- σ_{std} represents the dispersion, i.e., the oscillations in the measurement. It is computed as the square root of the sum of the squared standard deviations from the steady-state interval.

The setup for the CFX simulation includes the following features:

- The CFD domain includes the fluid, the AISI 316L steel for the structure and heaters (even though they are not actually made of steel), and the insulation. Material properties for LBE come from the Handbook of Liquid Metals [137], while steel properties come from Ref. [143], and insulation data from Ref. [141].
- BCs are defined at the top (Up) and bottom (Down) sections. A uniform mass flow rate is imposed at the bottom, and a zero relative pressure boundary at the top.
- Buoyancy forces are included.
- A uniform volumetric heat source is applied in the heater's domain.
- The SST $k - \omega$ turbulence model [144] is used with a constant turbulent Prandtl number of 2 [140]. Sensitivity tests with values between 1.5 and 3 showed negligible impact.
- The upwind advection scheme is used in the solver.

The axisymmetry can be modelled in CFX using either a 2D or 3D approach. The 2D approach involves a single azimuthal cell, and periodic or symmetry BCs can be applied at azimuthal boundaries. On such a model, a grid independence study has been carried out with the BCs corresponding to the first steady state of the transient described in Sect. 3.3.2. Results reported in Table 14 show that the global quantities variation is almost the same among the three meshes, but local temperatures corresponding to the TCs' positions change with the number of cells. "Mesh 2" has been selected since the maximum temperature difference with respect to the reference "Mesh 1" is lower than the TCs accuracy proposed by the manufacturer.

Table 14 – Grid independence study of the 2D model of the 3D Test Section

Quantities	**Unit**	**Mesh 1**	**Mesh 2**	**Mesh 3**
N° of cells	-	187.5 k	109.2 k	38.9 k
Temperature Up section	°C	256.1	256.1	256.1
ΔP	Pa	1001	1011	999
Average Temperature error at the TCs with respect Mesh 1	°C	-	0.15	0.62
Maximum TCs error respect Mesh 1	°C	-	1.11	6.88

The same "Mesh 2" setting parameters of the azimuthal faces (see Figure 75) have been adopted when generating all the other non-3D models. To evaluate the impact of using 2D vs 3D modelling, simulations were performed adopting 3° and 90° circumferential angles, with different numbers of radial points (5 for 3° and 150 for 90° cases, respectively). A symmetry BC has been adopted for both the models, while a periodic BC has been tested on the 3° model only.

Results of Figure 76 and 77 show that the temperature trends within the 3D-TS are well captured by all models both in the initial and final steady states, except for the ILW TCs at the initial steady state. However, the error remains below 10°C, and discrepancies among the presented cases are negligible in terms of temperatures and pressure drop across the TS. Given these results, the 2D model was chosen for the coupled simulation to minimize computational cost.

It has been observed that such a model does not accurately represent the thermal losses through the insulation, primarily due to the thermal bridges at instrumentation penetration points across the insulation. This was particularly evident in the horizontal surfaces of the 3D-TS, especially on the top surface. To address this, a modified insulation model with increased thermal conductivity (equal to the mean value between insulation and steel) was applied, resulting in improved agreement with experimental temperature measurements, particularly in the final steady state. The model is labeled as "2D Improved" in Figure 76 and 77, and it is taken as the reference model for the following simulations.

Figure 78 and 79 show the temperature distributions during these steady states, demonstrating the capability of the code to reproduce the pool mixing condition during the initial steady state due to the inlet jet, and the thermal stratification in the final state, except for the region near the inlet.

After the assessment of the model in steady state conditions, a transient simulation with BCs based on experimental data (i.e. mass flow rate, inlet and outlet temperatures) has been performed to evaluate the model's ability to simulate the pool's behavior over time. Figure 80 shows the temperature evolution at the upper (Up) and lower (Down) 3D-TS boundaries. In the transient phase, both models (with and without corrections for thermal conductivity) demonstrated good qualitative agreement, though the "Mesh 2" model overestimated the peak temperature at the "Up" boundary, while the "2D Improved" model showed better overall agreement throughout the transient. Therefore, the "2D Improved" model has been deemed satisfactory for use in the CFD-STH coupled tool, being able to capture steady and transient behaviors of the system.

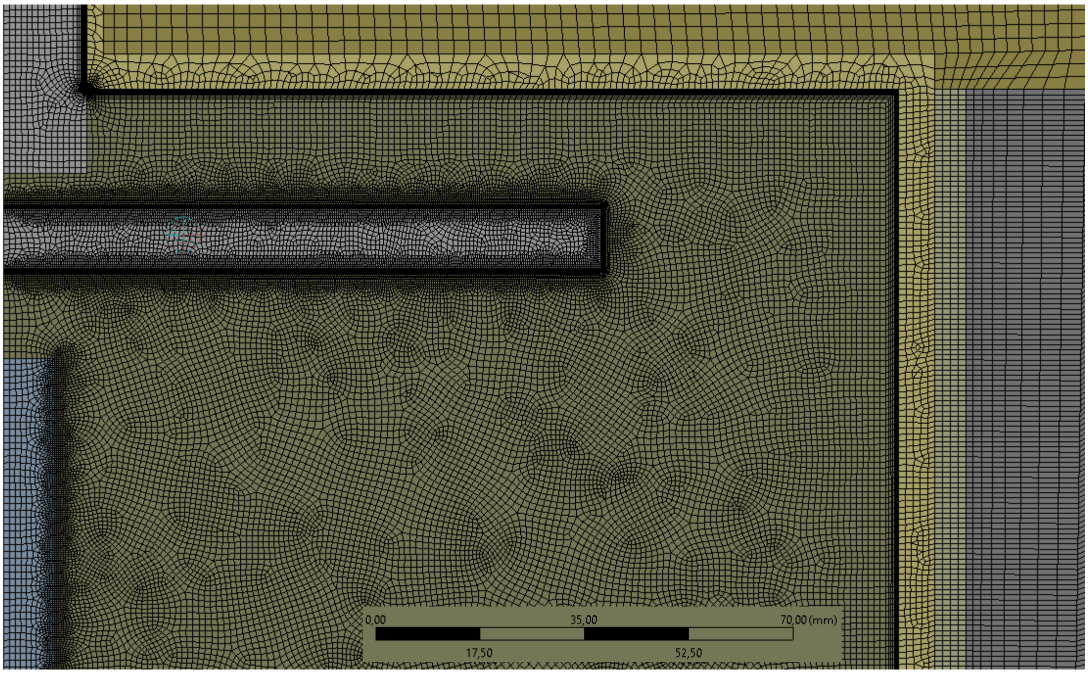

Figure 75 – Detail of the discretization in "Mesh 2"

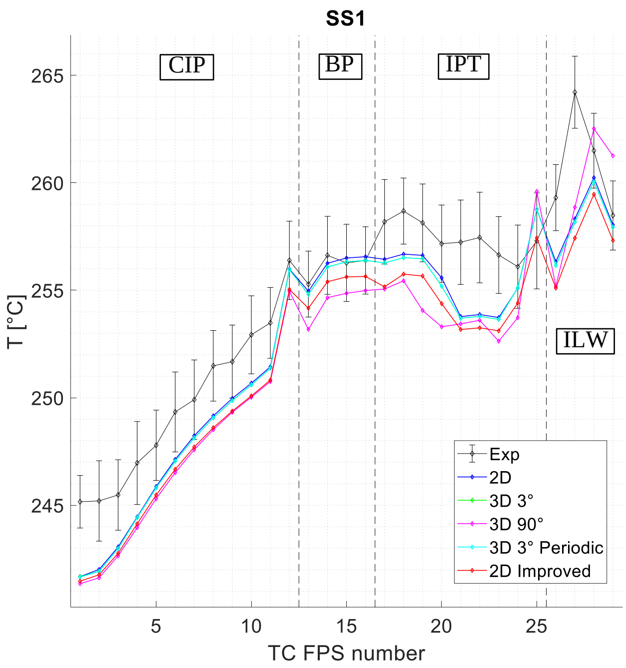

Figure 76 – Comparison between CFD and experimental data of the different modelling approaches of the 3D-Test Section during the initial steady state

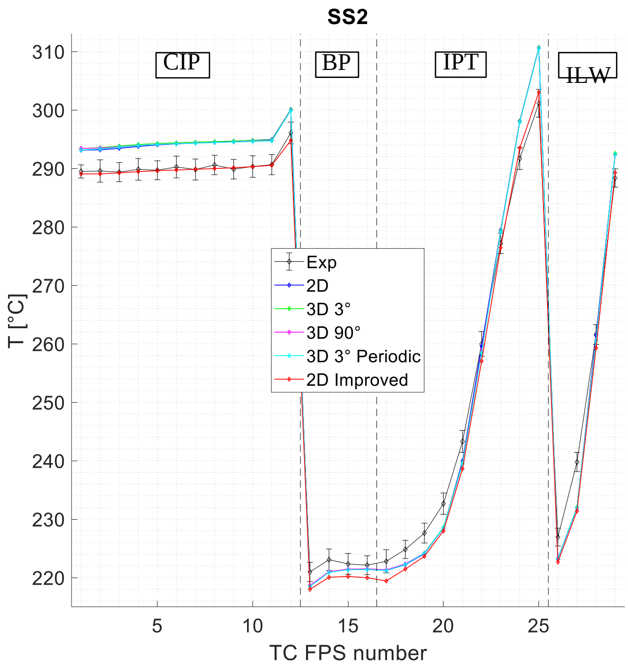

Figure 77 – Comparison between CFD and experimental data of the different modelling approaches of the 3D-Test Section during the final steady state

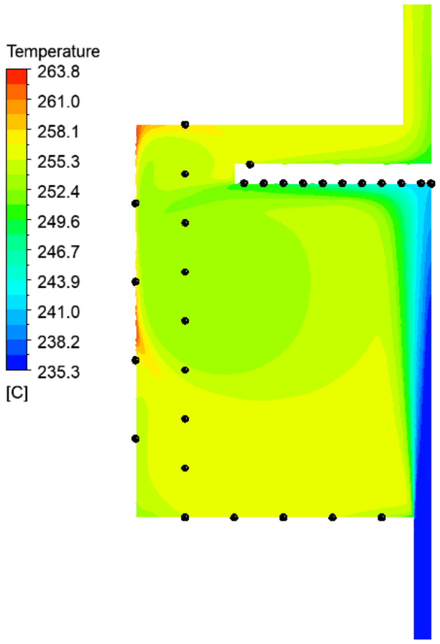

Figure 78 – Temperature distribution inside the 3D-Test Section during the initial steady state with the 2D improved model

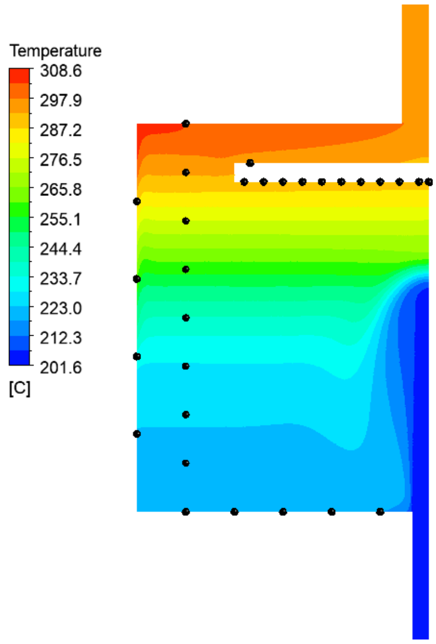

Figure 79 – Temperature distribution inside the 3D-Test Section during the final steady state with the 2D improved model

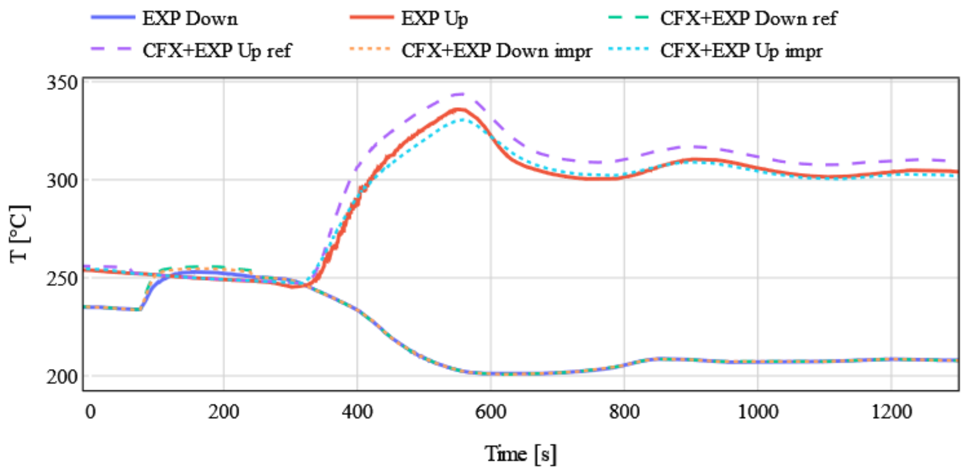

Figure 80 – Transient simulation with the Ansys CFX model and boundary conditions from experimental results

STH/CFD coupled model

To test all the coupled approaches described in Sect. 2.5 and 2.6, two coupled models have been developed to simulate the transient behavior of the TALL-3D facility, and explicit and semi-implicit simulations have been carried out with each model. Moreover, the domain overlapping model has been tested using the "friction factor" and the "K" approaches.

The model for the domain decomposition has been realized by replacing the 3D-TS with TMDPVOLs and TMDPJUNs in the RELAP5 model, and imposing BCs from the CFD calculations. In particular, RELAP5 receives the mass flow rate, temperature and pressure, while CFX receives the mass flow rate and temperature at the boundaries. Pressure imposed in the RELAP5 domain is calculated following the approach of Eq. (43), and the data exchange approach is analogous to the one presented in Figure 56. As for the NACIE-UP simulations, non-dimensional velocity and temperature maps were applied to the 1D RELAP5 results at the CFD inlet. CFD results were averaged to obtain 1D results to be passed to RELAP5.

The model for the domain overlapping approach has been realized by adding three HSs to match the temperatures at the boundaries, as well as the average temperature of the overlapped domain (see Sect. 2.6.2 for further details). Therefore, no exchange of mass flow rate or temperature occurs at the boundaries, but the pressure drop is considered when adjusting the friction factor or the localized pressure loss coefficient.

A first comparison involves the domain decomposition approach, in which both the explicit and semi-implicit methods have been tested, considering different coupling timesteps (i.e., 0.5, 0.1, and 0.02 s). To compare the results, the mass flow rate in the 3D-TS leg has been considered in Figure 81, 82, and 83. The simulations are labeled in the legends in the following way:

- "deco" or "over" indicate domain "decomposition" or "overlapping" approach.
- "f" or "K" indicate if the "friction factor" or "localized pressure drop coefficient" methods are used in the domain overlapping approach.
- "ex" or "si" refer to "explicit" or "semi-implicit".

The explicit scheme (see Figure 81) shows noticeable numerical oscillations when using a large timestep (e.g., 0.5 s) at the start of the transient. However, by decreasing the timestep, these oscillations can be eliminated. On the other hand, with the semi-implicit scheme, no oscillations are observed, and any oscillations that arise in the explicit scheme tend to dampen quickly. After this initial phase, the results from both schemes are almost identical.

A major discrepancy between the two schemes appears during the rapid drop of the mass flow rate due to the magnetic pump shutdown. Here, lower timesteps tend to give lower values in the first mass flow rate minimum. Despite this, the results of the explicit and semi-implicit schemes converge among each other after about 100 seconds, with no significant differences noted thereafter.

In terms of computational efficiency, as detailed in Table 15, the semi-implicit scheme takes roughly 1.5 times longer to compute compared to the explicit scheme. All the simulations have been run on 24 CPUs with the same solver setup. This is due to the number of iterations of the same timestep required to achieve the convergence between the CFX and RELAP5 results. However, it is emphasized that the comparison between the two time advancing schemes should be performed considering also that the semi-implicit one allows to adopt larger timesteps then the explicit ones, and that the number of iterations tends to 1 (as the explicit case) when a steady state is approached.

When comparing the domain overlapping approach (both explicit and semi-implicit) at different coupling timesteps, minimal differences are observed (see Figure 82). The only notable issue occurs with the explicit scheme at high timesteps, where mass flow rate distortions are seen when the velocity approaches zero and inverts, causing spikes due to discontinuities in friction factor calculations. The comparison with the domain overlapping with the "K" approach also shows negligible differences, suggesting that both formulations are valid.

Compared to the domain decomposition approach, the overlapping one showed no oscillations in the results, while the computational time is similar (not reported in Table 15). Finally, Figure 83 illustrates the results obtained using a timestep of 0.1 s for the explicit and semi-implicit schemes applied to the domain decomposition and both the overlapping approaches. The solution variance across these methods is minimal, demonstrating that the results are largely independent of the coupling approach used.

Table 15 – Computational time with the domain decomposition approach at different timestep for the explicit and semi-implicit time advancing schemes

Coupling timestep	Explicit	Semi-implicit	Semi-implicit/explicit ratio
2e-2 [s]	5.399e5 [s]	7.618e5 [s]	1.41
1e-1 [s]	1.336e5 [s]	2.186e5 [s]	1.64
5e-1 [s]	4.092e4 [s]	6.461e4 [s]	1.58

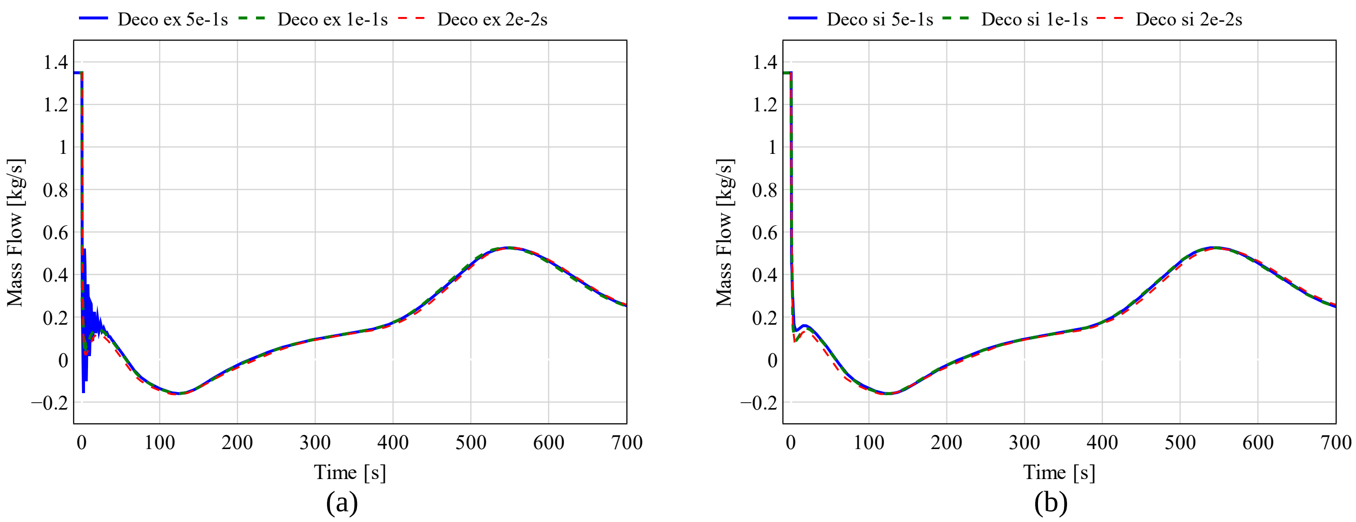

Figure 81 – Coupled simulations with the domain decomposition approach at different coupling timestep with the explicit (a) and semi-implicit (b) time advancing schemes

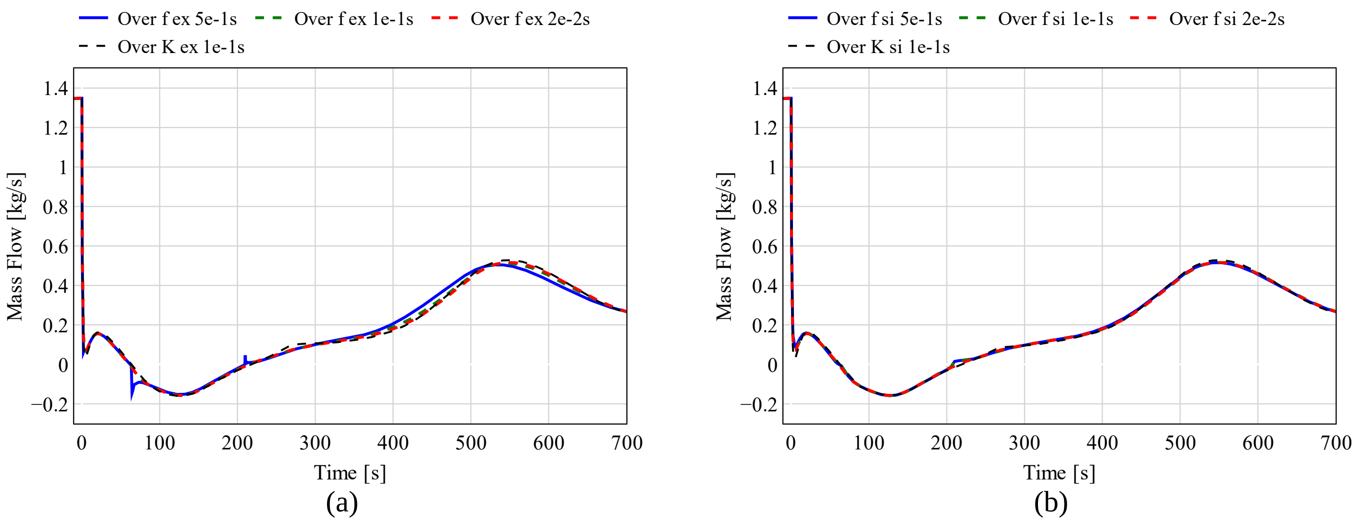

Figure 82 – Coupled simulations with the domain overlapping approach at different coupling timestep with the explicit (a) and semi-implicit (b) time advancing scheme

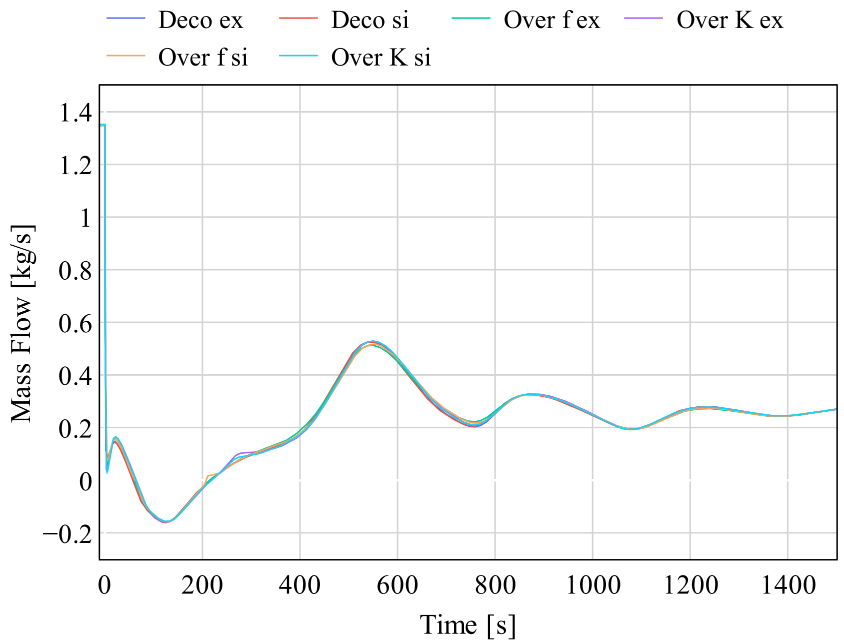

Figure 83 – Overlay of the mass flow rate in the 3D test section leg for all presented coupling approaches with a timestep of 0.1 s

3.3.4 Simulation results

System-level analysis

The comparison between the coupled CFD-RELAP5, the experimental data and the stand-alone RELAP5 simulation highlights several key improvements in representing the phenomena in the test section (local), as well as at a system level. The CFD contribution brings significant advantages, especially in capturing the oscillatory behaviour of mass flow rates and temperature variations more accurately than the stand-alone RELAP5. As a reference case, the semi-implicit simulation with the domain decomposition and a timestep of 0.1 s has been selected.

Figure 84 shows improvements with the coupled simulation (decomposition approach) in reproducing the frequency of the experimental oscillations of the mass flow rate in the 3D-TS, even though their amplitude is slightly higher than the numerical ones. Similar conclusions can be drawn from analyzing the mass flow rate on the MH leg (Figure 85), with a notable improvement in the phenomena representation by the coupled approach.

The reason for these improvements can primarily be attributed to the temperature at the 3D-TS model boundaries (see Figure 86):

- The first rise of the temperature at the lower section due to the inversion of the mass flow rate is well predicted by the CFX-RELAP5 tool, demonstrating a good representation of the initial steady state conditions inside the test section and the good prediction of flow reversal. However, the absolute value is underpredicted by both the coupled and stand-alone simulations for the remaining part of the transient, probably because of the use of a different secondary fluid in the HX instead of the Dowtherm RP fluid, causing different performances of the component.
- The temperature at the upper section is slightly underpredicted at the peak mainly because of the lower inlet temperature, plus the slight underestimation visible in Figure 80. However, an improvement in the representation of the oscillation frequency is visible.
- At the final steady state, the temperature variation across the 3D-TS is slightly lower in the experiments because of a slightly higher mass flow rate.

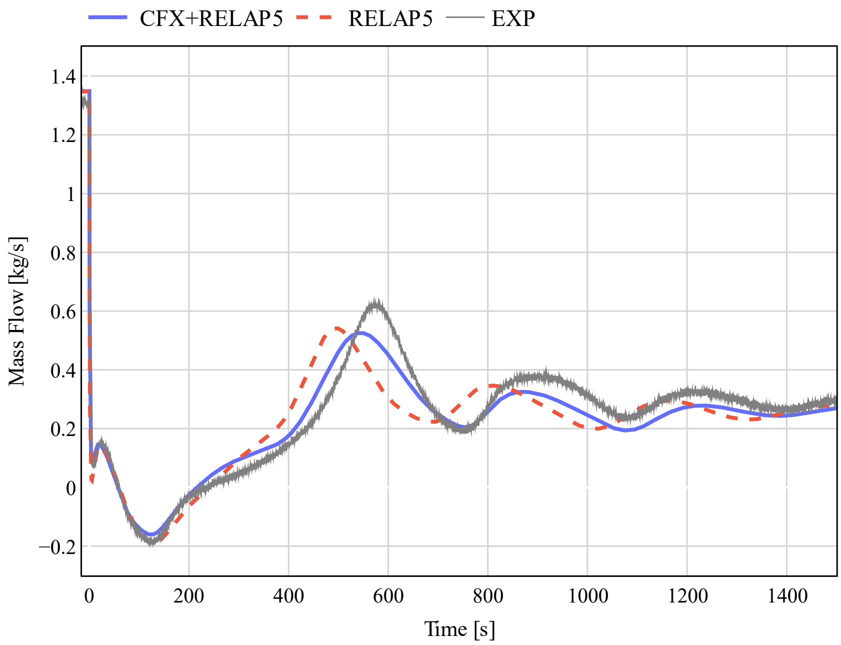

Figure 84 – Comparison between experiment, RELAP5 stand-alone and coupled simulation of the mass flow rate in the 3D test section leg

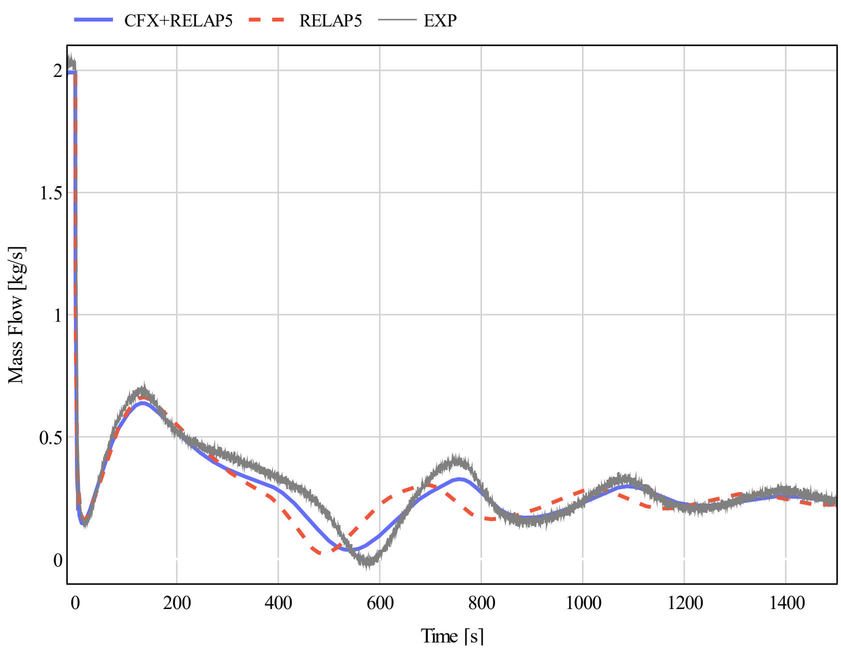

Figure 85 – Comparison between experiment, RELAP5 stand-alone and coupled simulation of the mass flow rate in the Main Heater leg

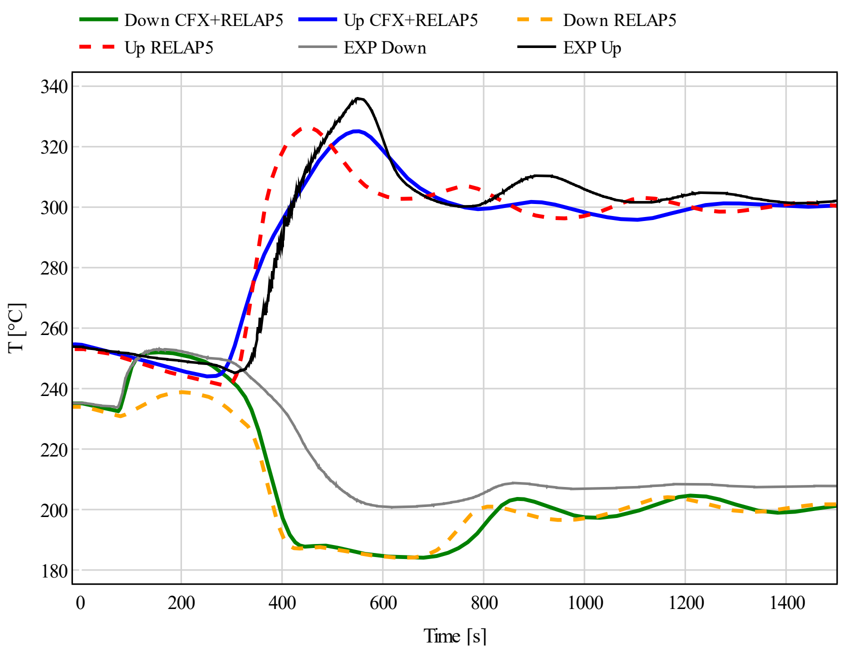

Figure 86 – Comparison between experiment, RELAP5 stand-alone and coupled simulation of the upper and lower surface temperature of the 3D test section

<u>3D-TS detailed analysis</u>

As highlighted also for the NACIE-UP FPBS, the coupled RELAP5-CFX tool allows for a comparison of temperature trends at a local (CFD) level. In this case, temperatures inside the pool during transient conditions can be compared with simulation results. The IPT TCs, which are mounted on vertical supports covering the pool height (see Figure 72a), provide data for comparison with simulation results. Figure 87 shows that the decomposition approach for the simulation demonstrates good agreement with experimental data, particularly in the upper region of the pool (TCs IPT 1-3), which is closer to the heaters.

Looking at the TCs in the lower part of the pool, temperatures are underpredicted. The reason can be found in the following:

- A poor local prediction of the thermal losses, which gain more importance when the mass flow rate is reduced.
- A slightly worse performance of the CFD model in the transition from a convective to an almost fully conductive-dominant heat transfer condition within the fluid.
- The underestimation of the temperature entering the pool from the lower section.

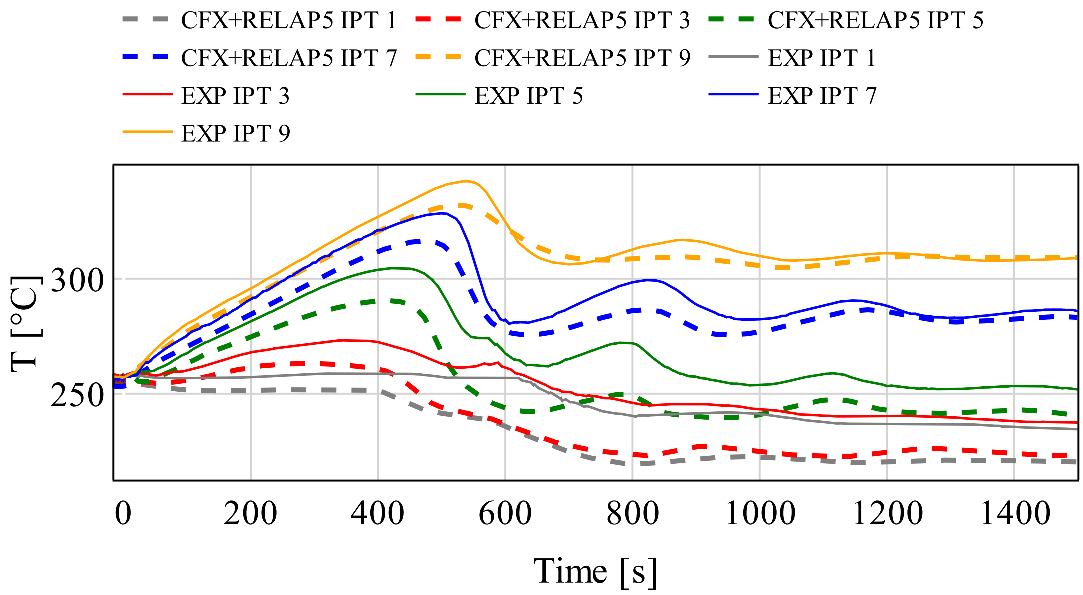

Figure 87 – Comparison between experiment and coupled (domain decomposition) simulation of thermocouples inside the 3D test section

3.4 Preliminary qualitative code assessment

Since the RELAP5/Mod3.3 stand-alone and the coupled tool have been used to simulate experiments across various facilities with different working fluids, it is useful to provide a qualitative evaluation of the codes' performances in representing the key phenomena observed in those experiments. This section contains a preliminary qualitative code assessment, emphasizing that the analyses proposed in Sects. 3.1, 3.2, and 3.3 were conducted to test the modified RELAP5/Mod3.3 version and the coupled tool against experimental data from facilities relevant to LFRs development. However, a comprehensive validation process for the tool will be required as new experiments involving additional phenomena and geometries are conducted.

Table 17 provides a qualitative evaluation of both the experimental facilities and codes' accuracy. Each facility is characterized by its working fluid, with two columns per facility assessing (i) the occurrence and measurement quality of the phenomena observed in the experiments ("Exp") and (ii) the accuracy of the numerical prediction ("Calc"). This evaluation is based on the legend outlined in Table 16. In particular, the phenomena are classified according to their occurrence in the experiment and the quality of their measurement, while the codes' accuracy is assessed on the basis of their capability to predict these phenomena. Table 17 has been compiled following the guidelines of the CSNI code validation matrices [145] [146] [147] [148].

Several thermal-hydraulic phenomena relevant to LFRs have been identified and grouped into the following macro-categories:

- A: Fluid flow characteristics (e.g., natural circulation, two-phase flow).
- B: Heat transfer (e.g., Boiling and condensation).
- C: Pool behavior (e.g., mixing, thermal stratification).
- D: Fuel assembly thermal-hydraulics (e.g., inter-wrapper flow, subchannel heat transfer).
- E: Inter-pool heat transfer (i.e., heat transfer between two pool regions, typical of LFR configurations).
- F: Thermal-hydraulic nuclear feedback (i.e., neutronic feedback on core thermal-hydraulics).

It is important to note that phenomena belonging to group E and F are absent in the analyzed facilities, despite being relevant for the LFR development. Experimental facilities focused on these phenomena are needed for a more thorough investigation and validation of numerical tools. ATHENA facility will address some of these aspects such as the inter-wrapper flow thanks to the core simulator geometry and instrumentation, while the inter-pool heat transfer will be only partially studied, since ATHENA envisages a configuration similar to ALFRED, but the instrumentation is currently not able to fully characterize such heat transfer mechanism.

For the sake of compactness, Table 17 merges assessments of facilities with different working fluids (LBE and water must be considered separately). Therefore, a good experimental investigation or good numerical prediction of a particular phenomenon in one fluid do not imply validation across all fluids. For instance, an accurate modelling of the thermal stratification in water pools does not ensure representativeness in LBE pools, and vice versa.

SIRIO facility – working with water and steam/air mixture – encompasses several phenomena such as single phase natural circulation to two phase flow, boiling (in pool and tubes), and condensation with and without non-condensable gases. The most reliable measurements in this facility are temperature and pressures, thus the comparison with numerical results should be limited to such quantities, while specific phenomena (e.g., water and steam/air interaction) should be evaluated through dedicated experiments. Overall, the modified version of the RELAP5/Mod3.3 code provided good to reasonable predictions of the phenomena, effectively representing the experiment. Nevertheless, additional tests are required to better understand certain aspects, such as the details of the condensation in presence of non-condensable gases at high pressure.

The NACIE-UP and TALL-3D facilities – working with LBE – primarily investigate the transition from forced to natural circulation regimes. However, their objectives differ:

- NACIE-UP is mainly devoted to the fuel assembly thermal-hydraulics. From the numerical perspective, the CFD contribution has provided significant insights in the coupled simulations, enabling the characterization of eventual hot spots and flow distribution among the subchannels.
- TALL-3D focuses on pool behavior characterization, specifically the transition from the pool mixing to thermal stratification inside the 3D test section. The coupled tool significantly enhanced the system level prediction by capturing the frequency of the mass flow rate oscillations and providing a detailed local representation of the temperature field within the pool.

These preliminary considerations emphasize the significance of the coupled approach and support the validation of the coupled tool carried out in Sect. 3, which is considered acceptable for the scope of this thesis. The coupled tool is then applied in Sect. 4 to perform pre-test simulations of the lead-cooled ATHENA facility.

Table 16 – Legend for the experimental facility and code qualitative phenomena prediction evaluation

	+	o	NA	-
Experimental data	Phenomenon occurred in the test and it is directly measured	Phenomenon occurred in the test and it is indirectly measured	Phenomenon occurred during the test but there is no instrumentation to detect (lack of instrumentation)	Phenomenon not occurred in the test
Calculated data	Phenomenon is clearly predicted by the code (**Excellent/ Reasonable**)	Phenomenon is partially predicted (i.e. the answer of the code is **reasonable** but closure relations are not appropriate, etc.)	Models are not appropriate to predict (i.e. nodalization strategy, etc.) (**Minimal**)	Phenomenon is not predicted by the code (**Unqualified**)

Table 17 – Preliminary qualitative experimental facility and code accuracy evaluation

Phenomenon	Fluid / Experimental facility	Water		LBE			
		SIRIO		NACIE-UP		TALL-3D	
		Exp	Calc	Exp	Calc	Exp	Calc
A1	*Natural circulation in one-phase flow*	o	o	+	+	+	+
A2	*Natural circulation in two-phase flow*	o	o	-	-	-	-
A3	*Thermo-fluid dynamics and pressure drops in various geometrical configurations*	o	o	o	+	+	+
A4	*Transition from forced to natural circulation regime*	-	-	+	+	+	+
A5	*Liquid/non-condensable mixture behavior*	o	o	o	o	-	-
A6	*Countercurrent liquid/non-condensable mixture behavior*	NA	o	-	-	-	-
B1	*Pool boiling heat transfer*	o	o	-	-	-	-
B2	*Flow boiling heat transfer*	o	+	-	-	-	-
B3	*Condensation heat transfer*	o	o	-	-	-	-
B4	*Convection heat transfer in presence of non-condensable gases*	o	o	-	-	-	-
B5	*One-phase turbulent heat transfer*	+	+	+	+	+	+
B6	*One-phase transition heat transfer*	-	-	+	o	-	-
C1	*Behavior of pool: thermal stratification*	+	+	-	-	+	+
C2	*Behavior of pool: mixing*	-	-	-	-	+	+
C3	*Behavior of pool: natural convection*	o	+/o	-	-	+	+
D1	*Behavior of the fuel assembly in subchannels*	-	-	+	+	-	-
D2	*Behavior of the fuel assembly: inter-wrapper heat transfer*	-	-	-	-	-	-
E	*Inter-pool heat transfer*	-	-	-	-	-	-
F	*Thermal-hydraulic nuclear feedback*	-	-	-	-	-	-

4 MULTISCALE SIMULATION OF ATHENA INTEGRAL TEST FACILITY

In the previous sections, the development and validation of the coupled RELAP5/Ansys CFX tool were thoroughly explored. Sect. 2 detailed the coupling methodology, which combines the RELAP5 system-level simulations with the detailed CFD modelling of Ansys CFX. Two spatial discretization approaches – domain decomposition and overlapping– were implemented, along with two time advancing schemes, namely the explicit and semi-implicit schemes.

In Sect. 3, the coupled tool was validated against experimental data from facilities like NACIE-UP and TALL-3D, demonstrating its accuracy in predicting mass flow rates, temperature profiles, and transient behaviors. The validation emphasized the tool’s enhanced performance compared to RELAP5 stand-alone simulations in capturing complex flow and heat transfer, especially in components such as the FPBS and the 3D-TS, where the 1D approximation of STH codes is generally not applicable.

Sect. 4 now shifts its focus to applying this validated coupled tool to the ATHENA integral test facility, designed to support the ALFRED development. After a presentation of the facility in Sect. 4.1, Sect. 4.2 deals with the description of the numerical models developed with RELAP5/Mod3.3 and Ansys CFX, as well as the coupling technique adopted for the ATHENA simulations. Sect. 4.3 includes the design of the Main Heat eXchanger (MHX), along with its verification with the RELAP5 code. Then, RELAP5 simulations of both steady state and transient conditions, including accidental scenarios like the LOHS [149] and LOFA, have been carried out. Moreover, the results of the LOFA transient will be compared to the coupled tool results to assess its capability of reproducing relevant TH phenomena in a LFR core for reactor safety analysis.

4.1 Description of the facility

ATHENA is a large-scale, multipurpose pool-type facility with an installed power of 2.21 MW, utilizing pure lead as the primary coolant and pressurized water in the secondary cooling system. Its main vessel, which measures 3.2 meters in diameter and 10 meters in height, is designed to accommodate tests of LFRs components at a representative scale, allowing for reliable replication of the key TH phenomena that occur in large lead-cooled pool-type reactors. The facility is specifically intended to simulate the lead thermal cycle envisioned for the ALFRED reactor, following a staged operational approach.

The design of ATHENA benefits from ENEA’s extensive experience, particularly from prior design activities and experimental work carried out on the CIRCE (CIRColazione Eutettico, Eutectic Circulation) facility [150], both in its HERO (HEavy liquid metal – pRessurized water cOoled Tube) [151] [152] [153] and THETIS (Thermal-hydraulic Helical Tubes Innovative System) [154] [155] configurations, located at the ENEA Brasimone Research Centre.

The ATHENA facility offers extensive capabilities for investigating various aspects of LFR technologies. It enables studies on pool TH, heat transfer in the Inter-Wrapper (IW) region within a multi-assembly core, HX performance, and the assessment of Main Circulation Pump (MCP) behavior under both normal and transient conditions. In addition, ATHENA serves as a platform for safety-related tests, such as simulating a heat exchanger tube rupture or a FA partial blockage. These tests will generate a valuable database of experimental data for code validation and facilitate R&D investigations related to lead technology, including full-scale component testing.

The ATHENA facility also plays a crucial role in the experimental platform being developed in Romania to support the licensing process for LFR technologies, as already mentioned in Sect. 1.3. This platform aims to understand the key TH phenomena in pool systems, qualify materials, test the operational stages of ALFRED, and validate simulation computational tools [32] [86] [156]. ATHENA is dedicated to advancing HLM-based technologies through the testing of relevant-scale systems and components, the investigation of operational and accidental TH phenomena (such as natural circulation and coolant stratification), and the evaluation of chemistry control capabilities in large pool systems.

4.1.1 Primary system

The ATHENA primary system is composed of a large pool containing pure lead as the primary coolant and is coupled to the secondary system through the MHX, which uses pressurized water as the secondary coolant. Inside the main vessel, an internal vessel, named barrel, is placed to ensure efficient lead circulation, promoting mixing and maintaining a uniform thermal profile within the cold pool. At the bottom of the vessel, cold lead at 400°C enters through the feeding conduit into the Core Simulator (CS), where it is heated up to 480 or 520°C, depending on whether ALFRED Stage 2 or 3 is reproduced. Figure 88 shows pictures of the main vessel and the storage vessel, respectively.

The total power of 2.21 MW is provided by an electrically heated CS (see Figure 89 and 90) that comprises 126 heated pins and one central dummy, with the diameter and pitch of the fuel pins based on those of the ALFRED reactor [156]. The electrical power is representative of an average ALFRED's FA. However, in ATHENA, the pins are arranged in a central hexagonal assembly and six peripheral trapezoidal assemblies. This layout allows for detailed investigations of lead flow in the IW region and heat transfer within the central assembly and among the other FAs, providing the peripheral ones with realistic BCs.

The active length of each pin in the CS is 810 mm, while the total pin length in the lead is 3115 mm, measured from the bottom grid, which maintains the pins in their correct positions, to the flange that seals the lead from the dead volume. In addition to the bottom grid, the pin bundle is secured by an upper grid and three spacer grids, ensuring structural stability throughout the entire assembly. Figure 91 shows the design of these spacer grids for the various assemblies. Additional parameters of the CS engineering design are listed in Table 18.

From the CS, hot lead flows into the fitting volume, passes through the riser, where it is pushed by the vertical axial MCP (see Figure 92) toward the hot pool. From there, lead enters the MHX, which is of a BT type, each one composed of three concentric tubes (see Figure 93 and 94), with 3 meters submerged in the lead. According to the design reported in Sect. 4.3.1 and in Ref. [157], the tube bundle consists of 91 BTs with an active length of 3 meters submerged in lead. This length is essential to maintain the same height difference between the thermal barycenters of the heat source (CS) and the heat sink (MHX), i.e. about 3.3 m, ensuring consistency with the ALFRED reactor design. Among the three concentric tubes, the innermost one functions as the downcomer, while the riser is formed between the first and second tubes. The gap between the second and third tubes is filled with pressurized helium at 0.5 MPa, which serves as an insulator. This arrangement enables the BTs to handle significant thermal gradients without inducing excessive thermal stress on the materials and allows the detection of eventual leakages before the rupture of the tube. The BTs are organized in a cylindrical array (see Figure 95) with a minimum pitch-to-diameter ratio of 1.3, and the entire bundle is enclosed by a cylindrical double-wall shell, isolating it from the pool. Details of the tube arrangement can be found in Table 19 and 20.

At the MHX outlet, the lead is cooled to around 400°C before rising through the barrel and circulating downwards through the annular space between the main vessel and the barrel, eventually re-entering the CS from the bottom. The coolant flow path is schematically drawn in Figure 96.

(a)

(b)

Figure 88 – Pictures of the ATHENA Main Vessel (a) and the Transfer Tank (b)

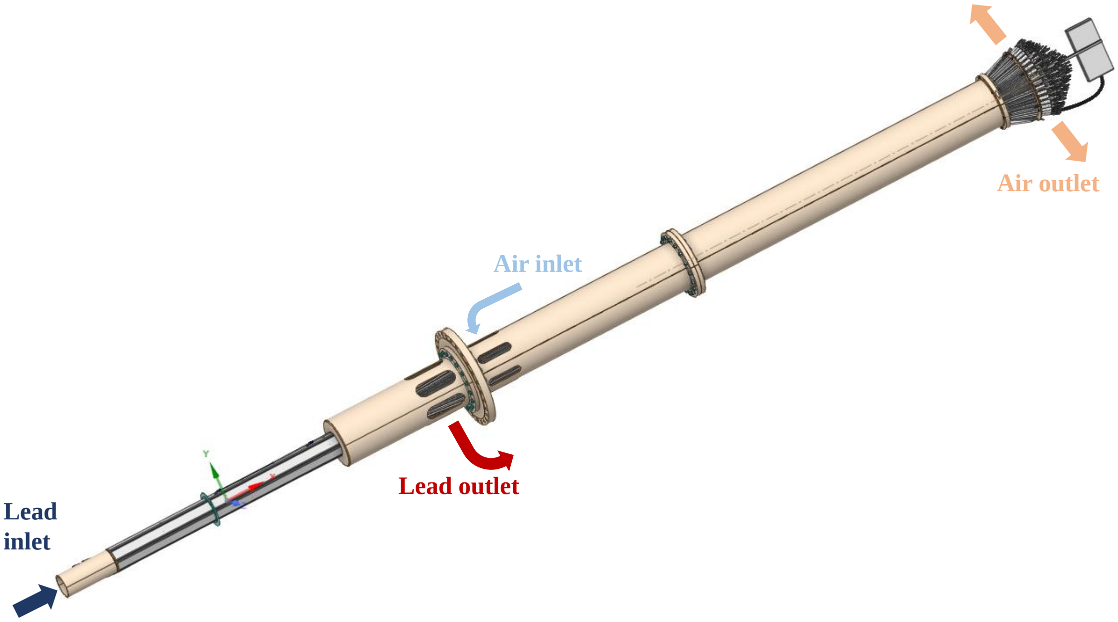

Figure 89 – 3D drawing of the ATHENA core simulator

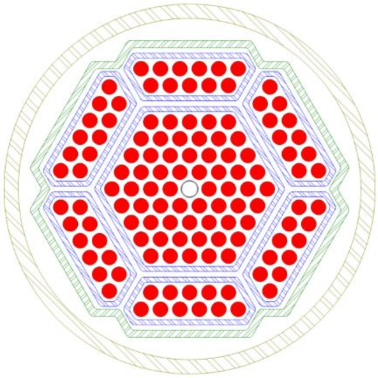

Figure 90 – Schematic layout of ATHENA core simulator

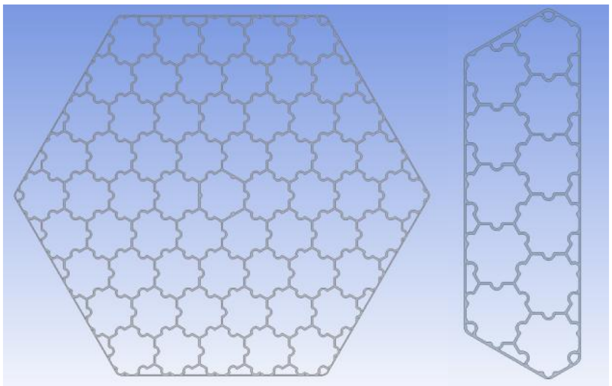

Figure 91 – Schematic layout of the core simulator spacer grids

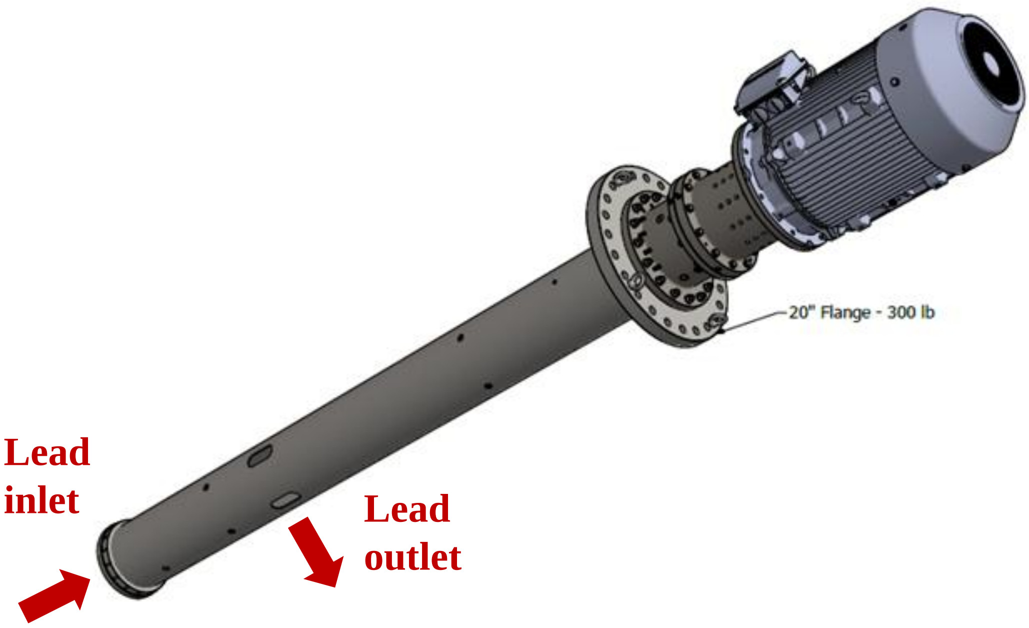

Figure 92 – 3D drawing of the ATHENA main circulation pump

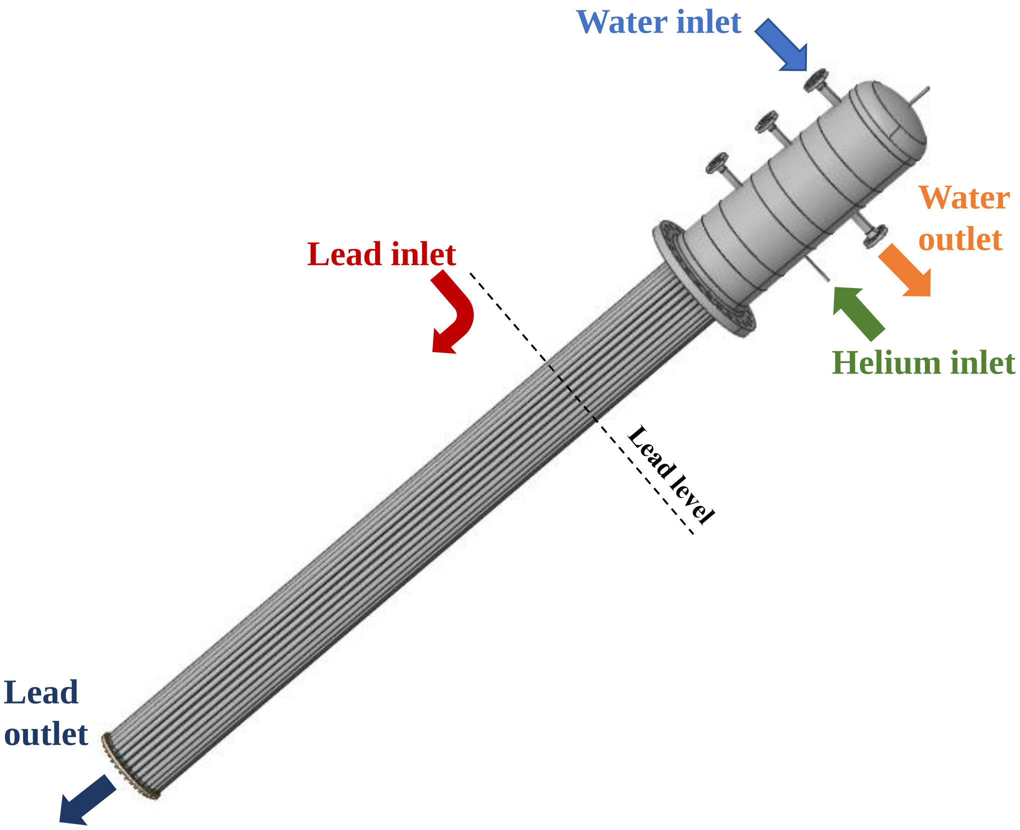

Figure 93 – 3D drawing of the ATHENA main heat exchanger

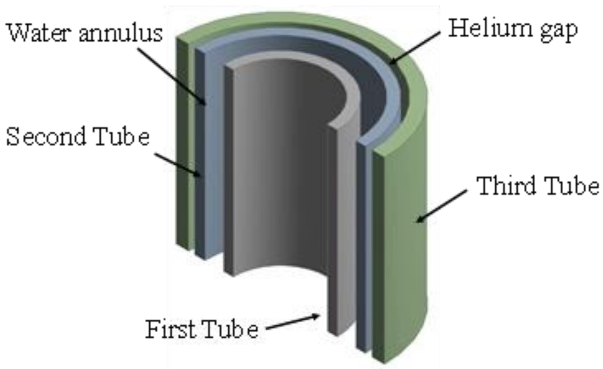

Figure 94 – Sketch of the internal structure of the bayonet tube

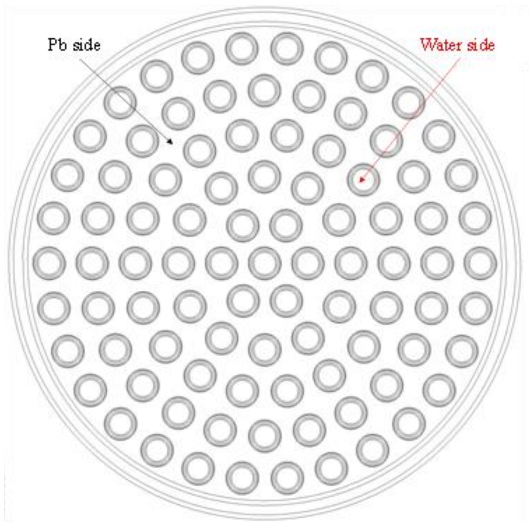

Figure 95 – Cross section view of the tube bundle arrangement

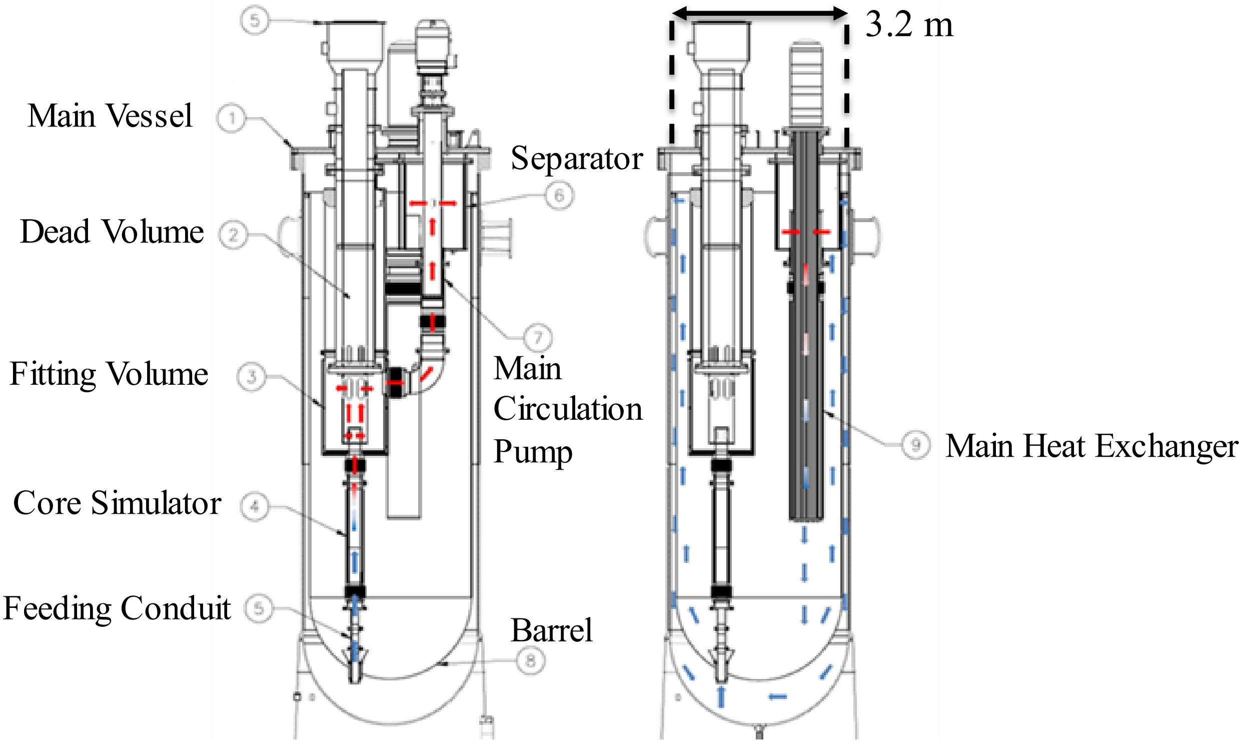

Figure 96 – ATHENA Main Vessel layout and primary coolant flow path

Table 18 – Core simulator geometry and power of the pins

Parameter	**Unit**	**Value**
Pin diameter	mm	10.5
Central pin diameter	mm	12.0
Pitch	mm	13.6
Pitch to Diameter ratio	----	1.29
Number of pins	----	126 (active)+1 (dummy)
Active length	mm	810.0
Pin total length	mm	8550.0
Central wrapper hexagonal key	mm	109.0
Shroud hexagonal key	mm	199.0
Total power	MW	2.21
Linear power	kW/m	21.65
Max wall heat flux	kW/m^2	656.0
Number of FAs	-	1 (61 pins) + 6 (11 pins)

Table 19 – ATHENA MHX tube bundle configuration

Parameter	**Unit**	**Value**
Number of bayonet tubes	----	91
Tube bundle active length	mm	3000
Pitch to Diameter ratio	----	1.3
Pitch geometry	----	Cylindrical
Bayonet tube geometry	----	3 coaxial tubes
Shell inner diameter	mm	499

Table 20 – ATHENA MHX tubes dimensions

Parameter	**I.D. [mm]**	**O.D. [mm]**	**Thick. [mm]**	**Size**
First tube	22.90	25.40	1.25	1” BWG 18
Second tube	28.45	31.75	1.65	1 ¼” BWG 16
Third tube	33.15	34.93	0.89	1 3/8” BWG 20

4.1.2 Secondary system

Primary and secondary systems are thermally coupled through the MHX, which is fed by a dedicated loop. The cold water is collected in the upper chamber of the MHX, flows downward through the first tube, inverts its direction at the bottom of the BTs, and then moves upward in the annular riser, where it is heated by the lead. Hot water then exits through the outlet collector that is located at the bottom of the inlet one. Both the collectors are located outside the main vessel.

Hot water flows inside the 2” pipe towards the Air Cooler (AC), that consists in a horizontal tube bundle, outside of which air is blown by fans to remove the required power from the water. Heat transfer is enhanced by the fins on the outer surface of the tubes. Water circulation is ensured by a centrifugal pump, placed between the AC and the MHX. Pressure regulation in the loop is done by the pressurizer (PRZ) – which also acts as an expansion tank – by injecting/discharging nitrogen in/from the cover gas region.

Bypass and venting lines, regulation and interception valves, electrical heaters, the technical gas, and auxiliary systems enable the facility to operate and control the start-up and shutdown phases. The P&ID of the secondary loop is shown in Figure 97, where the main components, i.e., MHX, AC, pump and PRZ, are placed inside dashed boxes, and the hot and cold legs are highlighted in red and blue, respectively.

TH conditions for both Stage 2 and Stage 3 of the primary and secondary systems are summarized in Table 21. It should be noted that the conditions of the secondary system are not representative of the ALFRED reactor, but the adoption of a liquid single phase secondary system allows a simplification of the operation of the facility and a cost saving, being the secondary loop at a lower pressure compared to a secondary system of a NPP. Nevertheless, the particular design of the MHX allows to face two fluids, i.e., lead and water, with a high temperature difference without stressing the materials, and allows the primary system to fulfill its objectives.

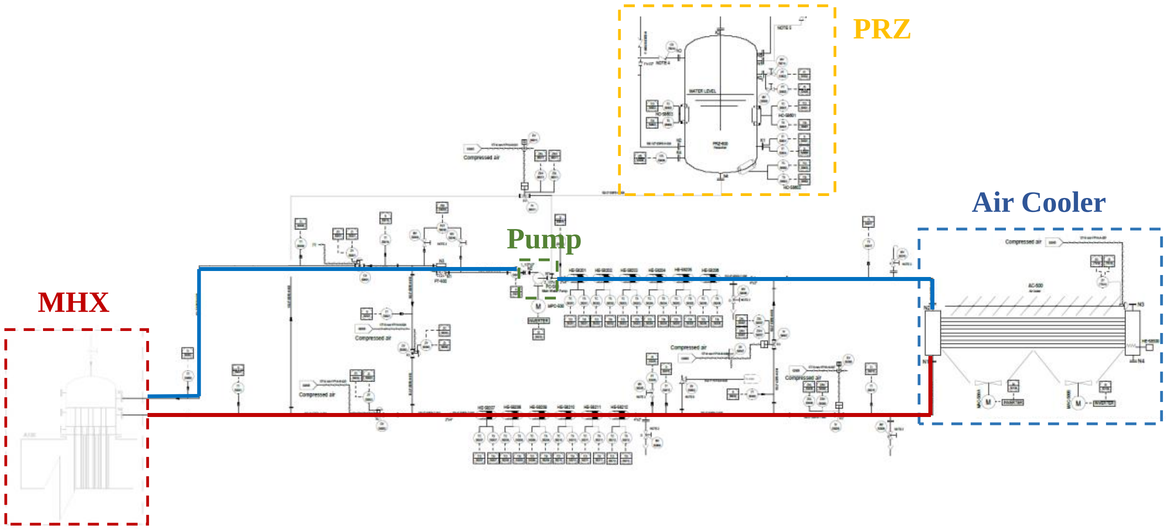

Figure 97 – P&ID of ATHENA secondary system

Table 21 – Thermal-hydraulic conditions of ATHENA

Parameter	**Unit**	**Stage 2**	**Stage 3**
Total power	MW	2.21	2.21
Pb temperature at CS inlet	°C	400.0	400.0
Pb temperature at CS outlet	°C	480.0	520.0
Lead mass flow rate	kg/s	189.3	126.5
Water temperature at MHX inlet	°C	110.0	110.0
Water temperature at MHX outlet	°C	160.0	180.0
Water mass flow rate	kg/s	10.34	7.50
Water pressure (in the PRZ)	MPa	1.20	2.50

4.2 Numerical models

4.2.1 STH model

The entire ATHENA facility, including the lead, water, and AC domains, has been simulated using the modified version of the RELAP5/Mod3.3 code which includes the lead as a coolant and allows for the representation of the lead free level in the main vessel. The fluid domain is simulated using PIPE, BRANCH, SINGLE JUNCTION, PUMP, and VALVE components, while the metallic and insulating structures are simulated by HEAT STRUCTURES. BCs such as the air mass flow rate, the lead and water cover gas pressures, TMDPVOLs and TMDPJUNs are used. For the convective heat transfer towards the environment, constant HTC and temperature are set to 8 W/m^2 °C and 10°C, respectively.

The nodalization strategy employed for the lead domain, including the MHX, follows the "sliced modelling approach" [132]. As highlighted in the previous cases, this approach helps the simulation to better replicate phenomena like natural circulation by ensuring uniform axial discretization across the entire pool. Being the pool (3D region) characterized by large fluid volumes, an average control volume length of 30 cm was chosen to meet the L/D > 1 criterion typical of STH codes [69].

For the "1D" active regions (e.g., CS and MHX), a mesh sensitivity analysis was conducted, starting with a reference length of ~15 cm and testing both refined and coarser meshes by halving or doubling the reference mesh length, respectively. Figure 98 and 99 show the results, with the CS mass flow rate largely unaffected by mesh size, while the MHX ΔT showed slightly more sensitivity. However, even in the MHX, the maximum discrepancy in lead temperature was ~0.4°C, corresponding to a 0.4% difference in exchanged power. Eventually, a 15 cm cell length was chosen for both components to achieve a balance between detail and homogeneity across the system, where each pool fluid element corresponds to two in the active regions. The axial nodalization of the 1D region is shown in Figure 100, where the further subdivision in three parallel pipes in the CS is reported. In this way, the central hexagonal FA, the trapezoidal FAs, and the bypass (or IW) region, are separately simulated, though the thermal coupling among them is ensured by a proper HS definition. Only the active (i.e., CS and MHX) HSs are represented in Figure 100 for simplicity, but each control volume is thermally connected to the corresponding volume in the pool to simulate the "internal" heat losses towards the pool region. Moreover, the pool side volumes are connected to further HSs modelling the main vessel to consider the "external" heat losses, i.e., towards the environment.

The pool side of the ATHENA vessel was further azimuthally discretized into three 120° sectors (see Figure 101), enabling the simulation of potential recirculation and fluid mixing. Each sector includes one of the primary components, i.e., the CS, MCP, or MHX, and they have almost the same cross-sectional area in such a way as to reduce numerical oscillations.

The secondary loop (see Figure 102) was discretized through 15 cm fluid elements in active regions such as the MHX and AC, and up to 25 cm in piping and pressurizer sections, where the larger flow areas allow for coarser meshes. The air side of the AC was modelled with a pipe component, and the BCs were imposed by two TMDPVOLs and a TMDPJUN, ensuring the correct mass flow rate for maintaining the target water temperature at the AC outlet. Figure 102 shows only the active HSs (i.e., MHX and AC), but the RELAP5 model contains also the passive structures to consider the heat losses towards the environment.

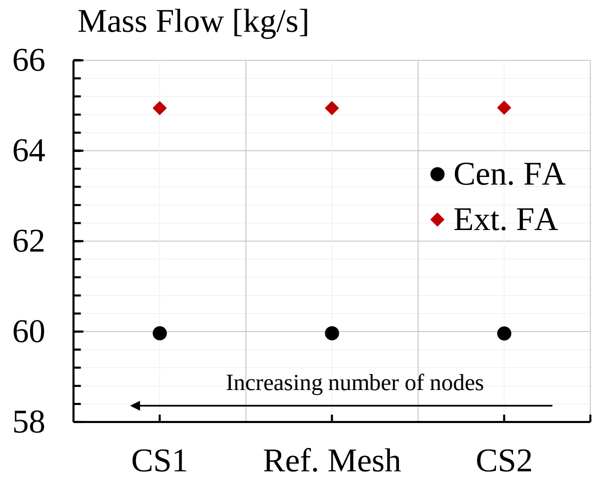

Figure 98 – Mesh sensitivity analysis in the CS

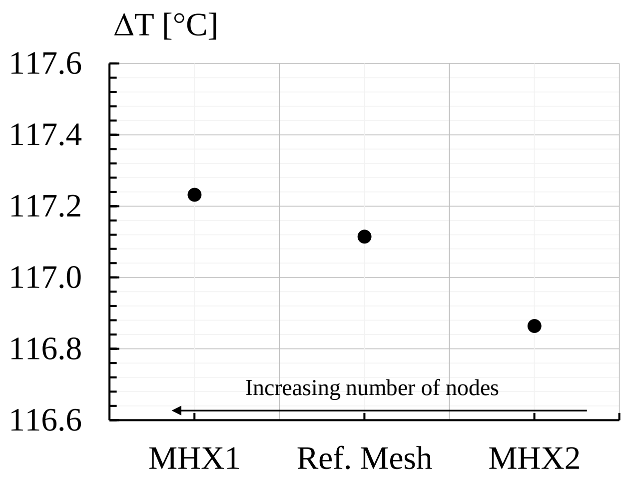

Figure 99 – Mesh sensitivity analysis in the MHX

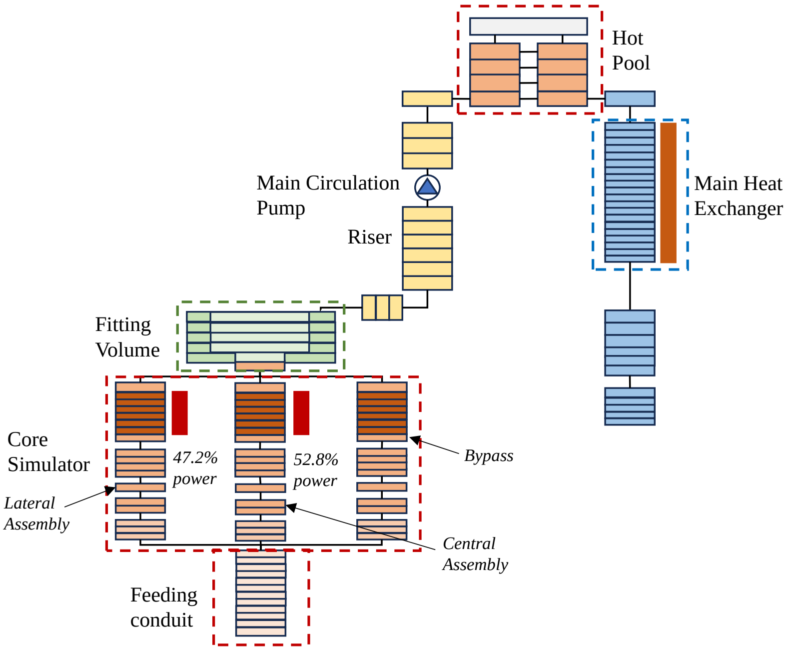

Figure 100 – "1D" region of the primary side axial nodalization

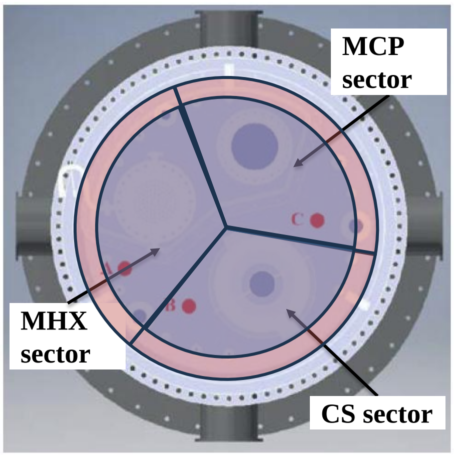

Figure 101 – Pool azimuthal nodalization

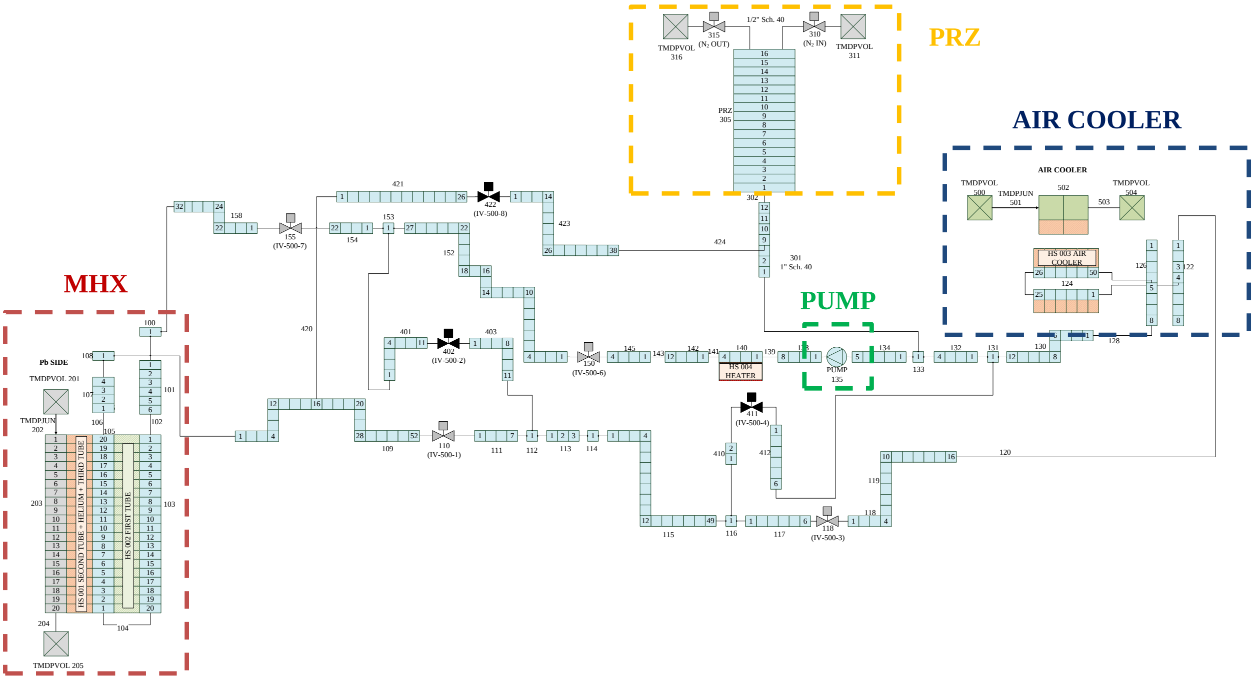

Figure 102 – Secondary loop nodalization

4.2.2 CFD model

The Ansys CFX model consists of four distinct domains (see Figure 103): the solid domain in the wrappers and external steel casing, the fluid region in the IW, and two porous regions representing the FAs zone including the grids.
The material properties for lead and steel are sourced from relevant handbooks in Ref. [137] and [158], respectively. To model the seven FAs, two different approaches were identified and discussed in Ref. [43]:

- A single porous medium, which well captures the temperature in the corners of the trapezoidal shape of the external FAs.
- A hybrid approach, which consists in dividing the central FA into an internal porous medium and a surrounding fluid layer. This method improves the representation of temperature gradients near the wrappers (see Figure 104) and the heat transfer to the IW.

The calibration of the porous media – achieved through a CFD analysis of the infinite lattice domain of the ATHENA CS geometry – along with the grid independence study, can be found in the detailed study in Ref. [43]. This method incorporates concentrated loss coefficients to represent the grids, obtained from separate CFD simulations at different mass flow rates. The mesh is composed of approximately 3.13 million cells, with a wall y^+ greater than 30 in the porous region, while it is less than 1 in the detailed fluid domain. The SST $k-\omega$ turbulence model and a turbulent Prandtl number of 2 [140] have been selected. Adiabatic conditions are imposed on the external casing.

The porous media approach represents a balance between the detailed, high-cost representation of the FAs and the simplified STH modelling, which lacks consideration of three-dimensional asymmetry and fluid conduction. However, the CS representation can be improved in future work with more reliable models to monitor local values like the peak temperature on pin's surface.

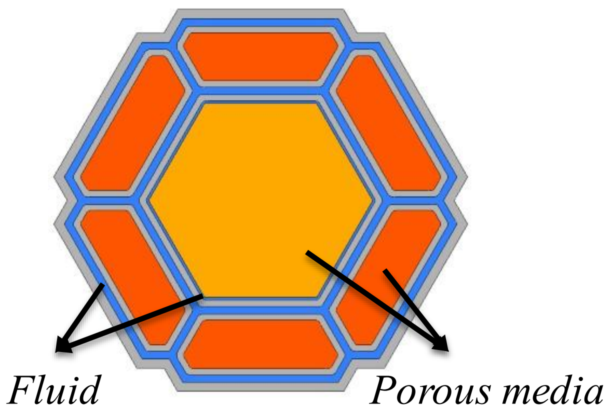

Figure 103 – Fluid domains in the Ansys CFX model: steel (gray), fluid lead (blue), central porous medium (orange) and external porous media (red)

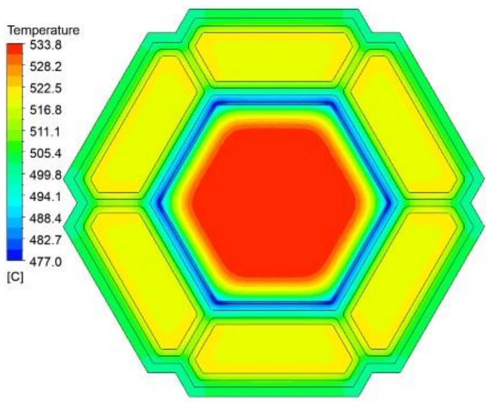

Figure 104 – Temperature distribution at the outlet section of the CS

4.2.3 STH/CFD coupled model

The model for the coupled simulation has been built similarly to those presented in Sect. 3.2.3, also applying in this case the domain decomposition approach. In particular, the RELAP5 model has been modified by removing the active part of the CS and replacing it with TMDPVOLs and TMDPJUNs, where the BCs from the CFD calculations are imposed. It should be noted that since the ATHENA CS was modelled with three parallel pipes, two TMDPVOLs and a TMDPJUN have been used to replace each removed pipe, as shown in Figure 105.

The information exchange occurs in a similar way to that described in Sect. 3.2.3, but each quantity (e.g., mass flow rate, temperature) is passed to/from the corresponding volume or junction. The pressure update in the STH model follows Eq. (43).

As with the NACIE-UP and TALL-3D cases, non-dimensional velocity and temperature maps have been applied at the CFD domain inlet to convert the 1D results from RELAP5 to CFX, and a mass flow averaging of temperatures and pressures has been performed to make the CFD results suitable for the RELAP5 calculation.

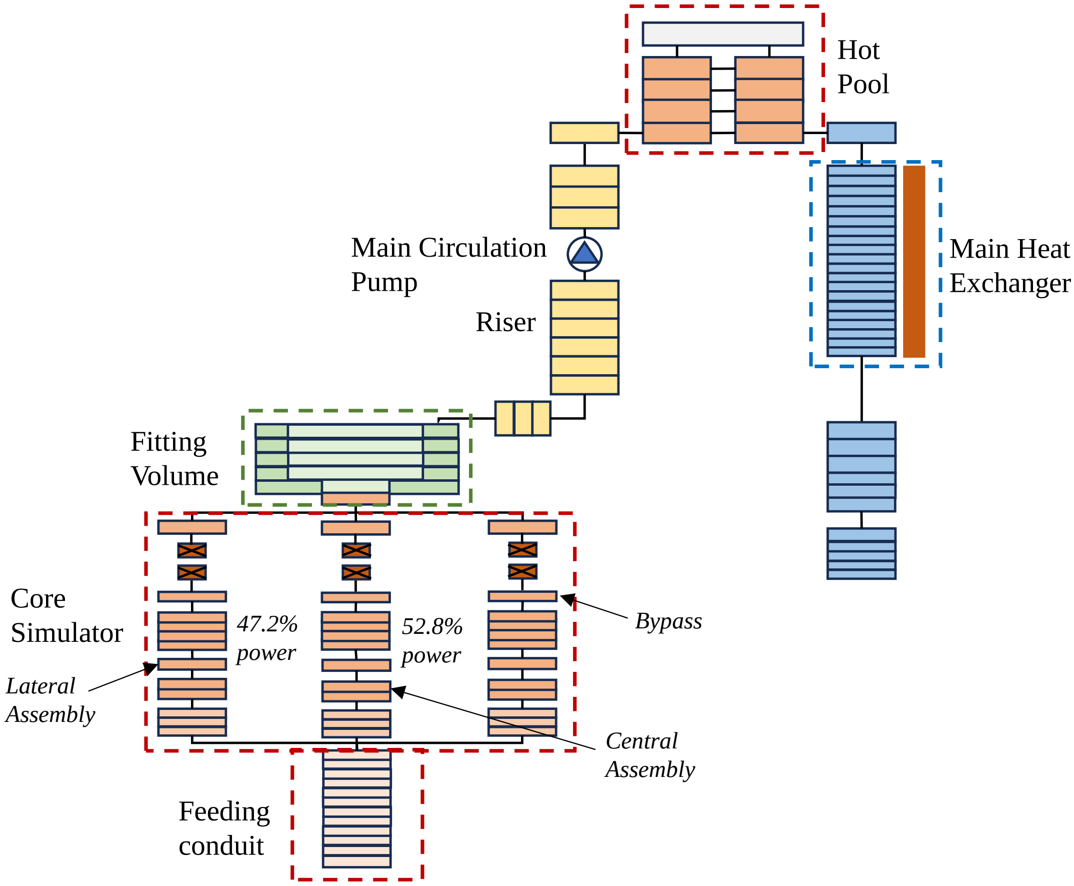

Figure 105 – ATHENA "open loop" coupled model

4.3 Simulation results

In this section, the focus is initially on the sizing of the MHX, where an analytical calculation is compared with the RELAP5 simulation, confirming the design data and qualifying the numerical model. Then, a steady state calculation has been performed to characterize the TH behavior of the facility in normal operation and to provide the initial conditions for the transient analysis described in Sect. 4.3.3.

4.3.1 Verification of the Main Heat Exchanger

Sizing calculation

The preliminary design of the MHX is based on an analytical calculation and it started with the requirement of having the distance between its thermal barycenter and the CS' one equal to 3.3 m. Being the main vessel 10 m high, and leaving the space upstream of the CS for the installation of a Venturi mass flow meter, the tubes length was determined to be 3 m.

The second requirement is associated to the thermal cycle specified for the secondary loop. In particular, the MHX must be designed to operate with a single-phase water at 110–160°C at 1.2 MPa. Once the power is established (2.21 MW), the water mass flow rate is determined by a simple energy balance:

$$\dot{m} = \frac{\dot{Q}}{\Delta h} = \frac{2.21 \cdot 10^6 \, W}{(675.9 - 462.1) \cdot 10^3 \, \frac{J}{kg}} = 10.34 \, kg/s \tag{45}$$

Since the active length is fixed, an overall flow area must be selected to reduce as much as possible the pressure drops inside the component. To evaluate the distributed pressure drops, an overall height of 4.5 m has been considered (3 m in the active region, plus 1.5 m in the cover gas region and outside the cover), for the downcomer and riser, respectively. The pressure drop can be calculated as follows:

$$\Delta p = f(\varepsilon, Re, D_h) \frac{L}{D_h} \frac{1}{2} \rho u^2 = f \frac{L}{D_h} \frac{1}{2} \frac{\dot{m}^2}{\rho A^2} = f \frac{L}{D_h} \frac{1}{2} \frac{\dot{m}^2}{\rho \cdot N_{tubes} A_{tube}^2} \tag{46}$$

where:

- f is the friction factor, which, in turbulent regime depends on the tube roughness (ε), the Reynolds number (Re), and the hydraulic diameter (D_h), according to the Colebrook equation:

$$\frac{1}{\sqrt{f}} = -2 \cdot \log \left[\frac{\varepsilon / D_h}{3.71} + \frac{2.51}{Re \sqrt{f}} \right] \tag{47}$$

- L is the height of the BT.
- ρ is the density.
- u is the velocity.
- D is the tube's inner diameter.
- N_{tubes} is the number of BTs.
- A_{tube} is the flow area of a single tube.

To continue the analysis, it should be considered that the number of tubes is generally an outcome of the thermal sizing of the HX. In this case, since a circular array has been selected for the tube bundle (as shown in Figure 95), it is necessary to choose a number of tubes in such a way that all the ranks are completed. To satisfy also other space constraints in the cover, 91 BTs have been chosen. Other characteristics of the tube bundle configuration are summarized in Table 19, including the pitch-to-diameter ratio, which is not uniform throughout the bundle since the equivalent subchannel is not triangular. The minimum pitch-to-diameter ratio is set to 1.3. To calculate the diameter of each tube, it is necessary to first evaluate the innermost tube diameter. Being the hydraulic diameter equal to the Inner Diameter (ID) in the downcomer of the tube bundle, Eq. (46) can be recast as:

$$\Delta p = f \frac{L}{ID_{tube1}} \frac{1}{2} \frac{\dot{m}^2}{\rho \cdot N_{tubes} \left(\frac{\pi}{4} ID_{tube1}^2 \right)^2} \tag{48}$$

Once the maximum pressure drop (along both the downcomer and the riser) has been determined, the ID of the first tube can be found:

$$ID_{tube1} = \sqrt[5]{\frac{8 \cdot f \cdot L \cdot \dot{m}^2}{\pi^2 \cdot \Delta p_{downcomer} \cdot \rho \cdot N_{tubes}}} \tag{49}$$

Once that ID_{tube1} is calculated, the hydraulic diameter of the annular riser can be evaluated as the difference between the inner diameter of the second tube and the outer diameter of the first tube. The latter is evaluated based on the result of Eq. (49), assuming a reasonable thickness. For the riser, Eq. (46) can be written in terms of these diameters:

$$\Delta p_{riser} = f \frac{L}{(ID_{tube2} - ID_{tube1})} \frac{1}{2} \frac{\dot{m}^2}{\rho \cdot N_{tubes} \left(\frac{\pi}{4}(ID_{tube2}^2 - OD_{tube1}^2)\right)^2} \tag{50}$$

where ID_{tube2} is the only unknown. From an iterative calculation, diameters of the first and the second tubes have been selected among those commercially available, and they are reported in Table 20. Therefore, the heat transfer area that the water sees is defined by the size of the second tube.

Now, only the third tube remains to be defined. Its size is of great importance since it defines the gap that will contain the helium, serving as a large thermal resistance between the primary and secondary sides that allows to face lead and liquid water at very different temperatures without stressing the tubes material. Since the reference thermal cycle for ATHENA is the one representative of ALFRED Stage 2, i.e., 400–480°C, both the thermal cycles for lead and water are known. Therefore, the Logarithmic Mean Temperature Difference (LMTD) can be easily evaluated:

$$LMTD = \frac{(T_{Pb,in} - T_{H_2O,out}) - (T_{Pb,out} - T_{H_2O,in})}{ln\left(\frac{T_{Pb,in} - T_{H_2O,out}}{T_{Pb,out} - T_{H_2O,in}}\right)} = 304.8°C \tag{51}$$

According to the LMTD method, the overall HTC based on the internal heat transfer area (U_i) can be calculated as follows:

$$U_i = \frac{\dot{Q}}{S_i \cdot LMTD} = \frac{2.21 \cdot 10^6\ W}{20.97\ m^2 \cdot 304.8°C} = 345.77 \frac{W}{m^2\ °C} \tag{52}$$

Assuming that heat transfer across the helium gap occurs by conduction only, U_i can be expressed in terms of the sum of the thermal resistances due to convection with water, conduction across the third tube (whose size is to be defined), the helium gap and the second tube, and convection with lead:

$$\frac{1}{U_i} = \frac{1}{h_i} + \frac{\frac{ID_{tube2}}{2} ln\left(\frac{OD_{tube2}}{ID_{tube2}}\right)}{k_{tube2}} + \frac{\frac{ID_{tube2}}{2} ln\left(\frac{ID_{tube3}}{OD_{tube2}}\right)}{k_{He}} + \frac{\frac{ID_{tube2}}{2} ln\left(\frac{OD_{tube3}}{ID_{tube3}}\right)}{k_{tube3}} + \frac{ID_{tube2}}{OD_{tube3}} \frac{1}{h_o} \tag{53}$$

where the thermo-physical properties of helium are taken from Ref. [159], h_i and h_o correspond to the convective HTCs with water and lead, respectively, and they can be evaluated by means of suitable correlations. In particular, the water side HTC can be evaluated through the well-known Dittus-Boelter correlation [104]:

$$Nu = \frac{h_{H_2O} \cdot D_{heat}}{k_{H_2O}} = 0.023 \cdot Re^{0.8} \cdot Pr^{0.4} \tag{54}$$

where D_{heat} is the heated diameter and Nu is the Nusselt number. The lead side HTC can be evaluated through the Ushakov correlation [160]:

$$Nu = \frac{h_{Pb} \cdot D_{heat}}{k_{Pb}} = 7.55 \frac{p}{D} - 20 \left(\frac{p}{D}\right)^{-13} + \frac{3.67}{90\left(\frac{p}{D}\right)^2} Pe^{0.56+0.19\frac{p}{D}} \tag{55}$$

where p/D is the pitch-to-diameter ratio, fixed at 1.3, and the Peclet number (Pe) is the product of the Reynolds and the Prandtl numbers. Since the outer diameter of the third tube affects the Reynolds number in Eq. (55), and also appears explicitly in Eq. (53) along with the inner diameter, an iterative calculation is required to achieve the target value of the overall HTC of Eq. (52). The commercial tube closest to the required value has been selected. The final design of the concentric tubes composing the bayonet is summarized in Table 20.

RELAP5 model

The numerical model of the MHX has been extracted from the complete nodalization of ATHENA (see Sect. 4.2.1), and a separate analysis on the component has been performed to verify its design using the RELAP5 code. The component is discretized into fluid volumes of 15 cm in height, meaning each pipe component is made up of 20 cells.

The primary side of the MHX has been modelled using a descendent pipe component (PIPE 203). The inlet conditions are set by TMDPVOL 201 and TMDPJUN 202, which specify the inlet temperature and mass flow rate, respectively. The outlet conditions are represented by TMDPVOL 205, which fixes the outlet pressure. PIPE 203 and TMDPVOL 205 are connected through SINGLE JUNCTION 204, completing the primary side nodalization.

The secondary side is modelled using a descendent pipe (103) representing the feedwater tube, and an ascendant ANNULUS component (105) representing the riser. These components are connected at the bottom by a single junction (104). The BCs for the secondary side are defined by two TMDPVOLs (101 and 107) and a TMDPJUN (102). The riser and outlet TMDPVOL are also connected by a single junction (106).

The thermal coupling between the primary and secondary systems has been implemented using HS 001, illustrated in light red in Figure 10. This HS contains the same number of axial meshes as the hydraulic components, with 13 radial mesh points creating 12 radial intervals for each axial mesh. The first and last four intervals correspond to the thicknesses of the second and third tubes, while the middle four intervals correspond to the helium gap thickness. Additionally, another HS (002), shown in green in Figure 10, models the heat transfer between the riser and the downcomer.

Figure 106 – RELAP5 nodalization of the MHX

Comparison between the analytical and numerical results

The results of the RELAP5 calculation can be compared with the sizing results, using the ALFRED Stage 2 thermal conditions for the lead as a reference. Table 22 presents the comparison between the analytical and RELAP5 results in terms of temperatures, power, and pressure drops. To quantify the difference (Δ) between the two methods, an absolute deviation is considered for the temperatures, while a relative value is defined for the other quantities:

$$\Delta_{rel} = \frac{RELAP5\ value - Analytical\ value}{Analytical\ value} \cdot 100\ [\%] \tag{56}$$

Inlet temperatures, mass flow rates and operating pressure are BCs, thus they have the same value both in the analytical and in the numerical calculations. Table 22 shows that the outlet temperatures calculated by RELAP5 code are very similar to the analytical sizing, with a discrepancy of about 2°C. In terms of exchanged power, the numerical calculation slightly overestimates the analytical value, confirming a certain conservativeness in the sizing. Pressure drops are also quite well predicted, being equal to 17.5 kPa, with a deviation of about 10% with respect to the analytical calculation. The major difference stands in the water temperature field "seen" by the lead. In fact, the LMTD method assumes inlet/outlet temperatures of 110/160°C, while the RELAP5 calculation has shown that the "actual" inlet temperature in the riser is about 132°C because of the feedwater pre-heating in the downcomer, as shown in Figure 107. Even though the MHX is sized with the LMTD method, thus assuming that the MHX was of a pure counter current type, the RELAP5 calculation confirmed the sizing results.

Since the MHX should work also when ALFRED Stage 3 conditions are adopted for the lead thermal cycle, the secondary side conditions should be modified accordingly. Since the water must face in this case higher temperatures, the operating pressure has been increased at 2.5 MPa to increase the margin to boiling. A RELAP5 calculation has shown that the most suitable conditions for the secondary side are 110/180°C with a mass flow rate of 7.5 kg/s.

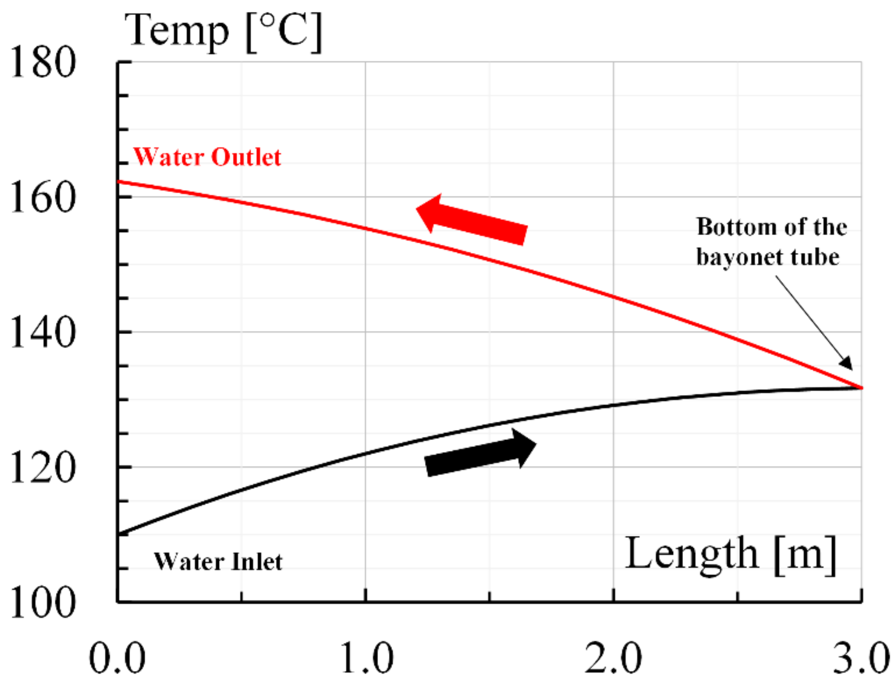

Figure 107 – Water temperature profile in the MHX

Table 22 – Analytical vs RELAP5 results

Parameter	Unit	Analytical	RELAP5	Δ
$T_{Pb,in}$	°C	480.0	480.0	--
$T_{Pb,out}$	°C	400.0	397.8	-2.2°C
$\dot{m}_{Pb}$	kg/s	189.3	189.3	--
p_{H2O}	MPa	1.20	1.20	--
$T_{H2O,in,DC}$	°C	110.0	110.0	--
$T_{H2O,in,riser}$	°C	110.0	131.7	+21.7°C
$T_{H2O,out}$	°C	160.0	162.3	+2.3°C
$\dot{m}_{H2O}$	kg/s	10.34	10.34	--
Power	kW	2210.0	2314.0	+4.7%
Δp	kPa	19.4	17.5	-9.8%

4.3.2 Steady state results

For the steady state characterization and the following transient analysis, the Stage 3 conditions are considered, since they are the most critical for the operation of the facility. A numerical steady state for the entire facility has been achieved through a 20000 s “null transient” calculation, in which BCs reported in Table 23 are adopted. It is also important to note that the lead and water mass flow rates in the system are the set point values for their respective control system of the pump speeds for both fluids. In contrast, the air mass flow rate in the AC is controlled by a regulation system that adjusts the air flow to ensure that the water outlet temperature from the AC remains at 110°C.

Table 23 – Boundary conditions for the ATHENA steady state operation

Parameter	Unit	Value
CS power	MW	2.21
Cover gas pressure	MPa	0.135
Cover gas temperature	°C	400.0
Pb mass flow rate set point	kg/s	126.5
Water pressure in the PRZ	MPa	2.50
Water temperature at AC outlet	°C	110.0
Water mass flow rate set point	kg/s	7.5
Environmental temperature	°C	10
Convective heat transfer coefficient with the environment	W/m^2 °C	8.0

Table 24 and 25 show a comparison between the RELAP5 steady state results and the design data obtained from CFD calculations [43] [161] and detailed component calculations [157] [162], demonstrating a good overall agreement. The total power supplied to the lead is delivered by the CS (2210 kW) and the MCP (7.41 kW). The power is removed from the system by the MHX (2200.29 kW) and heat losses to the environment (19.30 kW). The global energy balance shows a discrepancy of approximately 2 kW, which is less than 0.1% of the CS power, indicating that the steady-state condition has been successfully achieved.

The components between the CS and MHX feature double-wall structures, with two metallic layers separated by an air gap for effective insulation from the cold pool. However, there are exceptions, such as the curve downstream of the fitting volume and the bottom of the hot pool, which are not double-walled due to design constraints. This leads to significant heat losses from the hot leg to the cold pool, amounting to 38.39 kW.

The lead enters the CS at 404.2°C, with a total mass flow rate of 126.5 kg/s, distributed almost evenly among the central and the six external FAs, with only 1.26% entering the IW region. This results in different temperature rises across those regions, and the temperature after the mixing at the CS outlet is 522.3°C. Hot lead enters the MHX at 520.9°C and exits at 403.8°C.

The total pressure drop, corresponding to the MCP head, amounts to 89.67 kPa, mainly localized in the CS (77.81 kPa). The pressure drop in the MHX is negligible due to the low velocity (~0.1 m/s) compared to the CS (~1 m/s). Although the MHX pressure drop has the highest discrepancy with the design data, its effect on the total system pressure drop is minimal. The pressure drop between the MHX and the feeding conduit causes a 2.6 cm difference in the levels of the hot and cold pools, corresponding to a pressure drop of 2.7 kPa.

On the secondary side, the heat removed by the MHX (2200.29 kW) and the pump (6.87 kW) is dissipated by the AC (2228.49 kW) and heat losses (1.94 kW). Heat losses are small because of the relatively low temperature of the secondary loop. Pressurized water at 2.5 MPa enters the MHX at around 110°C, it is pre-heated by the hot water due to the BT design, enters the riser at 195.6°C and exits at 179.2°C, with a mass flow rate of 7.5 kg/s. The outlet temperature lower than the one at the bottom of the riser indicates that most of the heat transfer is regenerative and occurs in the downcomer, differently from what it was observed in the analysis in Sect. 4.3.1. The reason can be attributed to the inclusion in the complete model of the BT in the cover gas region, where water in the riser continues to exchange heat with the downcomer. The total pressure drop in the loop is around 4.2 bar, due to the relatively small piping dimensions (2”), which cause velocities around 3.8 m/s.

Table 24 – ATHENA primary side steady state characterization

Parameter	Unit	Location	R5	Design	Δ
Powers	kW	CS	2210.00	2210.00	0%
		MCP	6.37	N/A	N/A
		MHX	2200.29	2210.0	-0.4%
		Heat losses	19.30	N/A	N/A
		Internal heat losses	38.39	N/A	N/A
Temperatures	°C	CS in	404.2	400.0	4.2°C
		Ext. FAs outlet	523.2	521.2 [43]	2.0°C
		Cen. FA outlet	521.3	520.5 [43]	0.8°C
		IW outlet	520.3	514.0 [43]	6.3°C
		CS outlet	522.3	520.0°C	2.3°C
		MHX inlet	520.9	520.0°C	0.9°C
		MHX outlet	403.8	400.0°C	3.8°C
Mass flow rates	kg/s	MCP	126.5	126.5	0%
		Ext. FAs	64.94	64.52	-0.7%
		Cen. FA	59.97	59.96	0.0%
		IW	1.59	2.02	21%
Absolute pressures	MPa	Bottom of the pool	1.085	N/A	N/A
		Cover gas	0.135	0.135	0%
Pressure drops	kPa	CS	77.81	83.16 [161]	-6.4%
		MHX	0.63	0.42 [162]	-50.0%
		Total	89.67	91.36 [162]	-1.8%
Level difference between hot and cold pool	m	Hot and cold pool	0.026	N/A	N/A

Table 25 – ATHENA secondary side steady state characterization

Parameter	Unit	Location	R5	Design	Δ
Powers	kW	MHX	2200.29	2210.0	-0.4%
		AC	2228.49	2210.0	0.8%
		PC	6.87	N/A	N/A
		Heat losses	1.94	N/A	N/A
Temperatures	°C	MHX inlet	110.1	110	0.1°C
		MHX riser inlet	195.6	N/A	N/A
		MHX outlet	179.2	190.0 [157]	-10.8°C
		AC in	179.2	200.0	-20.8°C
		AC out	110.0	110.0	0%
Mass flow rate	kg/s	PC	7.5	7.5	0%
Absolute pressures	MPa	PRZ	2.50	2.50	0%
		MHX inlet	2.72	2.50	8.8%
Pressure drops	kPa	MHX	28.04	N/A	N/A
		AC	1.67	N/A	N/A
		Total	418.93	860.0*	N/A
* it is the maximum allowable value					

4.3.3 Transient analysis

From the initial conditions representative of ALFRED Stage 3, TH analyses have been carried out considering two relevant transients for safety: the LOHS and LOFA. The first has been analyzed by RELAP5 code only, being a transient in which the pump is assumed to continue working, therefore the main TH phenomena are driven by convection mechanisms, thus allowing the STH code to properly model such conditions. The presence of forced circulation is expected to prevent the occurrence of complex multidimensional flow paths within the pool components and to flatten the temperature distribution within the CS. Consequently, the coupled simulation was avoided since it was considered not necessary. In contrast, in the LOFA transient, the pump is switched off, thus the CS transitions from a fully convective to a mixed convective-conductive driven heat transfer mechanism, and flow regime changes from a turbulent to transition regime. Therefore, a coupled CFD-RELAP5 simulation has been carried out, and the results have been compared to the RELAP5 stand-alone ones.

LOHS Transient

The LOHS transient is triggered by the closure of the MHX interception valves: this event represents the SoT. As a result, the system loses its heat sink, leading to a rise in the lead outlet temperature from the MHX. To select a set point at which the CS must turn off, a sensitivity analysis on such set point has been carried out. To switch off the CS, a decay heat curve is applied simulating the one foreseen for the ALFRED reactor, as illustrated in Figure 108, where the power is reported as a percentage of the nominal value. The same curve was applied in other experiments simulating the ALFRED DHR [90] [91]. During the entire transient, the MCP is assumed to continue operating, ensuring the circulation of lead within the system.

Since ATHENA is not equipped with a DHR, the average pool temperature gradually increases over the long term. However, this rise is mitigated by the significant thermal inertia of the pool, which is much larger compared to the ALFRED's one. While the volume ratio between the two systems is 5.5 (ATHENA: 76 m^3; ALFRED: 416 m^3), the power ratio is 135 (ATHENA: 2.21 MW; ALFRED: 300 MW), meaning that ATHENA's power density is significantly lower. In the long term, the only heat sink is the heat dissipation to the environment, which becomes comparable to the decay heat generated in the system (as shown in Figure 118).

A hand calculation of the thermal inertia of ATHENA's system can be performed by considering the lead coolant inventory in the cold pool, which operates at 400°C during normal conditions. With a cold volume of around 64 m^3, the energy required to raise the pool temperature by 1°C is approximately:

$$E = V_{cold\,pool} \cdot \rho_{Pb}(400°C) \cdot c_{p,Pb} \cdot \Delta T = 64\,m^3 \cdot 10580 \frac{kg}{m^3} \cdot 153 \frac{J}{kg\,°C} \cdot 1°C = 104\,MJ \tag{57}$$

Assuming a long-term decay heat average of 35 kW (approximately 1.5% of the nominal power), the time required to transfer this energy to the lead is about 3000 seconds. This implies an average pool temperature rise of approximately 1.2°C per hour. The actual rate will be even lower, as this calculation does not consider the thermal inertia of solid structures and heat losses, which become increasingly relevant as the system operates at low power levels. Even under the worst-case scenario, there remains a substantial margin for intervention, allowing the CS to be completely shut down, preventing any hazardous scenarios for the facility.

To account for the differences in heat losses between ALFRED and ATHENA, the decay heat curve has been modified to minimize distortions due to the facility's scaling. This adjustment is necessary because experimental facilities often do not scale heat losses in proportion to the system size, as their surface-to-volume ratio tends to be higher compared to the full-scale system. The new decay heat curve is calculated by adding two contributions, as described in Eq. (58): the first accounts for the difference between ATHENA's and ALFRED's scaled heat losses, and the second considers the difference in thermal power provided by the MCP and ALFRED's primary pumps:

$$\begin{aligned} P_{decay,new} = P_{decay,old} &+ \left(P_{loss,ATHENA} - P_{loss,ALFRED} \cdot f\right) \\ &- \left(P_{pump,ATHENA} - P_{pump,ALFRED} \cdot f\right) \end{aligned} \tag{58}$$

where:

- $P_{decay,new}$ is the modified decay heat curve used in the transient.
- $P_{decay,old}$ is the scaled decay heat curve from ALFRED.
- $P_{loss,ATHENA}$ and $P_{loss,ALFRED}$ represent the heat losses of ATHENA and ALFRED, respectively, at steady state.
- P_{ATHENA} and P_{ALFRED} represent the nominal power of ATHENA and ALFRED, respectively (2.21 MW and 300 MW).
- f is the ATHENA-to-ALFRED power ratio (2.21/300 MW).

The heat losses for ALFRED were estimated assuming a cylindrical reactor vessel (8.8 m height and 8 m diameter) surrounded by 10 cm of insulation with a thermal conductivity of 0.07 W/m·°C, resulting in around 65 kW dissipated to the environment. The thermal power provided by ALFRED's primary pumps was calculated using the volumetric flow rate and pressure drop, assuming a pump efficiency of 0.8, resulting in about 83 kW delivered to the lead.

Transient simulations were performed with a maximum timestep of 10^{-3} s for the first 600 seconds, then gradually increased to 10^{-2} s as the system approached a new steady-state condition. Once the MHX is isolated from the secondary loop, the water inside the BTs starts to boil due to the high temperature difference between the lead and the water. The generated steam is initially vented into the PRZ, and then released into the environment once its condensation capability is terminated. A similar procedure was identified also for the shutdown operational transient of the facility [163]. Figure 109 illustrates that the mass flow rate directed to the MHX is stopped within 5 seconds, and the MHX reaches the saturation temperature in less than 300 seconds (see Figure 110), fully emptying the BTs.

To better explain the trend of the transient, the set point that triggers the CS shutdown is chosen at 450°C as a reference case. In that case, the set point is reached at 156 s after the MHX isolation (see Figure 111). Different Time Windows (TWs) during the MHX emptying process, before the final lead temperature decrease, can be identified and are outlined in Table 26:

- TW1 (0-78 s): Initial lead temperature increase due to the stop of the feedwater flow to the MHX.
- TW2 (78-112 s): Lead temperature reduction due to the cooling effect of the boiling water in the MHX, which is vented into the PRZ. The boiling process can be observed by looking at the high HTC and steam quality in the secondary side in Figure 113 and 114, respectively.
- TW3 (112-156 s): Lead temperature rise to the set point (450°C), as the MHX becomes nearly empty and can no longer remove the nominal power.
- TW4 (156-208 s): Continued temperature rise, as the colder lead plug has not yet reached the MHX.
- TW5 (208-400 s): A second lead temperature decrease occurs due to the cooling effect of residual cold water coming from the collector and passing through the bayonets when the PRZ venting valve opens. This means the PRZ has reached saturation conditions, and it is not able anymore to condense the steam coming from the MHX. Figure 115 shows the valve opening ratio during this period, and Figure 116 shows the pressure that is maintained at the nominal value.
- TW6 (400-482 s): Temperature increases again since hot lead coming from the hot pool is not cooled down because of the inability of the MHX to remove power anymore.
- TW7 (>482 s): Lead temperature decreases as the cold lead from the CS reaches the MHX.

Figure 112 demonstrates the power imbalance between the CS and the secondary side, where the power removed by the MHX is lower than the CS power in the short term but remains higher from the shutdown until about 500 seconds.

Regarding CS temperatures, once the heating elements are turned off, the temperatures in the active region begin to decrease due to the constant mass flow rate, as shown in Figure 117, 119, and 120. The axial temperature profiles in the cold pool for the barrel and vessel regions (Figure 121 and 122) reveal a modest temperature rise of approximately 12°C, which corresponds to about 1.1°C/h, consistently with the calculation of Eq. (57). The temperature of the system after 40×10^3 s is well within safe operating margins, thanks mainly to ATHENA's significantly large lead inventory and its high thermal inertia, which compensates for the power imbalance.

To assess the sensitivity of the system to the shutdown set point value, further set points at 430, 470 and 490°C have been tested. The sensitivity analysis also has the objective to assess the capability of the system to achieve a safe condition, despite uncertainties in both the numerical and experimental conditions that affect the temperature oscillations at the MHX outlet.

In the short term, varying the set points impacts the timing of the CS shutdown. Lowering the set point to 430°C results in an earlier shutdown by approximately 25 seconds (as shown in Figure 123 and 124, where cases at 430°C, 470°C, and 490°C are represented in red, blue, and green, respectively). The system's behaviour remains quite similar to the reference case at 450°C. Conversely, raising the set point to 470°C or 490°C delays the shutdown by about 300 seconds due to the efficient cooling provided by the boiling water in the MHX, which leads to a temporary drop in temperature before it rises again at around 400 seconds. At this point, the MHX is nearly emptied and no longer able to remove sufficient power. Thus, if the set point is chosen after the local maximum at 460°C, the shutdown system must wait for the water to boil before triggering the shutdown.

In the long term, as shown in Figure 125, all simulations reach a new quasi-steady state. However, the higher the CS shutdown set point, the higher the final equilibrium temperature will be due to the greater amount of energy absorbed by the system before shutdown. Despite these variations, no potentially harmful conditions for the facility are observed. This is confirmed by the temperature trends at the core outlet (Figure 126) and within the vessel region (Figure 127). Figure 128 further illustrates that the average increase of the lead temperature in the vessel region is around 17°C, compared to a 12°C increase in the 430 and 450°C.

Table 26 – Sequence of events during the LOHS transient

TW	Event	Time [s]
1	MHX isolation. Initial lead temperature increase	0-78
2	Start of pool boiling and lead temperature reduction	78-112
3	Pb temperature rise, and achievement of the shutdown set point	112-156
4	Pb temperature continues to increase	156-208
5	Cold water passage in the MHX due to the PRZ venting valve opening	208-400
6	No power exchange in the MHX	400-482
7	Cold lead reaches the MHX	>482

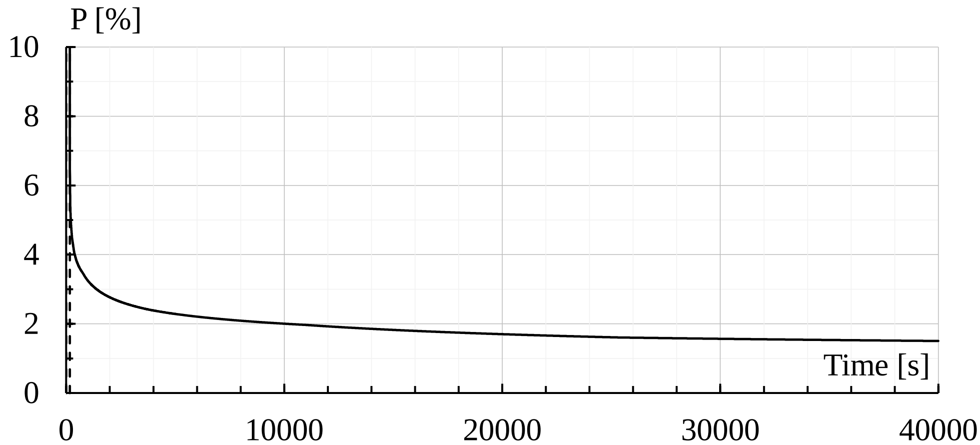

Figure 108 – Decay heat curve

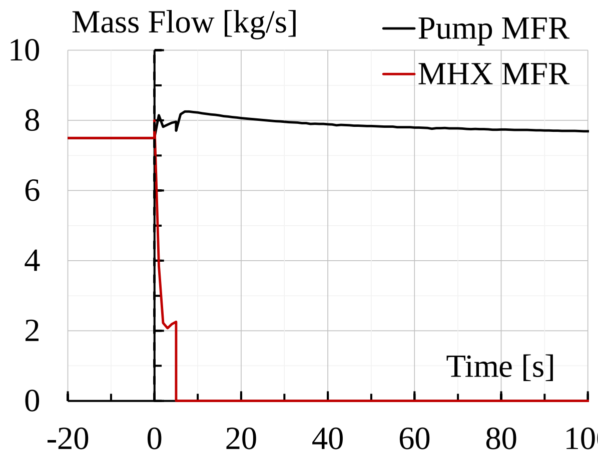

Figure 109 – Water mass flow rate at the pump and MHX inlet valve locations

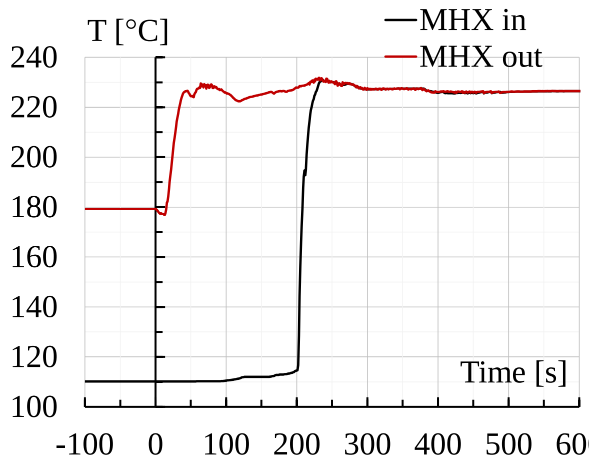

Figure 110 – Water temperatures at MHX inlet and outlet in the first 600 s

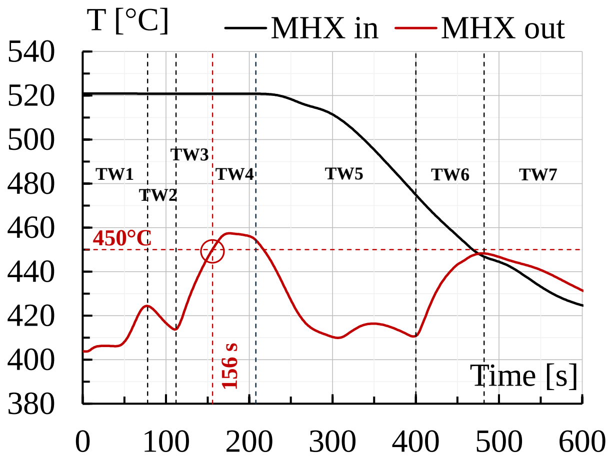

Figure 111 – Lead temperatures at MHX inlet and outlet in the first 600 s

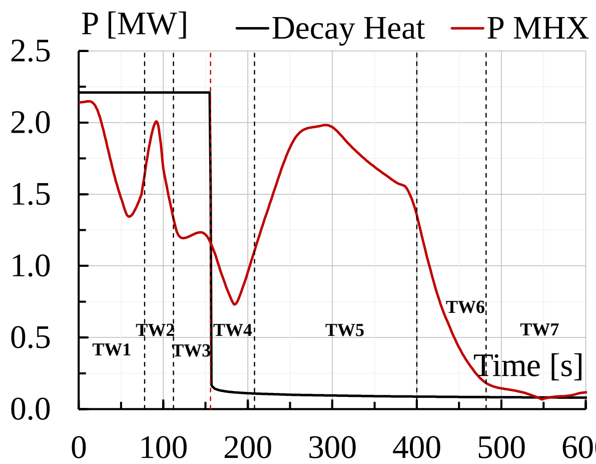

Figure 112 – Power balance in the first 600 s

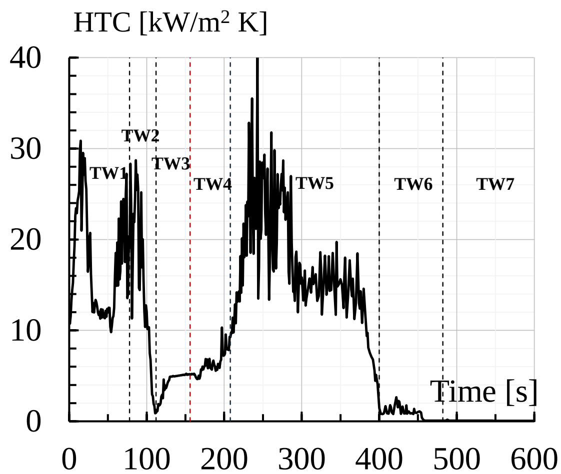

Figure 113 – Average heat transfer coefficient in the MHX (water side)

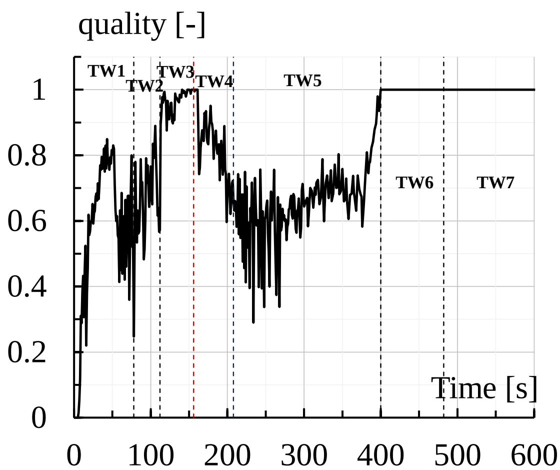

Figure 114 – Average quality in the MHX (water side)

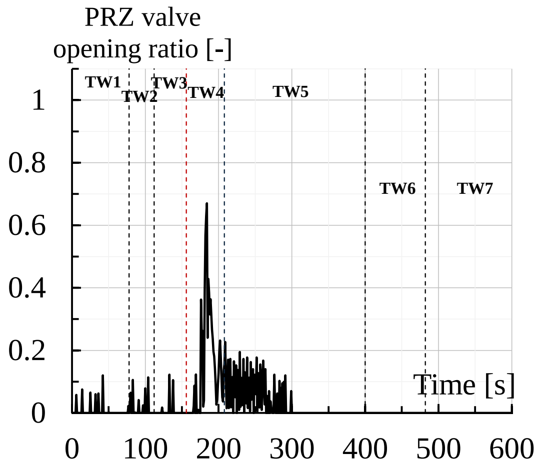

Figure 115 – Pressurizer venting valve opening ratio

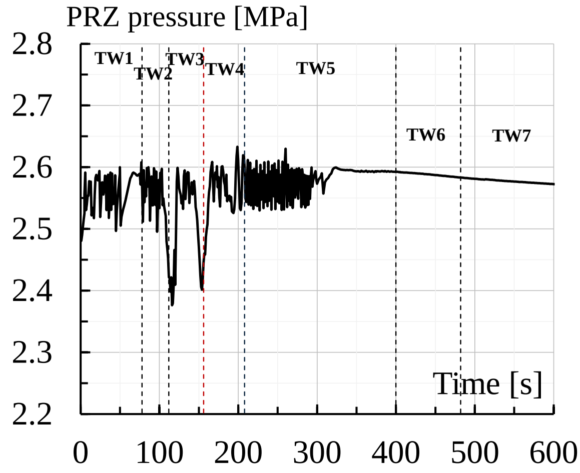

Figure 116 – Pressure transient in the pressurizer

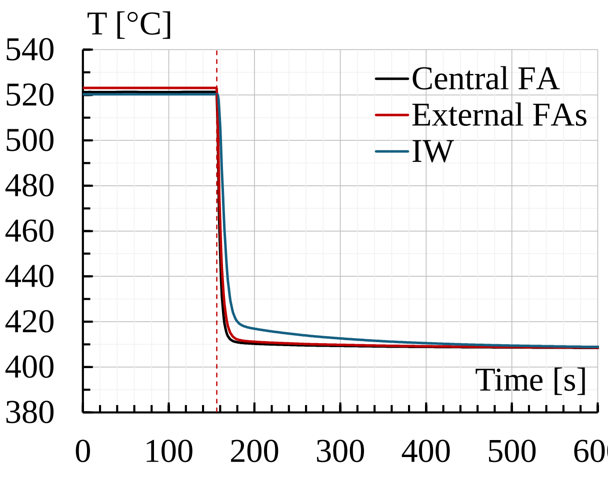

Figure 117 – Lead temperatures at CS outlet in the first 600 s

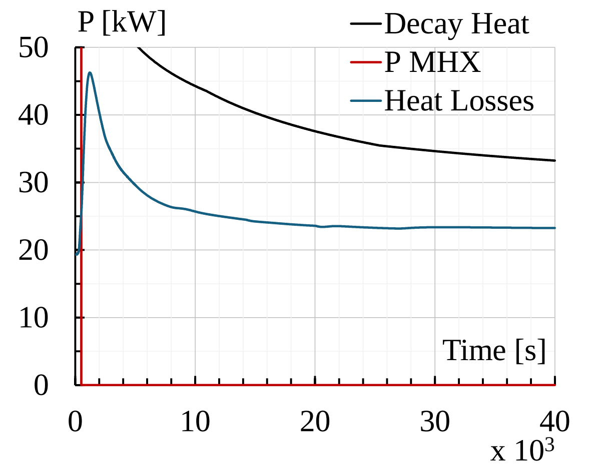

Figure 118 – Power balance in the long term

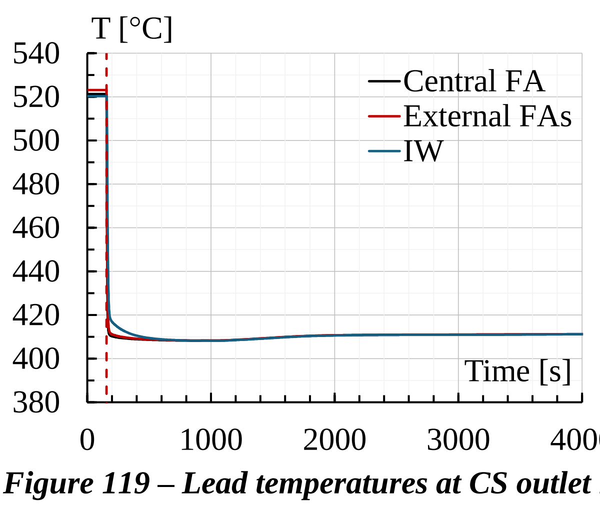

Figure 119 – Lead temperatures at CS outlet in the long term

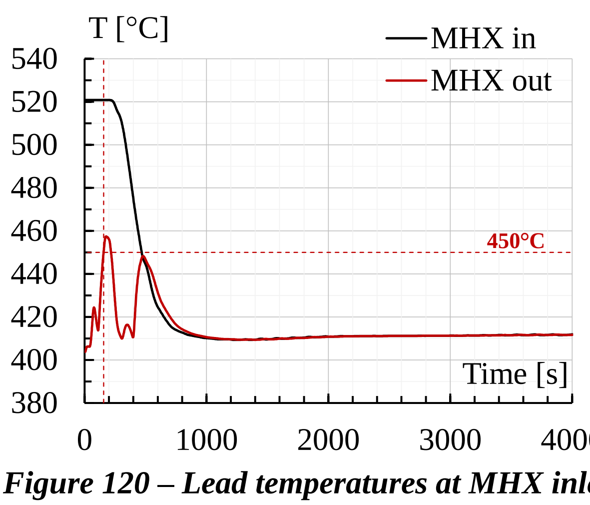

Figure 120 – Lead temperatures at MHX inlet and outlet in the long term

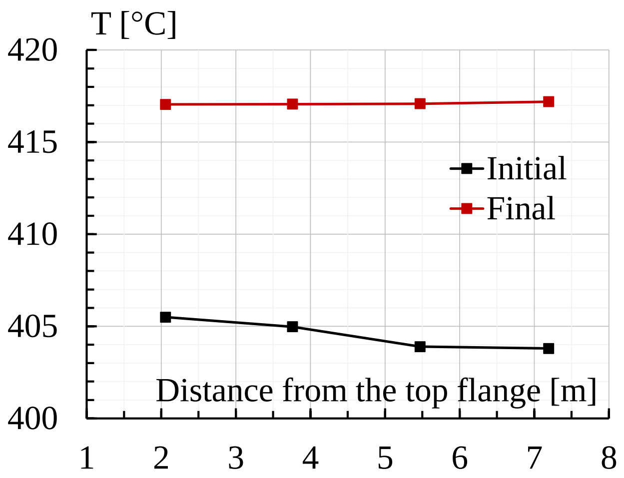

Figure 121 – Lead temperature profile in the barrel region before and after the transient

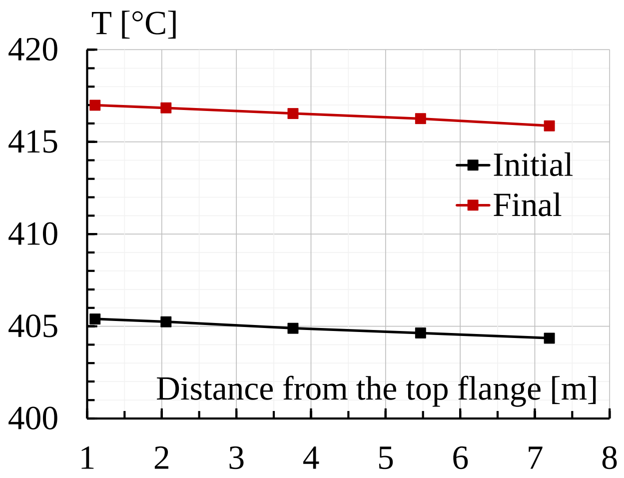

Figure 122 – Lead temperature profile in the vessel region before and after the transient

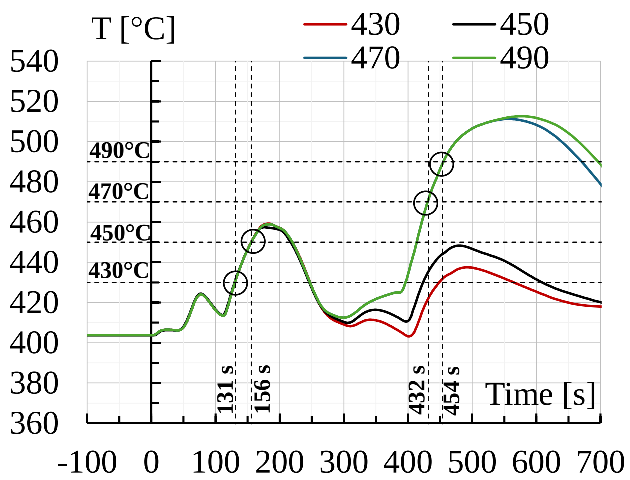

Figure 123 – Effect of different CS shutdown temperatures on the MHX outlet temperature in the short term

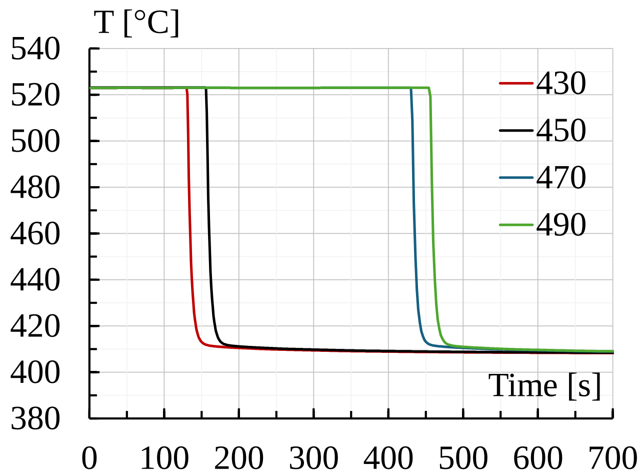

Figure 124 – Effect of different CS shutdown temperatures on the CS outlet temperatures in the short term

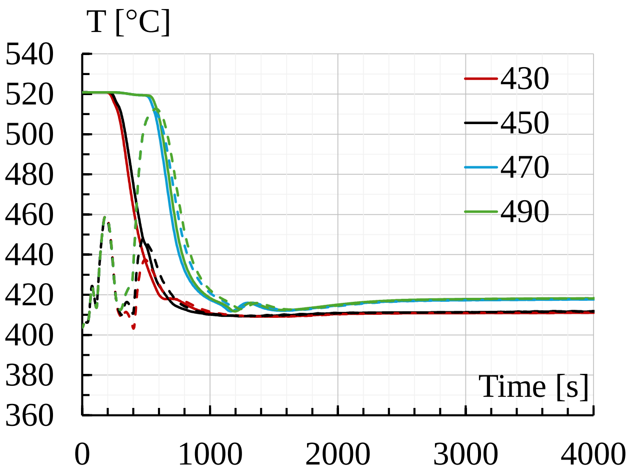

Figure 125 – Effect of different CS shutdown temperatures on the MHX inlet and outlet temperatures in the long term

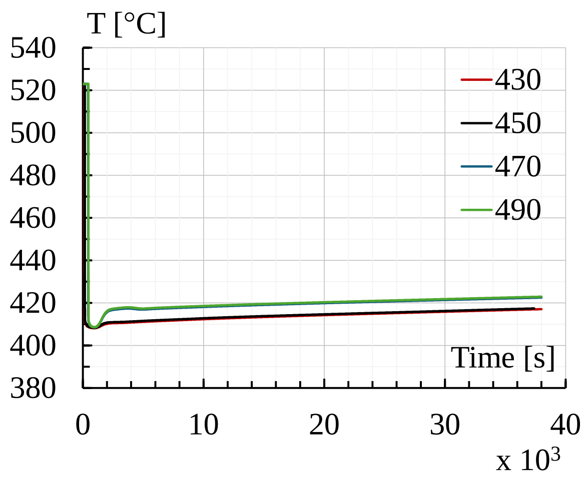

Figure 126 – Effect of different CS shutdown temperatures on the CS outlet temperatures in the long term

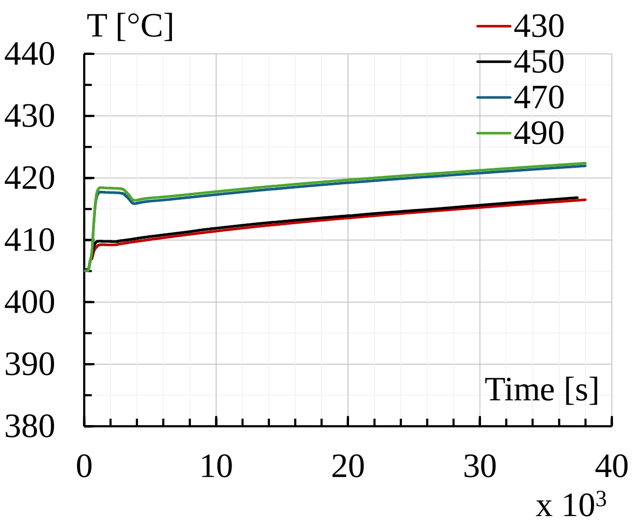

Figure 127 – Effect of different CS shutdown temperatures on the vessel region temperatures

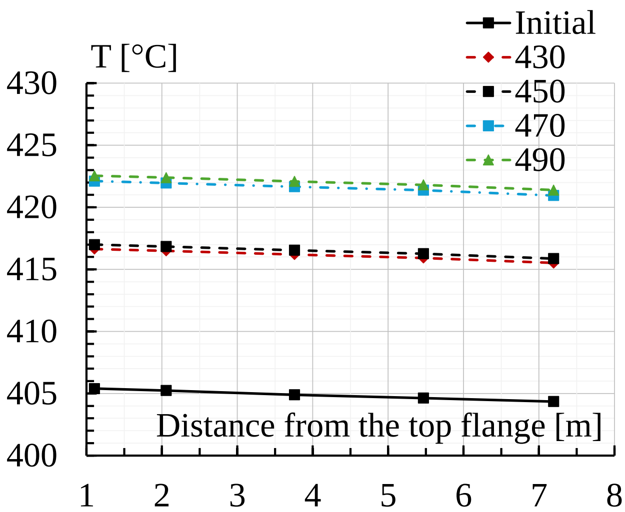

Figure 128 – Effect of different CS shutdown temperatures on the final temperature profile along the vessel

LOFA Transient

The LOFA transient is triggered by the trip of the MCP (this event represents the SoT), and when the temperature at the CS outlet reaches 800°C, the CS is switched off. In ATHENA, if the pump was switched off and the MHX continued operating, the lead temperature at the MHX outlet would reach values close to the solidification one (327°C), since the water inlet temperature is far below this value. To avoid such an issue, and to be more representative of the ALFRED reactor, the following actions are taken after the achievement of the steady state described in Sect. 4.3.2:

- Closure of the MHX interception valves and opening of the discharge valve which leads to a reduction in the enthalpy within the BTs due to the evaporation of the remaining fluid and the release of the generated steam (Figure 129).
- Actuation of the pump trip when the enthalpy inside the MHX equals that of the ALFRED reactor SG [22], scaled according to the power. This results in a target value of 1.01×10^7 J, in such a way that the MHX cooling power is representative of the ALFRED SG's one at the SoT.
- CS shutdown, which follows the decay curve [90] already described in the LOHS transient, occurs when the outlet temperature from the central FA reaches 800°C (see Figure 130).

The coupling simulation starts at the beginning of the MHX emptying. Compared to the RELAP5 stand-alone simulation, the target enthalpy condition in the MHX is achieved at a slightly different time. This discrepancy arises from the different conditions of the lead flowing from the CS to the MHX inlet. However, despite this difference in timing, the overall enthalpy reduction trends between the stand-alone and coupled models remain quite similar. To compare the stand-alone RELAP5 and coupled results, the time axes from Figure 130 to Figure 133 have been aligned. Therefore, it is assumed that the MCP trip occurs at the same instant.

The mass flow rate reduction for the three fluid channels (central and external FAs, and the IW region) is shown in Figure 131, where the coupled simulation predicts a faster transient than the stand-alone simulation for all channels. This difference arises due to the different pressure drop representation in the CS of the coupled model, which can be further enhanced by the transition to a different flow regime. In fact, the Reynolds number in the FAs switches from ~40000 (turbulent regime) to ~3500 (transition regime).

Regarding the outlet temperatures from the three fluid channels, Figure 132 highlights several key differences between the coupled and the STH simulations:

- The central and external FAs outlet temperatures rise more quickly and reach lower peak values in the coupled simulation.
- The IW outlet temperature peak is lower, and the trend is smoother than in the STH calculation, though the overall trend aligns with the STH stand-alone simulation toward the end of the transient.
- The temperature difference between the three fluid channels is more pronounced in the coupled approach, especially near the end of the simulation.

The faster but lower temperature peaks observed in the FAs in the coupled simulation can be attributed to the different mass flow rate transitions and the different heat capacity of the CS solid structures. The current porous media model does not account for the heat capacity of the pins, which contributes to this difference. Future improvements of the model will include also the heat capacity of the interior of the pins.

Regarding the temperature trend in the IW region, it must be highlighted that the heat transferred is due to the convection and conduction from the FAs to the bypass fluid. Figure 133 shows the power – calculated with an energy balance between the inlet and outlet of the CFD domain – transferred to the IW. As expected, the CFD model exhibits a notable difference from the RELAP5 simulation since the steady state before the SoT. During the transient, the coupled calculation predicts a higher peak in the power, and a lower peak in the temperature (see Figure 132). The discrepancy in the exchanged power can be attributed to the higher temperature field within the FAs in the coupled simulation, which leads to a higher peak, while the lower peak in the temperature trend is due to RELAP5 neglecting the 3D heat conduction within the fluid and axially in the structures.

Since the CFD model includes all heat transfer terms in its equations, it is expected to better represent the dynamics in the bypass region, especially during unprotected transients (e.g., loss of flow without SCRAM). In such cases, the heat transfer through the bypass can significantly impact the temperature distribution within the FAs and, particularly, the temperature profile of the pins. Nevertheless, the two approaches (STH and coupled simulation) converge to the same solution after the transient.

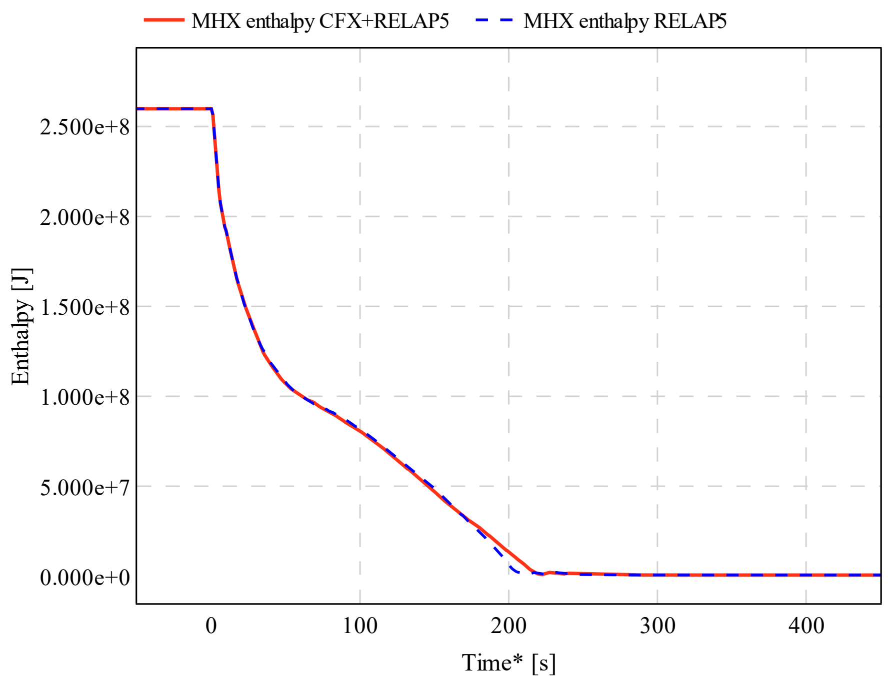

Figure 129 – Enthalpy inside the MHX

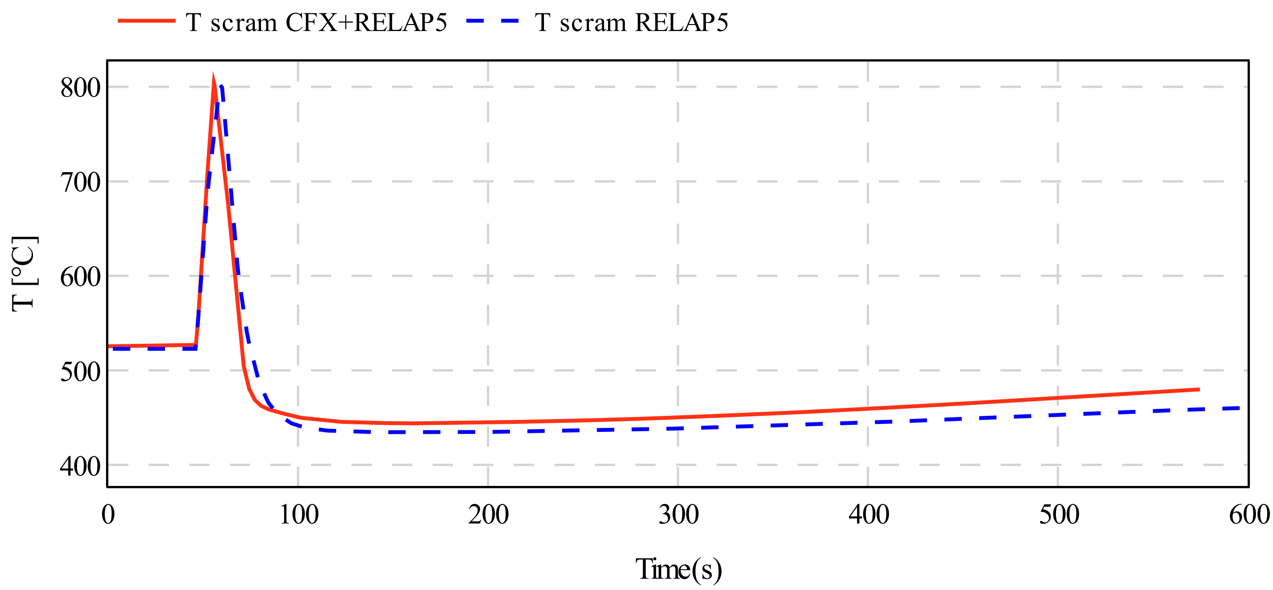

Figure 130 – Central fuel assembly outlet temperature

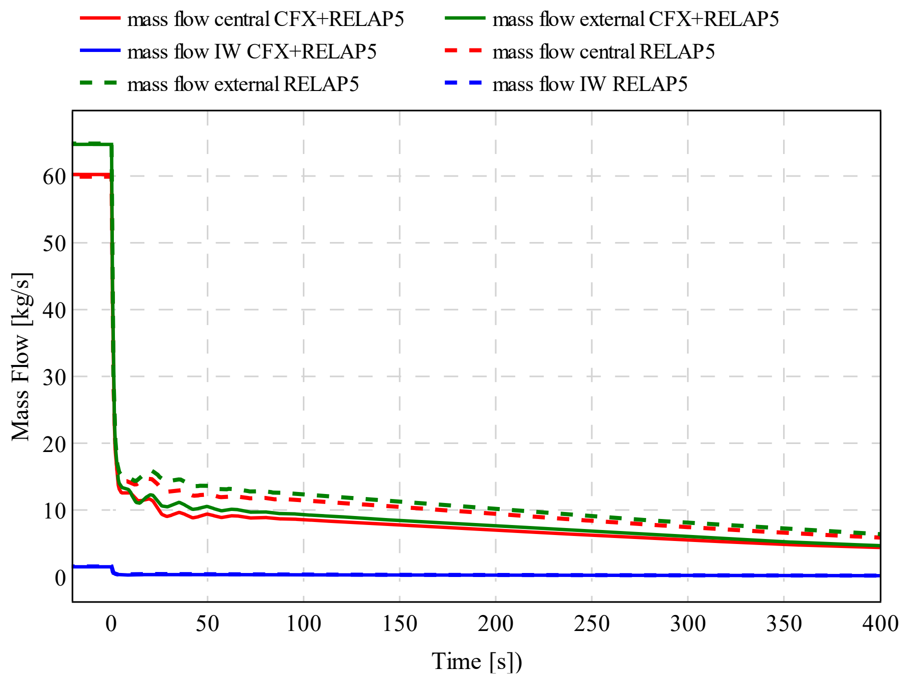

Figure 131 – Mass flow rate distribution during the LOFA among the core simulator channels (central FA, external FAs, and IW)

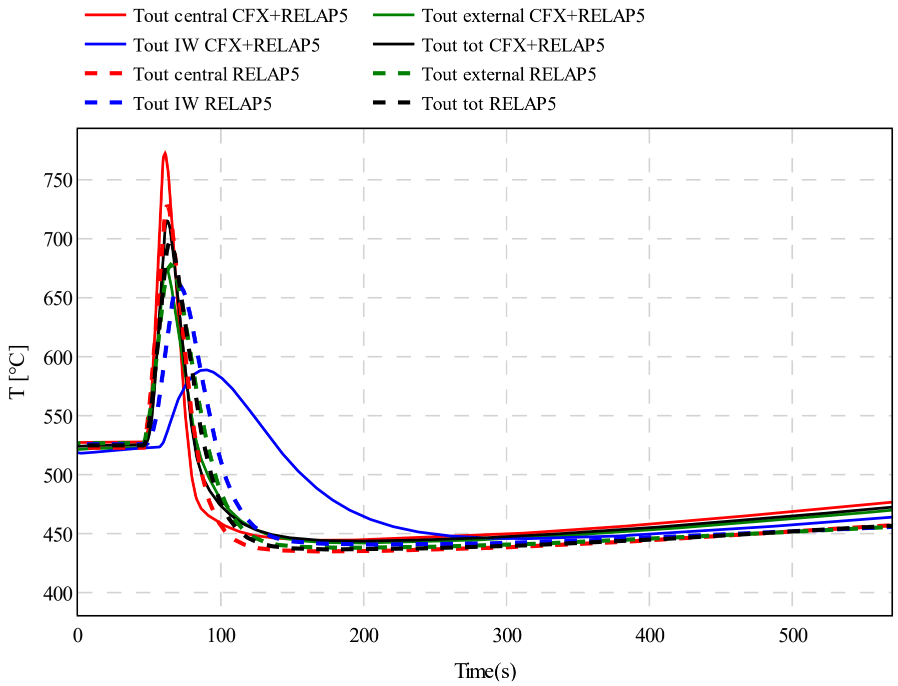

Figure 132 – Outlet temperatures from the different channels (central FA, external FAs, and IW) of the core simulator and global outlet temperature during the transient

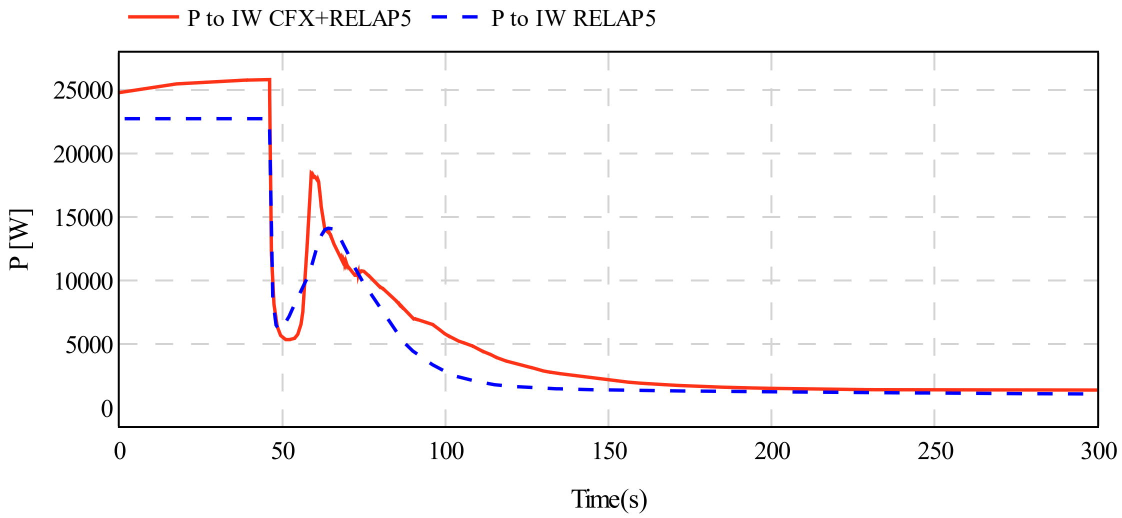

Figure 133 – Power transferred to the Inter-Wrapper region during the transient

5 CONCLUSIONS

Thermo-hydraulics of HLMs is still one of the challenges for LFR development. TH issues must be addressed from both experimental and numerical perspectives to give experimental evidence of the phenomena occurring in such reactors, and to develop and validate numerical codes capable of simulating HLMs behavior and the reactor safety systems during accidental scenarios. Multiscale codes coupling enables to consider the mutual feedback of local and system level phenomena, leveraging the strength of detailed CFD analysis and the low computational time required by STH codes. Within the framework of a collaboration between ENEA and Sapienza University of Rome, this thesis deals with the development, testing and validation activities of a novel multiscale coupling tool. The codes involved in this activity are the STH code RELAP5/Mod3.3 and the CFD code Ansys CFX.

A review of the existing TH codes and their application in HLM systems, as well as of the state of the art of the coupling methodologies, have been the starting point of the work. Even though previous works about the coupling between RELAP5 and CFX are present in the literature, the coupling methodology presented in this thesis is innovative because it relies on optimized in-house developed scripts which take care of data exchange, memory management, code synchronization, execution and post-processing. The tool is able to properly manipulate the results file to speed up the simulation, and it is flexible in the choice of the temporal advancing scheme and the spatial discretization approach. Moreover, the coupling tool is strictly connected to the "CFX Pre", where all the routines, scripts and maps can be selected, avoiding the use of intermediate tools to manage the data exchange. CFX is therefore the master code, and it imposes the constraint that its timestep must coincide with the coupling timestep, i.e., the time at which the codes exchange information. RELAP5 is allowed to run with a smaller timestep, and it was found that this technique generally improved numerical stability of the results.

Two different time advancing schemes have been developed: the explicit and semi-implicit scheme. A fully implicit scheme could not be implemented because of the nature of the selected codes, since each one relies on its solver. The explicit scheme consists in exchanging the results at each coupling timestep. Since RELAP5 is the first code to execute its timestep(s), it provides BCs at the end of the coupling timestep. In this way, CFX is allowed to use the RELAP5 results at the end of its timestep, leveraging its implicit resolution scheme. The main limitation of this method is that BCs for the RELAP5 run are, in contrast, constant throughout the coupling timestep since the corresponding timestep is calculated later by CFX. However, the explicit scheme proved to be reliable and stable as long as the coupling timestep is sufficiently small, and the gradients faced during the transient are limited. To overcome this limitation, the semi-implicit scheme has been developed, which consists in iterating the coupling timestep until the difference between the RELAP5 results between two consecutive iterations is smaller than a non-dimensional user-defined tolerance. Being RELAP5 the first code to resolve the timestep, such a scheme can converge in principle in a single CFX timestep, and after the second RELAP5 timestep. This technique allows to save computational time, and it tends to an explicit scheme when transients approach a new steady state. In the semi-implicit scheme, CFX provides BCs for the RELAP5 run also at the end of the coupling timestep, allowing RELAP5 to interpolate BCs between the initial and final time instants. In this way, larger coupling timesteps compared to the explicit scheme can be adopted without losing numerical stability, but at the cost of more iterations within the same timestep especially at the beginning of a transient.

Two domain discretization approaches have also been developed to make the tool as versatile as possible. The domain decomposition approach consists of replacing the region simulated by the CFD with BCs in the STH domain. In RELAP5, such BCs are provided through time-dependent volumes and junctions, which impose pressure, temperature, and mass flow rate. If a thermal coupling must be simulated, heat structures are introduced with a corresponding heat flux or heat transfer coefficient. To be used in the RELAP5 calculation, CFX results are averaged on the corresponding boundary and converted into 1D results. Conversely, RELAP5 results are multiplied by a non-dimensional map – previously calculated through a CFX stand-alone calculation – to provide 2D or 3D BCs. In this scheme, a check on the mass and energy conservation must be done between the inlet and outlet time-dependent volumes and junctions. Implementing the domain overlapping approach, this conservation is ensured by RELAP5 itself, since there is no mass flowing in or out of the system, and in some cases, it can result in a more stable result. With the domain overlapping, CFD results are considered through "CFD-informed" pressure loss coefficient or friction factor to impose the pressure drop across the overlapped domain, and fake heat structures (with infinite thermal conductivity and null thermal capacity) that impose temperatures at the inlet and outlet boundaries, and in the overlapped domain in order to match the average density of the CFD domain.

The validation activity has involved data from three experimental facilities: SIRIO, NACIE-UP, and TALL-3D. In particular, SIRIO experimental data produced within the PIACE project have been used to validate a version of the RELAP5/Mod3.3 stand-alone code modified by Sapienza, without using the coupled tool. This preliminary activity was necessary to provide the coupled tool with a STH code capable of simulating a variety of phenomena that are not studied in detail for LWRs applications, but that are relevant for passive safety systems of Gen-IV reactors. Such phenomena are mainly pool boiling and condensation at high pressure in presence of non-condensable gases. Separate effect test facilities are required to analyze independently the main phenomena occurring, in particular, in the IC (both tube and pool side) with dedicated instrumentation. In addition, integral effect tests similar to the one discussed in the current PhD thesis should be repeated to explore also a wider range of operating conditions, once the instrumentation in the SIRIO facility will be upgraded. The upgrade of the facility is foreseen within the framework of the Euratom LESTO project that started in November 2024. Currently, it is undergoing the procurement stage.

The work then focused on the validation of the coupled tool through a comparison with experimental data from the LBE-cooled facilities NACIE-UP and TALL-3D. Both the experiments involved a transition from forced to natural circulation regime. The main difference between the two facilities is that NACIE is a 1D loop, with focus on the fuel assembly TH, while TALL-3D features three vertical legs (two risers and one downcomer), with a pool-type test section installed in one of them. The transition from forced to natural circulation leads also to the transition from pool mixing to thermal stratification inside the pool, causing oscillations in the mass flow rate distribution between the vertical legs. The simulations with the coupled tool have confirmed the predominance of 1D phenomena in the NACIE-UP loop, since no significant differences have been observed with respect to a RELAP5 stand-alone calculation, while in the TALL-3D experiment, the CFD contribution in simulating the pool has given feedback on the timing at which the mass flow rate peaks during the oscillations are reached. However, in both cases, the CFD simulations were able to give local outlooks inside the test sections, providing information about local hotspots and thermal fields within the components.

After the validation phase, the coupled tool has been applied to simulate the ATHENA experimental facility, which is currently under construction, and it aims to support the ALFRED development by addressing the main LFR TH and coolant chemistry issues. A description of the facility has been provided, and the complete numerical model of the facility has been realized through the RELAP5 code, simulating the primary, secondary and tertiary systems. The CFX model of the CS has been described, and it has been used in the coupled simulation. After the sizing of the MHX, a verification of its design has been performed through a RELAP5 simulation using part of the complete model of ATHENA and applying suitable BCs. Then, the numerical steady state characterization of the facility has been realized, and two transient calculations have been performed to assess the behavior of the facility under accidental conditions. In particular, the LOHS and LOFA transients have been simulated through the RELAP5 stand-alone and coupled tool, respectively.

In the LOHS case, a sensitivity analysis on the set point temperature at the MHX outlet for the CS shutdown has been performed, considering values of 430, 450, 470, and 490°C to assess the system response if the set point temperature is reached later after the transient is triggered. Simulations have shown that the facility does not reach hazardous conditions because of the high thermal inertia of the cold pool, which absorbs a large amount of energy before the heat losses become competitive with the decay heat in the long term. Translated to the reactor, this outcome confirms the design of ALFRED, that, featuring a large cold pool compared to the hot pool, it gives more time for the intervention of safety systems.

The coupled tool has been adopted only for the LOFA simulations because, in the case of the pump stop and the consequent transition to the natural circulation regime, low velocities are expected in the system, and the suitability of the models and correlations implemented in RELAP5 must be evaluated. The coupled simulation has shown that the mass flow rate during the transient is slightly different compared to the RELAP5 stand-alone simulations, affecting the temperature field within the CS. Moreover, the CFD simulation of the CS has shown that the power transferred to the bypass region is higher than the those predicted by RELAP5. The capability of the CFD to consider conduction within the fluid and to deal with quasi-stagnant fluid, as in the bypass region, allows for a better prediction of the peak temperature inside the core, overcoming the intrinsic limitations of STH codes.

Future work will involve further validation of the coupled tool. A comparison with experimental data from ATHENA facility will be made as soon as they become available. Experiments conducted on other integral effect test facilities like CIRCE, located at ENEA Brasimone R.C., are expected also to provide a database available for codes validation, enhancing their accuracy and improving their readiness to be applied to reactor scale analyses. In this framework, this thesis offers a significant contribution to coupled code development and reactor simulation, making available a coupled tool to support design and safety assessment of HLM systems.

LIST OF REFERENCES

[1] United Nations. (2015). "Transforming our world: The 2030 agenda for sustainable development", https://sdgs.un.org/goals

[2] IPCC, 2023: Sections. In: "Climate Change 2023: Synthesis Report. Contribution of Working Groups I, II and III to the Sixth Assessment Report of the Intergovernmental Panel on Climate Change", [Core Writing Team, H. Lee and J. Romero (eds.)]. IPCC, Geneva, Switzerland, pp. 35-115, doi: 10.59327/IPCC/AR6-9789291691647

[3] U.S. DOE Nuclear Energy Research Advisory Committee, Generation IV International Forum, "A technology roadmap for Generation IV nuclear energy systems", USA, 2002. Report No.: GIF-002-00. https://www.gen-4.org/gif/jcms/c_40481/technology-roadmap

[4] U.S. DOE Nuclear Energy Research Advisory Committee, Generation IV International Forum, "Technology roadmap update for Generation IV nuclear energy systems", USA, 2014. https://www.gen-4.org/gif/jcms/c_60729/technology-roadmap-update-2013

[5] Gen IV International Forum (2020), "Generation IV Goals", https://www.gen-4.org/gif/jcms/c_9502/generation-iv-goals

[6] A. Alemberti, K. Tucek, M. Takahashi, T. Obara, M. Kondo, A. Moiseev, L. Tocheny, C. Smith, I. S. Hwang, Y. Wu, M. Jin, "Lead-cooled Fast Reactor (LFR) System Safety Assessment", https://www.gen-4.org/gif/upload/docs/application/pdf/2020-06/gif_lfr_ssa_june_2020_2020-06-09_17-26-41_202.pdf, GIF, 2020.

[7] P. Lorusso, S. Bassini, A. Del Nevo, I. Di Piazza, F. Giannetti, M. Tarantino, M. Utili, "Gen-IV LFR Development, Status & Perspectives", *Progress in Nuclear Energy*, 105, pp. 318-331, 2018. https://doi.org/10.1016/j.pnucene.2018.02.005

[8] F. Tassone, M. E. Ricotti, S. Lorenzi, G. Locatelli, "Economics and finance of lead fast reactors: A systematic literature review", *Progress in Nuclear Energy*, 174, 105298, 2024. https://doi.org/10.1016/j.pnucene.2024.105298

[9] A. Alemberti M. Frignani, G. Villabruna, P. Agostini, G. Grasso, M. Tarantino, I. Turcu, M. Constantin, D. Diaconu, F. Di Gabriele, N. Witzanyova, M. Krykova, "ALFRED and the lead technology research infrastructure", *Proceedings of European Research Reactor Conference (RRFM)*, Bucharest, Romania, April 19-23, 2015.

[10] M. Frignani, A. Alemberti, "ALFRED: A Strategic Vision for LFR Deployment", *ANS Winter Meeting 2017*, Washington, D.C., October 29-November 2, 2017.

[11] L. Cinotti, P. Briger, G. Grasso, "Simplification, the atout of LFR-AS-200", *International Conference on Fast Reactors and Related Fuel Cycles: Next Generation Nuclear Systems for Sustainable Development (FR17)*, 2017.

[12] Y. G. Dragunov, V. V. Lemekhov, A. V. Moiseev, L. V. Tocheny, A. A. Umansky, "Lead-Cooled Fast-Neutron Reactor (BREST) (Approaches to the closed NFC)", *Proceedings of Global 2015*, Paris France, September 20-24, 2015, Paper 5435.

[13] J. Wallenius, S. Qvist, I. Mickus, S. Bortot, P. Szakalos, J. Ejenstam, "Design of SEALER, a very small lead-cooled reactor for commercial power production in off-grid applications", *Nuclear Engineering and Design*, 338, pp. 23-33, 2018. https://doi.org/10.1016/j.nucengdes.2018.07.031

[14] G. Acharya, "Investigating the Application of Self-Actuated Passive Shutdown System in a Small Lead-Cooled Reactor", MS thesis, KTH Royal Institute of Technology, 2019. https://www.diva-portal.org/smash/get/diva2:1330700/FULLTEXT02

[15] M. Frignani, A. Alemberti, G. Villabruna, G. Grasso, M. Tarantino, M. Constantin, I. Turcu, S. Valeca, F. Di Gabriele, V. Romanello, "FALCON advancements towards the implementation of the ALFRED

Project", *International Conference on Fast Reactors and Related Fuel Cycles: Next Generation Nuclear Systems for Sustainable Development (FR-17)*, Yekaterinburg, Russian Federation, June 26-29, 2017.

[16] https://www.raten.ro/?lang=en

[17] https://www.ansaldoenergia.com/companies/ansaldo-nucleare

[18] https://www.enea.it/it/

[19] https://www.newcleo.com/

[20] https://www.blykalla.com/technology

[21] A. Alemberti, L Mansani, M. Frogheri, M. Constantin, I. Turcu, "ALFRED project – Conceptual Design Safety Features, and Perspective of Implementation", *The International Symposium on Nuclear Energy (SIEN)*, Bucharest, Romania, November 2013.

[22] E. Bubelis, K. Mikityuk, "Plant data for the safety analysis of the ETDR (ALFRED)", TEC058-2012, LEADER project, 2012.

[23] G. Bandini, M. Polidori, "Report on the results of analysis of DEC events for the ETDR (ALFRED)", DEL022-2013, LEADER project, 2013.

[24] M. Frignani, A. Alemberti, M. Tarantino, "ALFRED: A revised concept to improve pool related thermal-hydraulics", *Nuclear Engineering and Design*, 355, 110359, 2019. https://doi.org/10.1016/j.nucengdes.2019.110359

[25] M. Frignani, A. Alemberti, M. Tarantino, G. Grasso, "ALFRED staged approach", *Proceedings of the International Congress on Advances in Nuclear Power Plants (ICAPP 2019)*, Juan-les-pins, France, May 12-15, 2019.

[26] A. Alemberti, M. Caramello, M. Frignani, G. Grasso, F. Merli, G. Morresi, M. Tarantino, "ALFRED reactor coolant system design", *Nuclear Engineering and Design*, 370, 110884, 2020. https://doi.org/10.1016/j.nucengdes.2020.110884

[27] M. Tarantino, "ALFRED Overview and Safety Features", *Ninth Joint IAEA-GIF Technical Meeting/Workshop on the Safety of Liquid Metal Cooled Fast Reactors*, 2021. https://inis.iaea.org/collection/NCLCollectionStore/_Public/52/041/52041029.pdf

[28] V. S. Smirnov, "Safety features of a power unit with the BREST-OD-300 reactor", *International Conference on Fast Reactors and Related Fuel Cycles: Safe Technologies and Sustainable Scenarios*, 4-7 March, 2012, Paris, France.

[29] V. V. Orlov, A. I. Filin, A. V. Lopatkin, A. G. Glazov, L. P. Sukhanov, V. I. Volk, P. P. Poluektov, O. A. Ustinov, M. T. Vorontsov, V. F. Leontiev, R. S. Karimov, "The closed on-site fuel cycle of the brest reactors", *Progress in Nuclear Energy*, 47 (1-4), pp. 171-177, 2005. https://doi.org/10.1016/j.pnucene.2005.05.017

[30] J. Wallenius, "Status of Blykalla's commercial LFR development in Sweden", *Webinar GIF talks with industry series #2*, July 17, 2024.

[31] M. Tarantino, M. Angiolini, S. Bassini, S. Cataldo, C. Ciantelli, C. Cristalli, A. Del Nevo, I. Di Piazza, D. Diamanti, M. Eboli, A. Fiore, G. Grasso, F. Lodi, P. Lorusso, R. Marinari, D. Martelli, F. Papa, C. Sartorio, M. Utili, A. Venturini, "Overview on Lead-Cooled Fast Reactor Design and Related Technologies Development in ENEA", *Energies*, 14 (16), 5157, 2021. https://doi.org/10.3390/en14165157

[32] M. Constantin, G. Grasso, M. Tarantino, I. Turcu, C. Paunoiu, A. Toma, M. Caramello, M. Frignani, A. Alemberti, D. Diaconu, M. Nitoi, M. Apostol, D. Gugiu, P. Agostini, "The development of the research infrastructure in support of ALFRED demonstrator implementation in Romania", *EMERG – Energy. Environment. Efficiency. Resources. Globalization*, 7 (1), pp. 123-132, 2021. http://dx.doi.org/10.37410/EMERG.2021.1.10

[33] http://www.srs.it/

[34] https://www.fucinaitalia.it/home/

[35] E. Merzari, A. Obabko, P. Fischer, "Spectral element methods for liquid metal reactors applications", 2017. https://doi.org/10.48550/ARXIV.1711.09307

[36] H. K Versteeg, W. Malalasekera, "An introduction to Computational Fluid Dynamics (2nd ed.)", Pearson, 2007.

[37] A. Petruzzi, F. D'Auria, "Thermal-hydraulic system codes in nuclear reactor safety and qualification procedures", *Science and Technology of Nuclear Installations*, 2008, 460795. http://dx.doi.org/10.1155/2008/460795

[38] V Narcisi, F. Giannetti, G. Caruso, "Investigation on RELAP5-3D© capability to predict thermal stratification in liquid metal pool-type system and comparison with experimental data", *Nuclear Engineering and Design*, 352, 110152, 2019. https://doi.org/10.1016/j.nucengdes.2019.110152

[39] N. Forgione, D. Martelli, G. Barone, F. Giannetti, P. Lorusso, T. Hollands, A. Papukchiev, M. Polidori, A. Cervone, I. Di Piazza, "Post-test simulations for the NACIE-UP benchmark by STH codes", *Nuclear Engineering and Design*, 353, 110279, 2019. https://doi.org/10.1016/j.nucengdes.2019.110279

[40] G. Bandini, M. Polidori, A. Gerschenfeld, D. Pialla, S. Li, W. M. Ma, P. Kudinov, M. Jeltsov, K. Kööp, K. Huber, X. Cheng, C. Bruzzese, A. G. Class, D. P. Prill, A. Papukchiev, C. Geffray, R. Macian-Juan, L. Maas, "Assessment of systems codes and their coupling with CFD codes in thermal–hydraulic applications to innovative reactors", *Nuclear Engineering and Design*, 281, pp. 22-38, 2015. http://dx.doi.org/10.1016/j.nucengdes.2014.11.003

[41] V. Narcisi, L. Melchiorri, F. Giannetti, G. Caruso, "Assessment of RELAP5-3D for application on in-pool passive removal systems", *Proceedings of the 30th European Safety and Reliability Conference and the 15th Probabilistic Safety Assessment and Management Conference*, Venice, Italy, 2020.

[42] V. Moreau, M. Profir, A. Alemberti, M. Frignani, F. Merli, M. Belka, O. Frybort, T. Melichar, M. Tarantino, S. Franke, S. Eckert, A. Class, J. Yanez, D. Grishchenko, M. Jeltsov, P. Kudinov, F. Roelofs, K. Zwijsen, D. C. Visser, A. Badillo, B. Niceno, D. Martelli, "Pool CFD modelling: Lessons from the sesame project", *Nuclear Engineering and Design*, 355, 110343, 2019. https://doi.org/10.1016/j.nucengdes.2019.110343

[43] P. Cioli Puviani, I. Di Piazza, R. Marinari, R. Zanino, M. Tarantino, "Multiscale Thermal-Hydraulic Analysis of the ATHENA Core Simulator", *Nuclear Technology*, 210 (4), pp. 692-712. https://doi.org/10.1080/00295450.2023.2215682

[44] G. Lenci, J. Feng, E. Baglietto, "A generally applicable hybrid unsteady Reynolds-averaged Navier–Stokes closure scaled by turbulent structures", *Physics of Fluids*, 33, 105117, 2021. https://doi.org/10.1063/5.0065203

[45] A. Gerschenfeld, N. Forgione, J. Thomas, "Multiscale simulations of liquid metal systems", In F. Roelofs (Ed.), Thermal Hydraulics Aspects of Liquid Metal Cooled Fast Reactors (pp. 45-60), Woodhead Publishing, 2018.

[46] The RELAP5-3D© Code Development Team, "RELAP5-3D Code Manual Vol.1 Code Structure, System Models and Solution Methods", INL/MIS-15, 2015.

[47] GRS, ATHLET 3.3 User's Manual, Report GRS-P-1/Vol.1 Rev.9, November 2021.

[48] USNRC. (2008). TRACE V5.0 Developmental Assessment Manual. ADAMS ML120060208, ML120060187, ML120060191, ML120060172.

[49] Argonne National Laboratory. "SAM: A Modern System Analysis Tool for Advanced Nuclear Reactors", https://www.anl.gov/nse/system-analysis-module

[50] ANSYS FLUENT 12.0 Theory Guide, January 2009.

[51] ANSYS CFX-Solver Theory Guide, November 2011.

[52] Siemens 2021 STAR-CCM+ User Manual" [Online]. Available: https://docs.sw.siemens.com/documentation/external/PL20200617112215329/en-US/userManual/userGuide/ html/index.html#page/connect%2Fsplash.html

[53] D. L. Aumiller, E. T. Tomlinson, R. C. Bauer, "A coupled RELAP5-3D/CFD methodology with a proof-of-principle calculation", *Nuclear Engineering and Design*, 205, 83-90, 2001. https://doi.org/10.1016/S0029-5493(00)00370-8

[54] D. Bertolotto, A. Manera, S. Frey, H.-M. Prasser, R. Chawla, "Single-phase mixing studies by means of a directly coupled CFD/system-code tool", *Annals of Nuclear Energy*, 36 (3), pp. 310-316, 2009. https://doi.org/10.1016/j.anucene.2008.11.027

[55] D. Martelli, N. Forgione, G. Barone, A. Del Nevo, I. Di Piazza, M. Tarantino, "Coupled simulations of natural and forced circulation tests in NACIE facility using RELAP5 and ANSYS Fluent codes", *Proceedings of the 22nd International Conference on Nuclear Engineering (ICONE22)*, Prague, Czech Republic, July 7-11, 2014. ICONE22-30552, V004T10A020. https://doi.org/10.1115/ICONE22-30552

[56] D. Martelli, N. Forgione, G. Barone, I. Di Piazza, "Coupled simulations of the NACIE facility using RELAP5 and ANSYS FLUENT codes", *Annals of Nuclear Energy*, 101, pp. 408-418, 2017. https://doi.org/10.1016/j.anucene.2016.11.041

[57] N. Forgione, M. Angelucci, C. Ulissi, D. Martelli, G. Barone, R. Ciolini, M. Tarantino, "Application of RELAP5/Mod3.3 – Fluent coupling codes to CIRCE-HERO", *Journal of Physics: Conference Series*, 1224 (2019), 012032, 36th UIT Heat Transfer Conference, Catania, Italy, June 25–27, 2018. https://iopscience.iop.org/article/10.1088/1742-6596/1224/1/012032

[58] A. Toti, "Development and Validation of a System Thermal-Hydraulic/CFD Codes Coupling Methodology for Multi-Scale Transient Simulations of Pool-Type Reactors", PhD thesis, Ghent University, 2018.

[59] D. Grishchenko, M. Jeltsov, K. Kööp, A. Karbojian, W. Villanueva, P. Kudinov, "The TALL-3D facility design and commissioning test for validation of coupled STH and CFD codes", *Nuclear Engineering and Design*, 290, pp. 144-153, 2015. https://doi.org/10.1016/j.nucengdes.2014.11.045

[60] W. Li, X. Wu, D. Zhang, G. Su, W. Tian, S. Qiu, "Preliminary study of coupling CFD code FLUENT and system code RELAP5", *Annals of Nuclear Energy*, 73, pp. 96-107, 2014. https://doi.org/10.1016/j.anucene.2014.06.042

[61] T. P. Grunloh, A. Manera, "A novel domain overlapping strategy for the multiscale coupling of CFD with 1D system codes with applications to transient flows", *Annals of Nuclear Energy*, 90, pp. 422-432, 2016. https://doi.org/10.1016/j.anucene.2015.12.027

[62] T. P. Grunloh, A. Manera, "A novel multi-scale domain overlapping CFD/STH coupling methodology for multi-dimensional flows relevant to nuclear applications", *Nuclear Engineering and Design*, 318, pp. 85–108, 2017. http://dx.doi.org/10.1016/j.nucengdes.2017.03.027

[63] A. Huxford, V. C. Leite, E. Merzari, L. Zou, V. Petrov, A. Manera, "A hybrid domain overlapping method for coupling System Thermal Hydraulics and CFD codes", *Annals of Nuclear Energy*, 189, 109842, 2023 https://doi.org/10.1016/j.anucene.2023.109842

[64] A. Huxford, L. Zou, R. Hu, V. Petrov, A. Manera, "Validation of a Hybrid Domain Overlapping Coupling Between SAM and CFD Against the TALL-3D Transients", *Nuclear Technology*, 1-8, 2024. https://doi.org/10.1080/00295450.2024.2352665

[65] M. Caramello, M. Frignani, G. Grasso, M. Tarantino, D. Martelli, P. Lorusso, I. Di Piazza, "Improvement of ALFRED thermal hydraulics through experiments and numerical studies", *Nuclear Engineering and Design*, 409, 112365, 2023. https://doi.org/10.1016/j.nucengdes.2023.112365

[66] Information Systems Laboratories, “RELAP5/Mod3.3 code manual volume I: code structure, system models, and solution methods”, March 2003.

[67] Information Systems Laboratories, “RELAP5/Mod3.3 code manual volume II: user’s guide and input requirements”, March 2006.

[68] Information Systems Laboratories, “RELAP5/Mod3.3 code manual volume II: appendix A input requirements”, March 2006.

[69] Information Systems Laboratories, “RELAP5/Mod3.3 code manual volume v: user’s guidelines”, December 2001.

[70] Information Systems Laboratories, “RELAP5/Mod3.3 code manual volume VII: summaries and reviews of independent code assessment reports”, March 2006.

[71] Information Systems Laboratories, “RELAP5/Mod3.3 code manual volume IV: models and correlations”, December 2001.

[72] ANSYS CFX-Introduction Guide, November 2011

[73] https://www.ansys.com/

[74] OECD/NEA, “Best Practice Guidelines for the Use of CFD in Nuclear Reactor Safety Applications – Revision”, NEA/CSNI/R(2014)11, February 2015.

[75] International Atomic Energy Agency, “Summary Review on the Application of Computational Fluid Dynamics in Nuclear Power Plant Design”, IAEA Nuclear Energy Series No. NR-T-1.20, IAEA, Vienna, 2022.

[76] X. Cheng, A. Batta, G. Bandini, F. Roelofs, K. Van Tichelen, A. Gerschenfeld, M. Prasser, A. Papukchiev, U. Hampel, W. M. Ma, “European activities on crosscutting thermal-hydraulic phenomena for innovative nuclear systems”, *Nuclear Engineering and Design*, 290, pp. 2-12, 2015. https://doi.org/10.1016/j.nucengdes.2014.11.007.

[77] SESAME Project, EURATOM H2020, Grant Agreement N. 654935, April 2015. https://cordis.europa.eu/project/id/654935/results

[78] M. Tarantino, F. Roelofs, A. Shams, A. Batta, V. Moreau, I. Di Piazza, A. Gershenfeld, P. Planquart, “SESAME project: advancements in liquid metal thermal hydraulics experiments and simulations”, *EPJ Nuclear Science and Technologies*, 6, 18, 2020. https://doi.org/10.1051/epjn/2019046

[79] https://www.anselmus.eu/en

[80] A. Papukchiev, S. Buchholz, “Validation of ANSYS CFX for gas and liquid metal flows with conjugate heat transfer within the European project THINS”, *Nuclear Engineering and Design*, Volume 312, pp. 338-350, 2017. https://doi.org/10.1016/j.nucengdes.2016.07.028

[81] P. Cioli Puviani, T. Del Moro, B. Gonfiotti, D. Martelli, F. Giannetti, R. Zanino, M. Tarantino, “A novel Ansys CFX – RELAP5 coupling tool for the transient thermal-hydraulic analysis of liquid metal systems”, *Progress in Nuclear Energy*, 180, 105590, 2025. https://doi.org/10.1016/j.pnucene.2024.105590

[82] A. Pucciarelli, A. Toti, D. Castelliti, F. Belloni, K. Van Tichelen, M. Moscardini, F. Galleni, N. Forgione, “Coupled system thermal Hydraulics/CFD models: General guidelines and applications to heavy liquid metals”, *Annals of Nuclear Energy*, 153, 107990, 2020. https://doi.org/10.1016/j.anucene.2020.107990

[83] D. Martelli, “Experimental and Numerical Thermal-Hydraulic Analyses in support of GEN-IV Lead-cooled Fast Reactor Design”, PhD thesis, University of Pisa, 2015.

[84] F. Oriolo, W. Ambrosini, N. Forgione, A. Napoli, M. Tarantino, “Modifiche del Codice RELAP5 Versione MOD3.2 per la Simulazione di Sistemi Refrigerati con Leghe di Pb o Pb-Bi”, RL 031/00, University of Pisa, 2000.

[85] E. Martelli, F. Giannetti, C. Ciurluini, G. Caruso, A. Del Nevo, "Thermal hydraulic modeling and analyses of the water-cooled EU DEMO using RELAP5 system code", *Fusion Engineering and Design*, 146, Part A, pp. 1121-1125, 2019. https://doi.org/10.1016/j.fusengdes.2019.02.021

[86] K. Umminger, A. Del Nevo, "Integral Test Facilities and Thermal-Hydraulic System Codes in Nuclear Safety Analysis", *Science and Technology of Nuclear Installations*, 2012, 826732, pp. 1-3. https://doi.org/10.1155/2012/826732

[87] International Atomic Energy Agency, "Safety Assessment for Facilities and Activities", pp. 26, IAEA, Vienna, 2016.

[88] R. Marinari, M. Tarantino, F. S. Nitti, A. Alemberti, M. Caramello, A. Achilli, R. Ferri, E. Rizzo, F. Giannetti, "SIRIO: an experimental facility for a new heat removal system passively controlled by non-condensable gases", *Proceedings of the 2018 26th International Conference on Nuclear Engineering (ICONE26)*, London, England, July 22-26, 2018. ICONE26-82379, V06BT08A054. https://doi.org/10.1115/ICONE26-82379

[89] PIACE Project, EURATOM H2020, Grant Agreement N. 847715, 2020. https://cordis.europa.eu/project/id/847715/reporting

[90] P. Lorusso, M. Tarantino, F. S. Nitti, A. Achilli, M. T. Cauzzi, M. Caramello, T. Hamidouche, R. Fernandez, D. Rozzia, I. Kljenak, R. Krpan, G. Jimenez, C. Queral, T. Del Moro, "Numerical Analysis and Code Qualification Based on SIRIO Experiments Within the PIACE Project", *Proceedings of the 20th International Topical Meeting on Nuclear Reactor Thermal Hydraulics (NURETH-20)*, Washington, D.C., August 20-25, 2023. http://dx.doi.org/10.13182/NURETH20-40311

[91] T. Del Moro, F. Giannetti, G. Khalil Youssef, P. Lorusso, M. Caramello, M. T. Cauzzi, M. Tarantino, "Post-Test Analysis of SIRIO Facility Data by System Thermal-Hydraulc Codes for LFR Application", *Proceedings of the 20th International Topical meeting on Nuclear Reactor Thermal Hydraulics (NURETH-20)*, Washington, D.C., August 20-25, 2023. http://dx.doi.org/10.13182/NURETH20-40092

[92] https://www.siet.it/

[93] Cassa per i Servizi Energetici e Ambientali (CSEA), "*Progetto SIRIO: Sistema di rimozione della potenza di decadimento per reattori nucleari innovativi*", 2020. https://www.csea.it/avviso/approvazione-consuntivo-progetto-sirio-bando-b-2014

[94] M. Frogheri, A. Alemberti, L. Mansani, "The lead fast reactor demonstrator (ALFRED) and ELFR design", *Proceedings of the International Conference on Fast Reactors and Related Fuel Cycles: Safe Technologies and Sustainable Scenarios (FR13)*, International Atomic Energy Agency (IAEA), Paris, France, March 4-7, 2013. http://inis.iaea.org/search/search.aspx?orig_q=RN:45089496

[95] M. Caramello, M. Gregorini, C. Bertani, M. De Salve, A. Alemberti, B. Panella, "Thermal hydraulic analysis of a passively controlled DHR system", *Progress in Nuclear Energy*, 99, pp. 127-139, 2017. https://doi.org/10.1016/j.pnucene.2017.05.015

[96] M. Carelli, L. Conway, M. Dzodzo, A. Maioli, L. Oriani, G. Storrick, B. Petrovic, A. Achilli, G. Cattadori, C. Congiu, R. Ferri, M. Ricotti, D. Papini, F. Bianchi, P. Meloni, S. Monti, F. Berra, D. Grgic, G. Yoder, A. Alemberti, "The SPES3 Experimental Facility Design for the IRIS Reactor Simulation", *Science and Technology of Nuclear Installations*, 2009, 579430. https://doi.org/10.1155/2009/579430

[97] M. Caramello, M. Gregorini, M. De Salve, C. Bertani, A. Alemberti, B. Panella, "Thermal hydraulic analysis of Alfred bayonet tube steam generator", *Proceedings of the International Congress on Advances in Nuclear Power Plants (ICAPP 2015)*, Nice, France, May 3-6, 2015, pp. 838-845.

[98] A. Alemberti, M. Caramello, M. Frignani, P. Lorusso, F. S. Nitti, M. Tarantino, "ALFRED DHR system scaling verification and numerical pre-test analysis", *International Conference on Fast Reactors and Related Fuel Cycles FR22*, 2022.

[99] Dynalene Inc, "Dynalene MS-2 technical data sheet", 2020.

[100] J. C. Chen, "A correlation for boiling heat transfer to saturated fluids in convective flow", Brookhaven National Laboratory, Upton, New York, United States, pp. 2-6, 1962. BNL-6672. https://doi.org/10.2172/4636495

[101] W. Chen, X. Fang, "A note on the Chen correlations of saturated flow boiling heat transfer", *International Journal of Refrigeration*, 48, pp. 100-104, 2014. https://doi.org/10.1016/j.ijrefrig.2014.09.008

[102] J. C. Chen, "Correlation for boiling heat transfer to saturated fluids in convective flow", *Industrial & Engineering Chemistry Process Design and Development*, 5 (3), 1966. https://doi.org/10.1021/i260019a023

[103] H. K. Forster, N. Zuber, "Dynamics of vapor bubbles and boiling heat transfer", *AIChE*, 1 (4), 531–535, 1955. https://doi.org/10.1002/aic.690010425

[104] F. W. Dittus, L. M. K. Boelter, "Heat transfer in automobile radiators of the tubular type", *University of California Press*, Berkeley, California (1930), Vol 2, pp. 443-461.

[105] M. G. Cooper, "Heat flow rates in saturated nucleate pool boiling – A wide-ranging examination using reduced properties", *Advances in Heat Transfer*, 16, pp. 157–239, 1984. https://doi.org/10.1016/S0065-2717(08)70205-3

[106] V. Narcisi, L. Melchiorri, F. Giannetti, "Improvements of RELAP5/Mod3.3 heat transfer capabilities for simulation of in-pool passive power removal systems", *Annals of Nuclear Energy*, 160, 108436, 2021. https://doi.org/10.1016/j.anucene.2021.108436

[107] R. Ferri, A. Achilli, G. Cattadori, F. Bianchi, P. Meloni, "Design, experiments and Relap5 code calculations for the perseo facility", Nuclear Engineering and Design, 235 (10-12), pp. 1201-1214, 2005. https://doi.org/10.1016/j.nucengdes.2005.02.011

[108] F. Mascari, A. Bersano, F. Alcaro, M. Stempniewicz, L. Albright, T. Jevremovic, N. Andrews, R. Gauntt, H. Austregesilo, S. Buchholz, A. Bellomo, F. D'Auria, G. Di Palma, M. Lanfredini, G. Spina, C. Bertani, M. De Salve, N. Falcone, G. Caruso, F. Giannetti, V. Narcisi, C. Choi, K. Ha, B. G. Jeon, K. H. Kang, K. Kim, H. S. Park, I. Karppinen, L. F. Lahovský, R. Meca, Z. Parduba, P. H. Lien, D. Y. Tomashchik, L. Burgazzi, C. Lombardo, P. Meloni, R. Ferri, "OECD/NEA/CSNI/WGAMA PERSEO benchmark: Main outcomes and conclusions", *Nuclear Engineering and Design*, 405, 112220, 2023. https://doi.org/10.1016/j.nucengdes.2023.112220

[109] W. Nusselt, "Die Oberflachenkondensation des Wasserdampfes", Ver. deutsch. Ing. 60, 1916.

[110] M. M. Shah. "A General Correlation for Heat Transfer during Film Condensation Inside Pipes", *International Journal of Heat and Mass Transfer*, 22 (4), pp. 547-556, 1979. https://doi.org/10.1016/0017-9310(79)90058-9

[111] M. M. Shah, "An improved and extended general correlation for heat transfer during condensation in plain tubes", *HVAC&R Research*, 15 (5), pp. 889–913, 2009. https://doi.org/10.1080/10789669.2009.10390871

[112] M. M. Shah, "General correlation for heat transfer during condensation in plain tubes: further development and verification", *ASHRAE Transactions*, 119 (2), 2013.

[113] M. M. Shah, "Comprehensive correlations for heat transfer during condensation in conventional and mini/micro channels in all orientations", *International Journal of Refrigeration*, 67, pp. 22-41, 2016. https://doi.org/10.1016/j.ijrefrig.2016.03.014

[114] K. M. Vierow, V. E. Schrock, "Condensation in a natural circulation loop with noncondensable gases – Part 1: heat transfer", *Proceedings of the international conference on multiphase flows*, Tsukuba, Japan, September 1991. http://inis.iaea.org/search/search.aspx?orig_q=RN:24054054

[115] S. S. Kutateladze, "Heat transfer theory fundamentals", 1963, Atomizdat, Moscow/ Arnold Publishers, London/ Academic Press Inc., New York.

[116] F. Blangetti, E. O. Schlunder, "Local Heat Transfer Coefficients of Condensation in a Vertical Tube", *Proceedings of the 6th International Heat Transfer Conference*, 2, pp. 437-442, 1978.

[117] D. A. Labuntsov, "Heat transfer in film condensation of pure steam on vertical surfaces and horizontal tubes", *Teploenergetika*, 4 (7), pp. 72-79, 1957.

[118] D. Papini, A. Cammi, "Modelling of Heat Transfer Phenomena in Vertical and Horizontal Configurations of In-Pool Condensers and Comparison with Experimental Findings", *Science and Technology of Nuclear Installations*, 2010(1), 815754. https://doi.org/10.1155/2010/815754

[119] A. Bersano, N. Falcone, C. Bertani, M. De Salve, P. Meloni, F. Mascari, "Qualification of RELAP5-3D code condensation model against full-scale PERSEO Test-9", *Progress in Nuclear Energy*, 139, 103891, 2021. https://doi.org/10.1016/j.pnucene.2021.103891

[120] S. L. Chen, F. M. Gerner, C. L. Tien, "General film condensation correlations", *Experimental Heat Transfer*, 1 (2), pp. 93-107, 1987. https://doi.org/10.1080/08916158708946334

[121] M. Soliman, J. R. Schuster, P. J. Berenson, "A General Heat Transfer Correlation for Annular Flow Condensation", *Journal of Heat Transfer*, 90 (2), pp. 267-274, 1968. https://doi.org/10.1115/1.3597497

[122] F. P. Incropera, D. P. Dewitt, T. L. Bergman, A. S. Lavine, "Fundamentals of Heat and Mass Transfer", John Wiley & Sons, New York, USA, 2007.

[123] A. P. Colburn, O. A. Hougen, "Design of cooler condensers for mixtures of vapors with noncondensing gases", *Industrial & Engineering Chemistry*, 26 (11), pp. 1178-1182, 1934. https://doi.org/10.1021/ie50299a011

[124] https://www.iaea.org/projects/crp/i31038

[125] I. Di Piazza, H. Hassan, P. Lorusso, D. Martelli, "Benchmark Specifications For Nacie-Up Facility: Non-Uniform Power Distribution Tests", ENEA Report NA-I-R-542, CR Brasimone, 22 July 2022.

[126] G. Coccoluto, P. Gaggini, V. Labanti, M. Tarantino, W. Ambrosini, N. Forgione, A. Napoli, F. Oriolo, "Heavy liquid metal natural circulation in a one-dimensional loop", *Nuclear Engineering and Design*, 241 (5), pp. 1301-1309, 2011. https://doi.org/10.1016/j.nucengdes.2010.06.048

[127] I. Di Piazza, M. Angelucci, R. Marinari, M. Tarantino, D. Martelli, "Thermo-fluid dynamic transients in the NACIE-UP facility", *Nuclear Engineering and Design*, 352, 110182, 2019. https://doi.org/10.1016/j.nucengdes.2019.110182

[128] P. Cioli Puviani, A. Venturini, I. Di Piazza, V. Sermenghi, T. Del Moro, F. Papa, D. Martelli, R. Zanino, M. Tarantino, "Development of a thermal mass flow meter for heavy liquid metal applications", *Nuclear Engineering and Design*, 427, 113427, 2024. https://doi.org/10.1016/j.nucengdes.2024.113427

[129] R. Marinari, I. Di Piazza, M. Tarantino, M. Angelucci, D. Martelli, "Experimental tests and post-test analysis of non-uniformly heated 19-pins fuel bundle cooled by Heavy Liquid Metal", *Nuclear Engineering and Design*, 343, pp. 166-177, 2019. https://doi.org/10.1016/j.nucengdes.2018.12.024

[130] M. Angelucci, I. Di Piazza, M. Tarantino, R. Marinari, G. Polazzi, V. Sermenghi, "Experimental tests with non-uniformly heated 19-pins fuel bundle cooled by HLM", *Proceedings of the 26th International Conference on Nuclear Engineering (ICONE26)*, London, England, July 22-26, 2018. ICONE26-81216, V005T05A003. https://doi.org/10.1115/ICONE26-81216

[131] T. Del Moro, P. Cioli Puviani, B. Gonfiotti, I. Di Piazza, D. Martelli, C. Ciurluini, F. Giannetti, R. Zanino, M. Tarantino, "Analysis of the experimental tests performed at NACIE-UP facility through a novel CFX-RELAP5 codes coupling", *Nuclear Engineering and Design*, 429, 113676, 2024. https://doi.org/10.1016/j.nucengdes.2024.113676

[132] C. Ciurluini, M. Marra, V. Narcisi, G. Caruso, F. Giannetti, "Investigation of the fast flux test facility transient behavior during a loss of flow without scram test", *Nuclear Engineering and Design*, 428, 113534, 2024. https://doi.org/10.1016/j.nucengdes.2024.113534

[133] N. Forgione, D. Martelli, G. Barone, F. Giannetti, P. Lorusso, T. Hollands, A. Papukchiev, M. Polidori, A. Cervone, I. Di Piazza, "Post-test simulation for the NACIE-UP benchmark by STH codes", *Nuclear Engineering and Design*, 353, 110279, 2019. https://doi.org/10.1016/j.nucengdes.2019.110279

[134] I. E. Idelchik, "Handbook of hydraulic Resistance", 3rd edition, Jaico Publishing House, 2003.

[135] S. K. Chen, R. Petroski, N. E. Todreas, "Numerical implementation of the Cheng and Todreas correlation for wire wrapped bundle friction factors-desirable improvements in the transition flow region", *Nuclear Engineering and Design*, 263, pp. 406-410, 2013. https://doi.org/10.1016/j.nucengdes.2013.06.012

[136] S. K. Cheng, N. E. Todreas, "Hydrodynamic models and correlations for bare and wire-wrapped hexagonal rod bundles — Bundle friction factors, subchannel friction factors and mixing parameters", *Nuclear Engineering and Design*, 92 (2), pp. 227-251, 1986. https://doi.org/10.1016/0029-5493(86)90249-9

[137] OECD/NEA Nuclear Science Committee, "Handbook on Lead-bismuth Eutectic Alloy and Lead Properties", Materials Compatibility, edition, Thermal-hydraulics and Technologies, 2015.

[138] K. Gladinez, K. Rosseel, J. Lim, Y. H. Shin, G. Heynderickx, A. Aerts, "Determination of the lead oxide fouling mechanisms in lead bismuth eutectic coolant", *Nuclear Engineering and Design*, 357 (110382), 2020. https://doi.org/10.1016/j.nucengdes.2019.110382

[139] B. Chexal, G. Lellouche, "A Full-Range Drift-Flux Correlation for Vertical Flows (Revision 1)", EPRI NP-3989-SR, Electric Power Research Institute, September 1986. Available online at: https://www.epri.com/research/products/NP-3989-SR. Last visited: 19/09/2024.

[140] D. Martelli, R. Marinari, G. Barone, I. Di Piazza, M. Tarantino, "CFD thermo-hydraulic analysis of the CIRCE fuel bundle", *Annals of Nuclear Energy* 103, pp. 294-305, 2017. https://doi.org/10.1016/j.anucene.2017.01.031

[141] D. Grishchenko, I. Mickus, K. Kööp, M. Jeltsov, A. Karbojian, P. Kudinov, "TALL-3D experimental setup description for the first test series", SESAME Project, Deliverable N° D4.3.1_M09, 2015.

[142] P. Cioli Puviani, T. Del Moro, B. Gonfiotti, D. Martelli, C. Ciurluini, F. Giannetti, R. Zanino, M. Tarantino, "Performance evaluation of a coupled CFX-RELAP5 tool adopting experimental data from the TALL-3D facility", *Nuclear Engineering and Design*, 432, 113818, 2025. https://doi.org/10.1016/j.nucengdes.2024.113818

[143] C. S. Kim, "Thermophysical properties of stainless steels", ANL-75-55, 1975.

[144] F. R. Menter, "Two-equation eddy-viscosity turbulence models for engineering applications", AIAA-Journal., 32 (8), pp. 1598-1605, 1994. https://doi.org/10.2514/3.12149

[145] NEA, "Separate effects test matrix for thermal-hydraulic code validation", Vol. 1 and 2, NEA/CSNI/R(93)14/Part.1/Rev., OECD Publishing, Paris, September 1993. Nuclear Energy Agency (NEA) - Separate effects test matrix for thermal-hydraulic code validation, Vol.1 and 2, 1994.

[146] NEA, "CSNI integral test facility validation matric for the assessment of thermal-hydraulic codes for LWR LOCA and transients", NEA/CSNI/R(96)17, OECD Publishing, Paris, July 1996. Nuclear Energy Agency (NEA) - CSNI Integral Test Facility Validation Matrix for the Assessment of Thermal-Hydraulic codes for LWR LOCA and Transients

[147] NEA, "A state of-the-art report on scaling in system thermal-hydraulics applications to nuclear reactor safety and design", NEA/CSNI/R(2016)14, OECD Publishing, Paris, March 2017. Nuclear Energy Agency (NEA) - A State-of-the-Art Report on Scaling in System Thermal-hydraulics Applications to Nuclear Reactor Safety and Design

[148] F. D'Auria, G. M. Galassi, "Code validation and uncertainties in system thermalhydraulics", *Progress in Nuclear Energy*, 33, 1-2, pp. 175-216, 1998. https://doi.org/10.1016/S0149-1970(97)00097-8

[149] T. Del Moro, F. Giannetti, P. Cioli Puviani, I. Di Piazza, D. Diamanti, M. Tarantino, "Loss-of-heat-sink transient simulation with RELAP5/Mod3.3 code for the ATHENA facility", *Annals of Nuclear Energy*, 211, 110948, 2025. https://doi.org/10.1016/j.anucene.2024.110948

[150] M. Tarantino, P. Agostini, G. Benamati, G. Coccoluto, P. Gaggini, V. Labanti, G. Venturi, A. Class, K. Liftin, N. Forgione, V. Moreau, "Integral Circulation Experiment: Thermal-hydraulic simulator of a heavy liquid metal reactor", *Journal of Nuclear Materials*, 415 (3), pp. 433-448, 2011. https://doi.org/10.1016/j.jnucmat.2011.04.033

[151] P. Lorusso, A. Pesetti, M. Tarantino, V. Narcisi, F. Giannetti, N. Forgione, A. Del Nevo, "Experimental Analysis Of Stationary And Transient Scenarios Of ALFRED Steam Generator Bayonet Tube In CIRCE-HERO Facility", *Nuclear Engineering and Design*, 352, 110169, 2019. https://doi.org/10.1016/j.nucengdes.2019.110169

[152] P. Lorusso, A. Pesetti, G. Barone, D. Castelliti, G. Caruso, N. Forgione, F. Giannetti, D. Martelli, D. Rozzia, K. Van Tichelen, M. Tarantino, "MYRRHA primary heat exchanger experimental simulations on CIRCE-HERO", *Nuclear Engineering and Design*, 353, 110270, 2019. https://doi.org/10.1016/j.nucengdes.2019.110270.

[153] P. Lorusso, A. Pesetti, M. Tarantino, "ALFRED Steam Generator Assessment: design and pre-test analysis of HERO experiment", *Proceedings of the 2018 26th International Conference on Nuclear Engineering (ICONE26)*, London, England, July 22-26, 2018. ICONE26-81824, V06BT08A006. https://doi.org/10.1115/ICONE26-81824 .

[154] P. Lorusso, I. Di Piazza, D. Martelli, A. Musolesi, M. Tarantino, "Design of a novel test section for the LFR development: the CIRCE-THETIS facility", *28th International Conference on Nuclear Engineering (ICONE28)*, Virtual conference, August 4-6, 2021. ICONE28-65575, V002T07A032. https://doi.org/10.1115/ICONE28-65575

[155] M. Tarantino, P. Lorusso, A. Del Nevo, I. Di Piazza, F. Giannetti, D. Martelli, "Preliminary design of a helical coil steam generator mock-up for the CIRCE facility for the development of DEMO LiPb heat exchanger", *Fusion Engineering and Design*, 169, 112459, 2021. https://doi.org/10.1016/j.fusengdes.2021.112459

[156] G. Grasso, C. Petrovich, D. Mattioli, C. Artioli, P. Sciora, D. Gugiu, G. Bandini, E. Bubelis and K. Mikityuk, "The core design of ALFRED, a demonstrator for the European lead-cooled reactors", *Nuclear Engineering and Design*, 278, pp. 287-301, 2014. https://doi.org/10.1016/j.nucengdes.2014.07.032

[157] T. Del Moro, P. Lorusso, F. Giannetti, M. Tarantino, M. Caramello, D. Mazzi, M. Constantin, "ATHENA main heat exchanger conceptual design and thermal-hydraulic assessment with RELAP5 code", *ASME Journal of Nuclear Engineering and Radiation Science*, 9 (4), 041108, 2023. https://doi.org/10.1115/1.4056973

[158] D. P. Bentz, K. R. Prasad, "Thermal Performance of Fire Resistive Materials I. Characterization with Respect to Thermal Performance Models", NISTIR 7401, 2007, https://tsapps.nist.gov/publication/get_pdf.cfm?pub_id=860705

[159] J. R. Tallackson, "The thermal transport properties of helium, helium-air mixtures, water, and tubing steel used in the CACHE program to compute HTGR auxiliary heat exchanger performance", Oak Ridge National Laboratory (ORNL), United States, 1976. https://doi.org/10.2172/4028643

[160] P. A. Ushakov, A. V. Zhukov, N. M. Matyukhin, "Heat transfer to liquid metals in regular arrays of fuel elements, High Temperature", 15, pp. 868-873, 1977. Translated from Teplofizika Vysokikh Temperatur, 15 (5), pp. 1027-1033, 1977. https://www.osti.gov/biblio/7030158

[161] P. Cioli Puviani, "ATHENA Core Simulator. Thermo-Fluid Dynamic Design", ENEA Report AT-N-R-597, 2022.

[162] T. Del Moro, P. Cioli Puviani, "ATHENA Main Flow Path Analysis", ENEA Report AT-D-R-621, 2022.

[163] T. Del Moro, F. Giannetti, M. Tarantino, P. Lorusso, M. Caramello, D. Vitale Di Maio, M. Constantin, "Thermal-Hydraulic Characterization and Numerical Modelling with RELAP5 Code of ATHENA Secondary Loop", *Nuclear Technology*, 210 (4), pp. 591-607, 2023. https://doi.org/10.1080/00295450.2023.2183025